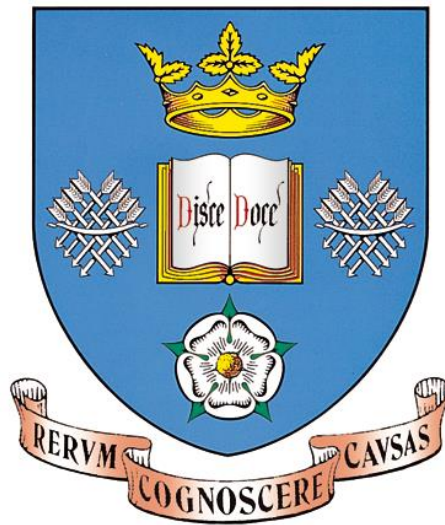**THE UNIVERSITY OF SHEFFIELD**

Axial field permanent magnet machines with high overload capability for transient actuation applications

By

Jiangnan Gong

ABSTRACT

This thesis describes the design, construction and testing of an axial field permanent magnet machine for an aero-engine variable guide vane actuation system. The electrical machine is used in combination with a leadscrew unit that results in a minimum torque specification of 50Nm up to a maximum speed of 500rpm. The combination of the geometry of the space envelope available and the modest maximum speed lends itself to the consideration of an axial field permanent magnet machines. The relative merits of three topologies of double-sided permanent magnet axial field machines are discussed, viz. a slotless toroidal wound machine, a slotted toroidal machine and a yokeless axial field machine with separate tooth modules. Representative designs are established and analysed with three-dimensional finite element method, each of these 3 topologies are established on the basis of a transient winding current density of $30A/mm^2$. Having established three designs and compared their performance at the rated 50Nm point, further overload capability is compared in which the merits of the slotless machine is illustrated. Specifically, this type of axial field machine retains a linear torque versus current characteristic up to higher torques than the other two topologies, which are increasingly affected by magnetic saturation. Having selected a slotless machine as the preferred design, further design optimization was performed, including detailed assessment of transient performance. A key feature of this design is the use of a solid (i.e. non-laminated) toroidal stator core. This provides a stator with increased mechanical robustness, improved heat transfer and a ready means of incorporating fixing points into the core. However, these advantages are gained at the expense of a significant eddy currents in the stator core. A series of three-dimensional, magneto-dynamic finite element simulations were performed. Although the resulting eddy current losses are excessive for continuous operation, the reduction in transient performance which results from the eddy currents is shown to be manageable. The loss analysis is supplemented by transient three-dimensional finite element thermal modelling. Three-dimensional mechanical analysis is performed in combination with analytical equation to analyse the stator and rotor plate deflection subject to axial attractive force.

I

The construction of a prototype double-sided axial field machine is described in this thesis which contains several interesting design features including a profiled rotor core to reduce mass, radially magnetised rotor magnets to produce torque from the axially oriented conductors on the inner edge of the toroidal winding. The testing of the machine is performed under a series of load points up to 75Nm to validate the predicted torque versus current density characteristics.

ACKNOWLEDGEMENT

Contents

NOMENCLATURE

Symbol	Definition	Unit
A	Contact surface area between the magnet face and the rotor core	m^2
A_{coil}	Surface area of coil	m^2
A_m	cross-sectional area of the magnet orthogonal to the direction of the magnetisation	m^2
A_{pole}	Surface area of magnet pole	m^2
A_s	Surface area of stator	m^2
A_t	Surface area of tooth tip	m^2
B	friction coefficient	-
B_{core}	Flux density in core	T
B_g	Airgap flux density	-
B_{gz}	Airgap flux density along z-axis	T
B_{peak}	Peak flux density	T
B_r	Remanence of magnet material	T
c_{Cu}	Specific heat capacity of copper	$Jkg^{-1}K^{-1}$
c_v	Specific heat capacity of copper	$Jkg^{-1}K^{-1}$
D	Plate constant	-
D_i	Inner diameter	m
D_o	Outer diameter	m
d_{ci}	Inner diameter of the containment	m
d_{co}	Outer diameter of the containment	m
d_{mi}	Inner diameter of the magnet	m
d_{mo}	Outer diameter of the magnet	m
E	Young's modulus	Pa

F	Force	N
f	Frequency	Hz
F_{cen}	Centrifugal loading	N
G	Shear modulus	Pa
h	Airgap heat transfer coefficient	W/m^{2}K
h_c	Coil thickness	m
I_{pk}	Peak phase current	A
J	Moment of inertia	kg·m^2
J_{pk}	Peak current density	A/m^2
J_{rms}	RMS current density	A/m2
k_e	EMF factor	-
k_{ex}	Excess loss coefficient	-
k_{hyst}	Hysteresis loss coefficient	-
k_i	Current waveform factor	-
k_p	Coil packing factor	-
k_{pw}	Power factor	-
k_1	Copper thermal conductivity	W/mK
k_2	Impregnation material thermal conductivity	W/mK
L	Coil length	m
l_g	Airgap length	m
l_m	Magnet length	m
l_s	Thickness of stator	m
l_{tot}	total width comprised by racetrack conductors over a whole circle	m
m	Mass of the object	kg

m_{eq}	Equivalent mass of the magnet	kg
M_r	Unit radial bending moment	N.m
N_c	Number of coils per phase	-
N_s	Number of slots	-
N_t	Number of turns	-
N_u	Nusselt number	-
n_p	Number of phases	-
n_s	Number of phases of each stator	-
P_{ed}	Eddy current loss	W
P_{ex}	Excess loss	W
P_{hyst}	Hysteresis loss	W
p	Number of pole	-
Q	Energy loss in winding	J
q	Stress	Pa
q_t	Heat flux density	W/m^2
Q_e	Electrical loading	A/m
Q_f	Unit shear force	Pa
$R_{e\delta}$	Reynolds number	-
R_g	Reluctance of airgap	H^{-1}
R_{re}	Copper resistance at reference temperature at 20^{0}C	Ω
r$_{ave}$	Average radius	m
r_i	Inner radius	m
r_{meq}	Equivalent radius of the magnet	m
r_o	Outer radius	m
s	Split ratio	-

T	Temperture	^{0}C
T_a	Taylor number	-
T_e	Output torque	Nm
T_l	Load torque	Nm
T_{ref}	reference temperature of 20^{0}C	^{0}C
V	Element volume	m^3
v	Poisson's ratio	-
w_t	Width of the slot tooth	m
w_{t1}	Width of slot tooth taken from the inner edge to form a trapezoidal shape slot	m
α	Magnet pole arc	^{0}
α_T	Temperature coefficient of resistance for copper	K^{-1}
β	Proportion of coil occupies overall coil span	-
γ	Proportion of the conductor covering at the inner edge of the coils	-
y_r	Maximum deflection of rotor	m
y_s	Maximum deflection of stator	m
δ	The proportion of conductors cover the pole face	-
η	Efficiency	-
μ_o	Permeability of free space	H/m
μ_r	Relative permeability	-
ρ_c	Density of copper	kg/m^3
ρ_{ct}	Density of the containment material	kg/m^3
ρ_{Fe}	Core material density	kg/m^3
ρ_{ip}	Inter pole density	kg/m^3
ρ_m	Density of the magnet	kg/m^3

XI

σ_{Fe}	Electric conductivity of the core material	S/m
σ_{max}	Maximum hoop stress on the inner bore of the containment	Pa
τ	Shear stress	Pa
Φ_r	Maximum flux entering tooth	Wb
ω	Rotational speed	Rad/s

CHAPTER 1.   INTRODUCTION

1.1   Motivation and objective of the work

There are many aerospace actuation applications, both on the airframe and within the aero-engine, in which electrical machines are being considered as replacements for the incumbent mechanical or hydraulic systems. Actuation applications, in which the electrical machine is usually used in tandem with mechanical elements such as high reduction gearboxes, leadscrews or hydraulic pumps are variously characterised by the following features:

- They are extremely demanding in terms of torque density and response time but not necessarily in terms of continuous power rating.

- Many applications have very intermittent duty cycles and hence the electrical machines must have high transient over-load capability.

- In order to locate the electrical machine in close contact with the mechanical end-effector, the space envelope into which the machine must be accommodated can often be constrained and require extremes of machine aspect ratios.

For some of these features of actuation applications, axial field machines may provide good fit with their combination of high torque density performance and short axial length.

The programme of research undertaken and reported in this thesis has the following objectives:

1. Establish the feasibility of employing electrical actuation for an aero-engine variable guide vane, particularly in terms of short-term torque density.

2. To develop and validate design and analysis methods for permanent magnet (PM) axial field machines encompassing electromagnetic, mechanical and thermal behaviour.

3. Design, optimise, manufacture and test a prototype axial field machine which embodies several novel design features.

1.2 Variable guide vane drive

Variable guide vanes are located within the stationary section of aero-engine compressors. A typical compressor comprises several stages of rotor blades arranged axially along a shaft each separated from the next stage by a set of stator vanes. These rotating and stationary elements work in tandem to progressively raise the pressure of the incoming air as shown in the schematic of Figure 1. 1. As shown the stationary vanes reverse the direction of the airflow generated by the preceding rotor section.
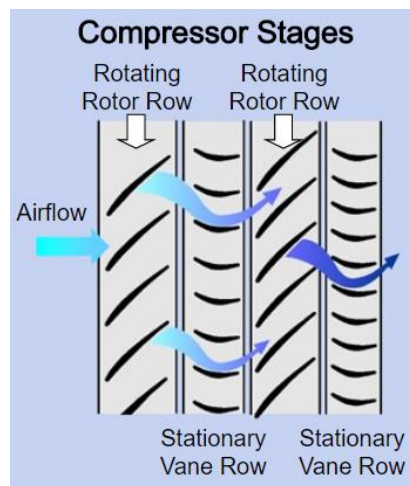
Figure 1. 1. Schematic of compressor action (Source: Rolls-Royce)

Aero-engines are required to operate a wide range of operating conditions from maximum thrust at take-off and climb to near idle conditions as an aircraft comes in to land. In order to optimise the operability and efficiency of the engine, it is commonplace to vary the angle of the stationary vanes for different operating conditions. This so-called Variable Stator Vane system (VSV) or Variable Guide Vane (VGV) is controlled by the engine management to position the stator vanes at the optimum angle. The angular movement of the adjustable vanes is usually achieved by an actuation system operating through a so-called unison ring as shown in Figure 1. 2.[1]

The unison rings are often driven by a series of actuators arranged around the periphery of the engine to both equalise the loading around the rings and provide some redundancy. The actuators, which are generally hydraulic in current systems, rotate the unison rings which are connected to one end of each vane. The other end of each vane is connected to a rotating pivot point to translate a small rotation of the unison-

ring around the engine into rotation of each individual blade to a defined angle. As will be apparent from the schematic of airflow in Figure 1. 1, there are large aerodynamic forces acting on each vane. The actuation mechanism is required to counteract these large forces. This is achieved through a combination of a high force density hydraulic actuator and a significant mechanical advantage through the series of rings and levers.
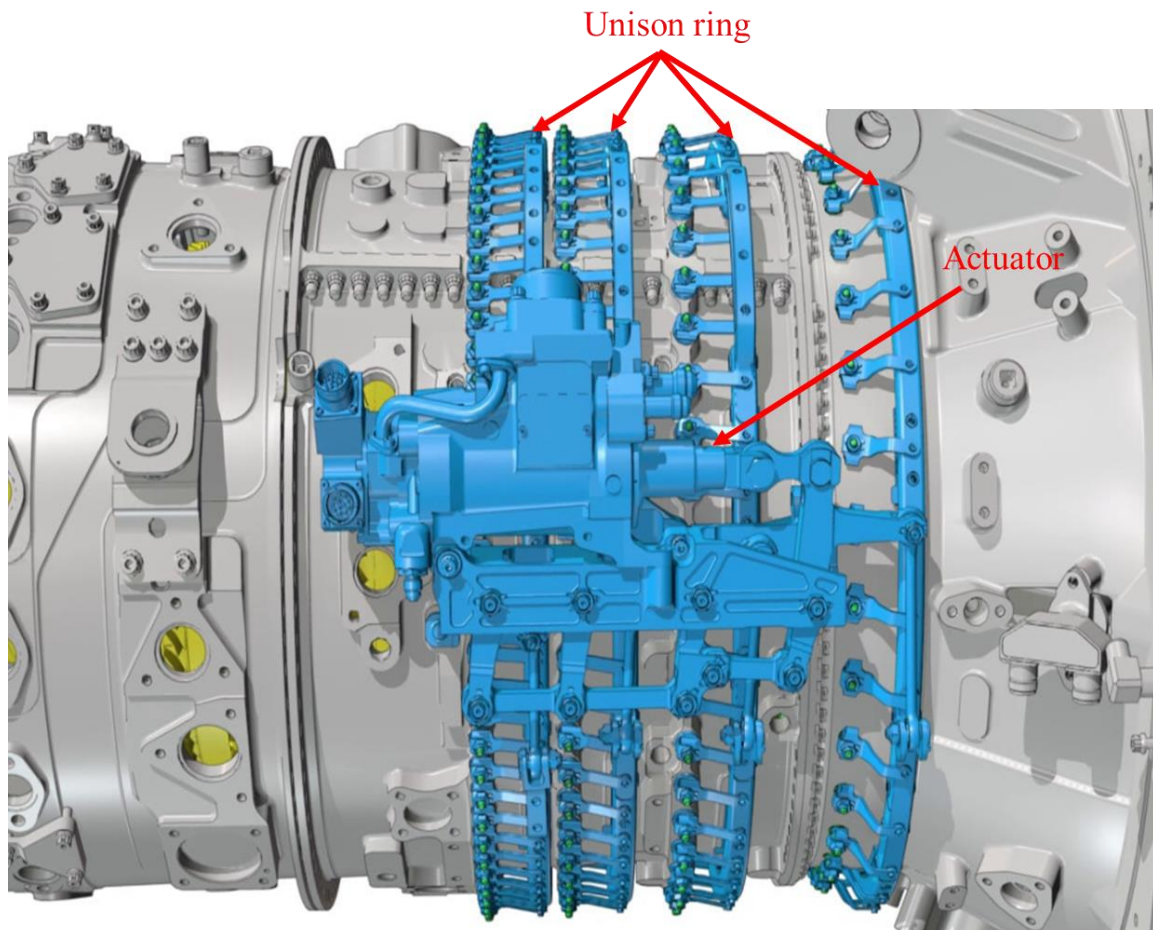
Figure 1. 2. Typical unison-ring VGV actuation system (Source: [1])

Although VGV actuation systems of the type shown in Figure 1. 2 with hydraulic actuation are widely used and perform their function reliably and with low mass, there is interest in the use of electro-mechanical systems for stator guide vane actuation. This is part of a wider interest in the electrical actuation of aero-engines sub-systems to enhance controllability and performance. These wider applications include entirely new actuation opportunities and the replacement of pneumatic and hydraulic

mechanisms in more established variable elements [2]. Electrical actuation provides the following advantages over hydraulic actuation:

- The control of the electric machine is more precise and potentially reconfigurable
- Electrical systems offer potential for reduced maintenance compared to hydraulic systems.
- Electrical systems provide many opportunities for precise and cost-effective equipment health monitoring (EHM).

The electrical actuation (E-actuation) of aero-engine stator guide vanes poses an interesting set of space and performance requirements. One interesting requirement is that to integrate an E-actuation systems around the engine casing there is a need to have a very low profile machine, i.e. a short axial length. The actuation system would be based on a very ratio leadscrew whose design requires a high torque (50Nm) and a relatively low speed input (max. 500rpm) because of the already high ratio. Both of the factors suggest that a strengths of permanent magnet axial field machine may well be a good fit to this application, e.g. high torque and modest speeds, compact and low profile geometry. Indeed, axial field machines had already been identified during an initial concept study as an attractive solution to the particular needs of this application.

Compared with radial field PM machines of the same mass, axial field PM provide higher torque density, compact planar construction which could fit some particular space envelope, also a planar and potentially adjustable airgap.

The top-level performance requirements for each electrical machine in the actuation system are summarised in Table 1. 1 - VGV E-actuation top-level specificationTable 1. 1. Whereas this set of performance specifications and features provides a useful starting point, the final size of the machine will be highly dependent on the duty cycle, in particular whether the 50Nm constitutes a near continuous rating or highly intermittent rating. Meeting the desired torque density target for a continuous 50Nm is likely to be extremely challenging given the limited cooling and space available. However, a more complex duty cycle in which the torque is markedly lower than 50Nm for much of the time, would allow the thermal mass of the machine to be exploited so as to significantly reduce the mass of the machine. A series of designs have been synthesised, based on

4

various incremented levels of current density in the stator coils. The higher values considered (i.e those above 8-10A/mm^2) are unlikely to be sustainable on a continuous basis, but provide a quantitative illustration of the benefits in mass which could be realised by fully exploiting the thermal capability of the machine and match closely to the anticipate duty. This also permits a useful level of design to be performed in the absence of a detailed representation of the cooling at this preliminary stage. Unfortunately, detailed operating cycles were not available for this application. The specification was therefore necessarily based on some simplifying assumptions for the machine performance specification. For the purposes of designing the machine, a broad-brush specification of ~20-30s intervals of rated torque was assumed with large gaps between such intervals which allowed the machine to cool down between successive cycles. It is worth noting that the programme of research in this thesis is based on developing an understanding of several different aspects of axial field machine behaviour and performance rather than establishing a very precise design to meet a particular detailed specification. Hence, the absence of a details duty cycle was not a first-order concern for this research.

Table 1. 1 - **VGV E-actuation top-level specification**

Feature	Value
Rated torque	50Nm
Maximum rotational speed	500rpm
Maximum rated power	~2kW
Transient overload capability	200% of rated for 1 second
Cooling	Air-cooled
Target torque density	>10Nm/kg

1.3 General features of axial field machines

Axial field machines, which are also occasionally referred to in literature and practice as 'pancake motors' or 'disc machines', differ very significantly from the more conventional radial field machines. It is worth noting that most electrical machine types have an axial field equivalent, e.g. axial field induction machines [3] and axial flux switched reluctance machine [4].

Axial field machine has been the subject of much in particular for applications requiring short axial length machines. However, there are many fewer publications on axial field machines than radial field machines. The short axial length of the axial field machine provides good fits for applications such as the wheel motor for electrical vehicles [5] or for elevator motors [6] and electric window actuation mechanisms. Due to its unique compact geometry, axial field machines are usually used in integrated applications which requires high torque density.

There are several claimed advantages offered by axial field machine in literature [7][8]:

- Disc shaped rotor and stator structure and large diameter to axial ratio

- Higher torque to weight ratio which lead to less core material and higher efficiency

- More compact machine than its radial flux counterpart in high torque, low speed applications it is smaller in size

- Adjustable and planar airgap which in principle provides a means of modulating the net permanent magnet flux in the machine over the operating range of the machine.

However, they also have many recognised drawbacks:

- Require significant structural elements to withstand high axial forces on the rotor in order to maintain a precise airgap. Indeed, in larger machines, the overall mass can become dominated by structural as opposed to active elements.

- Limited speed capability due to centrifugal loading on the disk shaped rotor(s)

- Stators are not amenable to the use of laminations, at least in a straightforward manner

- Heat transfer from the stator winding can be problematic, particularly in double-sided topologies.

Among the various type of axial field machine, PM variants offers some unique features. PM machines tend to achieve high airgap flux densities with small rotor loss (compared to an induction machine or wound-field machine). This is particularly the case with high performance rare earth permanent magnet materials.

Despite having the potential for high torque density, the case for high power density in the axial field machines is less convincing.

The output power of a permanent magnet radial field machine can be defined by this general purpose sizing equation [9],[10]

$$P_R = \frac{n_p}{n_s} \frac{\pi}{2} K_e K_{pw} K_i \eta B_g A \frac{2f}{p} s^2 D_o{}^2 L_e \qquad (1.1)$$

While for permanent magnet axial field machine, the output power is expressed by

$$P_A = \frac{n_p}{n_s} \frac{\pi}{2} K_e K_{pw} K_i \eta B_g A \frac{2f}{p} (1 - s^2) \frac{1+s}{2} D_o{}^3 \qquad (1.2)$$

Based on these sizing equation, it can be seen that for an axial field machine, the power is proportional to $D_o{}^3$ while for a radial field machine, it is proportional to $D_o{}^2 L$. The $D_o{}^3$ relationship is a scaling which is greater than the scaling of mass, while for the radial field machine the $D_o{}^2 L$ scaling is the same as the mass scaling. This would suggest that axial field machines have an inherent torque and power density advantage over radial-field machines.

However, in practice this does not directly lead to a conclusion that the power density of the axial field machine is higher than a radial field machine in most applications. It can be observed from the equations that the power density is closely related to the split ratio $s = \frac{D_i}{D_o}$, By optimizing the value for s, the maximum power density can be obtained. Optimal values of s are determined by multiple factors such as machine topology, electrical loading, flux density, and cannot be universally applied.

Although the conclusion that an axial field machine offer higher power density over radial field machine (particularly as the diameter increase) cannot be universal drawn from these equations, there are examples in literature [11] of rare-earth PM axial field machines achieving power densities which is 3 times that of a traditional induction machine.

1.4 Review of main axial field permanent magnet machine topologies

In this section, the various types of axial field machine are described and the merits and drawbacks of each type are discussed. Axial field machine topologies can be divided into several groups from the point of view of construction, being either single sided, double sided or multistage, equipped with a stator core or coreless, and equipped with slots or slotless cores. For the double sided axial field topologies, the rotor can be either internal or external, and the magnet can be surface mounted or embedded [12]. A means of categorising axial field PM machines is shown in Figure 1. 3.
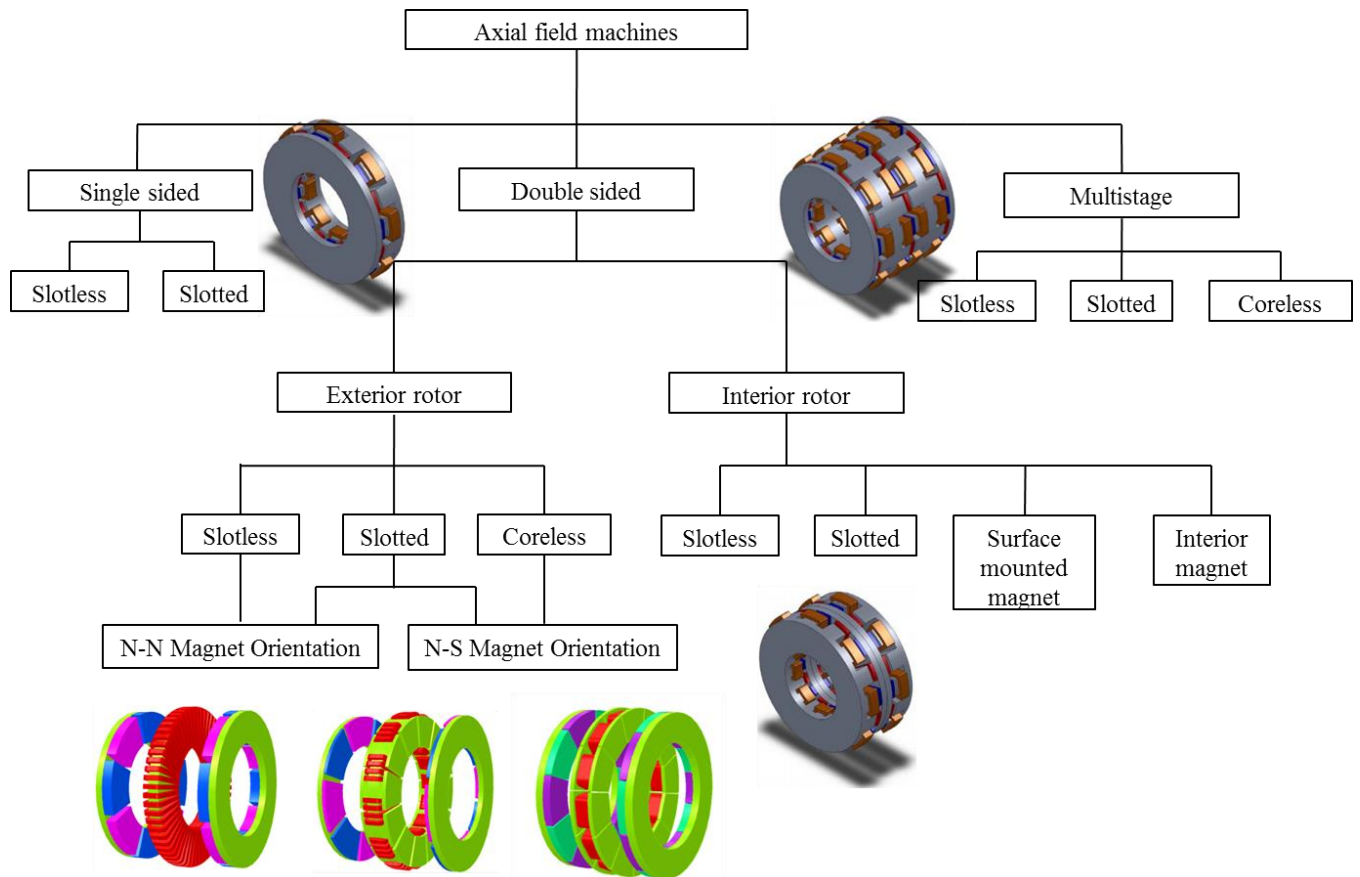
Figure 1. 3. Topology variations of the PM Axial field machine [13]

Single-sided topologies

A single sided topology represents a single rotor- single stator structure, with the stator being either slotted or slotless. A single sided machine is simpler than the double sided and multistage topologies from the construction point of view, although this is usually at the expense of lower torque capacity. In addition, unbalanced axial force between rotor and stator is also a drawback, requiring additional structural support, even though the axial attractive force would be smaller with a slotless stator as it has a larger airgap. It also requires a thicker rotor back iron plate based on either electromagnetic or mechanical consideration.

Double-sided topologies

A double-sided topology can be either two rotor – one stator arrangement or two stator – one rotor. They usually have a higher torque capacity than their single sided counterparts. The two rotor – one stator construction is equipped with two external facing rotors located on either side of a central stator. There are many variations that can be found in both stator structure and rotor magnet arrangement. The stator can be slotless, slotted and even coreless. To enable topologies with slotless stator structure, only north-to-north magnet orientation on the rotor is employed. As for the slotted stator, both north-to-south and north-to-north magnet orientations can be used by alternating the winding configuration which will be discussed in detail in the following sections. The coreless stator in the double-sided topology is formed by several segments and some external mechanical constraints. The magnet arrangement in this topology is always north to south.

The two stator – one rotor geometry has an interior rotor and two slotted or slotless stators on either side. The rotor magnet location can be surface mounted, which is by far the most common, or interior embedded. In common with radial-field machines, embedded magnet arrangements provides a higher armature reaction than surface mounted structure, which can be beneficial for field weakening but at the expense of higher leakage flux in magnet ends. A double sided stator arrangement offers potential for redundancy since the machine can still operate even with one stator winding faulted. However, if the machine is to be operated in this mode, the mechanical design needs to take into account the increased axial force on the rotor.

Multistage topology

Normally, if a higher rated torque is required machine parameters such as machine outer diameter is scaled up to achieve the goal. However, often there is limit on the outer diameter that can be used, e.g. centrifugal loading or space constraints. An alternative in such circumstances is to employ several stator and rotor arranged on the same shaft which is often called multistage topology [14]. The assembly of an axial field machine can be easier than the radial field machine since the surface area of the airgap remains constant as machine stacked up [15].

Among all possible topologies double sided exterior rotor topologies are often regarded as offering the best torque density and efficiency. They have found niche applications in low powers, where they offer a compact and cost-effective solution. In terms of axial field machines of meaningful power ratings and torque densities, these tend to be based on a pair of permanent magnet rotors which are mechanically connected to each other and stacked either side of a single stator structure comprising stator coils and some form of soft magnetic core. Of the topologies that have been shown to be capable of achieving high torque densities, arguably the leading options are various toroidal core type machines (often referred to as TORUS type machines) and modular machines, of which the most high profile of late is the range of YASA motors [16]. Within the broad category of TORUS type machines, the stator can be either slotted or non-slotted, with general designations in the literature of TORUS-S and TORUS-NS respectively.

1.4.1   TORUS non slotted

A non-slotted version of a TORUS machine is shown in Figure 1. 4. The structure consists of a slotless stator based on plain toroidal core equipped with a so-called 'airgap' windings and two rotors on either side with axially magnetized permanent magnet poles of alternating polarity.

A schematic representation of the flux paths within this machine is shown in Figure 1. 4. The flux is driven by the N pole magnet through the airgap and passes circumferentially along the stator core until it returns to the adjacent S pole magnet, ultimately returning to the original N pole magnet via the rotor core. The stator core must be dimensioned to carry the flux from both sides circumferentially through the core without saturating. The absence of stator slots essentially eliminates cogging torque in this type of TORUS-NS machine [17]. This machine is characterised by compact end-windings and is amenable to direct surface cooling of the winding. However, the large effective magnetic airgaps in these machines (which is made up of the mechanical clearance and the axial thickness of the stator coil) dictates that they tend to have lower torque densities than their slotted counterpart.
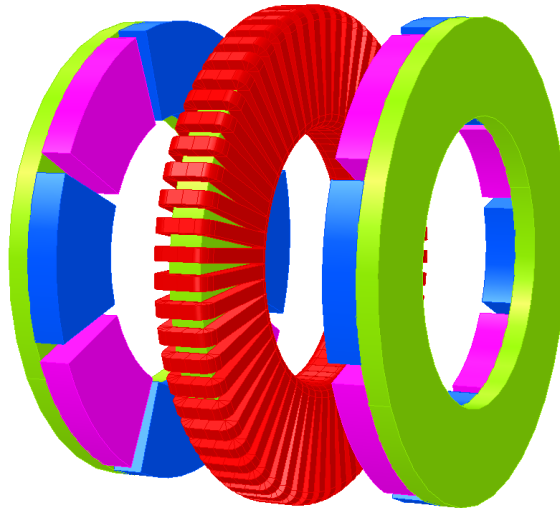
Figure 1. 4. Exploded view of a representative double-sided TORUS-NS type axial field permanent magnet machine
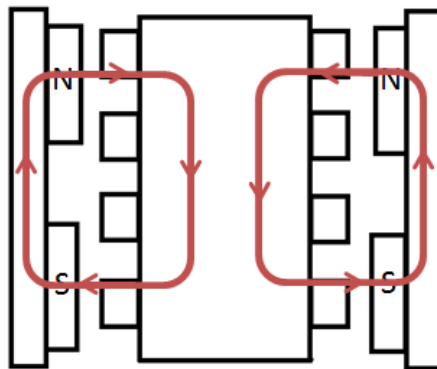
Figure 1. 5. Schematic representation of flux paths in a TORUS-NS machine

1.4.2 TORUS slotted

The basic structure of the TORUS-slotted (TORUS-S) machine has many similarities with the TORUS-NS machine, in that it is also employs a single stator with two rotors. The rotor structures are essentially identical in general layout as the same as the TORUS-NS machine, although there is scope to use thinner magnets given the greatly reduced magnetic airgap. The stator on the other hand is a far more complex arrangement which in many aspects mimics the layout of a conventional machine in which the stator winding is incorporated within stator slots.

The topology can be divided into two types based on the orientation of the magnets on the two rotor cores, viz. the so-called NN type and the NS type. Schematic flux paths for these two variants are shown in Figure 1. 6. The nature of the flux path for NN type is similar to the non-slotted TORUS-NS machine, albeit that the effective magnetic airgap is now much shorter. The physical structure of the NS type is similar to the NN type other than the stator yoke can be reduced since the flux path does travel circumferential along the stator.

The winding structure in the NN and NS types are rather different. In the NN type, either a back-to-back winding or a lap winding can be used, but in NS type, only a lap winding is capable of producing torque. However, this lap winding can lead to the poor fill factor and long end windings [18] [19]. When compared to a non-slotted TORUS-NS machine, the greatly reduced airgap will lead to a combination of increased airgap flux density and/or reduced magnet axial length. This will tend lead to higher torque densities, at least at current densities that are likely be sustainable on a continuous basis. This increased torque density is however gained at the expense of greater complexity and increased axial force on the rotors (which may require additional stiffening depending on the rotor back iron thickness and properties).

One important consideration in the design, manufacture and performance of slotted TORUS machines is the difficulty in producing the intricate shaped core in a material of low core loss. The complex geometry is not readily suited to being laminated, although tape-winding of thin sheet steel with progressive individual slot stamping or post-winding machining of the slots have been proposed [20]. Alternatively, soft magnetic composites (which consist of near full density pressed iron powder in a binder) have been proposed as a means of producing a single piece intricate core with reasonable low levels of loss and relative permeability of the order of many hundreds [21][22]. However, the mechanical integrity and long-term stability of such composites remains an issue to be fully explored.

NN type   NS type
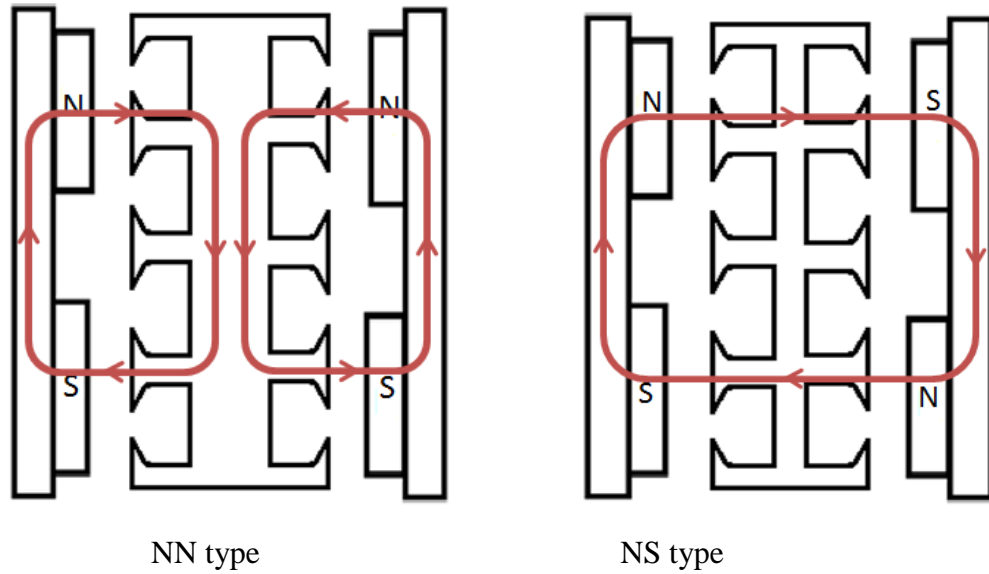
Figure 1. 6. Schematic flux paths in two variants of the TORUS-S axial field machine

1.4.3 YASA topology

Despite numerous claims of novelty, the so-called YASA topology (**Y**okeless **A**nd **S**egmented **A**rmature) has a great deal in common established topologies, notably the NS type TORUS-S type machine, albeit with some important distinctions. The stator consists of a series of separate stator tooth modules that are not magnetically connected to each other, which gives rise to the designation of yokeless (yoke being a historical term for the back-iron). The basic geometry of a YASA motor is shown in Figure 1. 7. The individual tooth modules have a face adjacent to the airgap which spans the majority of the tooth pitch to collect the airgap flux. The cross-section is then reduced to form the main body of the tooth around which a simple coil which can be readily wound.
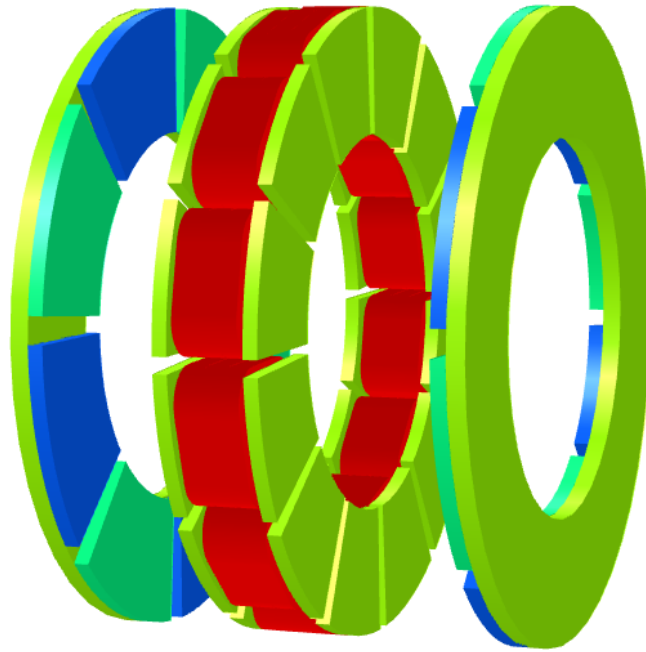
Figure 1. 7. Exploded view of a representative double-sided YASA type axial field permanent magnet machine

In many respects, the YASA topology attempts to combine the positive features of both NN and NS type TORUS-S machines. Since it employs an NS arrangement of magnets, there is no significant circumferential flux path in the stator and hence the individual teeth can be separated. This allows a compact coil to be used, overcoming the main drawback of the need for a lap winding with a NS type TORUS-S machine.

As is the case with TORUS-S type machines, the stator core (in this case a series of tooth modules) are not readily amenable to being manufactured from laminated core material. Again, soft magnet composites tend to be promoted as the preferred means of manufacturing these tooth modules. The recent launch of products based on this machine topology by YASA Motors [23] provides some interesting claimed performance data, as summarised in Table 1. 2**Error! Reference source not found.**. These are all oil-cooled machines (fairly high flow rate of 6 to 10 Litres/min) and the ratings are qualified as being subject to the thermal conditions and duty cycle.

It is interesting to note, that in terms of continuous ratings, these are very competitive in terms of torque density with published ratings of radial field machines for traction

applications, but the power densities are rather less compelling. This is in part due to the limited speeds which can be achieved.

Table 1. 2 YASA motor performance data

	YASA 250*	YASA 400	YASA 750
Overall diameter	280mm	280mm	350mm
Axial length	66mm	75mm	66mm
Total mass	18kg	24kg	33kg
Peak torque	250Nm	360Nm	790Nm
Continuous rated torque	160Nm	250Nm	400Nm
Max. rotational speed	9000rpm	7500rpm	3250rpm
Continuous power	65kW	85kW	75kW
Continuous rated torque density	8.9 Nm/kg	10.4 Nm/kg	12.1 Nm/kg
Continuous rated power density	3.6kW/kg	3.54kW/kg	2.27kW/kg

* - now discontinued

1.5 Thesis Structure

The remainder of this thesis addresses many of the axial field performance issues is introduced in this chapter and is structured as follows:

- Chapter 2 introduces the material selection issues, sizing equations and explores flux density calculation and pole number selection.
- Chapter 3 compares the performance of three alternative topologies of machines.
- Chapter 4 presents detailed electromagnetic, loss and thermal performance predictions for a preferred design.
- Chapter 5 describes the mechanical design and optimisation of a prototype machine to meet the performance specification.
- Chapter 6 describes the construction of a prototype machine.
- Chapter 7 describes the testing of a prototype machine.
- Chapter 8 provides some conclusions to the research

CHAPTER 2.   BASELINE DESIGN AND ANALYSIS OF REFERENCE MACHINE TOPOLOGIES

2.1   Introduction

On the basis of the specification of the VGV e-actuation detailed in Chapter 1, design methodologies are developed for TORUS machines of both slotted and non-slotted variants. The materials used in permanent magnet electrical machines are reviewed and sizing equations of the two topologies established. Initial dimensions for both topologies are generated from the sizing equation, including the use of both two- and three-dimensional finite element methods for in-depth investigations into methods for calculating airgap flux densities.

2.2   Design methodology

Analytical design equations provide a useful starting point for the sizing and design of electrical machines. Although some useful analytical design and analysis equations have been developed for the analysis of various of axial field machines topologies [24] [25] [26], many of these are reliant on several assumptions. The geometries of axial field machines and the resulting magnetic field distributions are not well suited to one-dimensional or often even two-dimensional analysis due to the very pronounced three-dimensional nature of the magnetic field.

Numerical analysis techniques such as finite element analysis are essential for detailed modelling and optimisation of design features, as well as for the investigation of novel topologies with complicated geometries. Two-dimensional finite analysis method can also be used to predict some aspects of machine behaviour, usually with some empirical corrections factors, but ultimately recourse to three-dimensional finite element analysis is required to capture the full behaviour and impact of design trade-offs. Three-dimensional finite element analysis offers the opportunity to build a model of the full geometry, while also accommodating the non-linear behaviour of magnetic materials and generating performance predictions with relatively few assumptions.

The key challenge, particularly for machines with airgap windings (which are more common in axial field rather than radial-field machines) is the prediction of the airgap

flux density. Well-established one-dimensional design equations for predicting the airgap flux density tend to produce poor estimates due the presence of significant end-effects and inter-pole flux leakage.

In radial-field machines, reliable estimates of airgap flux density can be derived without many of the dimensions of the machine having been specified. The remaining dimensions of the machine can then be sized on the basis of this flux density, resulting in an initial design. This may require some refinement, but there is clear progression starting from a simple flux density estimate.

There is a challenge in the design of axial field machines, particularly airgap winding machines, since the absence of a simple method for predicting airgap flux density makes initial sizing difficult while the flux density can only be predicted with a reasonable degree of precision for a specific set of dimensions. This circular problem can be tackled by starting with an initial representative value of flux density in combination with analytical design equations to undertake initial sizing followed by iterations of the flux density calculation and subsequent dimensions using finite element analysis.

2.2.1 Finite element analysis

The finite element modelling package used for the detailed modelling of axial field machines considered in this thesis project is the OPERA suite of programs developed by Vector Fields. It provides a powerful finite element environment for the design and analysis of electromagnetic devices such as motors, generators, actuators and magnet circuits in both 2D and 3D. The overall package includes various electromagnetic analysis modules which include static and continuous analysis method, thermal and mechanical analysis programmes. The package includes both geometric modelling and post process capabilities [27][28].

OPERA 2D magneto-static package has been used for preliminary estimation of the airgap flux density in this chapter. However, for the vast majority of the modelling undertaken in this thesis, three-dimensional magneto-static and magneto-dynamic analysis proved necessary. This was achieved using the OPERA 3D package. This includes transient electromagnetic analysis with motion in the machine optimisation studies discussed in chapter 4. The mechanical and thermal capability of OPERA 3D

has been used for predicting deformation of the rotor due to attractive forces and temperature rise within the machine due to losses.

2.3 Material selection

Before establishing the key dimensions, it is necessary to select the materials to be used in the machine, specifically for the rotor permanent magnets and the cores of the stator and rotor. In common with many aerospace applications, there are a number of considerations that influence the choice of magnetic materials in this case:

- There is a significant premium associated with mass savings that can offset the use of high cost materials.
- Long-term reliability is critical and therefore long-term intrinsic material stability is a key requirement.
- The local environment will include periods of elevated temperatures and hence good temperature stability is likely to be important.

2.3.1 Rotor permanent magnet materials

There are two hard magnetic materials commonly considered for use in high performance electrical machine, viz. Samrium Cobalt (SmCo) and Neodymium Iron Boron (NdFeB). However, before considering the properties of these two materials, it is useful to consider briefly the historical development of permanent magnet materials. The first permanent magnets of any technical value were the various Alnico materials that were developed in the early 1930s. Their properties were improved significantly during World War II, driven by the need for improved radar. Alnico magnets are based on various alloys of Aluminum, nickel, cobalt, copper, iron and titanium, [29] and are manufactured by either casting or power-sinter methods. Ultimately, this material can achieve only moderate energy product up to $75.6 kJ/m^3$ (corresponds to 9.5MGOe). Alnico magnet possess a high operating temperature limit of 450^0C to 550^0C. Although Alnicos have a high remanence (>1T in many grades) they suffer from both a low coercivity and highly non-linear demagnetization characteristic. In combination, these two factor tend to lead to sensitivity to irreversible demagnetization in many machine applications. They have therefore found little application in permanent magnet machines other than in a few niche applications such a small hybrid stepper motors.

In the 1950s, permanent magnets based on ceramic ferrites became commercially available. Due to its very low cost, these materials were widely adopted in brushed permanent magnet DC machines, loudspeaker and many other mass-market and cost sensitive applications. It can be produced by either a powder-sinter route (which yields the best magnetic performance) or by injection molding of ferrite powder in a thermoplastic. It has very modest magnetic properties and is very temperature sensitive. It nevertheless remains a very significant material in terms of volumes and sales in low to medium performance applications.

In the late 1960s and early 1970s, the emergence of Samarium Cobalt, initially at 1:5 and then 2:17 compositions, started the commercialisation of rare earth permanent magnets. Again, for the highest magnetic properties, a powder-sinter route is required to produce an essentially full-dense magnet. The various Samarium Cobalt magnets exhibited greatly improved performance compared to previous magnets but at the expense of very high cost raw materials and a complex manufacturing route. Samarium Cobalt provides a good thermal stability (remanence reduces at -0.03% per °C) as well as an operating temperature limit of 350^0C. These materials retain a high remanence, high coercivity and linear characteristic up ~300°C. The energy products of the fully dense sintered Samarium Cobalt are in the range 16MGOe to 33MGOe. Its high resistance to demagnetizing nature and its good high temperature properties makes it a preferred choice for high performance applications such as aerospace and motorsport. NdFeB emerged commercially in 1983 with magnetic properties that were an improvement on both $SmCo_5$ and Sm_2Co_{17} and at reduced cost, e.g. it offers improved room temperature magnetic properties with a cross-over at ~180°C [30]. However, early magnets suffered from problems with corrosion resistance and poor elevated temperature properties. These properties have improved over the past 30 years with new process routes and compositional modifications, but NdFeB still lag well behind Samarium Cobalt magnets in terms of temperature stability and corrosion resistance. Although still a high cost material, it does have cost advantage over Samarium Cobalt. The maximum energy product ranges from 24MGOe to 50MGOe. However, its limited maximum operating temperature and its propensity to oxidation, particularly at higher temperatures, are very significant obstacle to it being used in aerospace applications.

Typical B-H demagnetization curves at room temperature for each of the permanet magnet materials described are shown in Figure 2. 1. It can be seen that NdFeB magnets possess the highest remanence and coercivity but in the case of the high remenance grade does not have a linear in the second quadrant characteristic. The particular grade of SmCo magnets has a slightly lower remanence than the NdFeB magnets but the corecivity is very high and it remains linear throughout the second quadrant. The Ferrite magnets exihibuts some linearity in the second quadrant but the cannot compete with the rare earth magnet materials. The Alnico magnets on the other hand, has higher remanence than the ferrite but exihbits a highly non-linear characteristic and therefore can be readily demagnetized.
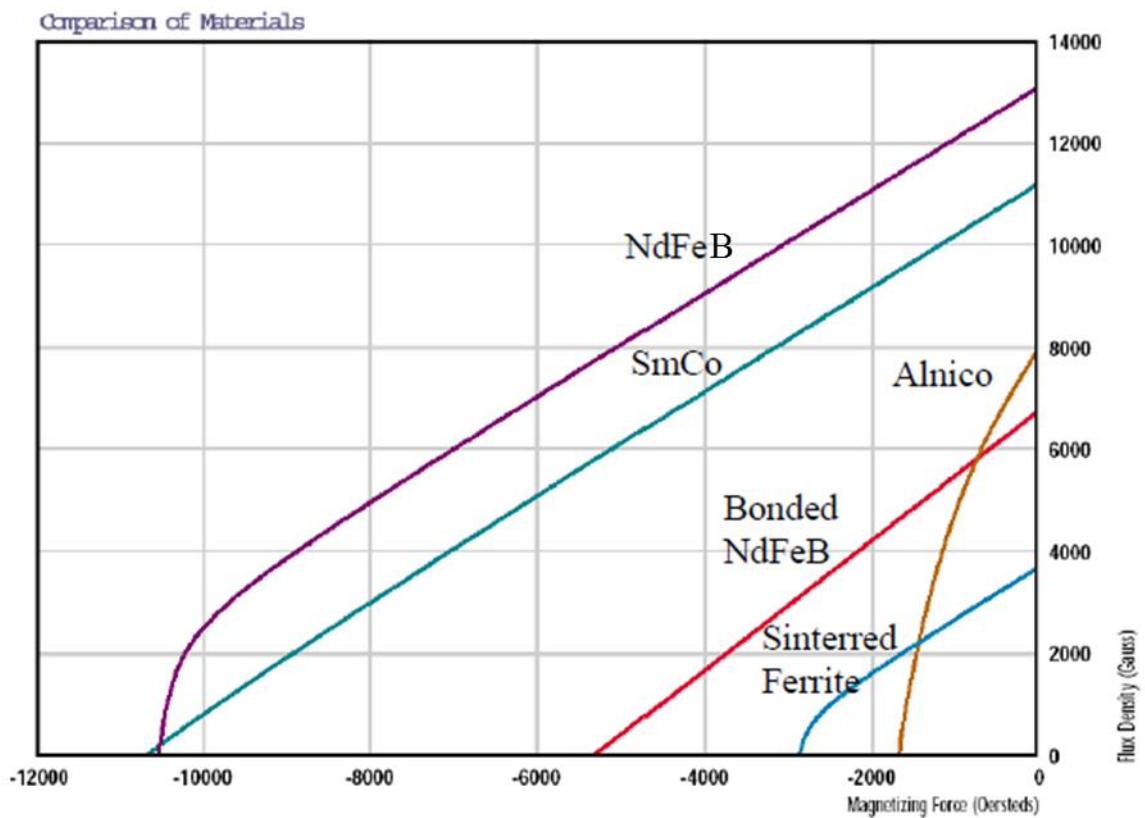
Figure 2. 1. Permanent magnet material BH curve comparison in second quadrant [31]

Figure 2. 2 shows a plot of operating temperature versus energy product for the common permanent magnet materials.
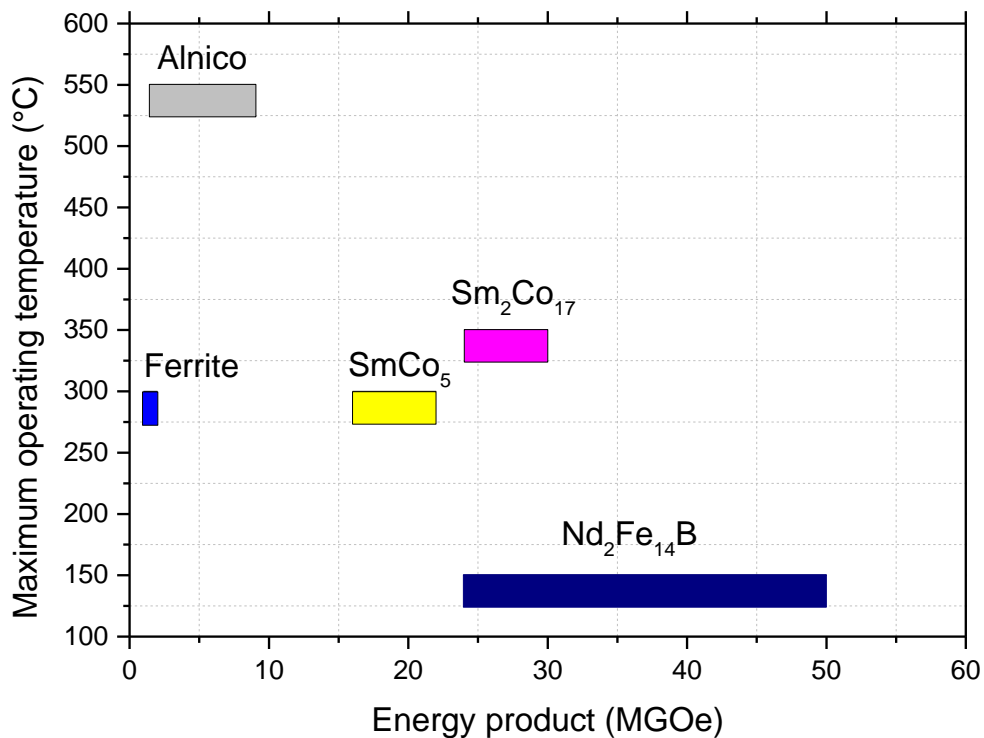
Figure 2. 2. Maximum operating temperatures and energy products for each permanent magnet material

For an operating temperature above $150\text{-}180^0\text{C}$, SmCo magnets will outperform NdFeB magnets in terms of remanence and demagnetization withstand. Moreover, it is well recognized that SmCo magnets offer significantly better long-term stability, including better corrosion resistance. These two factors, in particular the greater stability, dictate that SmCo magnets are universally preferred for aerospace applications. Within the broad category of SmCo permanent magnets, there are different types of material.

- $SmCo_5$- This is first generation of SmCo materials with grades having energy products in the range 16 to 22MGOe.
- Sm_2Co_{17}- This second generation of materials has improved magnetic properties with energy products in the range 24MGOe to 34MGOe.

As a result of their superior magnet properties, Sm_2Co_{17} is the dominant permanent magnet material choice for high performance aerospace application.

The variation in the demagnetization characteristics of a typical grade Sm_2Co_{17} (VACOMAX 225HR) [32] with temperature is shown in Figure 2. 3. In this case, both the intrinsic and normal curves are shown. As will be apparent, the remanence, normal coercivity and intrinsic coercivity all reduce with increasing temperature. The second quadrant of B-H normal curve indicates a very linear behavior, and the irreversible demagnetization starts to take place as the external field reaches the knee point. As the temperature increases, the knee point tend to move from the third quadrant towards the second quadrant.
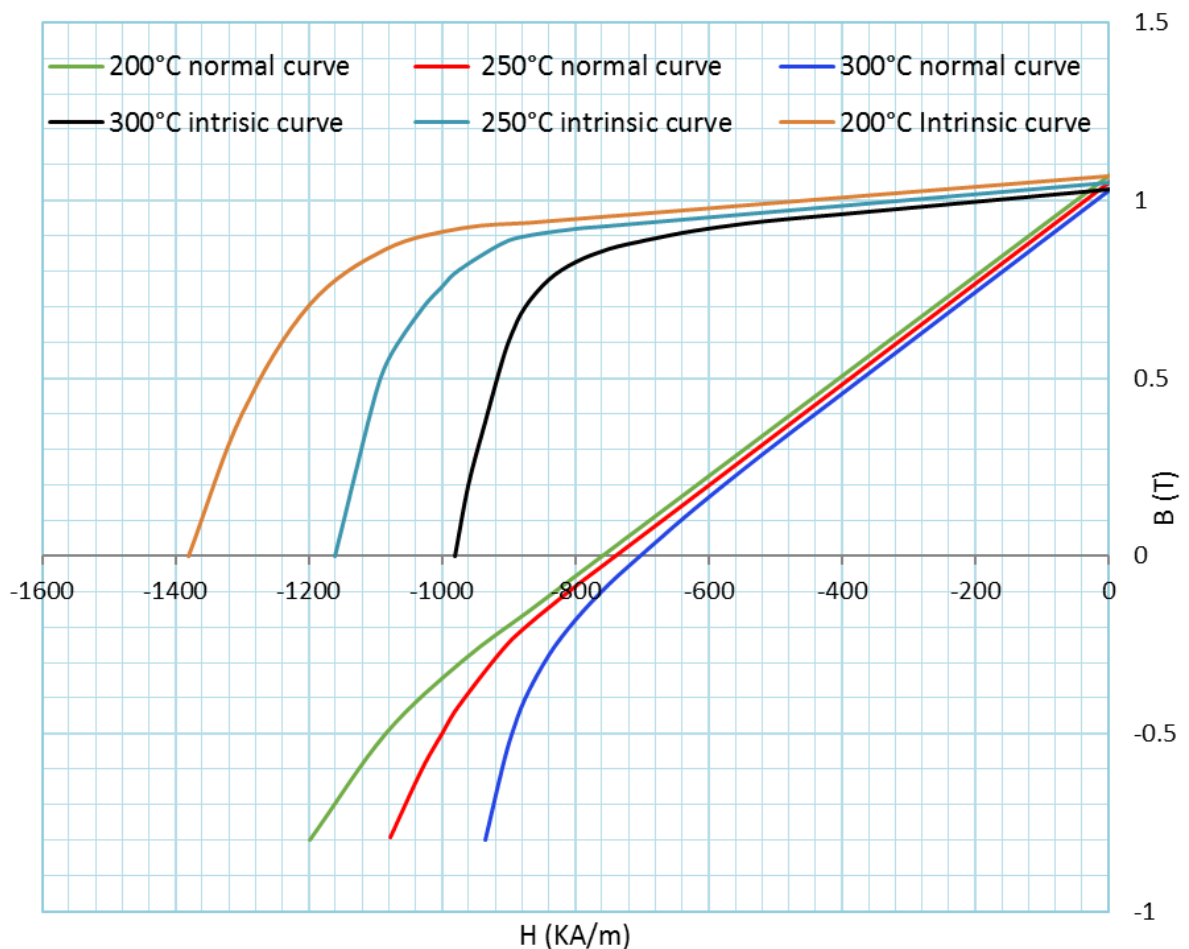
Figure 2. 3. B-H curves of a high performance grade of Sm_2Co_{17} (VACOMAX 225HR) under different temperature level

2.3.2 Soft magnetic materials

Soft magnetic materials are used for both the stator and rotor cores in electrical machines. Desirable properties for most electrical machine core materials include a

high saturation flux density, high permeability and low AC losses. By far the most widely used soft magnetic material used in the cores of medium and high performance machines is Silicon Iron, often in the form of thin laminations. Non-oriented grades of Silicon Iron for machine cores contain 0.5% to 3.25% of Si to increase resistivity and up to 0.5% of Al. Silicon Iron typically has a saturation flux density of the order of 2.0T depending on the exact Silicon content. The saturation flux density of a soft magnetic material determines the cross-sectional areas in the stator and rotor core that are required to pass the flux. In this regard, the various alloys of Cobalt Iron offer a useful advantage over Silicon Iron with typical saturation flux densities of 2.34T. It was shown in [33] that by employing cobalt-iron laminations instead of conventional silicon-iron laminations, the maximum rated torque of a given machine design can be increased by 25%. However, this performance benefit is obtained at a very significant increase in cost, with Cobalt Iron typically being 50-80 times more expensive than Silicon Iron on a per kg basis. Its use is therefore limited to high value and high performance applications such as aerospace and motorsport.

In the vast majority of electrical machine designs, laminated non-oriented Silicon iron (also known as 'electrical steel') is used as the core material. It is supplied as thin laminations with standard thicknesses ranging from 0.10 to 0.65mm. The use of thin laminations is required to reduce induced eddy currents in the core. The surface is generally insulated with a very thin coating to ensure that successive laminations in a core are electrically insulated from each other, thus constraining eddy currents within one lamination. This prevents induced eddy currents from circulating throughout the core. Since a core is made up from many individual laminations (usually 100s-1000s) a stacking factor is introduced into many calculations to account for the inevitable gaps and insulation layers within the core. Stacking factors typically take values between 0.94 to 0.97. From the point of view of manufacturing, thinner laminations increased the difficulties which manufacture and assembly the laminations.

Whereas the cores of conventional radial field electrical machines laminations are almost exclusively manufactured from a large number of laminations, this is often not a viable approach to the various stator geometries encountered in axial field machines. Since the process of assembling a core from a series of laminations is not well suited to axial field machines, there has been inevitable interest in the use of so-called soft magnetic composites for many unconventional geometries of electrical machines [34] [35]. These composites are formed by pressing iron power with small fraction

(typically no more than 1%) of binder to produce a net shape three-dimensional component with isotropic magnetic properties which suits 3-dimensional field path [36] [37]. From a geometry point of view, these would seem of offer a good solution [38]. However, these materials have some drawbacks which have hindered their adoption. Firstly, although they are pressed to near full density, they only exhibit relative permeability in the hundreds, with some amount of trade-off between relative permeability and high frequency losses. The typical relative permeabilities in SMCs are 200 to 400. From a mechanical point of view, SMC cores do not exhibit competitive mechanical properties with laminated Silicon iron and cobalt iron. Moreover, the core loss in SMC material is typically higher than in laminated structures at relative low frequencies because of the dominance of hysteresis loss caused by the stress induced during the pressing process. As the frequency increases, the loss in SMC material can become lower than a corresponding laminated core, although the cross-over frequency clearly depends on the lamination thickness. The total loss against frequency curve for SMC material is relatively linear.

The BH magnetization characteristic of typical grade of silicon iron, cobalt iron and soft magnetic composite are shown in Figure 2. 4. Cobalt Iron exhibits the best electromagnetic performance with the highest saturation level, the SiFe material exhibits similar but lower saturation level and the SMC material on the other hand exhibits very inferior magnetic properties.
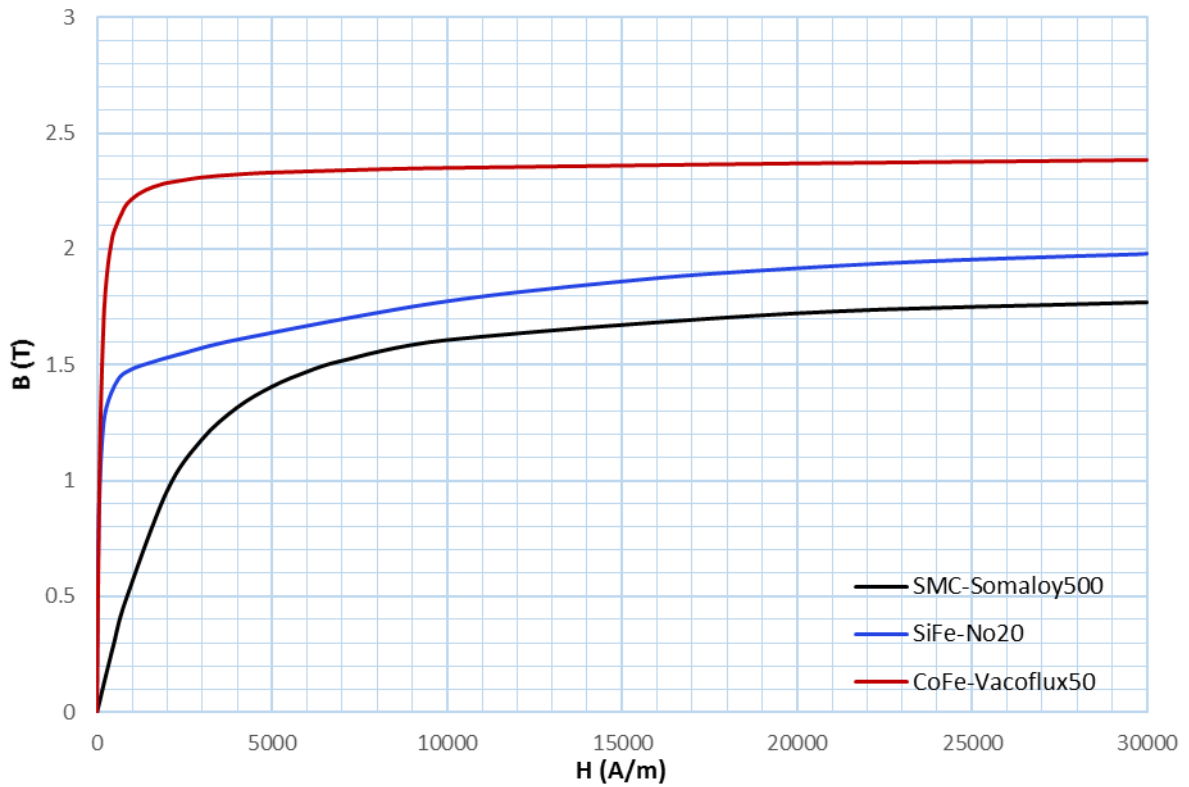
Figure 2. 4. B-H characteristic curves of the silicon iron, cobalt iron and SMC

In order to reflect the practice in aerospace applications, Sm_2Co_{17} was chosen for the rotor magnets and a 49% Cobalt Iron (Vacoflux 50) was selected for the rotor and stator cores. The key properties of these materials are summarised in Table 2. 1.

Table 2. 1 – Summary of key material properties

Properties	Units	Machine components		
		Permanent magnet	Stator and rotor back iron	Coils
Material		Sm_2Co_{17}	Cobalt iron (VACOFLUX 50)	Copper
Density	Kg/m^3	8400	8120	8900
Remanence	T	1.0	-	-

Relative permeability		1.05	7000	-
Max operating temperature	°C	350	-	-
Coercivity H_c	kA/m	740	-	-
Saturation	T	-	2.35	-
Electrical resistivity	$\Omega \cdot mm^2/m$	0.86	0.42	0.017

2.4 Initial sizing of a non-slotted toroidal machine (TORUS-NS)

2.4.1 Sizing equations for TORUS non-slotted machine

The first machine topology considered was a non-slotted toroidal core machine (TORUS-NS) of the type shown previously in Figure 1. 4. Exploded view of a representative double-sided TORUS-NS type axial field permanent magnet machineFigure 1. 4. Having specified an initial estimate of the airgap flux density to initiate the iterative design cycle, a series of analytical design equations were developed to establish initial estimates of the dimensions required to meet a given torque specification subject to specific constraints, e.g. maximum rms current density in the coil.

An important factor when employing analytical equations for a TORUS-NS machine is the need to account for two fill or packing factors:

- The first is the usual packing factor k_p within each individual coil, i.e. the proportion of the cross-sectional area of the coil which is comprised of the copper conductor as opposed to insulation and gaps. This was assumed to be 50% in this design study.
- The second packing factor is specific to this particular topology of axial machine and accounts for the proportion of the overall pole face that is covered

by conductors. The number of conductors is constrained by the space available on the inner radius of the core as this fixes the maximum width of each coil as shown in Figure 2. 5. The space between each successive turn increases with increasing radius, leading to a triangular void gradually opening up with increasing radius. Hence, the utilisation of the available pole face area diminishes with increasing radius and is represented analytically by a factor β that takes a value of less than one. This factor β is equal to the proportion of the each coil span that is occupied by conductors at the mean radius.

2.4.2   Sizing equations for TORUS non-slotted machine

For the TORUS-NS machine, given an estimate of the axial component of airgap flux density, B_g, the tangential force on the conductors, and hence the torque, can be estimated to a reasonable degree using straightforward Lorentz force principles. Taking the region shown in the close up of Figure 2. 5 as a starting point, the average force on the one side of this coil over one sinusoidal cycle, can be established in terms of the rectified mean of the sinusoidal current:

$$F = \frac{2}{\pi} N_t B_{gz} I_{pk} L \qquad (2.\,1)$$

where,

$$N_t I_{pk} = \frac{\pi}{2} (D_o + D_i) \cdot h_c \cdot \beta \cdot J_{pk} \qquad (2.2)$$
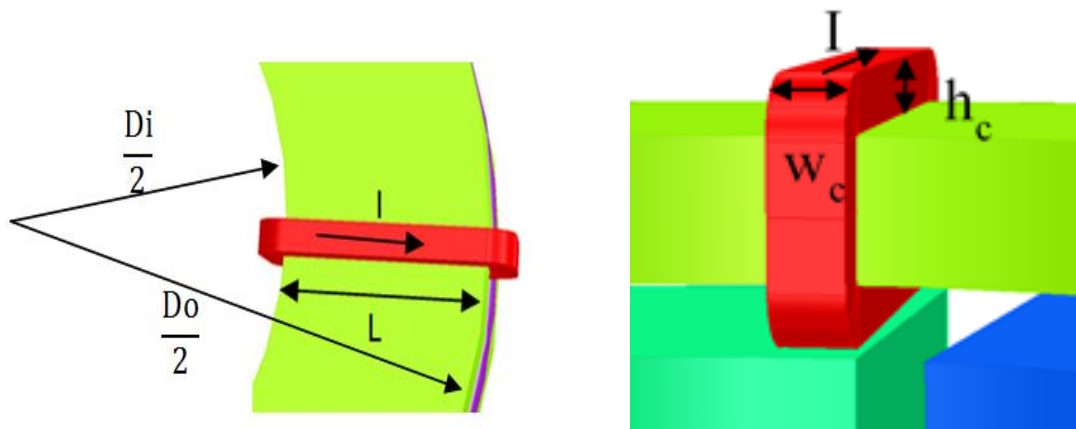
Figure 2. 5. Close up of single coil

Substituting for NI into (1) yields:

$$F = \frac{h_c \, \beta}{2} B_{gz} J_{pk} (D_o + D_i)(D_o - D_i)$$

(2.3)

Hence, the force produced by the conductors on both sides of the coils is given simply by:

$$F = B_{gz} \, h_c \, \beta \, J_{pk} (D_o + D_i)(D_o - D_i)$$

(2. 4)

The corresponding torque produced at the mean radius $\frac{D_o + D_i}{4}$ is hence given by:

$$T = \frac{B_{gz} \, h_c \, \beta \, J_{pk}}{4} (D_o + D_i)^2 (D_o - D_i)$$

(2. 5)

By introducing a split ratio, which is defined as s=D_i/D_o, then this can be rewritten as:

$$T = \frac{B_{gz} \, h_c \, \beta J_{pk}}{4} D_o{}^3 (1+s)^2 (1-s)$$

(2. 6)

The factor β which represents the proportion of the stator pole face which is occupied by conductors is given by:

$$\beta = \frac{l_{tot}(\frac{D_o}{2} - \frac{D_i}{2})}{\frac{\pi}{4}(D_i{}^2 - D_o{}^2)} = \frac{l_{tot}}{\frac{\pi}{2}(D_i + D_o)}$$

(2. 7)

The conductors are assumed to be touching each other at the inner edge so as to achieve the maximum number of coils in the available space, this leads to:

$$\gamma = \frac{l_{tot}}{\pi(D_i - 2 \times h_c)}$$

(2. 8)

Where γ is the proportion of the conductor covering at the inner edge of the coils at $(D_i - 2 \times h_c)$, and this tends to be near unity since it determines the number of turns

that can be adopted in the stator core. In this design study it was set to be 0.9 as an initial design parameter, and hence the factor β can be given by:

$$\beta = \gamma \frac{(D_i - 2 \times h_c)}{\frac{1}{2}(D_i + D_o)}$$

(2. 9)

The split ratio of the machine is an important parameter to be considered in the design process, the optimum value recommended in published literature tends to be between 0.58 to 0.71 for small machines and 0.5 to 0.58 for medium and large machine [12]. In line with this published guidance, in this design the split ratio was set to 0.6. Having established these initial factors, the overall dimension can then be established.

The remaining dimensions of the core can be readily selected by simply dimensioning them to operate at a flux density just below the onset of appreciable magnetic saturation. In the case of the Cobalt-Iron selected for this machine, a core flux density of 2T was used as a guideline for the following sizing equations:

$$B_{gz}A_{pole} = B_{core}A_s$$

(2. 10)

where,

$$A_{pole} = \frac{\pi}{p}(r_o{}^2 - r_i{}^2)\alpha$$

(2. 11)

$$A_s = l_s(r_o - r_i)$$

(2. 12)

A similar procedure can be used for the calculation for the rotor back iron thickness.

2.4.3 Initial design synthesis

Adopting an assumed airgap flux density, B_{gz}, of 0.5T, allows the dimensions of a design to be established for different values of current density, which range from comparatively modest values up to values which could only be sustained for short periods. Table 2. 2 summaries the various dimensions and corresponding machine mass established using the series of analytical design equations from section 2.4.1 for a series of different rms current densities. In all these designs the magnet pole arc was assumed a typical value of

160° (elec) with magnet axial length of 6.3mm, the coil thickness is fixed at 5mm and the packing factor of the coil was assumed to be 0.5. Each machine has 12 stator coils and 8 rotor poles.

As would be expected, the dimensions and weight decrease with increasing current density, although not in a straightforward manner given the radial scaling of torque which occurs in axial field machines. Of particular interest in the relatively small contribution that copper makes to the overall weight of the machine.

Table 2. 2. Series of designs established from sizing equations for 50Nm with an average airgap flux density of 0.5T

Parameter	Conductor rms current density (A/mm²) for a coil packing factor of 0.5										
	10	12	14	16	18	20	22	24	26	28	30
D_o (mm)	255.0	240.0	228.0	218.0	209.6	202.4	196.1	190.4	185.4	180.9	176.8
D_i (mm)	153.0	144.0	136.8	130.8	125.8	121.4	117.6	114.3	111.3	108.6	106.1
Stator core length (mm)	18.0	17.0	16.0	15.0	15.0	14.0	14.0	13.0	13.0	13.0	12.0
Rotor back iron length (mm)	9.0	8.5	8.0	7.5	7.0	7.0	7.0	6.5	6.5	6.5	6
Axial length (mm)	72	70	68	66	65	64	64	62	62	62	60
Stator mass (Kg)	4.72	3.94	3.37	2.95	2.62	2.36	2.15	1.97	1.82	1.69	1.57
Magnet mass (Kg)	3.07	2.72	2.46	2.25	2.08	1.94	1.82	1.72	1.63	1.55	1.48
Rotor mass (Kg)	4.72	3.94	3.37	2.95	2.62	2.36	2.15	1.97	1.82	1.69	1.57
Coil mass (Kg)	1.47	1.20	1.15	1.10	0.89	0.86	0.84	0.82	0.80	0.79	0.77
Total mass (Kg)	14.00	11.79	10.35	9.26	8.22	7.52	6.95	6.47	6.06	5.71	5.40

Values of current density above ~8A/mm² in the table are unlikely to be sustainable on a continuous basis with the proposed natural convective heat flow. However, they provide a quantitative illustration of the benefits in mass reduction which could be realised by fully exploiting the thermal mass of the machine and the intermittent duty cycle.

As will be apparent, the final size of the machine is highly dependent on the duty cycle, in particular whether the 50Nm constitutes a near continuous rating or highly intermittent rating. Meeting the desired torque density target for a continuous 50Nm is likely to be extremely challenging given the limited cooling available. However, a more complex duty cycle in which the torque is markedly lower than 50Nm for much of the time, would allow the thermal mass of the machine to be exploited so as to significantly reduce the mass of the machine.

2.5 Airgap flux density investigation for non-slotted TORUS machine (TORUS-NS)

A key challenge in sizing a TORUS-NS is the calculation of the axial component of the airgap flux density that interacts with the radially oriented current in the stator winding to produce circumferential torque. The designs presented in Table 2. 2 were based on an average flux density of 0.5T. This section explores the feasibility of achieving this flux density using a series of estimation methods.

A TORUS NS machine, is a so-called airgap winding machine with a large effective magnetic airgap. Hence one-dimensional airgap flux density calculation methods are unlikely to provide reasonable estimates for any cases other than the very thinnest coils. In most practical designs there will be a significant variation in axial flux density across different regions of the coil. These variations are likely to occur both across the span of a pole and between the inner and outer radius. Hence, ultimately, only a three-dimensional representation will capture the flux density variation to which the stator coils are exposed. Hence, a reliable appropriately weighted mean value of axial component of flux density is problematic without recourse to three-dimensional analytical field calculation models or finite element analysis.

2.5.1 One-dimensional model

The most straightforward model is based on the well-established magnetic circuit representation of a single magnet working into a single airgap:

$$B_g = \frac{B_r}{1 + \mu_r \frac{l_g}{l_m}}$$

(2. 13)

This very simple model neglects the effect of any leakage flux and assumes infinitely permeable cores. Figure 2. 6 shows the variation in the airgap magnetic flux density, which is assumed in this model to be entirely oriented along the Z-axis of the machines, as a function of airgap length for magnet axial length of 6mm and 12mm. The curves shown in Figure 2. 6 were calculated for a magnet remanence of 1.1T and a relative recoil permeability of 1.05.
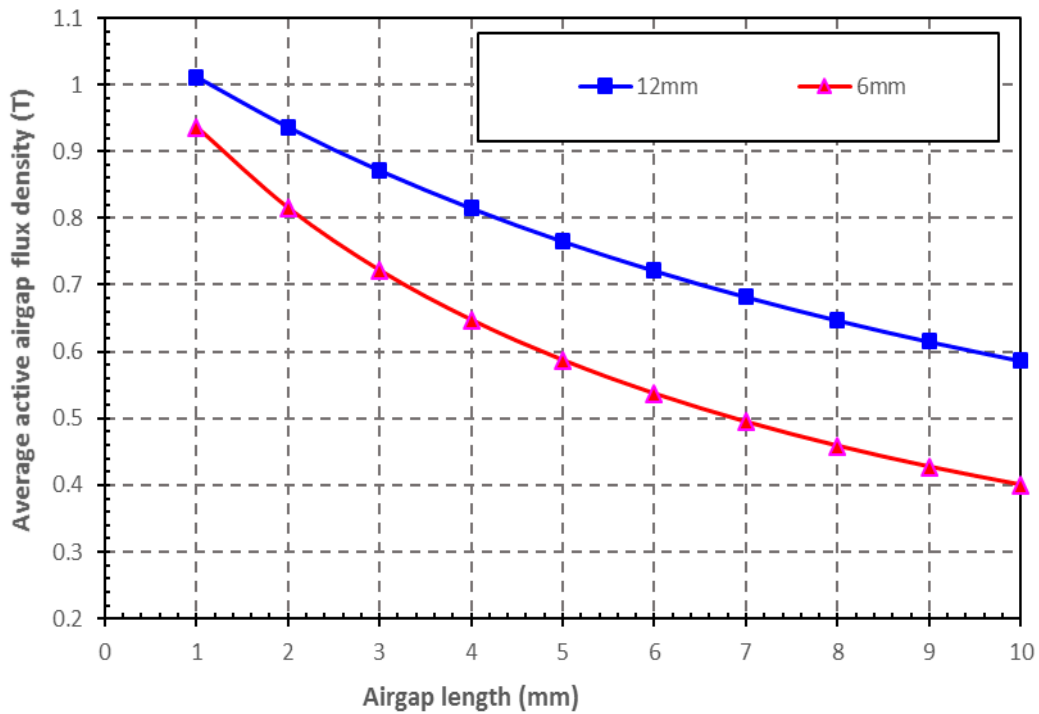
Figure 2. 6. Variation in the axial component of airgap flux density as a function of total airgap length for magnet axial length of 6mm and 12mm

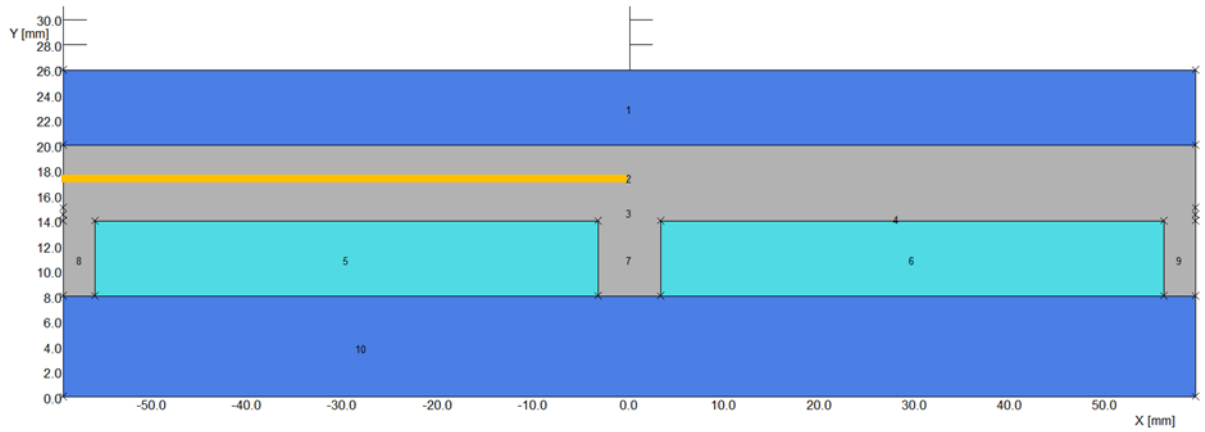### 2.5.2   Two-dimensional finite element model

A series of two-dimensional planar finite element models can be employed to approximate the geometry of the rotor magnet segment. The models are based on a two-dimensional planar model in which the width of a magnet pole is equal to the

length of a curved path along average radius. The model is established at the average radius of a machine with outer diameter of 189.3mm and inner diameter of 113.5mm. This two-dimensional approximation was used to investigate the influence of magnet and coil thickness on the resulting airgap flux density. Two value of magnet axial length were considered, 6mm and 12mm, in each case with the coil thickness varying from 1mm to 10mm in 1mm increments. In all cases, the same permanent magnet remanence of 1.1T and relative recoil permeability of 1.05 was used. In each case, the axial mechanical clearance is fixed at 1mm. Figure 2. 9 shows the variation in axial component of the flux density (y-direction component in the two-dimensional planar model) across the magnet pole at the centre of the airgap. In these particular cases, the planar model approximates a curved path at the means radius of the magnet.

As would be expected, the average flux density drops with increasing coil thickness, but at a diminishing rate. In compensation, an increased coil thickness results in a proportional increase in the electrical loading for a given current density. Hence the torque produced will continue to increase providing the reduction in airgap flux density does not become greater than proportional to an increase in airgap. This might suggest that continual increasing in the coil thickness would yield improved designs, but the following should be noted:

- The copper losses of coil operating at a given current density increase in direct proportion to the coil thickness.
- The coil mass increases in direct proportion to the coil thickness.
- The removal of heat from the centre of the coil becomes more problematic in thicker coils and it may be necessary to reduce the current density to account for this.

As will be apparent, there are several combinations of magnet and coil thicknesses which meet or exceed the 0.5T value assumed in the initial sizing.

Figure 2. 7. Two-dimensional finite element model representing a circular path at the mean radius of the coil
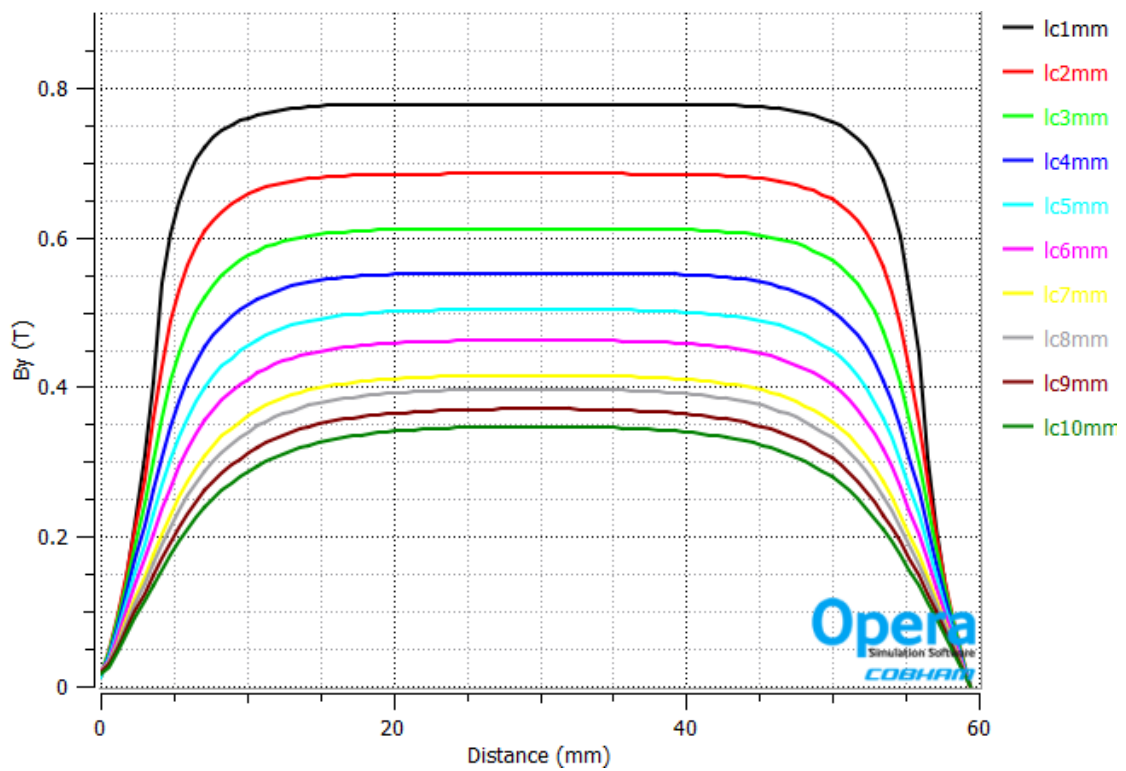
(a). Magnet axial length of 6mm model
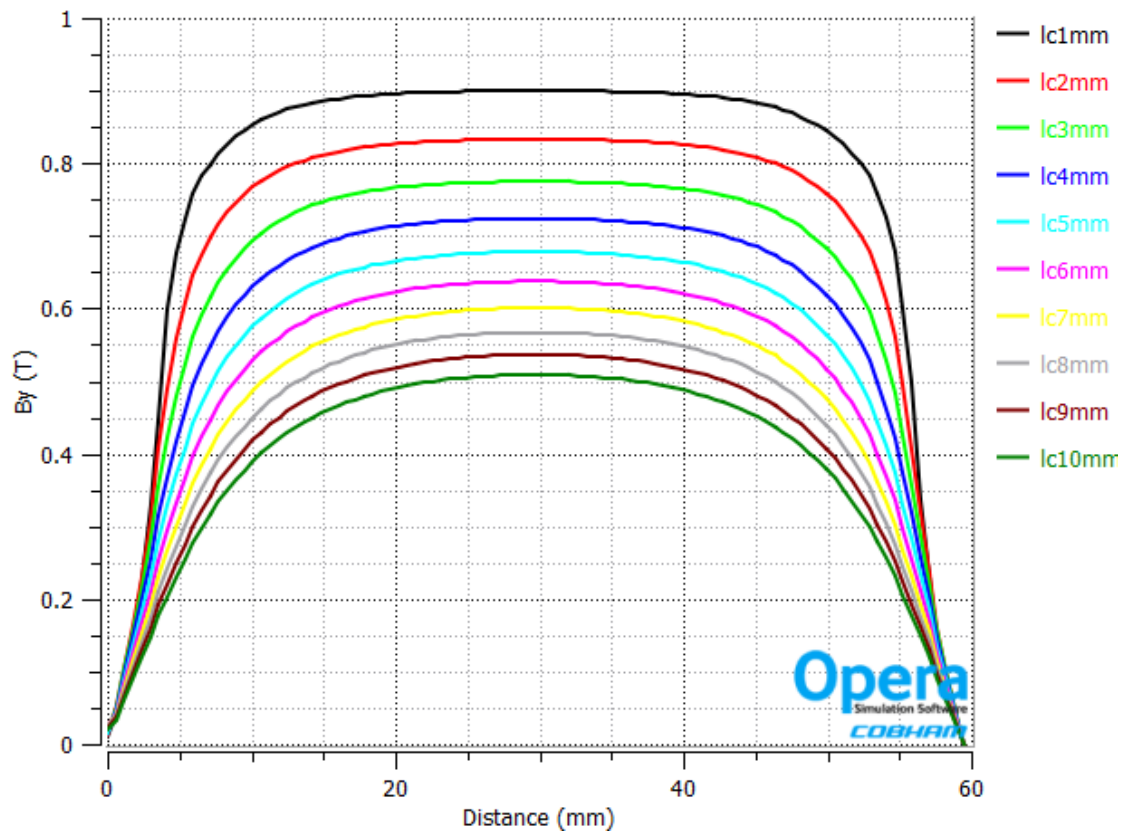
(b). Magnet axial length of 12mm model

Figure 2. 8. Flux density variation at the mid-point of coil thickness for the 2D model
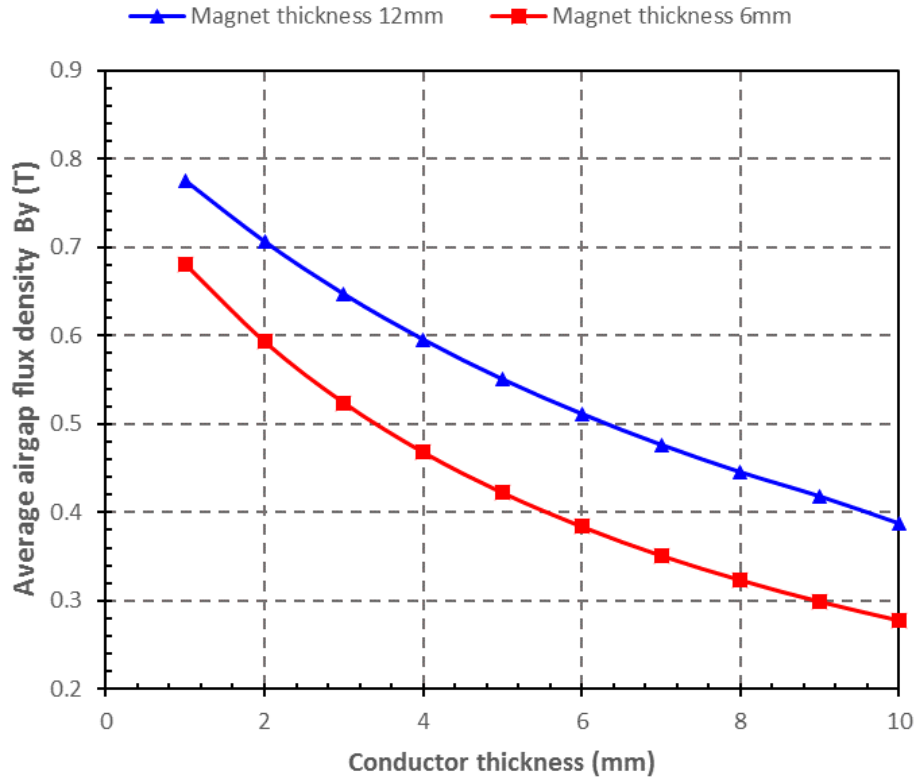
Figure 2. 9. Variation in average flux density across pole as a function of conductor thickness

2.5.3 Three-dimensional finite element model

The three-dimensional model of a reference design with outer diameter of 189.3mm and inner diameter of 113.5mm model using non-linear, three-dimensional finite element analysis. A representative magnetic flux density distribution from this model under open-circuit conditions is shown in Figure 2. 10.
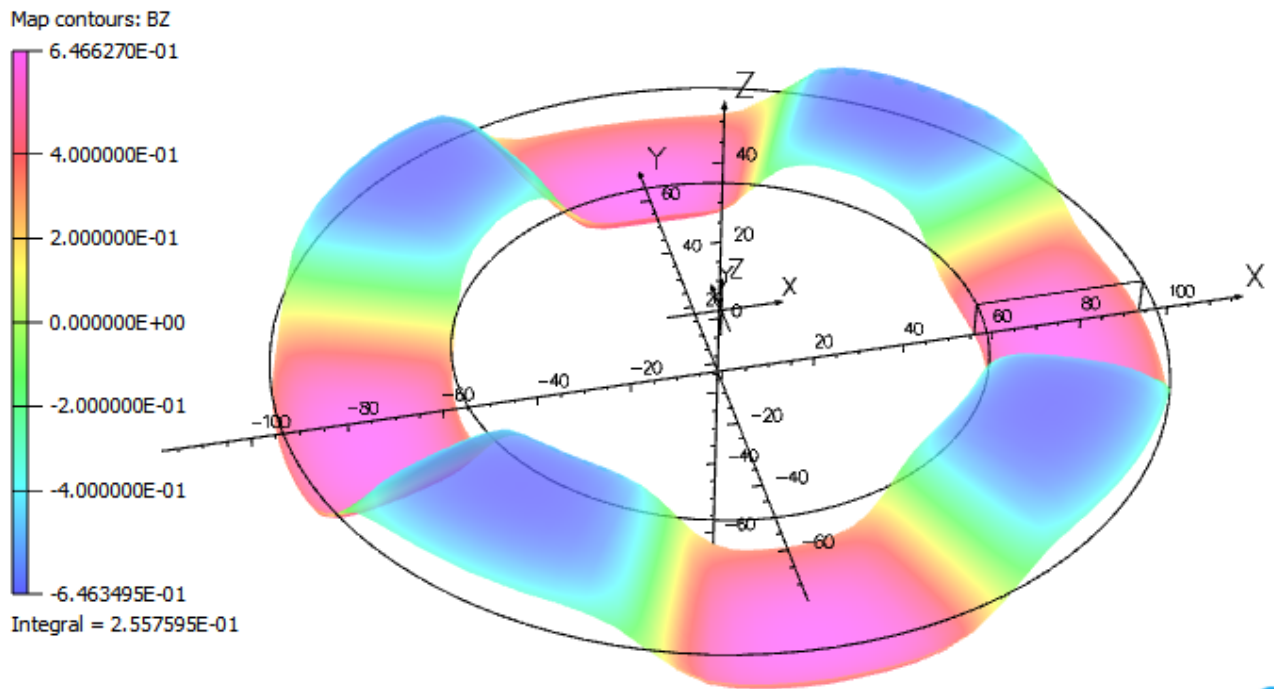
Figure 2. 10. Three-dimensional representation of airgap flux density distribution under open-circuit conditions

Profiles of flux density across one magnet pole at three axial locations (defined in Figure 2. 12 are shown in Figure 2. 11. The profile closest to the core is taken 0.1mm from the core surface to avoid the difficulties with exact surface values at the interface between the regions in the model. As would be expected, there is some variation in the magnitude of flux density across at different depths within the winding. Although the nature of these profiles will depend on the specifics of the design, this serves to illustrate the challenges in specifying a single value of effective flux density from the perspective of torque production.

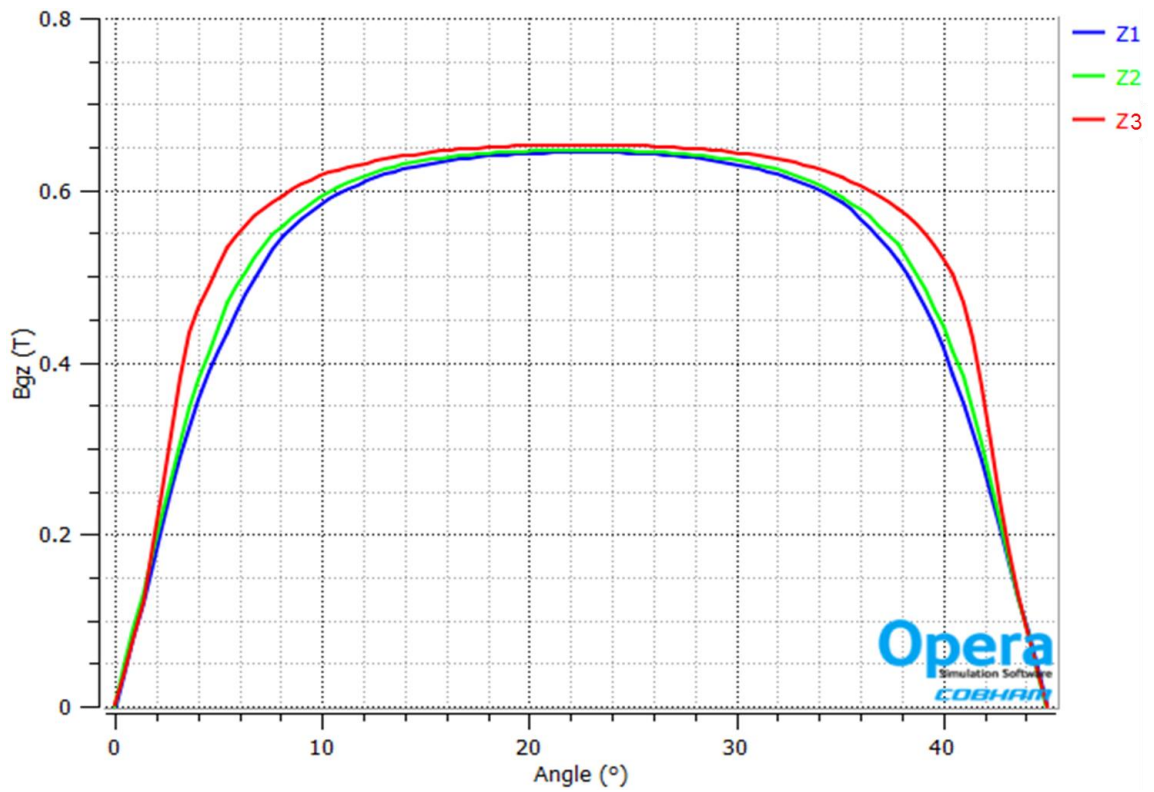**Figure 2. 11. Finite element predicted variation in the normal component of airgap flux density at 3 different axial positions in the airgap (as defined in Figure 2. 12)**
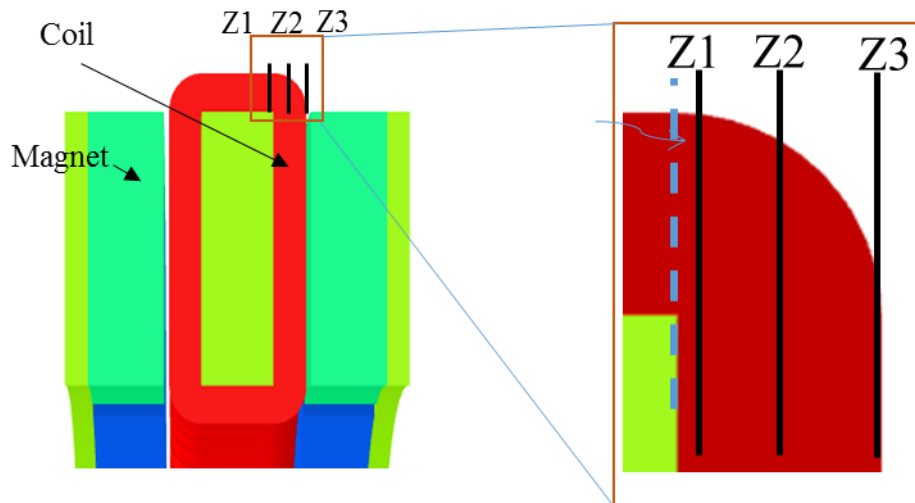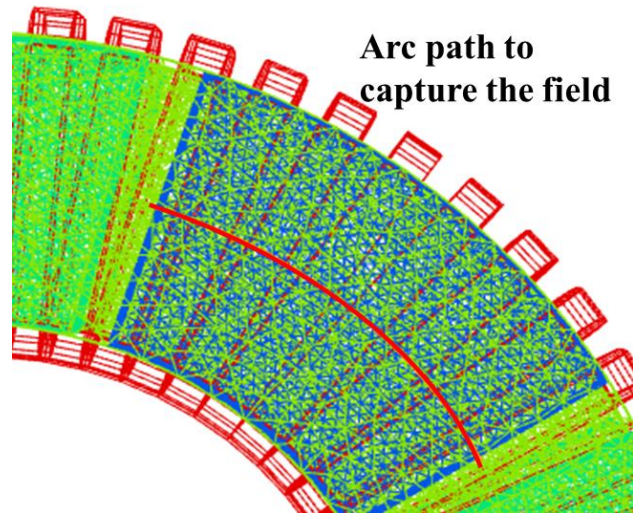
Figure 2. 12. **Location of profile positions within the coil and the arc along which the flux density was evaluated**

To further investigate the relationship between the airgap flux density and various dimensions, two separate 3D models with magnet axial length of 6mm and 12mm were simulated. The conductor thickness was set as a variable between 1mm to 10mm, and a series of analyses performed with both 6mm and 12mm thick magnets. All the airgap flux densities in this particular analysis were obtained under no-load conditions. The model dimension employed in the analysis is an 8 pole rotor with 12 coils mounted on a core with an outer diameter of 189.3mm, a magnet pole arc angle of 160°(elec), a mechanical clearance of 1mm.

The airgap flux density over one magnet pole at the mean radius of the magnet with different conductor thickness is shown in

Figure 2. 13, (a) and (b) for the representing 6mm and 12mm thick magnets respectively. A more detailed three-dimensional plot of airgap flux density variation over one pole is shown in Figure 2. 14, for the case of a 5mm thick conductor thickness. As would expected give the presence of leakage at the inner and outer radius, the flux density is lower near the inner and outer edges of the magnet than in the middle of the pole.

40
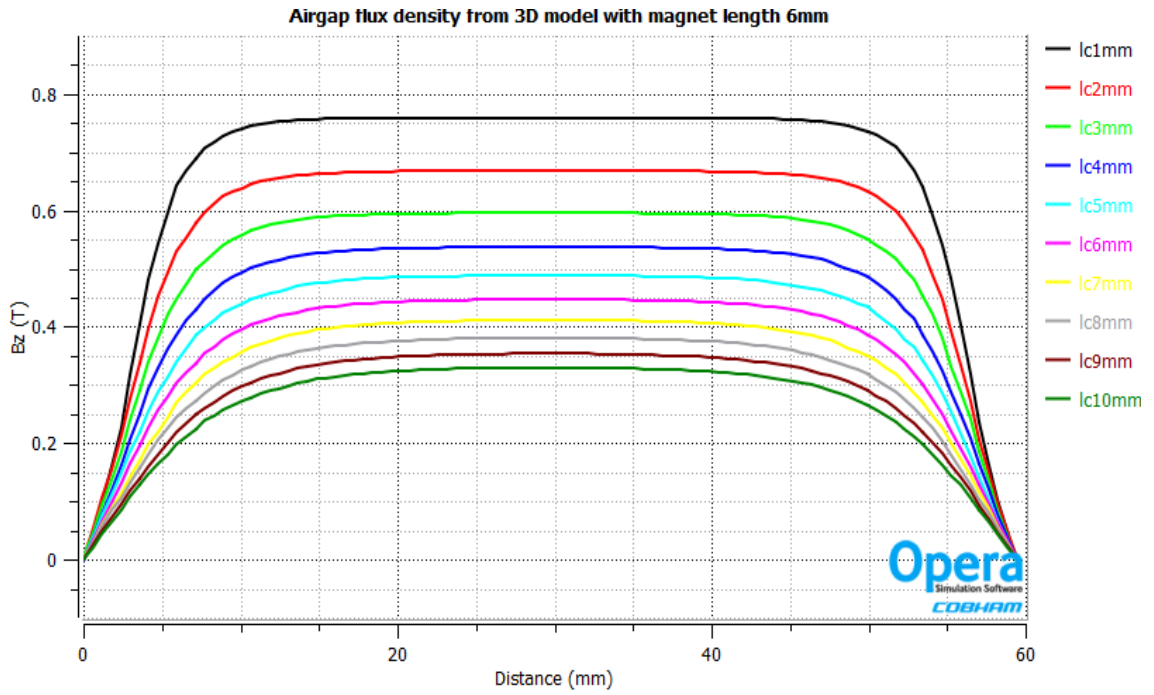
(a). Magnet axial length of 6mm model
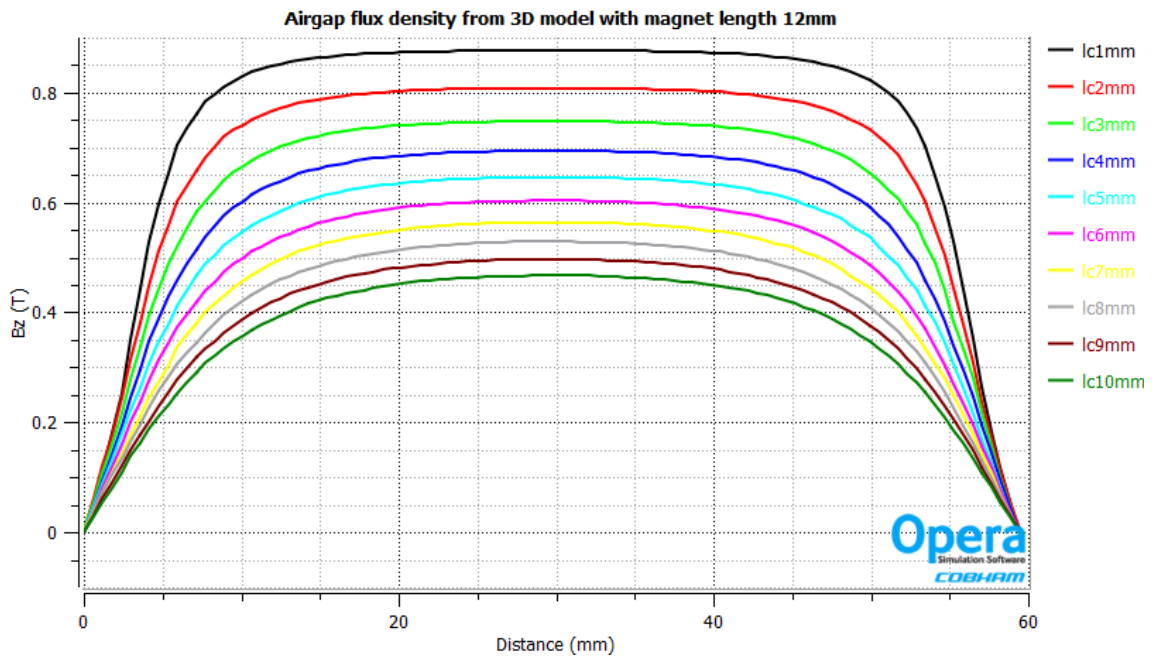
(b). Magnet axial length of 12mm model

Figure 2. 13. Three-dimensional finite element predicted flux density variation across one magnet pole at an axial location that corresponds to the middle of the stator coil
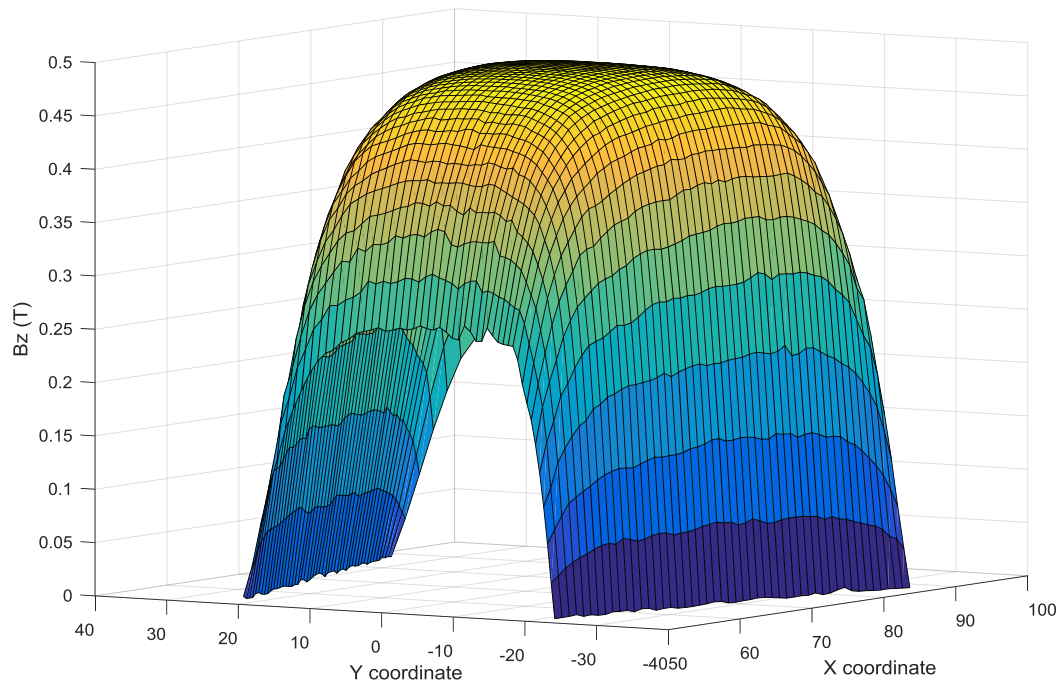
Figure 2. 14. Detailed 3D airgap flux density over one magnet pole for a magnet axial length of 6mm and a coil thickness of 5mm

Figure 2. 15 shows the airgap flux density comparison obtained separately from one-, two- and three-dimensional finite element analysis in all cases for the axial component. The two- and three-dimensional predicted airgap flux density are the values at an axial location which corresponds to the middle of the coil.

As would be expected, the axial component of flux density (which is the component of interest in terms of generating torque) reduces as the number of dimensions in the model is increased. Figure 2. 15 also shows that recourse to three-dimensional analysis is required to accurately predict the airgap flux density to a level which is required for detailed performance predictions and optimisation.
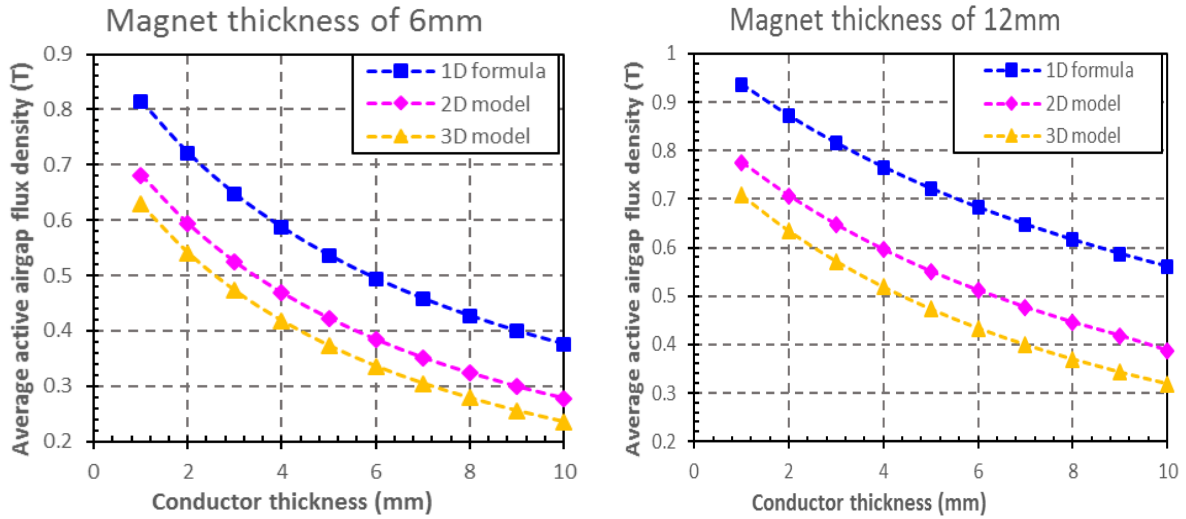
Figure 2. 15. Average flux density against conductor thickness for 1D,2D and 3D models

2.5.1 Pole number selection

The selection of the pole number for the non-slotted TORUS machine is studied and discussed in this section. There are a number of conflicting requirements in the selection of the pole number. A higher pole number will reduce the cross-sections of the stator core (which also reduces the coil resistance) and the rotor back-iron thickness and may increase the winding factor depending on the number of stator coils. However, these benefits come at the expense of increased inter-pole leakage which is a particular concern in a machine with a large effective airgap and increased core losses due to the increased electrical frequency at a given rotation speed. As will be discussed in detail in subsequent chapters, the prototype machine is equipped with a solid cobalt iron core (i.e. non-laminated). In this particular case, the increased eddy current screening in the core will be a particular concern in terms of reducing the net torque constant of the machine.

In order to establish the relationship between pole number and the static airgap flux density, a series of three-dimensional models with different number of poles are simulated and compared. The benefits of using a high pole number in terms of reducing cross-sections were not factored into this analysis since the focus was on airgap flux density. Hence, the stator and rotor core dimensions remained fixed at outer diameter of 189.3mm and inner diameter of 113.5mm. Models for pole numbers between 6 and 16 were considered. A fixed magnet axial length of 6mm and a fixed coil thickness of

43

5mm were adopted for all models. The axial component of flux density in the airgap across one magnet a pole arc is plotted in Figure 2. 16 at an axial location which corresponds to the middle of the coil and at an arc radius at the average radius of the stator core. As would be expected, as the pole number increases up, the flux density is reduced as a consequence of inter-pole leakage. As noted earlier, this is a particular concern for a slotless topology because of the large effective magnetic airgap. The calculated average airgap flux density across the pole number is shown in Figure 2. 17. The flux density progressively with increased pole number, dropping ~15% between 8 poles to 16 poles.

On the basis of this static analysis and the concerns over induced eddy currents in the solid core (behaviour which is studied in greater detail in chapters 3 and 4) a pole number of 8 was selected for the subsequent machine design optimisation and the ultimately the prototype machine.
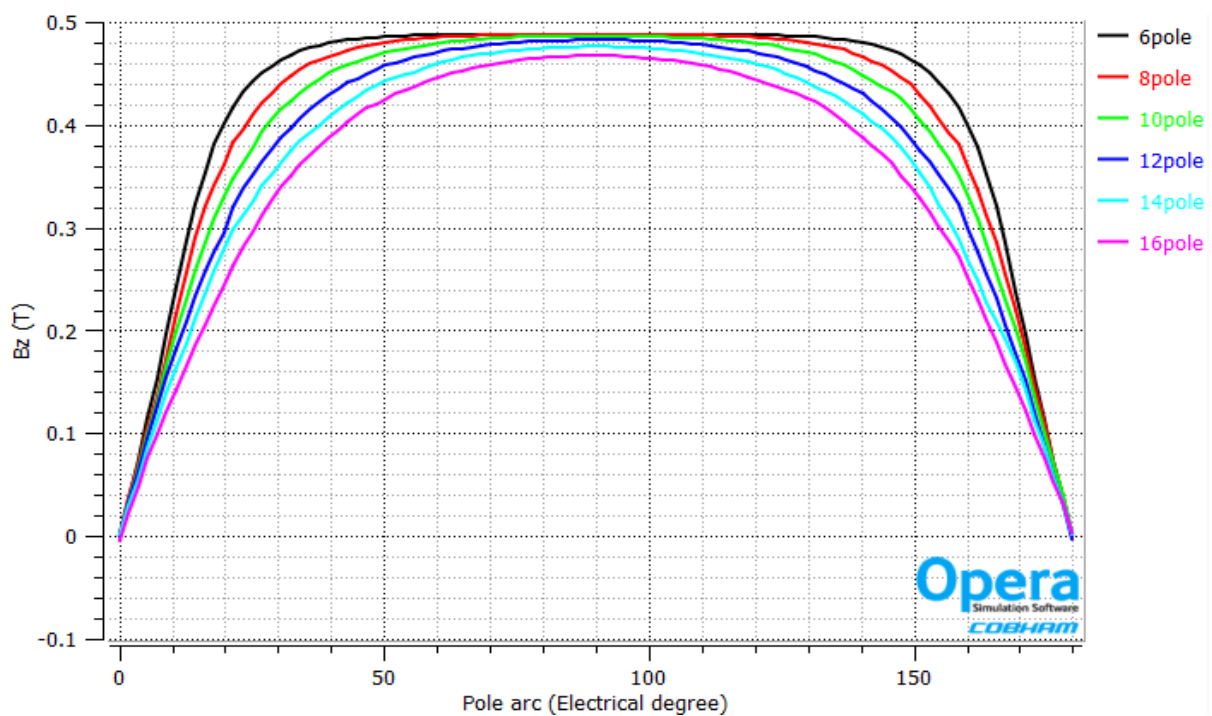
Figure 2. 16. Three-dimensional finite element predicted flux density profiles for a range of pole numbers
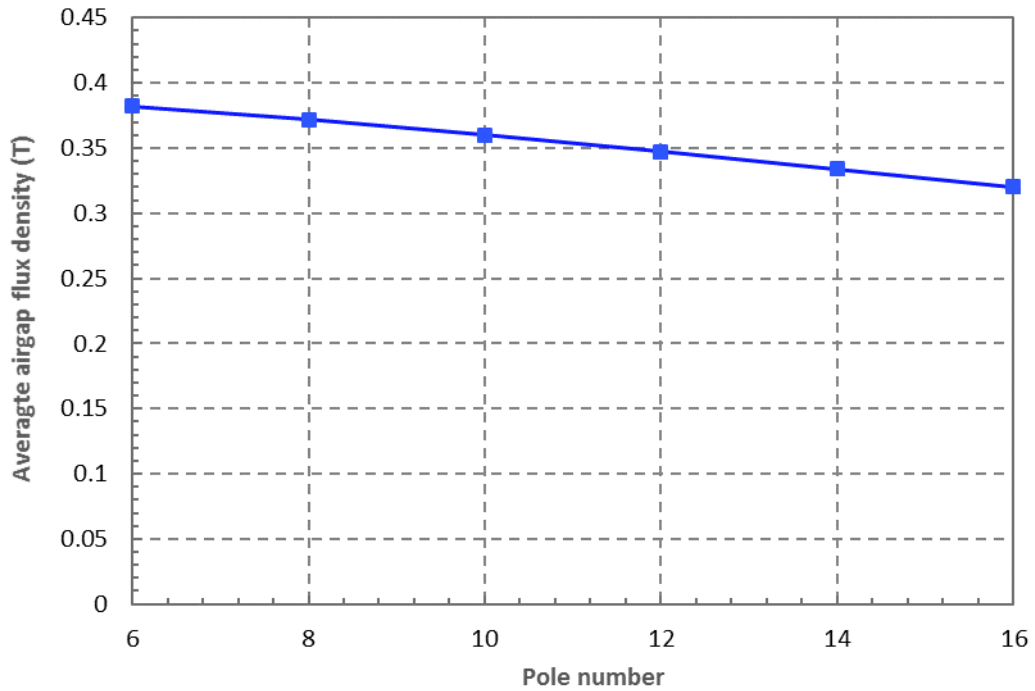
Figure 2. 17. Variation in average axial component of airgap flux density with pole number

2.6 Optimisation of coil thickness

The predicted relationship between the airgap flux density and the coil thickness can be used to establish a preferred coil thickness that provides an acceptable trade-off between torque capability, losses and overall mass. The calculated flux density distributions can be used to establish the current density required for each coil thickness in order to meet the 50Nm torque specification. This in turn allows the copper loss at 50Nm to be calculated. The resulting variation in the copper loss at 50Nm as a function of the conductor thickness is shown in Figure 2. 18, for both 6mm and 12mm thick magnets. As shown by Figure 2. 18, the copper loss reaches minima at a coil thickness of 5mm for a 6mm thick magnet and at 7mm for the 12mm thick magnet. As would be expected, the higher flux density achieved with the thicker magnets results in a reduced copper loss at 50Nm.

It is important to recognise that the localised temperature rise in the coil is likely to the most limiting factor on torque performance rather than overall copper loss. The localised temperature is closely linked to the copper loss density. Figure 2. 19 shows

45

the variation in copper loss density with coil thickness for a torque of 50Nm, from which it can be seen that there is a continued reduction in copper loss density with increasing coil thickness. One other factor that will influence the conductor thickness selection is the copper mass, which linearly increases with coil thickness.

On the basis of this analysis, a preferred coil thickness of 5mm was identified for the subsequent detailed optimisation as offering a reasonable compromise between the different performance factors and the machine mass.
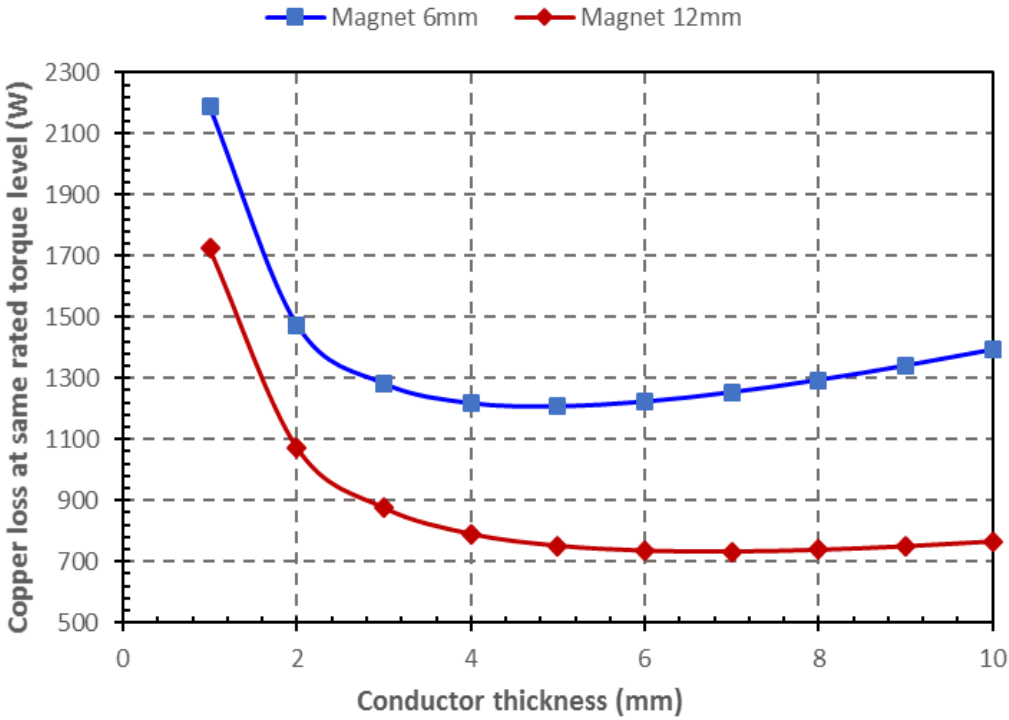
Figure 2. 18. Copper loss for different conductor thickness with same rated torque
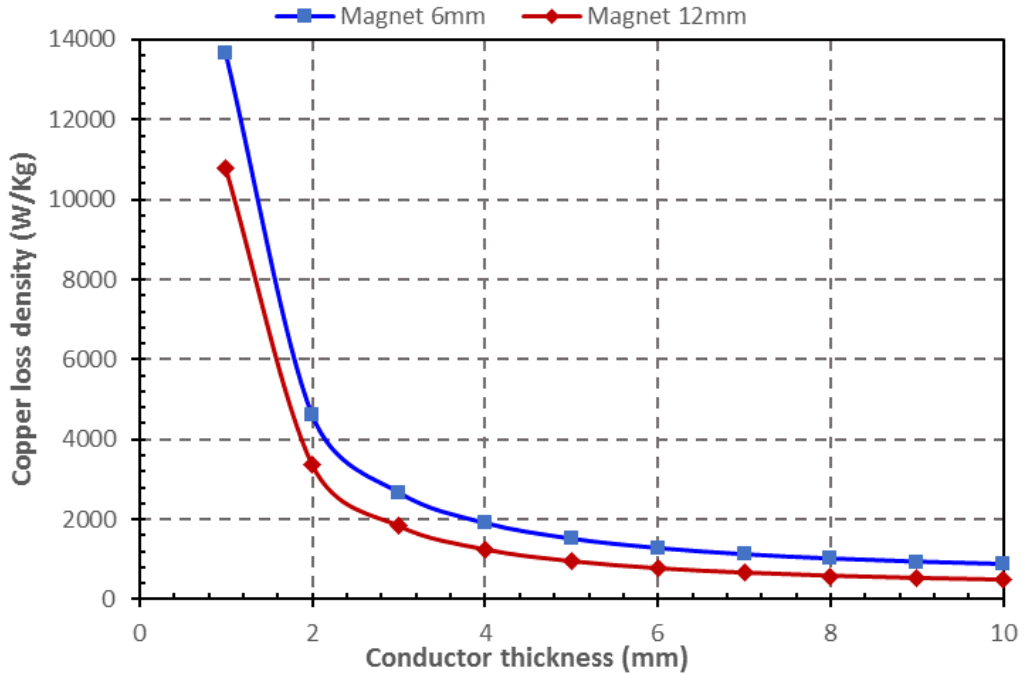
Figure 2. 19. Copper loss density under same rated torque

2.7   Initial sizing of a slotted toroidal machine (TORUS-S)

2.7.1   Sizing equations for TORUS slotted machine

The theory and design equations for a TORUS slotted machine shows many similarities with its non-slotted counterpart. Whereas the configuration of the non-slotted machine makes it difficult to establish a reliable estimate of the airgap flux density because of the large effective airgap, it is more straightforward in slotted machine due to the much small airgap making a one-dimensional model more appropriate. Despite being slotted, the space constraint imposed on the winding at the inner edge of the toroidal core means that the two winding fill and packing factors introduced previously in the design of the non-slotted machine are also necessary for the analytical design for the TORUS slotted machine.

Figure 2. 20 shows a typical slot arrangement for a TORUS slotted machine along with the definition of some key dimensional parameters, in Figure 2. 20 the tooth tips which result in semi-closed slots have been removed to aid clarity but would be present in the full machine. A close up of the stator slot, which includes the tooth tips is shown in Figure 2. 21.
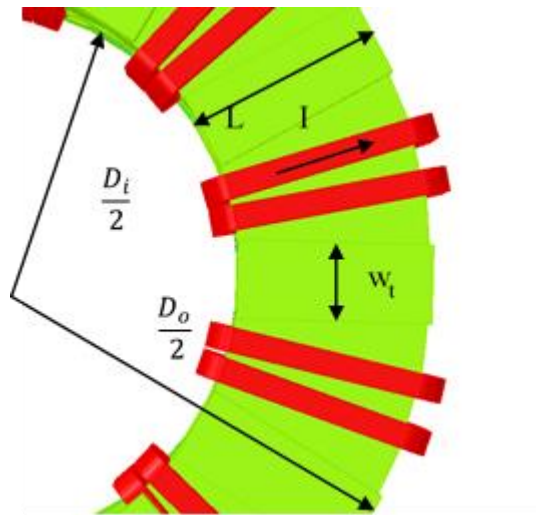
Figure 2. 20. Geometry of the stator TORUS-S machine (tooth tips removed in this view to improve view of coils)
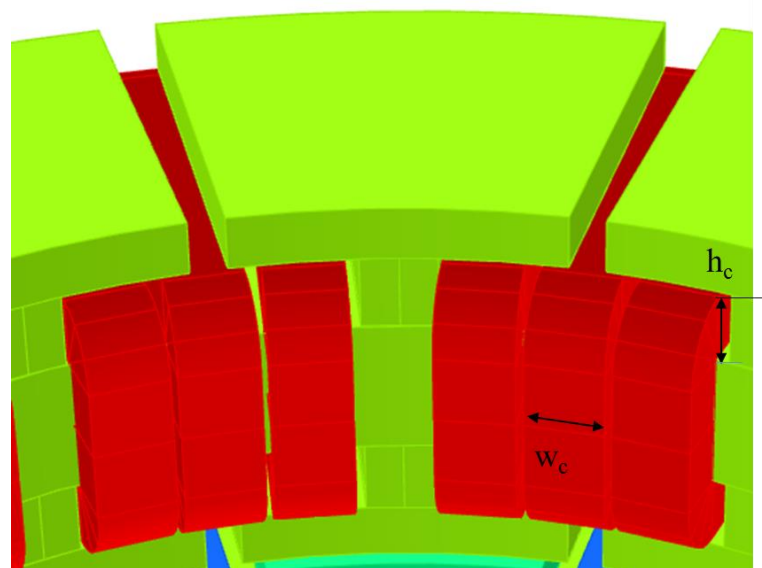
Figure 2. 21. Close up detail of the slot and conductors (includes tooth tips)

General purpose simplified sizing equation for axial field machine is [31]

$$T = \frac{\pi}{16} B Q_e D_o^3 (1 + s)^2 (1 - s) \qquad (2.14)$$

The average electrical loading Q_e over one sinusoidal cycle of coil current, can be expressed in terms of the rectified mean of the current in one coil with appropriate scaling for the number of stator slots and coils per slot. The resulting expression is given by:

$$Q_e = \frac{N_t N_c \frac{2}{\pi} I_{pk}}{\pi \left(\frac{D_o + D_i}{2} \right)} \qquad (2.15)$$

In the absence of a particular number of turns, this equation can be specified in terms of the coil cross-sectional area and the current density, assuming 1 turn:

$$N_c \frac{2}{\pi} N_t I_{pk} = N_c \frac{2}{\pi} A_{coil} J_{pk} \qquad (2.16)$$

$$N_c A_{coil} J_{pk} = \left[\frac{\pi}{2} (D_o + D_i) - w_t N_s \right] \cdot h_c \cdot \beta \cdot J_{pk} \qquad (2.17)$$

where w$_t$ can be expressed in terms of:

$$\frac{D_o - D_i}{2} w_t B_{core} = B_{gz} \frac{\pi (D_o + D_i)^2}{4p} \alpha \qquad (2.18)$$

which leads to:

$$w_t = \frac{B_{gz}}{B_{core}} \times \frac{\pi (D_o + D_i)}{2p} \alpha \qquad (2.19)$$

Substituting the resultant electrical loading into (2.14), the torque produced at mean radius $\frac{D_o + D_i}{4}$ can be readily derived as:

$$T = \frac{B_{gz}h_c\beta J_{pk}}{4}\left(1 - \frac{B_g}{pB_{core}}\alpha N_s\right)Do^3(1+s)^2(1-s) \qquad (2.20)$$

The complexity of the estimating the airgap flux density in order to calculate the torque and/or size the machine is greatly simplified in the slotted machine, since the small airgap (comprising the 1mm mechanical clearance only) means that a simple one-dimensional model can be used to establish a reasonable estimate of flux density. Typically, in slotted machines the airgap flux density is of the order of 70% of the remanence of the permanent magnet material.

The principle of establishing the factor β and the split ratio for the slotted TORUS machine is the same as for the non-slotted TORUS machine, hence same values for the those values can be obtained.

Having set the outer and inner diameter of the machine and assuming an airgap flux density of 0.7T, the remaining dimensions such as rotor and stator back iron length, magnet axial length and tooth width can be sized from simple geometrical relationships. These relationships are based on the assumption that the flux is evenly divided into two opposite directions when it enters the stator core. Similar process can be carried out for calculation of rotor back iron length.

The magnet length required to achieve a prescribed airgap flux density can be established by means of the well-established equation for airgap flux density which is based on a simple one-dimensional representation:

$$B_g = \frac{B_r}{1 + \mu_r \dfrac{l_g}{l_m}} \qquad (2.21)$$

The original tooth design can be modified by changing the shape from a rectangle into trapezoidal in order to maximize the space for conductors at the inner radius of the stator core. By maintaining the same tooth width at the average radius to that in the original rectangular design, the overall cross-sectional area of the tooth can be maintained. The least length w_{t1} can be established using:

$$(w_t - w_{t1})N_s + \frac{w_c N_c N_s}{\delta} = \pi D_i \tag{2.22}$$

The proportion of conductors cover the pole face, δ, can be calculated from:

$$\delta = \frac{D_i}{\frac{(D_o + D_i)}{2}}\beta \tag{2.23}$$

The optimised tooth body shape is shown in Figure 2. 22 (in which the tooth tips have been removed to provide an improved view). This demonstrates the improved utilisation of the slot volume.
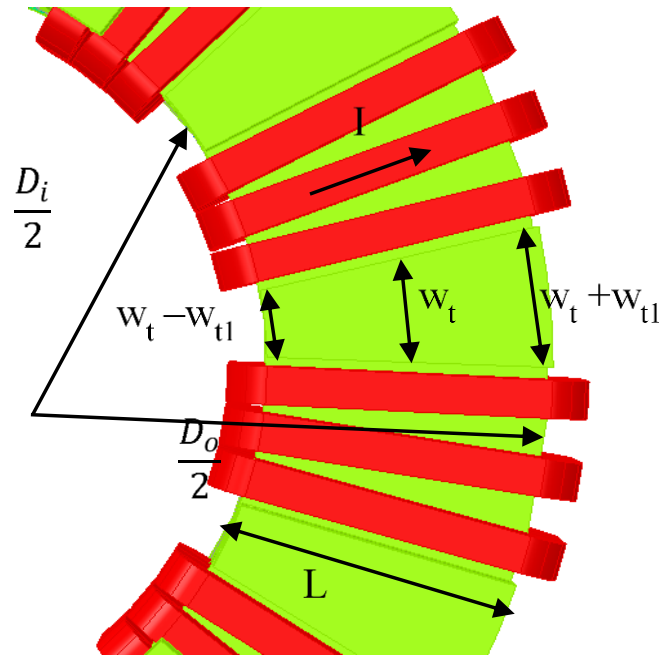
Figure 2. 22. Region taken from the machine after tooth optimization

2.8 **Slot-pole combination for slotted machine**

In many respects the geometry of a stator TORUS slotted machine shares many similarities with the stator of radial-field slotted machines with concentrated coils. However in a concentrated coil radial field machine the coils are wound onto the tooth body while for the TORUS machine, the coils are wound around the yoke which connects successive teeth. In many ways, this is the same arrangement as a radial field machine in which the coils are wound around the stator back-iron. Hence, the variation in the coil flux-linkage in a slotted TORUS machine does not necessarily follow the

general behaviour of a radial field machines in terms of tooth flux. The way that flux in a stator tooth in a radial field machine divides at the back of the tooth to return by the two alternative return paths is the aspect of behaviour that more resembles a slotted TORUS machine. As a consequence, it is possible that the same combinations of slot and pole numbers that are regularly used in radial field machines may not produce competitive torque density in slotted TORUS machines. In order to understand which slot-pole combinations can be used with a slotted TORUS machine a systematic investigation was undertaken.

The back EMF waveform for the TORUS slotted topology with 12 slot 8 pole combination (referred as 12s8p), 12 slot 10 pole combination (referred as 12s10p), and 12slot 14 pole combination (referred as 12s14p) were obtained from a series of three-dimensional finite element simulations, in which each combination had the same nominal dimensions. The resulting predicted 3-phase induced emfs for these 3 combinations at a rotational speed of 500rpm are shown in Figure 2. 23, while Figure 2. 24 shows the corresponding Fourier spectrums of the emfs.
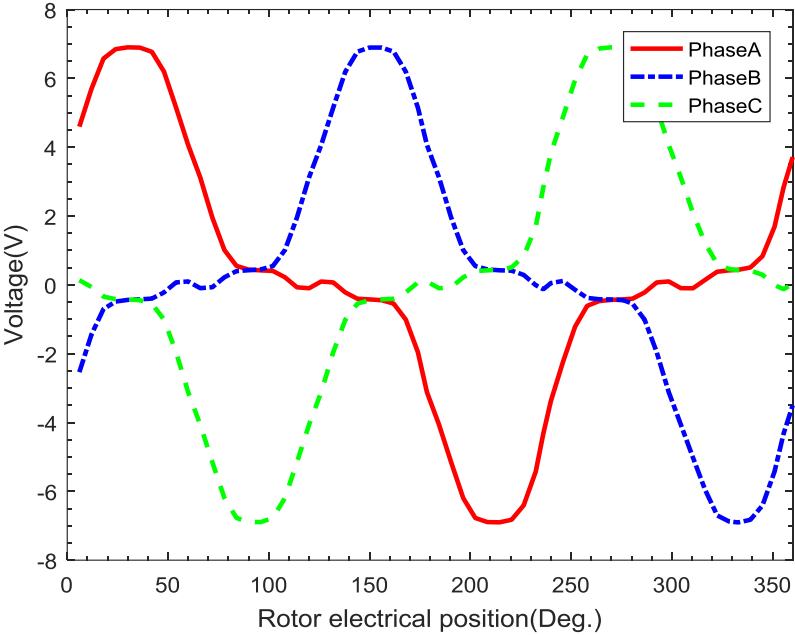
(a). 12s8p
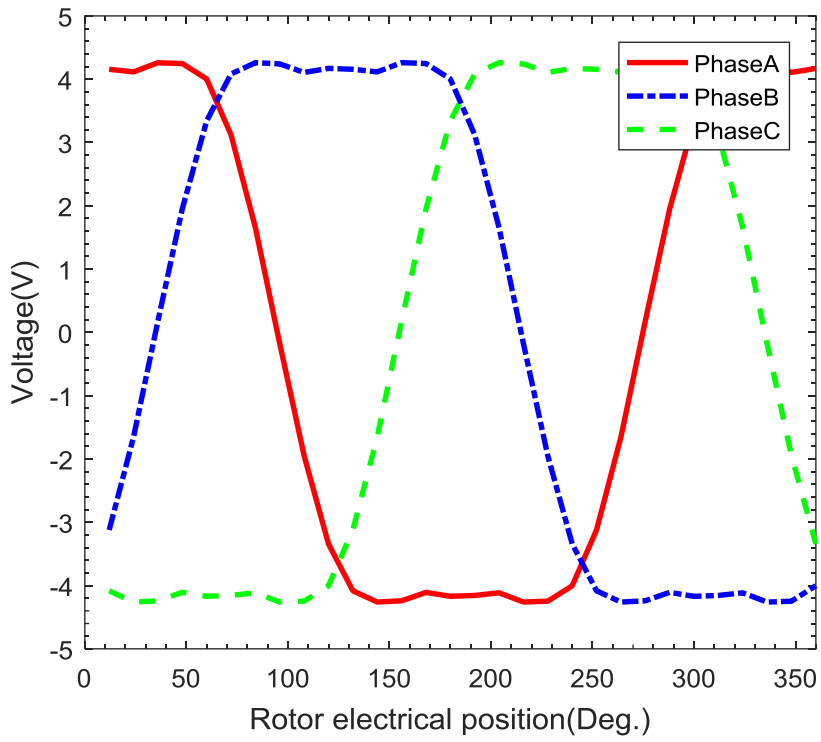
(b). 12s10p
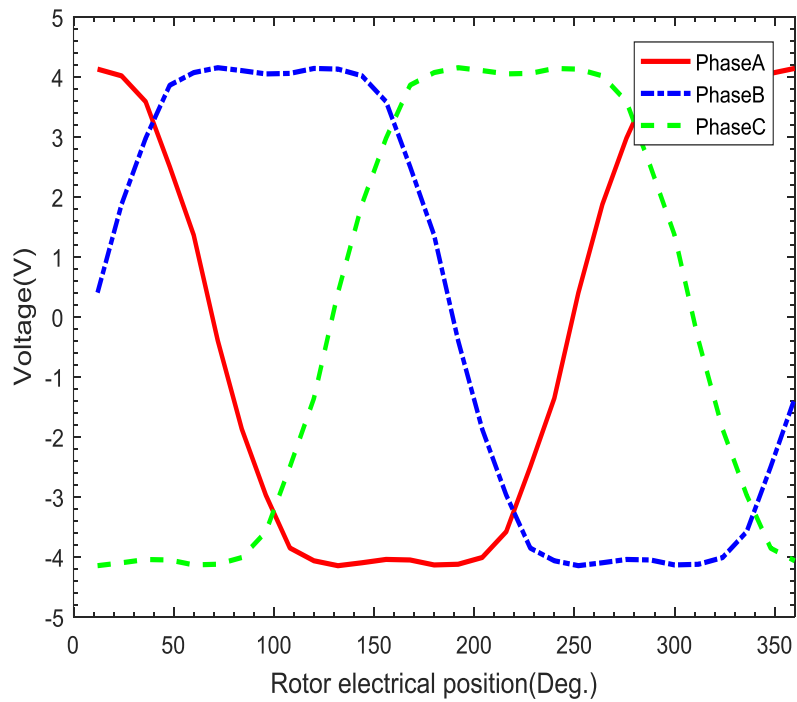
(c). 12s14p

Figure 2. 23. Three dimensional fintie element predicted back EMFs for three slot-pole combinations at a rotational speed of 500rpm
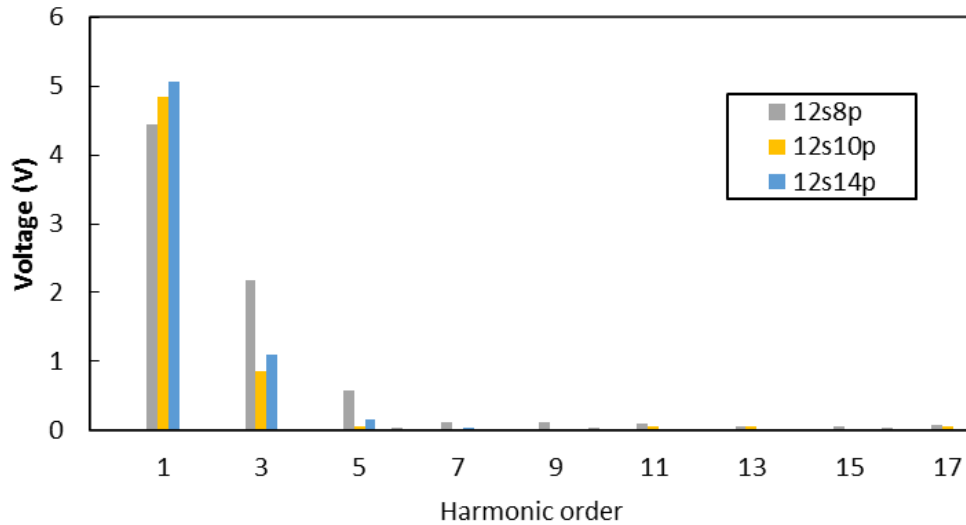
Figure 2. 24. Fourier analysis of the back EMF waveforms

The back EMF waveforms for the 12slot-8pole combination (which is a common combination in radial field machines) is the least suitable of the three emfs, with a long interval over which there is little or no emf. The 12slot-10pole and 12slot-14pole combination exhibit trapezoidal back EMF waveforms which would provide useful torque.

The Fourier analysis of Figure 2. 24 shows that the 12-8 slot pole combination has ~50% 3rd harmonic and 13% of a 5th harmonic in the waveform. In the other two combinations, the 5th harmonic is almost entirely suppressed, while there is ~20% of 3rd harmonic still present. According to the back EMF waveforms obtained for the three combinations, 12 slot 8 pole slot-pole combination seems to be unsuitable for a TORUS slotted topology even though it is arguably the most common 12-slot combination in three-phase, radial-field brushless permanent magnet machines

2.8.1 Lumped parameter model

In order to provide a means of identifying viable slot-pole combinations, simplified analytical model was developed based on a magnetic circuit approach. A rectilinear approximation of one quarter of a 12 slot 8 pole combination is shown in Figure 2. 25. It should be noted that for the 12s8p combination, there is a quarter rotational symmetry, whereas there is no rotational symmetry for the 12s10p and 12s14p combinations.
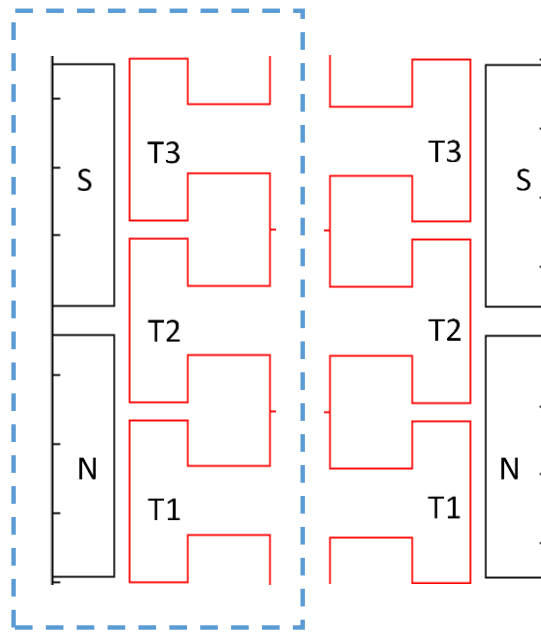
Figure 2. 25. Rectilinear representation of a quarter of the topology for 12s8p combination

The magnetic circuit shown in Figure 2. 26 represents half of the model shown in Figure 2. 25. The flux contributed by the magnet to the tooth is represented by a flux source connect in parallel with the permeance of the magnet itself [12] Since the flux variation over one rotation is the focus of this investigation, the magnet source is represented by a varying waveform with the peak value equal to the peak flux contributed by the magnet. The relative position of the magnets and the tooth determines the shape of the magnet source waveform. When the magnet is fully covering the tooth, the flux that enters the tooth is assumed to be one unit of the maximum, and when the magnet is only covering 2/3 of the tooth surface area for example, the flux that enters the tooth is assumed to be 2/3 of the maximum.

The maximum flux is calculated by $\Phi_r = B_r A_t$, where B_r is the remanence of the magnet and A_t is the surface area of the tooth tip. The internal reluctance of the magnet Rm is calculated via $R_m = \frac{l_m}{\mu_0 \mu_r A_m}$ where l_m is the magnet axial length, and A_m is the cross-sectional area of the magnet orthogonal to the direction of the magnetisation.

The variation of the flux source in the magnetic circuit is shown in Figure 2. 27 with the maximum flux normalised to unity. For the 12s8p and 12s10p combinations, the

maximum flux is $B_r A_t$ as the magnets surface area is larger than the tooth tip area. While for 12s14p combination, the maximum flux is $B_r A_m$ as the magnet is smaller than the tooth tip so that all of the magnet flux is contributing to the tooth.

The airgap is represented by a linear reluctance element and the reluctance of the back iron of the stator is represented by a very small resistance based on a fixed relative permeability of 4500. The reluctance of the airgap is calculated by $R_g = \frac{l_g}{\mu_0 A_t}$.
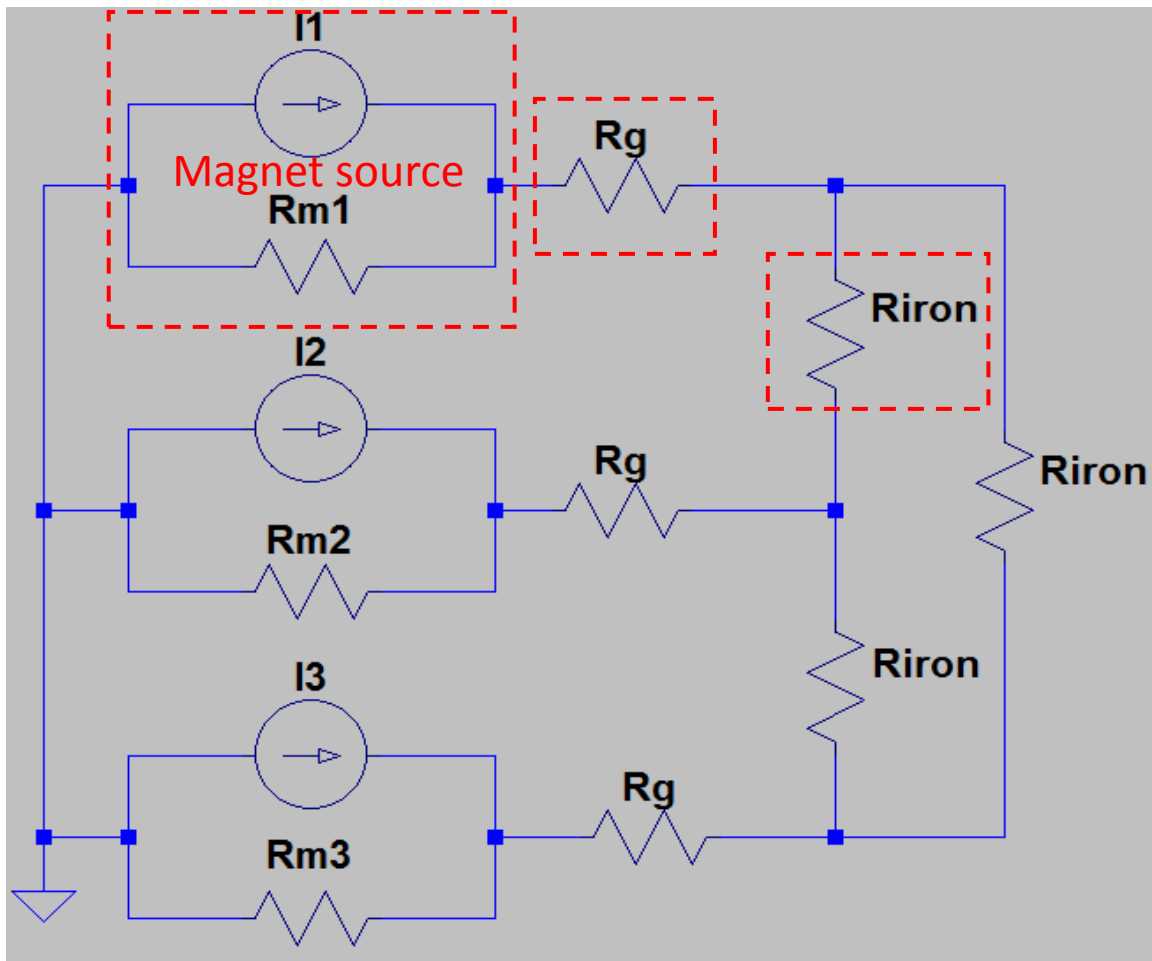
Figure 2. 26. Magnetic circuit representation for 12s8p combination
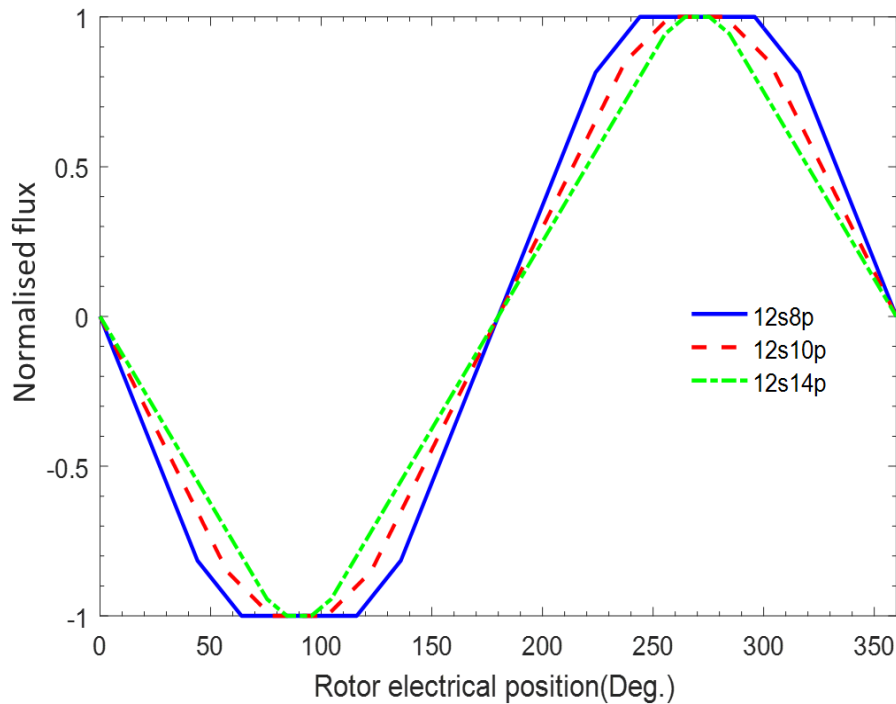
Figure 2. 27. Position dependent flux source variation for all three slot-pole combinations (individually normalised to unity)

2.8.2 Comparison between analytical and finite element model

The magnetic circuit model was analysed in the Simulink modelling environment. The Simulink model of the 12s8p combination is shown in the Figure 2. 28. The 12s10p and 12s14p model have very similar arrangements to that shown for the 12s8p machine. With the magnetic circuit, the flux variation in the back iron can be calculated and hence the back EMF can be derived. The magnetic circuit model are compared with FE predicted results for all three combinations in Figure 2. 29. To provide direct comparison, the core material used in the finite was assigned a linear fixed relative permeability of 4500.
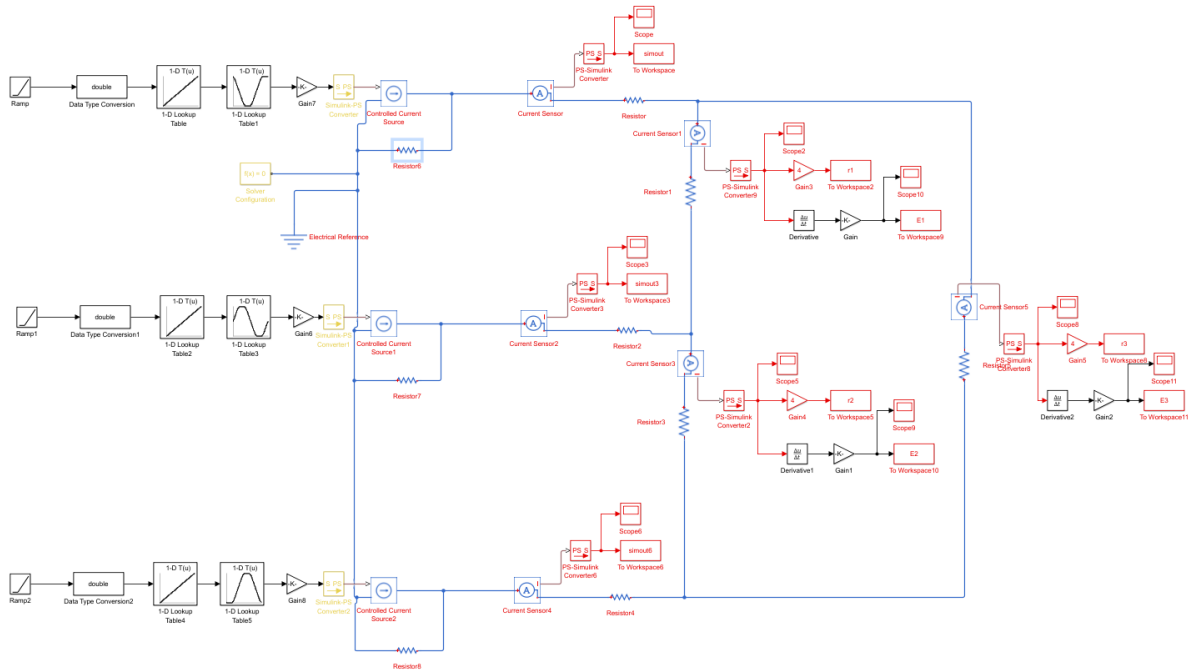
Figure 2. 28. Simulink implementation of the magnetic circuit solution for the 12s8p combination
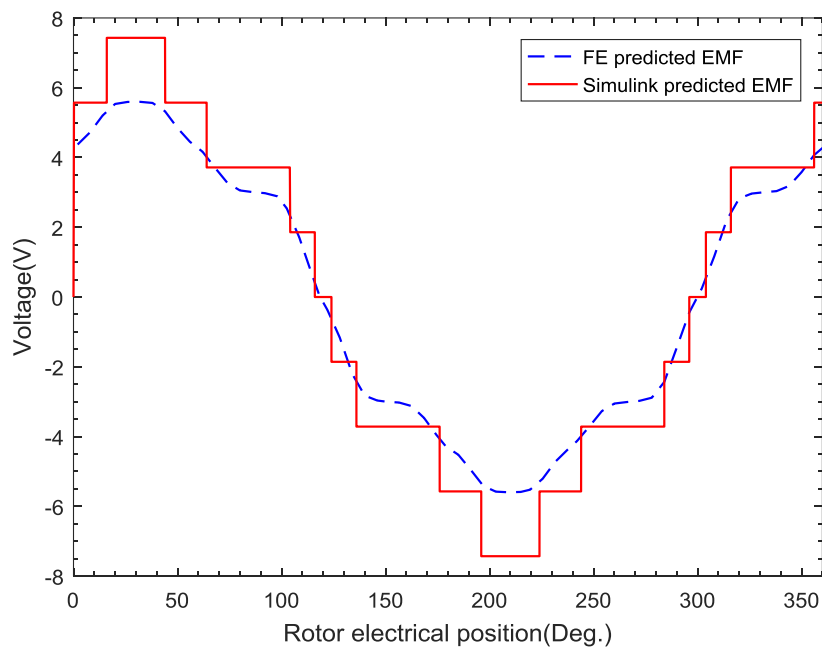
(a). 12s8p
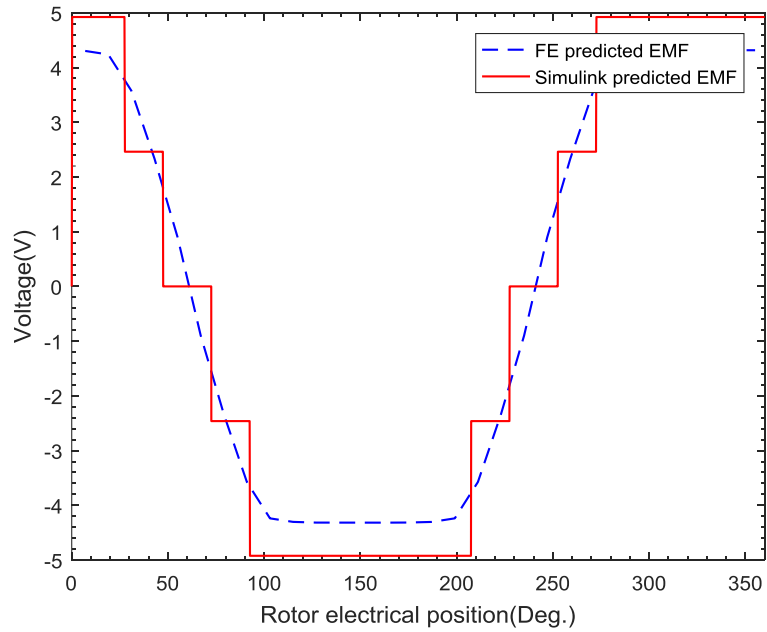
(b). 12s10p
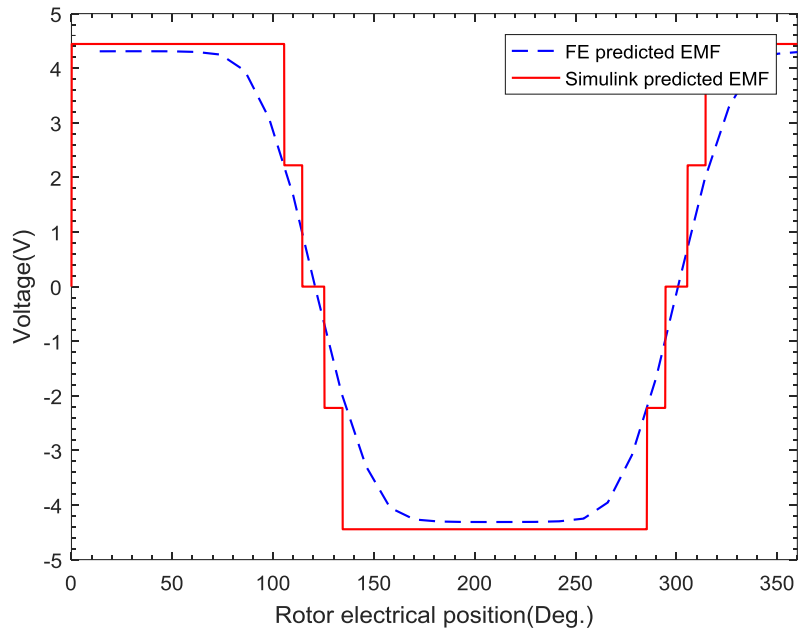
(c). 12s14p

Figure 2. 29. Back EMF waveforms comparison for analytical model and FE model with linear core material

The Fourier analysis of the back EMF waveform for the linear finite element model is carried out and shown in Figure 2. 30. As it can be seen that with linear material, the 3rd harmonic for the 12s8p combination is substantially reduced compared to the non-linear solutions presented earlier. This indicate that magnetic saturation, even under open-circuit conditions, is a significant contributor to the presence of a significant third harmonic.
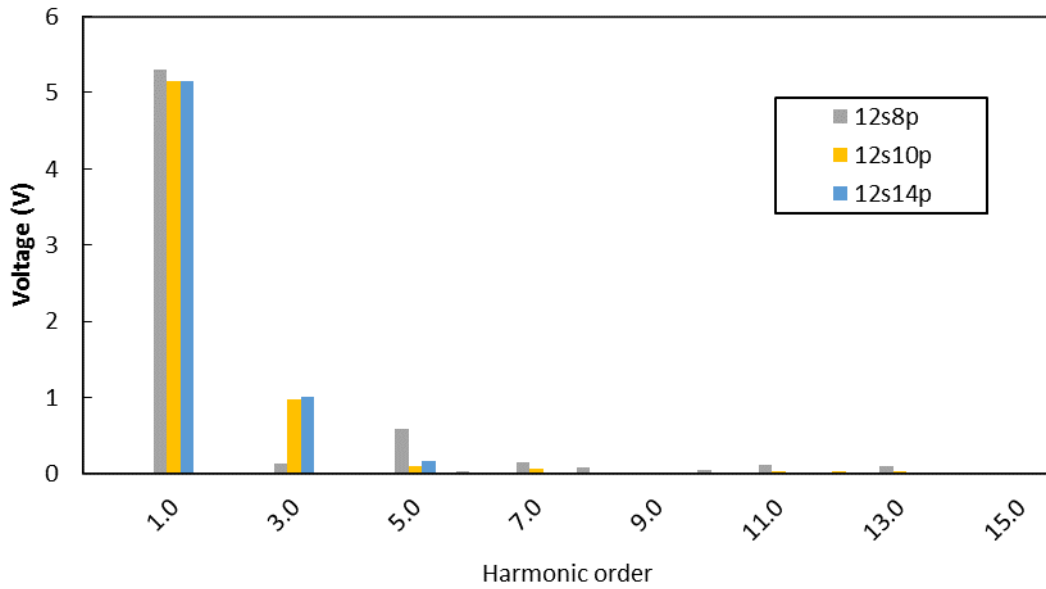
Figure 2. 30. Fourier analysis of the back EMF waveform predicted by FE model with linear material

The amount of flux entering a particular coil, i.e. passing through the appropriate stator yoke section for each combination is shown in Figure 2. 31. As can be seen, for the 12s8p combination, the peak flux that enters the stator back iron is the highest which potentially would lead to a more severe saturation for same back iron thickness compared to the 12s10p and 12s14p combination.
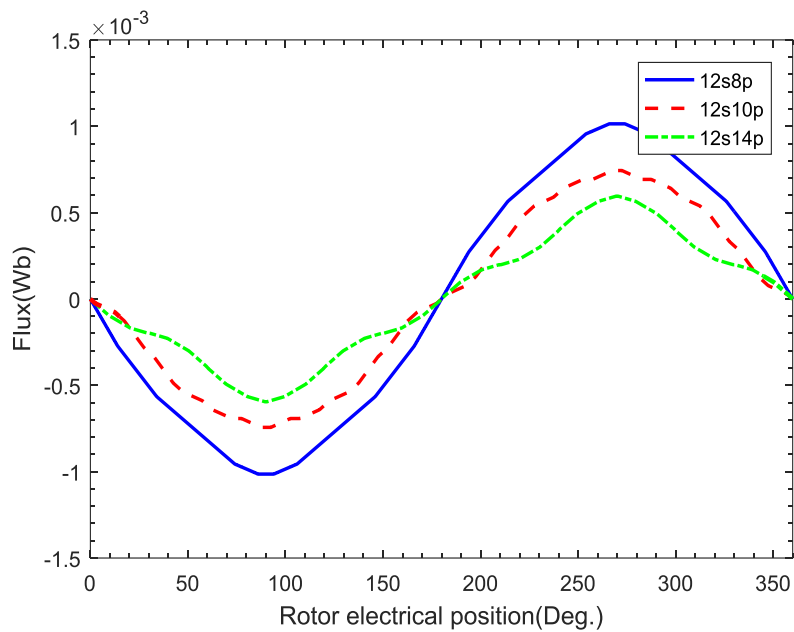
Figure 2. 31. Flux entering one coil for three combinations predicted by magnetic circuit model

To investigate the influence of saturation, a modified design of the 12slot-8pole variant was modelled using non-linear finite element analysis. In this modified design, the stator yoke thickness was increased from 15mm to 24mm which should be sufficient to alleviate magnetic saturation under open-circuit conditions. The resultant three-phase back EMF waveforms are shown in Figure 2. 32. As will be evident, the increase the yoke thickness improves the shape of the back EMF waveform compared to the 12slot-8pole is largely improved but is still some way short of the waveform that would be required for effective torque production. However, as also predicted by both the magnetic circuit model, a 12slot-8pole combination does not appear to be well-suited to this topology because of the nature of the flux return paths from the main stator teeth.
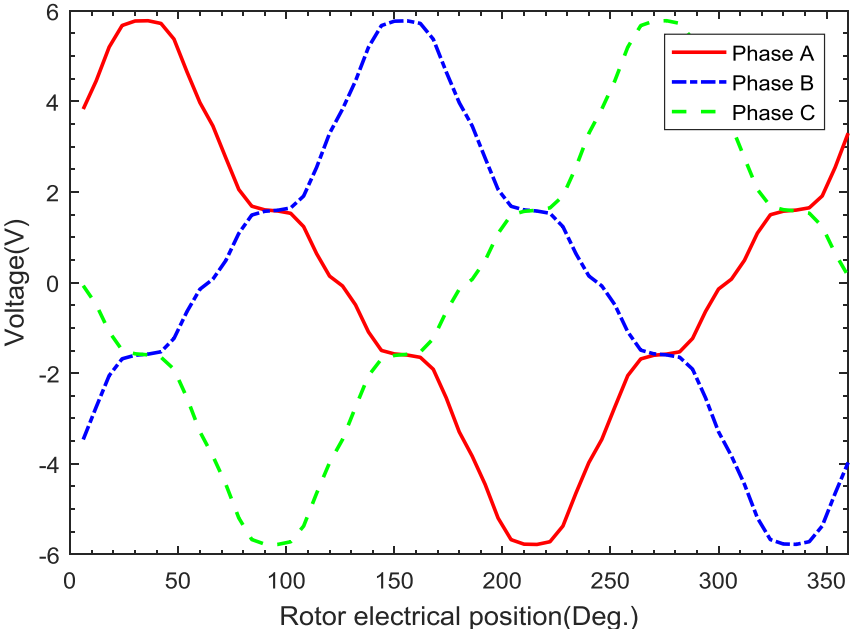
Figure 2. 32. Back EMF waveform of the 12s8p combination predicted by FE model with a thicker back iron

CHAPTER 3.   COMPARISON OF TOPOLOGIES

3.1 Introduction

The aerospace VGV application considered in this thesis is characterised by relatively high intermittent operation at high current densities. Whereas many of the usual considerations for continuously operating electrical machines also apply in this case, there are some additional electromagnetic and thermal considerations for machines operating under transient over-load conditions.

In this chapter, different machine topologies described in previous chapters are investigated and compared quantitatively within the context of a representative VGV actuator application. The topologies considered are a TORUS non-slotted machine, a TORUS slotted machine and the so-called YASA machine topology described previously in Chapter 1. Detailed finite element predictions are used to compare several aspects of performance including overload capability, magnet demagnetization at a high current density and induced eddy currents in solid cores.

A key challenge in the manufacture of many topologies of axial field permanent magnet machines is the requirement in many applications to laminate the magnetic core to inhibit the flow of induced eddy currents and hence reduce core loss. As discussed in Chapter 2, in some cases soft composites have been considered. However, for many applications, the reduced magnetic performance and modest mechanical properties of these materials means that they cannot compete with fully dense soft magnetic alloys. Unlike radial field machines in which individual laminations are stacked axially, lamination in axial field machines needs to be arranged as either a spiral or transversly as shown in Figure 3. 1 to be effective in reducing eddy currents. This feature brings both manufacturing difficulties as well compromising mechanical integrity.
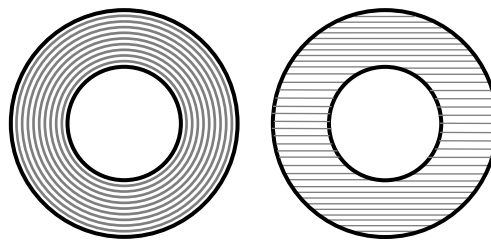
(a). Spiral lamination   (b). Transverse lamination

Figure 3. 1. Schematic of the spiral and axial lamination for axial field machine

However, in this particular VGV application, the combination of a low speed (maximum of 500rpm) and the very intermittent duty cycle mean that losses due to eddy currents and hence efficiency are not critical design factors. Hence, there may be scope to employ a solid (i.e. non-laminated) stator core. They key factor will be the extent by which torque capability is reduced by eddy current screening effects in the core rather than average core loss. The effect on performance of eddy currents in solid cores is investigated in this chapter using transient three-dimensional finite element analysis.

3.2 **Overall performance prediction**

As noted above, there are three machine topologies which are modelled and compared in this chapter, the TORUS non-slotted machine, TORUS slotted machine and the YASA machine.

Using the sizing equation developed in Chapter 2 and the 50Nm specification with transient rms current density of 30A/mm^2, the dimensions of TORUS non-slotted machine and TORUS slotted machines to meet these requirements were established. In the case of the YASA machine, this was sized along the same size as the reference design of the TORUS-Slotted reference machine, since it is an essence a variant of TORUS slotted topology. More specifically the same leading dimensions were adopted but with a modified core geometry and winding arrangement. The key dimensions for the three designs are summarised in Table 3. 1. As will be apparent, since these machines were designed to produce 50Nm, the resulting masses are different in the 3 cases, which in large part reflects the different torque density capability of the various topologies. As would be expected, the heaviest machine is the non-slotted TORUS with the YASA machine being lightest. However, it is important to note that the masses shown in Table 3. 1 comprise the active masses only. It is likely that the additional structural masses will differ between topologies, in particular the YASA machine in which some means of supporting the separate tooth modules is required.

63

Table 3. 1. Key dimensions and performance comparison for all three topologies

		TORUS non slotted	TORUS slotted	YASA
Topology information	Number of phases	3	3	3
	Pole number	8	14	8
	Slot or coil number	12	12	12
Key dimensions Unit (mm)	Outer diameter	176.80	174.30	174.30
	Inner diameter	106.08	104.60	104.60
	Magnet axial length	12.00	4.20	4.20
	Airgap length	6.00	1.00	1.00
	Stator axial length	12.00	29.81	29.81
	Rotor axial length	8.00	4.04	4.04
	Axial length	64.00	49.70	49.70
Weight Unit (Kg)	Magnet mass	2.82	0.96	0.96
	Coil mass	0.74	0.45	0.45
	Core mass	3.57	3.77	2.86
	Total mass	7.13	5.17	4.27

Having established the key dimensions using analytical design methods, the performance of these three reference designs were compared using three-dimensional finite element modelling. The finite element predicted flux density distributions in each machine topology under no-load conditions are shown in Figure 3. 2, Figure 3. 3 and Figure 3. 4.

<div align="center">
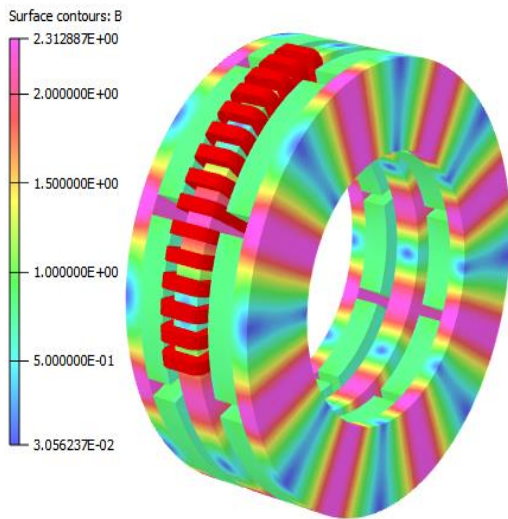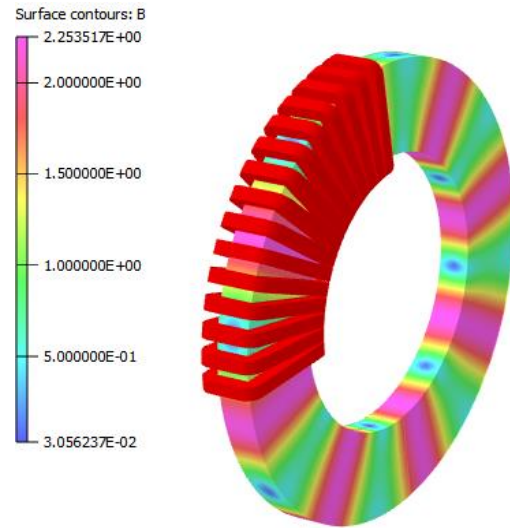
(a). Overal flux distribution   (b). Stator flux distribution

Figure 3. 2. Flux density distribution for TORUS non-slotted machine topology

</div>

<div align="center">
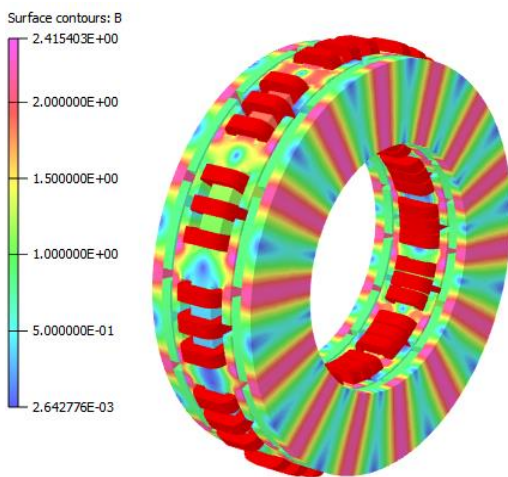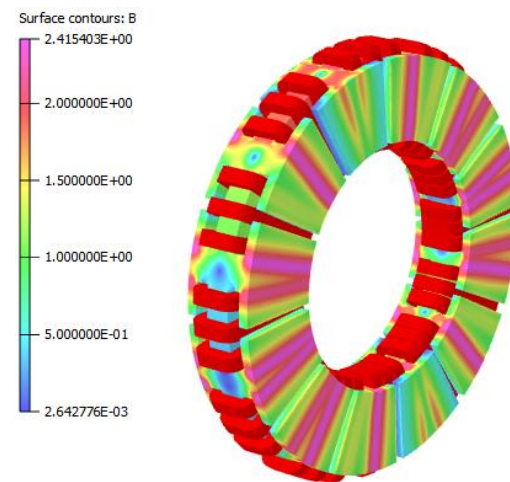
(a). Overal flux distribution   (b). Stator flux distribution

Figure 3. 3. Flux density distribution for TORUS slotted machine topology

</div>

(a). Overal flux distribution   (b). Stator flux distribution
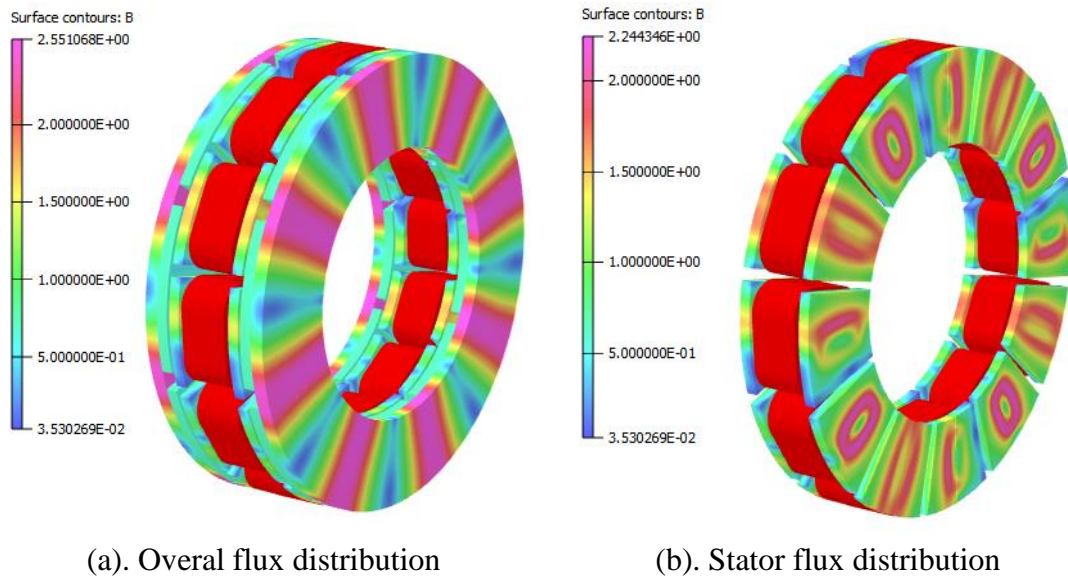
Figure 3. 4. Flux density distribution for YASA machine topology

The back EMF waveform at a rotational speed of 500rpm for three machine topologies are shown in Figure 3. 5, with the corresponding Fast Fourier Transform spectra shown in Figure 3. 6. Comparing emfs per turn between different machine topologies is not necessarily a useful comparison as it does not reflect the different slot areas available and hence the torque producing capability. To provide a more useful indication of the relative torque producing capability, the emf waveforms are shown per turn and normalised by the associated conductor cross-sectional area.

As will be apparent, when normalised to coil cross-sectional area, all three topologies show very similar peak magnitudes of emf. As would be expected, the TORUS non-slotted topology provides the most sinusoidal back EMF waveform with the lowest higher order harmonic content, e.g. the only discernible harmonic is a 5th harmonic with a magnitude of 1.2% relative to the fundamental. The remaining two topologies which have discrete slot openings exhibit relatively high 3rd and 5th harmonic content. The back EMF waveform for TORUS slotted machine more resembles a trapezoidal emf than sinusoidal with a 3rd harmonic content which corresponds to 26% of the fundamental. As would be expected, in terms of the shape of the waveform, there is a similarity between the YASA topology and the TORUS slotted topology given that the YASA topology is the transformation of the TORUS slotted machine. The Fourier transform of the back EMF waveform for YASA machine shows 12.9% of 5th harmonic in the waveform.
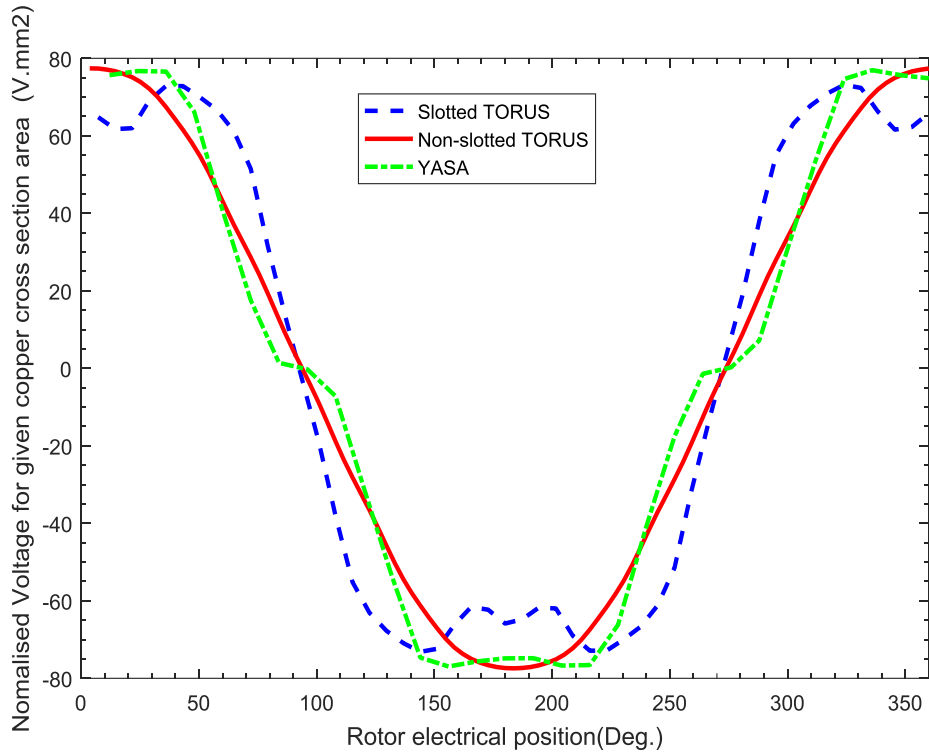
Figure 3. 5. Normalised back EMF waveform for three reference topologies
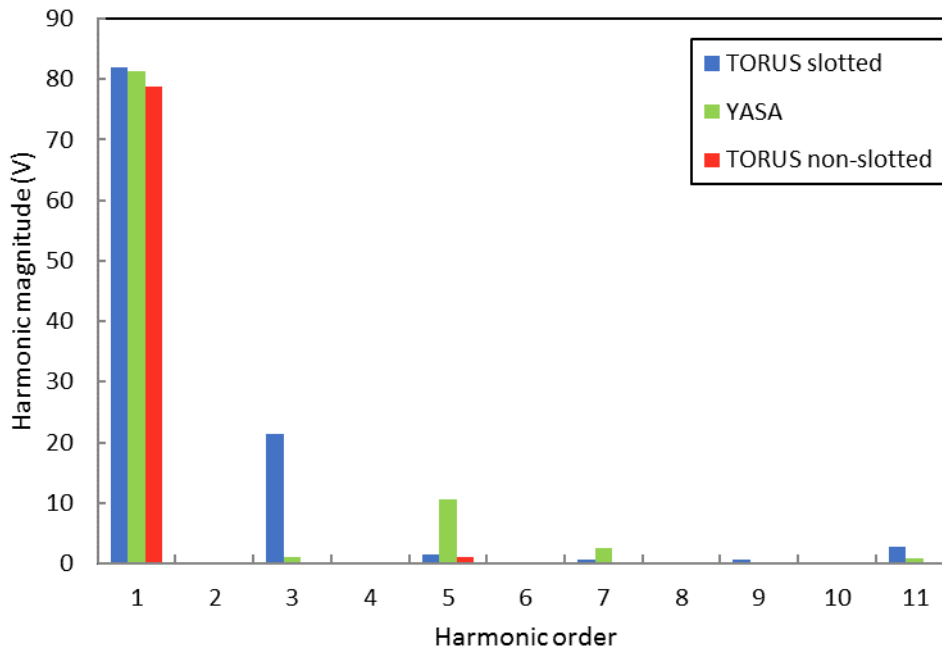
Figure 3. 6. Fourier transforms of the back EMF waveforms for three reference topologies

Using the predicted back EMF, estimates of rated torque can be established assuming that the stator is supplied with sinusoidal currents that correspond to an rms current

67

density of 30A/mm^2 for a 0.5 packing factor. This extrapolation from the open-circuit emf does not account for magnetic saturation. In order to evaluate the effect of magnetic saturation, the average values of torque for the three machine topologies over a full cycle of the torque waveform were calculated using three-dimensional, non-linear, magneto-static finite element analysis. A summary of the average torques calculated using these two methods for the three machine topologies is shown in

Table 3. 2. Values of average torque calculated at a current density of 30A/mm^2 and a packing factor of 0.5

Machine	Calculation method	Average torque (Nm)
Non-slotted TORUS	Extrapolation from open-circuit emf	48.1
	3D non-linear finite element	47.7
Slotted TORUS	Extrapolation from open-circuit emf	47.8
	3D non-linear finite element	45.0
YASA	Extrapolation from open-circuit emf	43.9
	3D non-linear finite element	41.2

The slotted TORUS and YASA topologies both exhibit lower torque predictions with the non-linear finite element models, which is consistent with magnetic saturation being more pronounced in these topologies. The torque waveforms produced by the three different designs are shown in Figure 3.8 for the same operating conditions of an rms current density of 30A/mm^2 in a coil with a packing factor of 0.5. The torque ripple for the non-slotted TORUS machine is ~3% whereas that for the YASA is ~34%.

The torque was also predicted for the slotted TORUS and YASA topologies with square-wave current waveforms of the same rms value as the sinusoidal current waveforms. The resulting torque waveform for both current sinusoidal and square-wave waveforms are shown in Figure 3. 7. As can be seen, for both topologies, the average torque produced by a square-wave current is lower than that achieved with a sinusoidal current waveform. The torque ripple produced by the square-wave current

wave is smaller than that achieved with sinusoidal current waveform for the TORUS slotted topology but the converse is the case for the YASA topology.

(a). TORUS slotted machine   (b). YASA machine
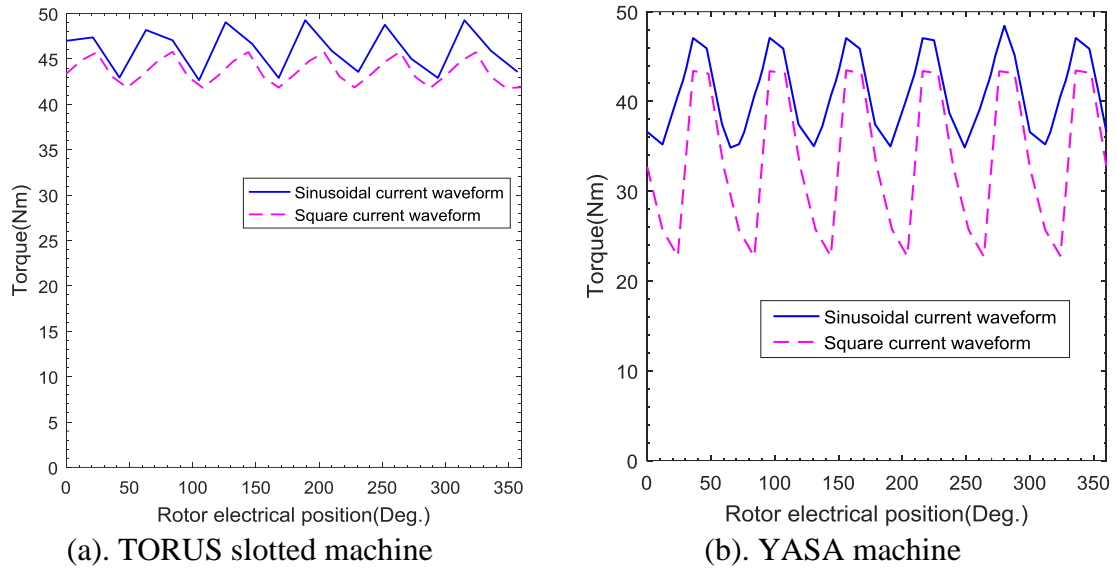
Figure 3. 7. Finite element predicted torque waveforms with square-wave and sinusoidal current waveforms

The calculated masses shown previously in Table 3. 1 can be used to calculate the torque densities of the 3 machine design based on the actual average torque calculate using non-linear three-dimensional finite element analysis. These torque densities are summarised in Table 3. 3. Despite the fact that YASA design did not meet its 50Nm target, it still offers the highest torque density by some margin, in large part because of the low stator core contribution. However, with the same overall diameter and length envelope, the torque produced by YASA machine is 8.5% less than the TORUS slotted machine. It has a lower volumetric torque density but the reduced core volume within this overall envelope ensures that it has higher gravimetric torque density.
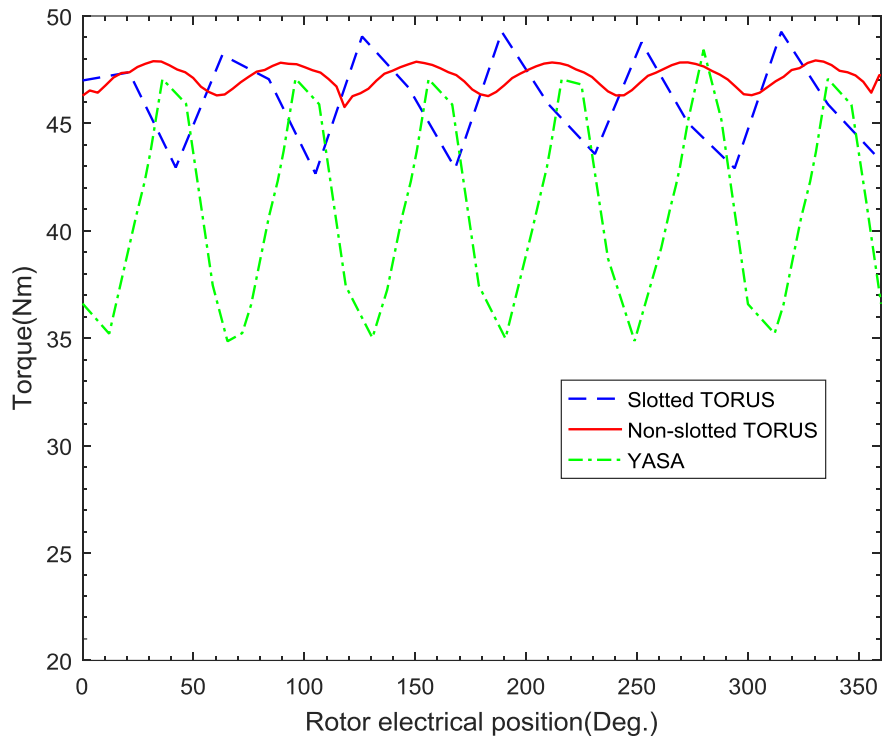
Figure 3.8. Torque waveforms with 30A/mm² sinusoidal current waveform for all three reference topologies (assumed coil packing factor of 0.5)

Table 3. 3. Summary of torque densities at 30A/mm² (based on active mass only)

	TORUS non slotted	TORUS slotted	YASA
FE predicted torque (Nm)	47.70	45.00	41.20
Mass of active components (kg)	7.13	5.17	4.27
Torque density (Nm/Kg)	6.69	8.70	9.65

3.3 Investigation of transient capability

3.3.1 Overload capability

As shown previously in Table 3. 2, the slotted TORUS and YASA motors are beginning to show indications of significant magnetic saturation at 30A/mm^2 with the non-linear finite element predicted torque being lower than that predicted using the finite element predicted open-circuit back-emf. This suggests that further short-term transient increases in the torque might be limited by saturation for these two machines. In order to explore the short-term overload capability of the three machine types, a further series of three-dimensional, non-linear finite element calculations were performed for current densities up to 100A/mm^2. The resulting variations in the average torque for the 3 designs of Table 3. 1 are shown in the Figure 3. 9. As will be apparent, the torque produced by the three designs are very similar at 10A/mm^2, which demonstrates the usefulness of the design equations. However, as the current density increases beyond 10A/mm^2, magnetic saturation starts to afect the slotted TORUS and in particular the YASA machine. This explains the shortfall in torque at the 50Nm design point for the YASA machine. As will be apparent, the non-slotted TORUS machine retains a near linear torque versus current density relationship right up to ~100A/mm^2. At this highest level of current density, the non-slotted TORUS produced over twice the torque of the YASA machine. The variation in the torque density of the three designs is shown in Figure 3. 10. As will be apparent, although the heavier non-slotted TORUS has the lowest torque density at the 30A/mm^2 operating point, at higher current densities the comparison is more favourable and there is a cross-over point at ~62A/mm^2 and a torque of 102.3Nm.
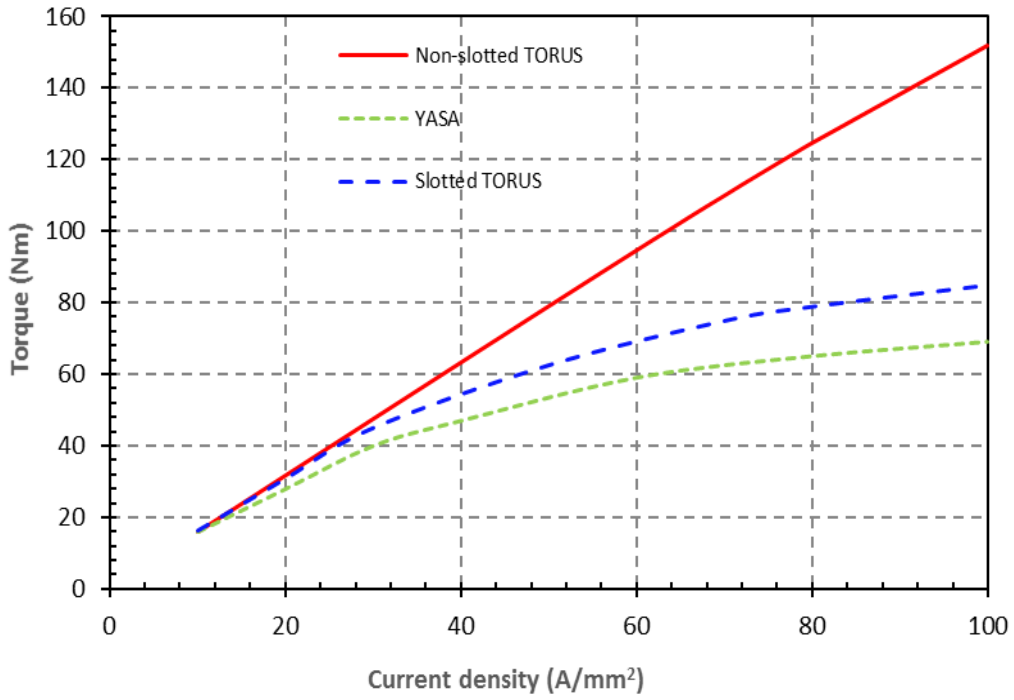
Figure 3. 9. Overload torque capability comparison for reference topologies
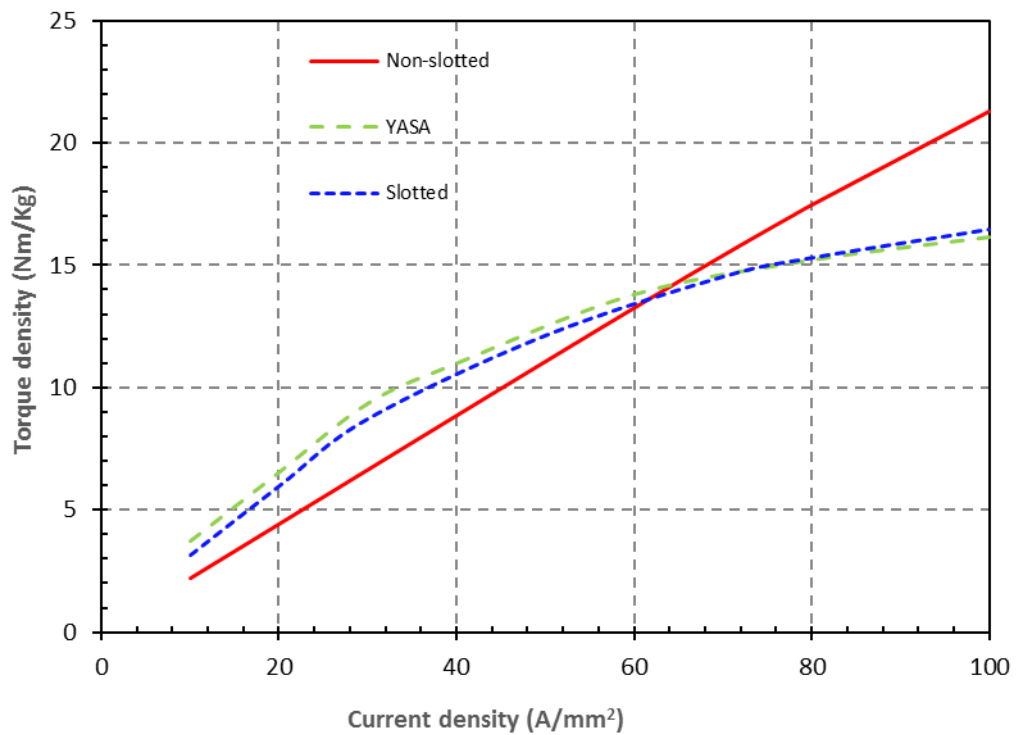
Figure 3. 10. Overload torque density capability comparison for reference topologies

This superior linearity of the non-slotted TORUS machine is to be expected given that it is the corollary of the difficulty in achieving competitive airgap flux densities and the need for thick magnets for the TORUS non-slotted topology. The influence of armature reaction will inevitably be modest given the high reluctance of the magnetic circuit. Ultimately, it is necessary to consider irreversible demagnetisation as the current density is increased. By applying some degree of safety margin, it may be that consideration of demagnetisation becomes the limiting factor on torque capability. However, notwithstanding these considerations, this graph shows the potential of a non-slotted topology for very high overload capability, despite it inevitably having a lower torque density than TORUS-S and YASA at modest levels of stator current density.

3.3.2   Current density limitations

The continuous rms current rating which can be sustained by a particular machine design is determined by cooling method employed. Typical values range from 5A/mm^2 with natural convection through up to 20A/mm^2 for direct liquid cooling. For forced air-cooling over the surface of the coil, the current density tolerated by the machine is 7.5A/mm^2 to 9A/mm^2, while the value increases up to 15A/mm^2 for forced air-cooling through embedded conduct or vents. [39] However, the thermal mass of the machine can be exploited to use much higher short-term current densities than the continuous rating. For a given continuous rms current density, the value of current density that can be sustained with a continuous repetition of a particular duty cycle can be estimated on the basis of an adiabatic approximation to the heating of the copper. This provides a worst-case estimate, particularly for longer durations, since in practice, some of the loss will be dissipated to adjacent structures bringing their thermal mass into play. However, this worst-case estimate provides a useful indication of the duty cycle that can be sustained at higher current densities. The adiabatic temperature rise for a given total energy loss is given by:

$$\Delta T = \frac{\Delta Q}{c_{Cu} m} \tag{3.1}$$

The energy loss in a winding of cross-sectional area *A* and length *l* for a duration t is given by*:*

$$Q = \frac{J_{rms}{}^2 Al\Delta t}{\sigma} \qquad (3.2)$$

The mass of the winding is given by:

$$m = \rho_{cu} Al \qquad (3.3)$$

Substituting for Q and m in (1) yields:

$$\Delta T = \frac{J^2 \Delta t}{c_{Cu}\rho_{cu}\sigma} \qquad (3.4)$$

It is necessary to account for the fact that the copper resistivity will change during the period in which the temperature is rising. The resistance at a temperature T is given by:

$$R_T = R_{re}\left[1 + \alpha_T\left(T - T_{ref}\right)\right] \qquad (3.5)$$

A simple time-stepping approach can be used to predict the temperature rise for a given current density with account of the temperature dependency of resistance. The maximum duration that a particular current density can be sustained was calculated using equations (3.1) to (3.5) using the following methodology:

- For a given continuous rms current rating, the corresponding current density at various set duty-cycles can be calculated assuming that the current remains at zero for the remainder of the duty cycle.

- This current density was input to a time-stepped calculation and the temperature rise monitored.

- The time taken for the stator winding to rise from 20°C to 200°C was recorded.

Table 3. 4 shows the calculated short-term current density for a given duty cycle and continuous rating along with the time taken for the temperature to rise adiabatically from 20^0C to 200^0C. As an example, for a machine that can dissipate losses continuously at a rate that would allow a continuous current density of 10A/mm² rms to be used, then for a 1% duty cycle, this machine could sustain a current of 100A/mm² on a repeating basis. With this 100A/m² short-term current, a temperature rise from 20^0C to 200^0C would occur in 2.81s on the basis an adiabatic heating process. This duration would need to be shortened if the cooling was not able to reduce the starting

temperature to 20°C within the following 278s (i.e. 99×2.81s). Taking a less extreme case, the design current density specification of 30A/mm^2 would be capable of operating for at least 31.3s, recognising that this is worst-case adiabatic process. However, despite its limitations and assumptions regarding the starting temperature for each short-term overload interval, Table 3. 4 provides a useful indication of the trade-off between torque rating and duty cycle.

Table 3. 4. Current density limitations for different duty cycle

J_{rms} (A/mm^2)	10% duty cycle		5% duty cycle		3% duty cycle		1% duty cycle	
	J_{on} (A/mm^2)	Time (s)	J_{on} (A/mm^2)	Time (s)	J_{on} (A/mm^2)	Time (s)	J_{on} (A/mm^2)	Time (s)
3	9.49	313.06	13.42	156.56	17.32	93.99	30	31.32
4	12.65	176.20	17.89	88.09	23.09	52.88	40	17.62
5	15.80	112.85	22.40	56.15	28.90	33.73	50	11.27
6	19.00	78.04	26.80	39.22	34.60	23.53	60	7.83
7	22.10	57.68	31.30	28.76	40.40	17.26	70	5.75
8	25.30	44.01	35.80	22.01	46.20	13.20	80	4.40
9	28.50	34.68	40.20	17.43	52.00	10.42	90	3.47
10	31.60	28.21	44.70	14.10	57.70	8.46	100	2.81
11	34.80	23.26	49.20	11.64	63.50	6.99	110	2.33
12	37.90	19.61	53.70	9.77	69.30	5.87	120	1.96
13	41.11	16.69	58.14	8.35	75.06	4.99	130	1.67
14	44.27	14.36	62.61	7.18	80.83	4.31	140	1.44
15	47.43	12.55	67.08	6.26	86.60	3.75	150	1.25
16	50.60	11.00	71.55	5.50	92.38	3.30	160	1.10
17	53.76	9.75	76.03	4.86	98.15	2.92	170	0.97

T_{ref} = reference temperature of 20^{0}C

3.4 Magnet irreversible demagnetization

When current density is increased to higher values, in addition to the thermal constraints, the potential for irreversible demagnetisation of the magnets must also be taken into consideration. Irreversible demagnetisation leads to a permanent reduction in performance (unless the machine is disassembled and re-magnetised) and is usually regarded as a condition that must be avoided under any circumstances.

In order to establish the limits on current density from a demagnetisation point of view, for each of the machine topologies a series of finite element models were used to calculate the maximum localised demagnetisation limits. The permanent magnet material selected for this study is VACOMAX 225 HR which is a grade of Sm_2Co_{17} manufactured by Vacuumschmelze [32]. Figure 3. 11 shows a close-up of the manufacturer supplied third quadrant demagnetisation curve at magnet temperatures of 200°C, 250°C and 300°C. Also shown are the knee-points of the demagnetisation which set the limit for demagnetisation.
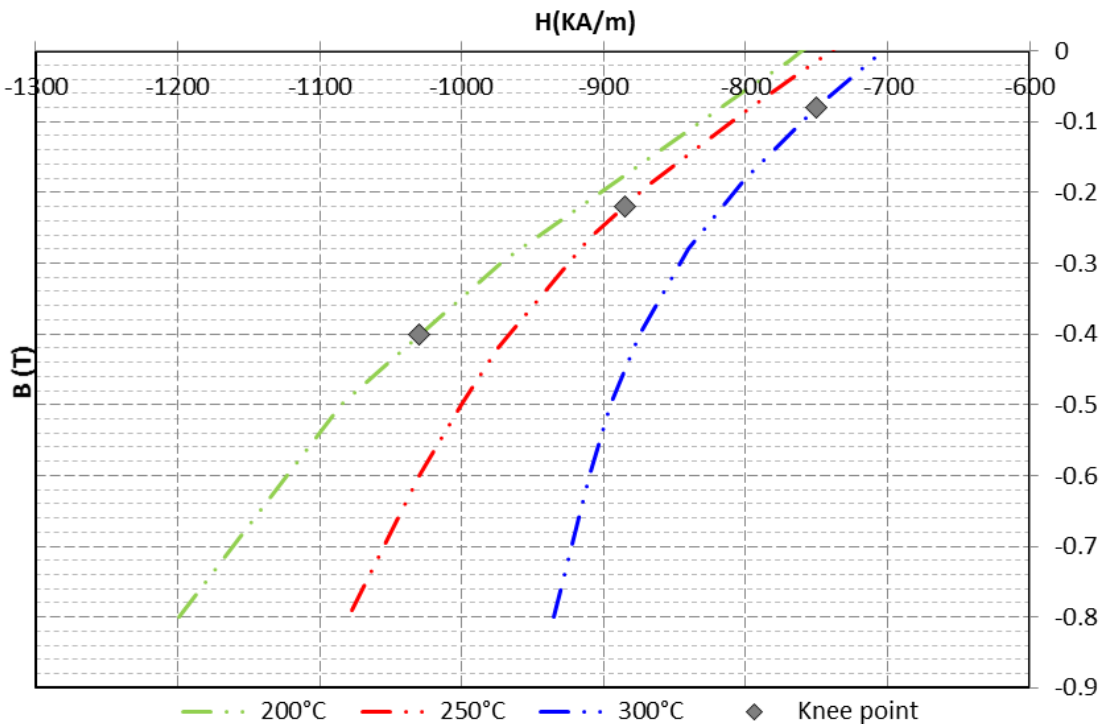
Figure 3. 11. Knee point of the magnet material under different operating temperature

The characteristics of Figure 3. 11 can be used in combination with localised calculated flux densities throughout the magnets to assess whether any irreversible demagnetisation will occur at a given value of current density. In terms of assessing the presence of irreversible demagnetisation, the flux density limits for the magnet under different level of operating temperature is shown in Table 3. 5.

Table 3. 5. Flux density limit for magnet irreversible demagnetization under different temperature

Operating temperature (^{0}C)	Irreversible demagnetization flux density level (T)
200	-0.4
250	-0.22
300	-0.08

It is important to recognise that these negative values correspond to demagnetisation of a magnet which is of a polarity that produced positive flux densities. It is necessary to change the sign of these limits for magnet regions of the opposite polarity.

3.4.1 Magnet demagnetization for TORUS non-slotted machine

The first essential step for assessing demagnetisation is to identify the rotor position at which the rotor magnet demagnetisation is the most severe.

The first case considered was based the maximum current density of 100A/mm^2 considered in the torque calculations. Figure 3. 12 shows the minimum value of flux density in any of the magnets (corrected in each pole so that a negative flux density corresponds to the third quadrant of the demagnetisation characteristics of the pole) as a function of rotor position. It can be seen that the lowest point falls between 75° and 80°. A finer analysis is then carried out and the rotor position for the most severe level of demagnetization for the magnets is identified. As will be apparent, the lowest flux density obtained from this model under the current density of 100A/mm^2 is well within the limiting values for VACOMAX 225HR as the flux density of the magnets needs to be negative to be demagnetized and hence there is no danger of demagnetisation at this value of current density.
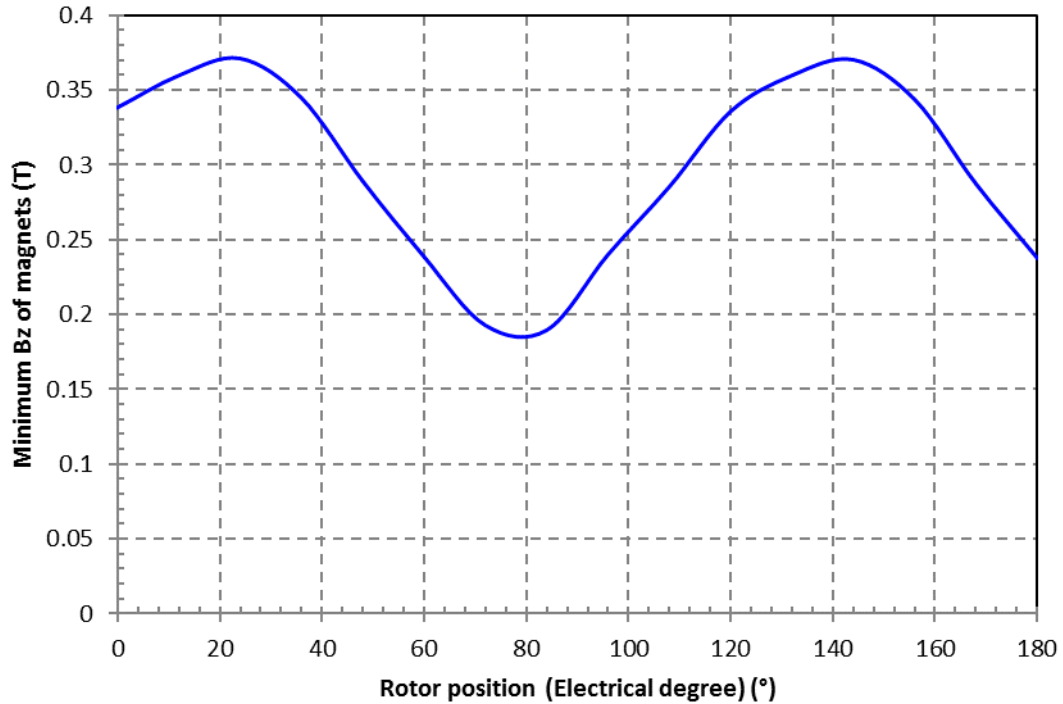
Figure 3. 12. Minimum z-direction flux in any magnet versus rotor position at a current density of 100A/mm²

A simple scaling was applied to estimate current densities at which demagnetisation would become a problem. The next case modelled was 340A/mm² (at a packing factor of 0.5) as this is likely to be close to the limiting value for irreversible demagnetisation at 200°C. The flux density distribution in a magnet exposed to this demagnetizing field is shown in Figure 3. 13. The coloured contour on the surface of the magnets represent the z-component of flux density (which is the direction of magnetisation of the magnets). As shown, the flux density is negative (i.e. in the opposite direction to the direction of magnetisation) at the edge of the magnet. The orientation of the flux density in the machine around the region of the demagnetised edge is shown in Figure 3. 14. The arrows indicates the direction of the local flux. As shown, this is an extreme case since the flux densities in the core are ~2.6T.
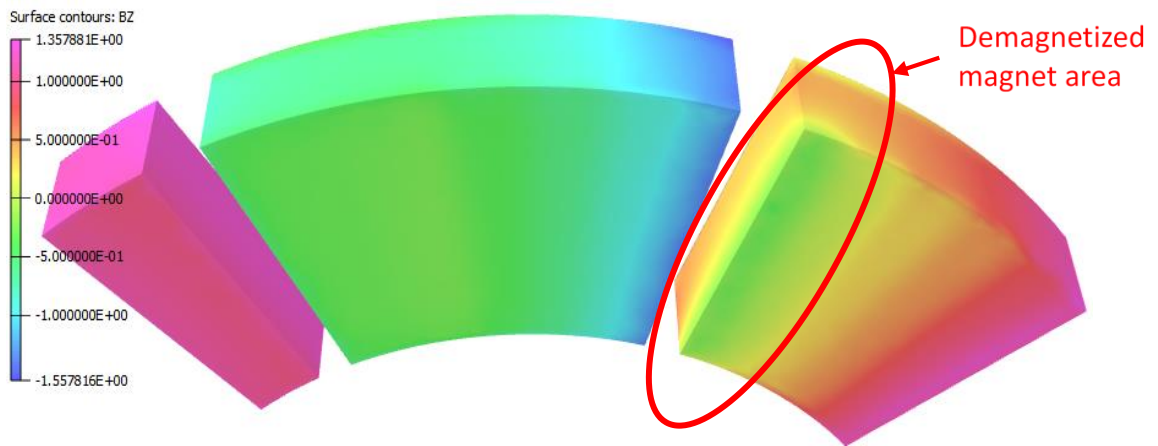
Figure 3. 13. Flux density distribution for the demagnetised magnet
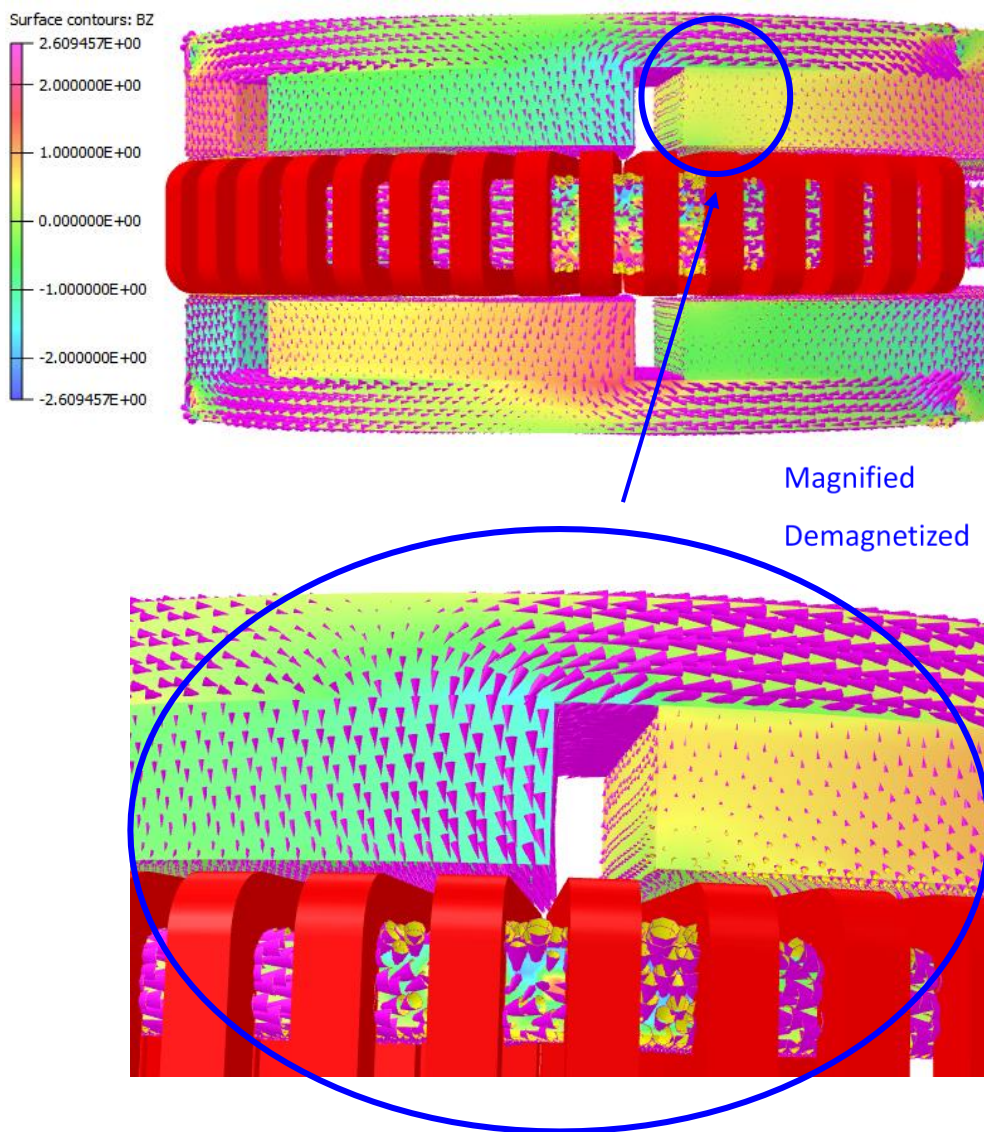
Figure 3. 14. Flux direction in the vicinity of the magnet demagnetised area

A series of further models were analysed at various current densities for the rotor orientation which is the worst case for demagnetisation. Since the permanent magnet demagnetisation characteristic is a function of temperature, as shown previously in Figure 3. 11. In order to calculate the limiting current density at each of the three temperature of interest, separate series of calculations were performed with magnet demagnetisation characteristics at 200°C, 250°C and 300°C.

Table 3. 6 shows the resulting calculated maximum current densities allowable before the magnet undergoes irreversible demagnetization for the TORUS non-slotted machine at a series of magnet temperatures.

For the magnets operating at 300°C, the maximum current density level is 188A/mm^2, increasing to 240A/mm^2 at the 250°C and further increasing 340A/mm^2 at 200°C. All of these values are well above the current densities that could be applied in practice because of the thermal limits, e.g. even the lowest value of 188A/mm^2 could only be sustained for 0.81s using the adiabatic temperature rise model described in section 3.3.2. This illustrates that irreversible demagnetisation is not a significant issue in this machine compared to the thermal constraints. This is due to a combination of thick magnets and a large effective airgap.

Table 3. 6. Summary of current density limits for magnet demagnetization

Magnet Temperature (°C)	B_{lim} (T)	J (A/mm^2) (at packing factor of 0.5)	Bmin (T)
300	-0.08	186	-0.071
		190	-0.084
		188	-0.08
250	-0.22	260	-0.26
		250	-0.23
		240	-0.21
200	-0.4	300	-0.3
		330	-0.36
		340	-0.39

3.4.2 Magnet demagnetization for the slotted TORUS machine

The same process of establishing demagnetizing limits was undertaken for the slotted TORUS machine. Again it is necessary to establish the worst-case rotor angular position for demagnetisation. Figure 3. 15 shows the minimum flux density of all south-oriented magnet on one rotor side for the case of a current density of $100A/mm^2$. As will be apparent, the worst-case demagnetisation occurs at a rotor angular position of 84^0.
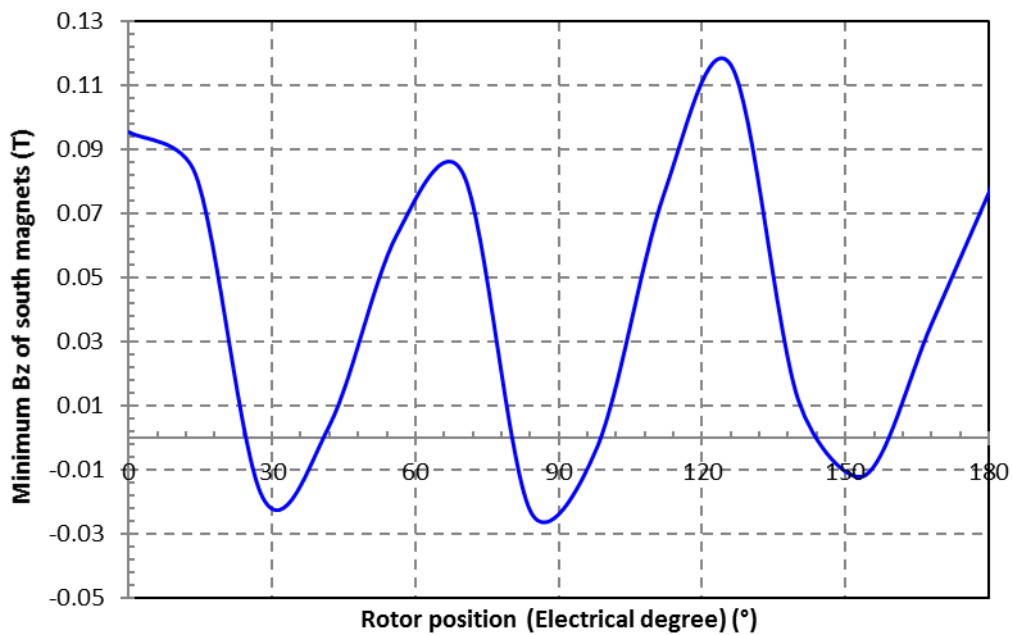
Figure 3. 15. Minimum z-direction flux density for the magnet versus rotor position

The variation in the surface flux density of the magnets is shown in colour contour map in Figure 3. 16, while Figure 3. 17 shows the flux density distribution and the direction of the flux in the region of the machine in the vicinity of the magnet for a current density of $100A/mm^2$. In many slotted machines, the maximum demagnetization rotor position for magnets coincides with the edge of the magnet coming into alignment with the tooth tip. However, the worst-case angular position for TORUS slotted machine proved to be rather different , although as would be expected the most vulnerable region was the edge of the magnet. For the slotted TORUS machine, the worst case demagnetisation occurred when magnet edge was aligned with the centre of the tooth body.

81
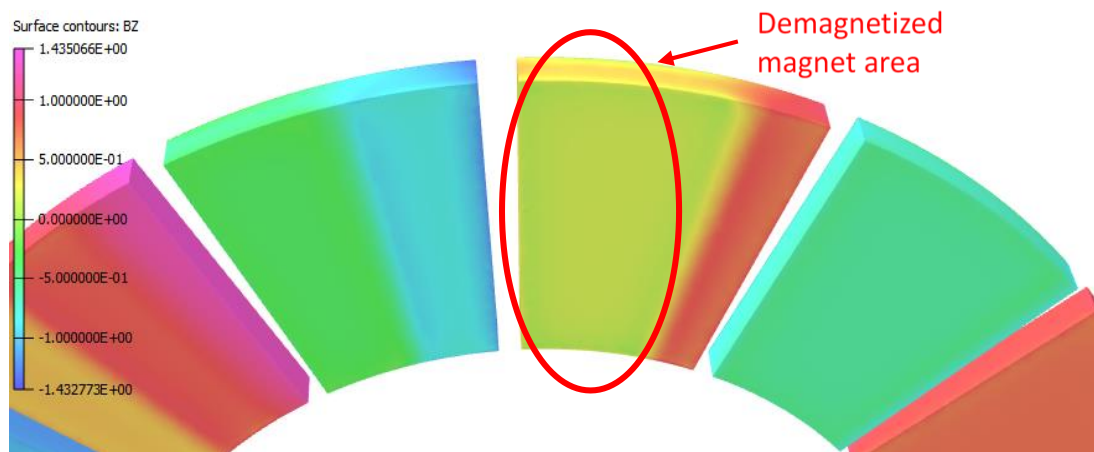
Figure 3. 16. Flux density distribution colour contour for the demagnetized magnet
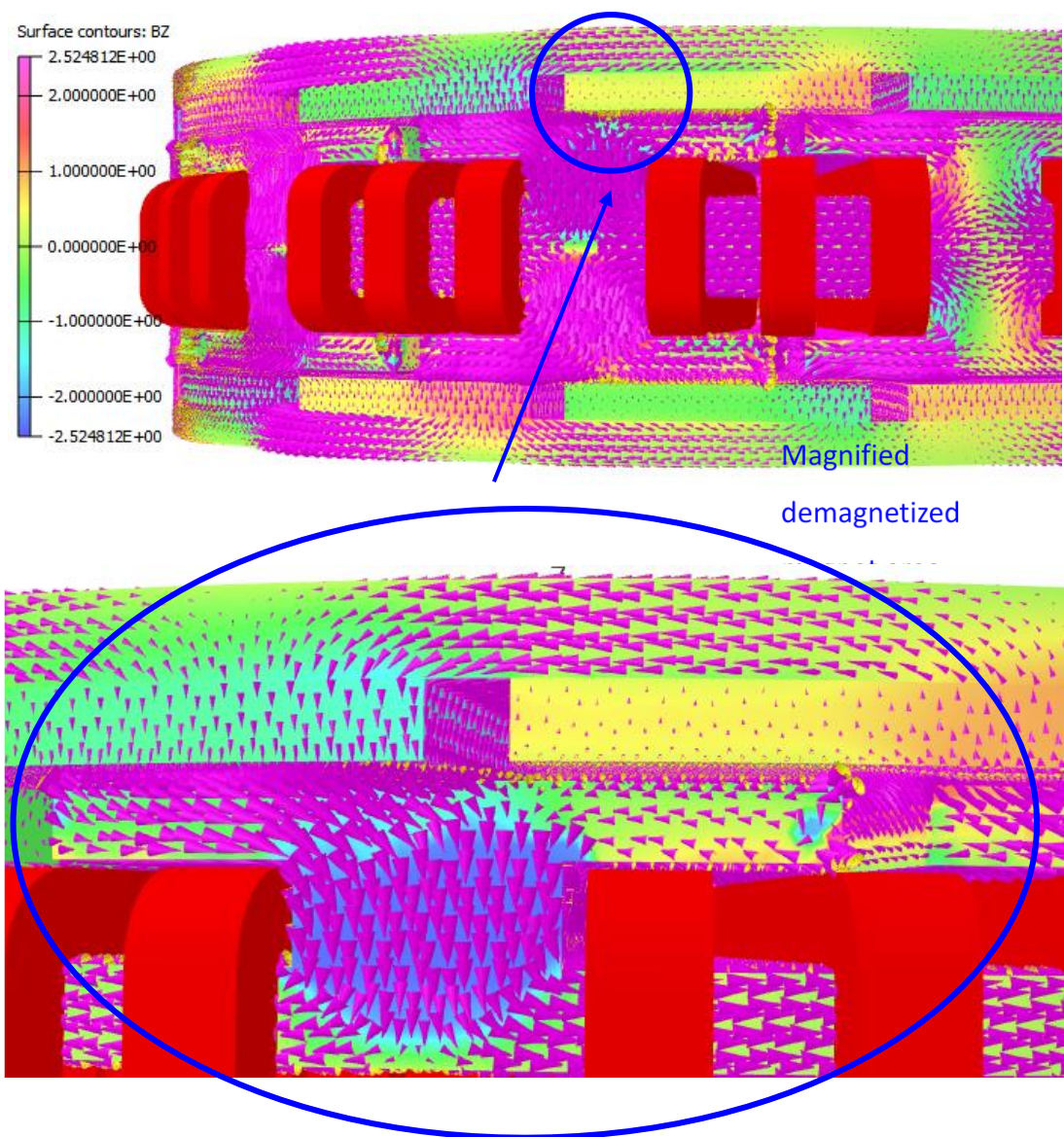
Figure 3. 17. Flux distribution in the magnet demagnetised area

The current density limits for the slotted TORUS machine were calculated in the same way as was done for the non-slotted TORUS. In the case of the slotted machine, the current density limits at 200°C, 250°C and 300°C were 600A/mm^2, 260A/mm^2 and 150A/mm^2 respectively. The very high 600A/mm^2 reflects the fact that at very high flux density levels, the permeability of the stator core will not be sufficient to direct the flux towards the magnet. With the stator heavily saturated, the magnetic property of the material performs as air and the slotted TORUS machine could be treated as a non-slotted TORUS machine with very large airgap length which leads to a large airgap reluctance.

Figure 3. 18 shows the variation in the predicted torque for both the non-slotted and slotted machines up to the various demagnetisation limits. As will be apparent, although the slotted TORUS machine has a higher demagnetisation limit, it does not result in a useful increase in torque.

It is also interesting to note that beyond ~120A/mm^2, the non-slotted machine starts to exhibit the effects magnetic saturation in terms of the torque constant of the machine.
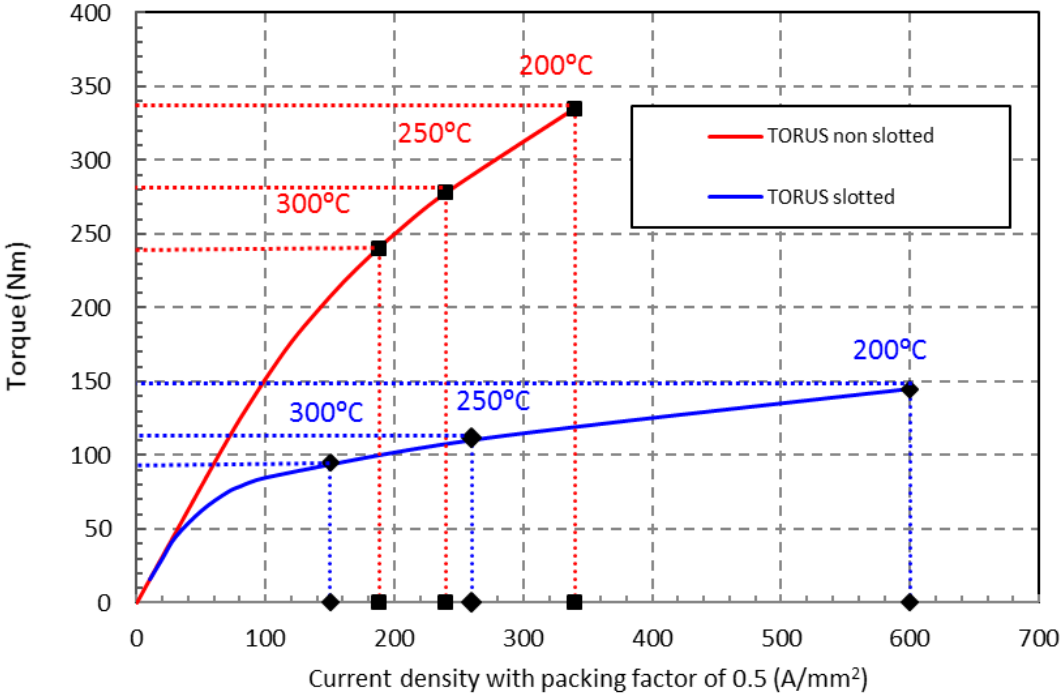
Figure 3. 18. Average torque as function of current density up to various temperature demagnetisation limits for both TORUS non-slotted and TORUS slotted machines

3.5 Eddy current effects with solid stator cores

As discussed earlier in this chapter, the laminating the stator cores of axial field permanent magnet machines is very challenging and usually compromises the mechanical integrity of the core. Taking into consideration the highly intermittent nature of the target application in which efficiency under continuous operation is not an important factor, there is potential to employ solid stator cores. Whereas this will improve mechanical strength and aid heat transfer it may result in significant eddy current screening in the core which could reduce the effective torque constant of the machine. In order to investigate the feasibility of adopting solid stator cores, a series of magneto-dynamic transient, three-dimensional simulations were performed.

The material adopted in the model for the stator and rotor cores of the non-slotted TORUS machine is VACOFLUX 50, which is a high performance grade of Cobalt Iron manufactured by Vacuumschmelze. The rotor and stator cores were assigned the magnetic properties and electric conductivity of VACOFLUX 50 and the rotor magnets were assigned the magnetic and electrical conductivity of VACOMAX 225 HR.

A sinusoidal current waveform corresponding to an rms current density of 30A/mm^2 (with the packing factor of 0.5) was applied to the stator coils. These coils were modelled as so-called 'stranded-coils' in which no eddy currents flow. The open-circuit emf was calculated at a three rotational speeds of 500rpm, 1500rpm and 5000rpm. Although the latter two values are greater than the specification, they provide some insight into the limitations of solid cores at higher excitation frequencies.

The resulting normalised phase emf waveforms are shown in Figure 3. 19, along with the original back EMF waveform calculated at 500rpm with a magneto-static model is also presented in the figure. As would be expected, the presence of eddy currents in the stator core reduces the magnitude of the back EMF and introduces a phase shift in the waveform which becomes more pronounced at the higher speeds.

The magnitude of induced back EMF voltage at the rated speed of 500rpm with eddy current effect is 97.1% of the corresponding waveform calculated with a magneto-static model, which in terms of this aspect of performance suggests that the adoption

of a solid core will only result in a modest reduction in performance at 500rpm. As might be expected, the performance at 5,000rpm shows a very marked effect due to eddy currents.

The influence of eddy currents on the torque waveform for the TORUS non-slotted machine was also investigated using a magneto-dynamic three-dimensional transient finite element model. In this case, a rotational speed of 100rpm was also considered and the rms current density was set to $30A/mm^2$ for all speeds. The resulting torque waveforms are shown in Figure 3. 20. As shown, at 500rpm, the average torque is reduced by 22.1% compared to the corresponding magneto-static analysis. Interestingly, this is far greater than the reduction in the open-circuit emf and indicative of a more pronounced effect of eddy currents on the stator field. Although this is a large reduction in torque, it should be recognised that the machine will spend a significant proportion of its time accelerating up to 500rpm and decelerating back down.
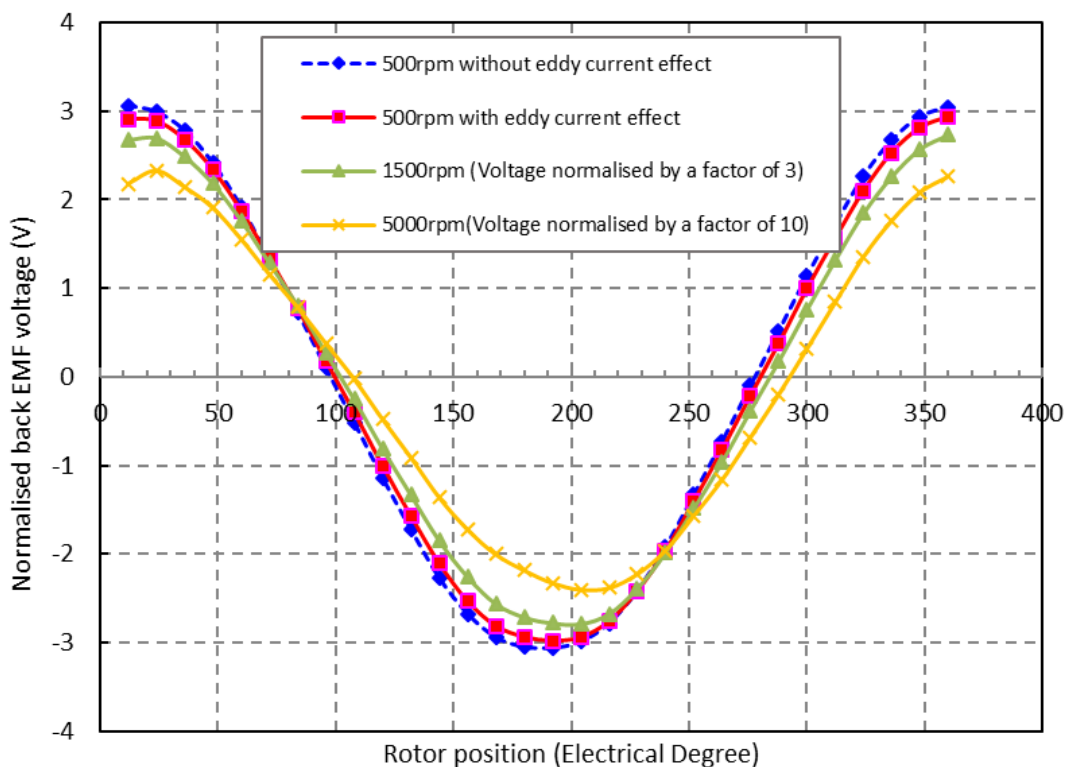
Figure 3. 19. Finite element predicted back EMF waveforms at a range of rotational speeds
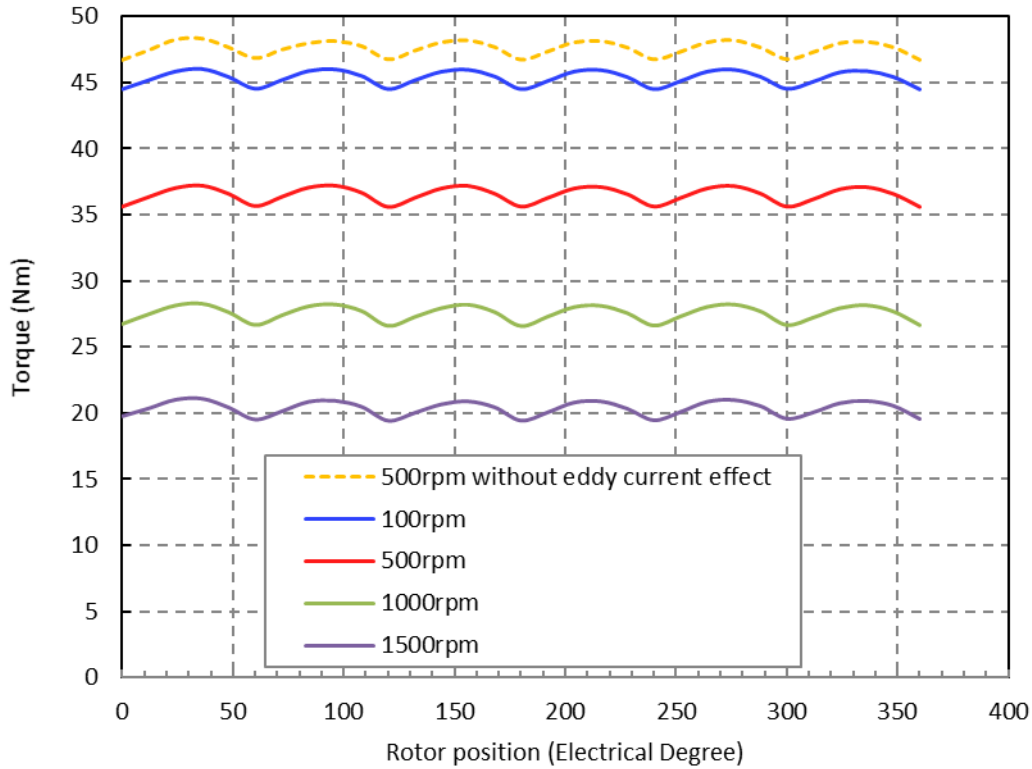
Figure 3. 20. Eddy current effect on torque waveform at a range of different rotational speed (stator coil current density of 30A/mm^2 at a packing factor of 0.5)

Similar analysis was carried out for the slotted TORUS machine and the YASA machines with solid stator and rotor cores. The resulting variation in the torque performance with rotor speed due to the presence the eddy currents is shown in Figure 3. 21. In all case, the models wer fed with sinusoidal current waveforms corresponding to an rms current density of 30A/mm^2. As would be expected, the non-slotted TORUS shows the least reduction in torque with increasing rotational speed. The YASA machines shows a similar, but marginally greater, drop off in torque with speed.
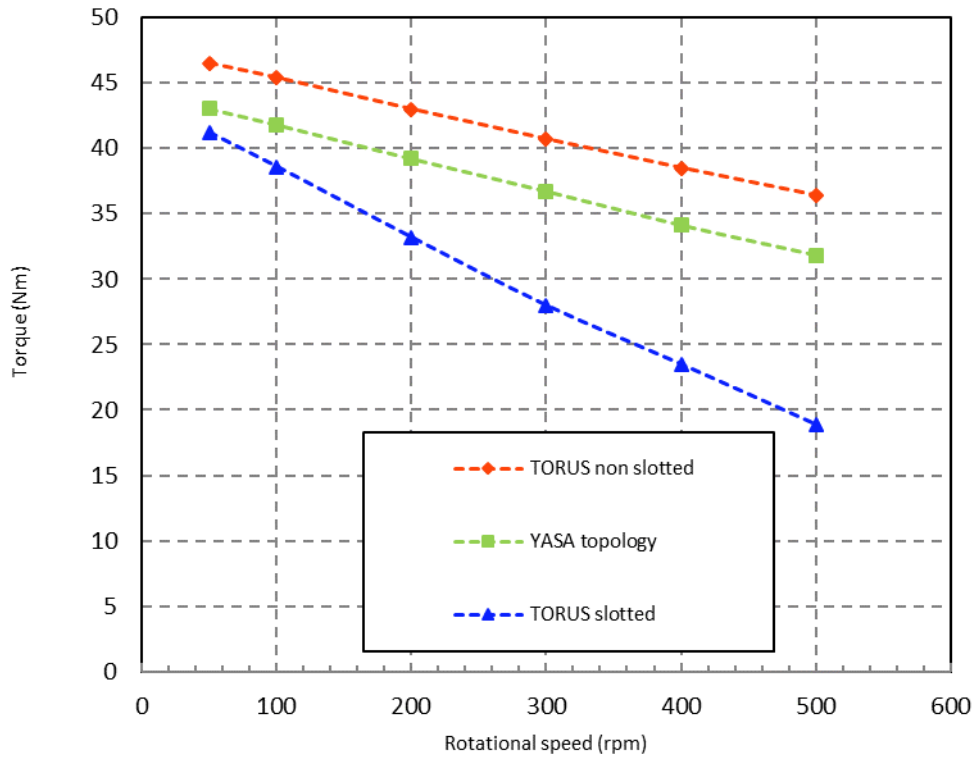
Figure 3. 21. Effect of speed on torque for reference machines

CHAPTER 4.   OPTIMIZATIONS AND DETAILED PERFORMACNE MODELLING

4.1 Introduction

Due to its high overload capability and potential for high torque density in a transient application , the TORUS non-slotted machine topology was identified as the preferred solution for this application in chapter 3. In this chapter further optimisation of the initial design established in chapter 3 is described. Optimization of the machine configuration and dimensions to enhance electromagnetic performance is carried out, followed by the evaluation of electrical loss generated, with the machine using solid iron core. The flux density and induced current density data within each volume element is obtained from the 3D FE, by post processing the data via Matlab, the machine iron loss is calculated. The calculated power loss is used as the heat source for the later on thermal performance modelling of the machine. Transient and static 3D thermal modelling is performed for the optimised machine.

4.2 Electromagnetic performance optimization

4.2.1   Optimisation of permanent magnet design

The design of the permanent magnets in the machine is principally focused on the magnet pole arc and thickness in the direction of magnetisation. Whereas increasing the pole arc and magnet axial length will always tend to increase the airgap flux density and hence torque capability, the magnets in a double-sided axial field machine can constitute a significant proportion of the overall mass. Hence, there is a need through detailed analysis to establish a trade-off between machine mass and torque capability.

- **Magnet pole arc**

The variation in the average airgap flux density as a function of magnet pole arc was investigated for the TORUS non-slotted machine. In many topologies of permanent

magnet machine, the magnet arc is an important factor to consider due to its influence on cogging torque. However, in this slotless machine, there is no need to consider cogging torque and the pole arc can be selected solely in terms of the influence on torque capability and mass.

Three-dimensional, magneto-static finite element modelling was employed to model a range of magnet arcs from 100^0 electrical to 180^0 electrical for a 8 pole rotor. The coil thickness used in the model was 5mm with an additional 1mm mechanical clearance. The magnet axial length was set to 6mm. The resulting variations across one magnet pole in the axial component of flux density at the average magnet radius and at an axial position that correspond to the middle of the conductor is shown in the Figure 4. 1.
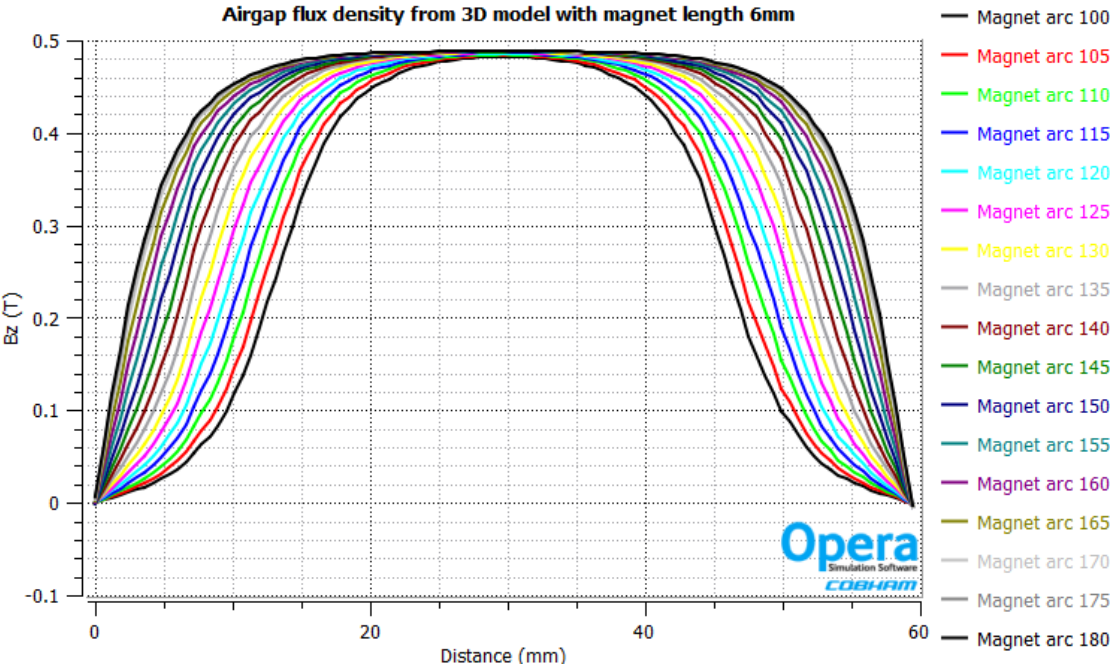
Figure 4. 1. 3D model predicted airgap flux density at average radius

As would be expected, the narrower pole arcs tend to reduce the span over which the flux density is essentially a flat-top. However, since the effective magnetic airgap is large at 6mm, inter-pole leakage is a major issue particularly in terms of the axial component of flux density towards the edge of the poles. As the magnet pole arc increased larger, and two adjacent magnet edges get closer, the benefit in the axial component of airgap flux density become less pronounced due to inter-pole leakage. Figure 4. 2 shows a summary of the average value of the axial component of the airgap flux density as a function of magnet arc. For pole arcs of beyond 160^0 or so, the rate

of increase in the axial flux density begins to tail-off. Further increasing the magnet pole arc does not bring significant benefits in terms of airgap flux density, and there is indeed penalty in doing so. As the leakage becomes more pronounced, rather than contributing to the useful axial component of airgap flux density, the leakage flux simple increases the flux in the rotor back iron. This requires a thicker back iron to avoid the onset of magnetic saturation.

On the basis of this sensitivity study, a magnet arc of 160 was selected as this provides a good trade-off between airgap flux density and magnet mass.
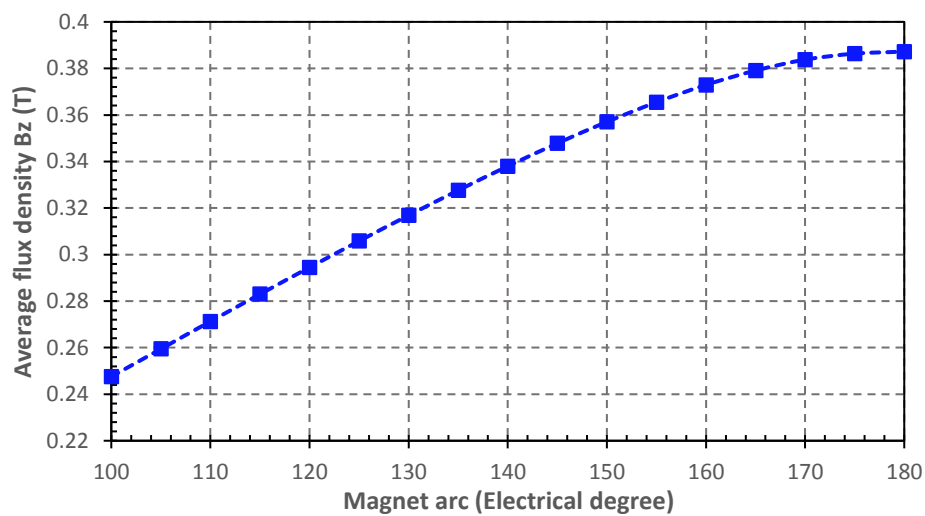
Figure 4. 2. Variation in average airgap flux density with magnet arc

- **Magnet axial length**

Given the large effective magnetic airgap which is inevitable in a TORUS non-slotted topology, a relatively thick magnet is required in order to maintain a competitive flux density level in the airgap. Although it is important to maximise the airgap flux density, the additional mass of a thick magnet should also be taken into consideration. In the original design, to achieve a relative high airgap flux density level, a 12mm thick magnet was employed in the initial design. In this double-sided topology, the permanent magnets made up 40% of the total active mass of the machine. In order to establish the sensitivity of the torque to magnet axial length, a further series of finite element simulations were performed for a range of magnet axial length between 1mm and 20mm, with the remaining of the dimensions to be the same. All calculations were

90

performed with the preferred magnet pole arc of 160 and at a coil current density of 30A/mm^2 rms. The resulting variation in torque as a function of magnet length is shown in Figure 4. 3. Although the 12mm thick magnets selected in the reference design in Chapter 3 provides a reasonable selection, it does not provide the optimised value as the rate of increase in torque with magnet axial length is modest. Whereas the intermittent nature of the VGV application provides the possibility of employing short intervals of very high current density, the requirement for a high magnetic loading remains important.

In order to explore the variation in torque with current density for a range of magnet axial length, a further set of three-dimensional finite element calculations were performed. Figure 4. 4. Shows the resulting variation torque with increasing current density for a series of magnet axial length. With a thinner magnet, the linearity of the increase torque with current density is inevitably reduced. Taking a 50% reduction in magnet axial length to 6mm as an example (which would reduce the active mass of the entire machine by ~20%) then for the same rms current density of 30A/mm^2, the torque only drops by 19%. This torque deficit can be made up by increasing the rms current density from 30A/mm^2 to 38A/mm^2. On the basis of this analysis, the magnet axial length was reduced to 6mm for the preferred design at this point.
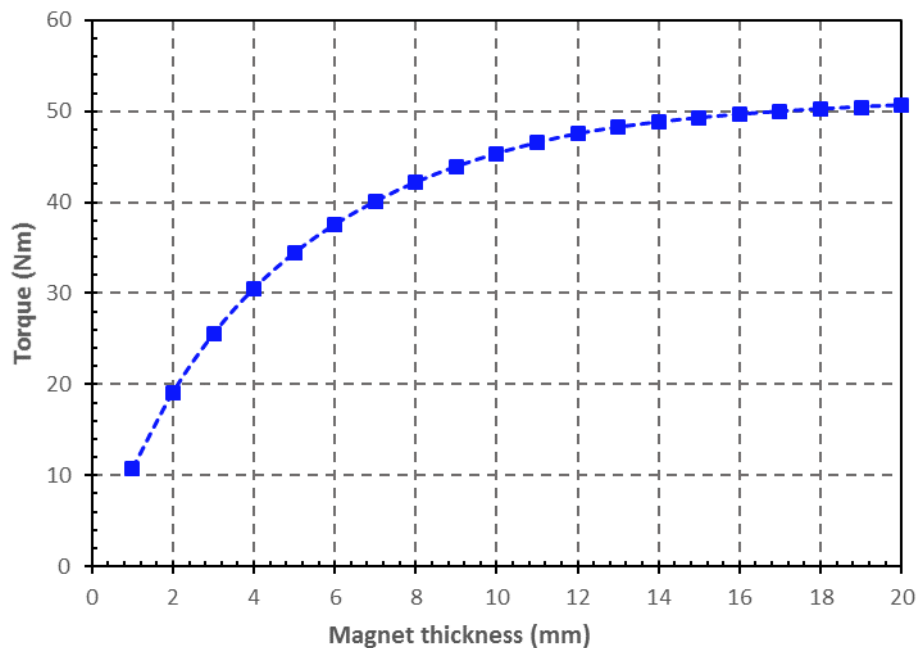
Figure 4. 3. Three-dimensional finite element predicted variation in torque at a coil current density of 30A/mm^2 as a function of different magnet axial length
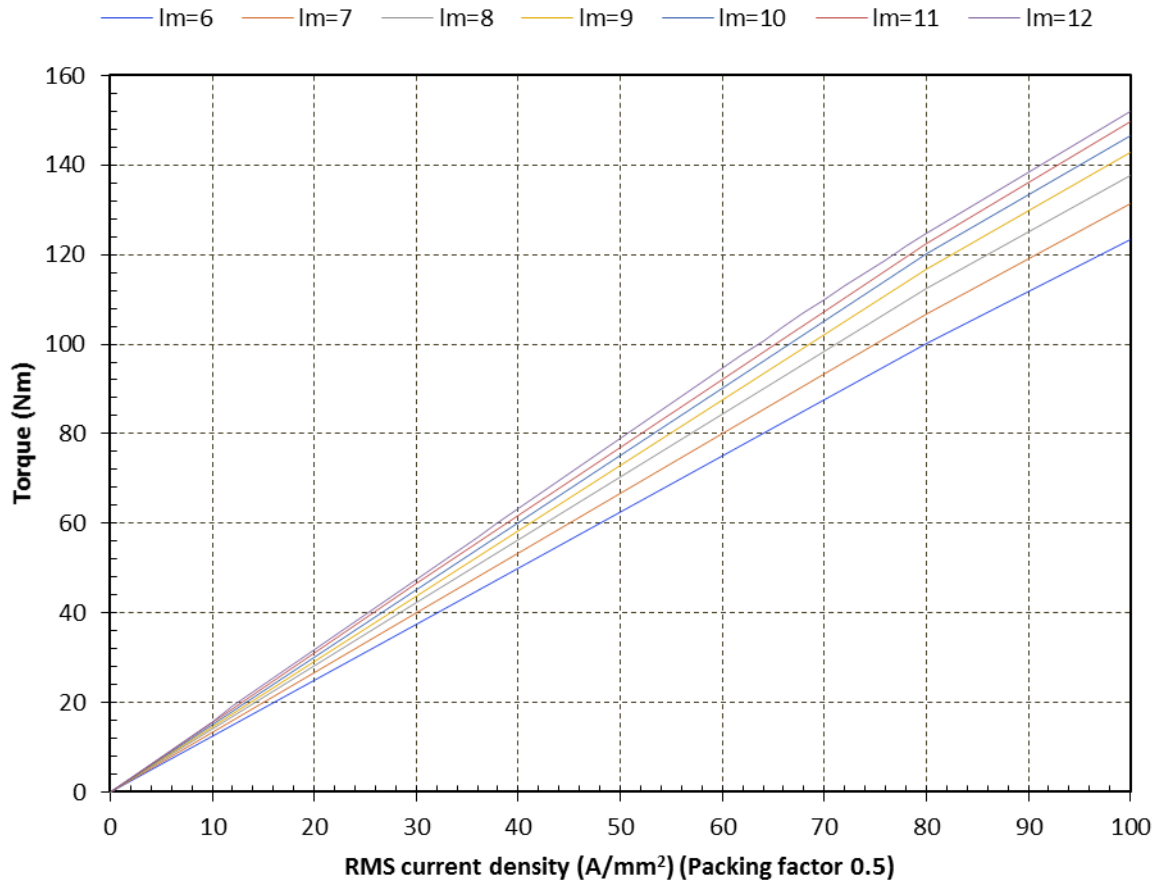
Figure 4. 4. Resultant rated torque variation with current density for different magnet length

4.2.2 Rotor geometry optimization

The rotor geometry proposed in Chapter 2, provides a reasonable torque density but is based on a number of straightforward geometrical assumptions, e.g. no magnet overhang at the inner and out edges, no attempt to generate torque on the axially oriented conductors on the inner and outer surface of the stator core. In this section, several design features to enhance torque density are proposed and evaluated using three-dimensional finite element analysis.

The first feature considered was the merit of extending the magnet outer and inner radii to over-hang the core. For the original design in which the rotor inner and outer radii are the same as those of the stator core, the axially oriented component airgap flux density along arcs at the inner, outer and average radius over one magnet pole are shown in Figure 4. 6. The location of the three arc profiles are shown in Figure 4. 5. The outer arc radius was selected to be half way between the rotor outer radius and the

92

coil outer radius. Likewise, the inner edge radius was set half way between the inner radius of the rotor and the inner radius of the coil. As will be apparent from the calculated profiles in Figure 4. 6, there

Compared with the flux density at the average radius, a significant drop of the flux density at the inner and outer edge is observed which indicates that a certain length of conductor at the inner and out edge are not being exploited in terms of producing torque.
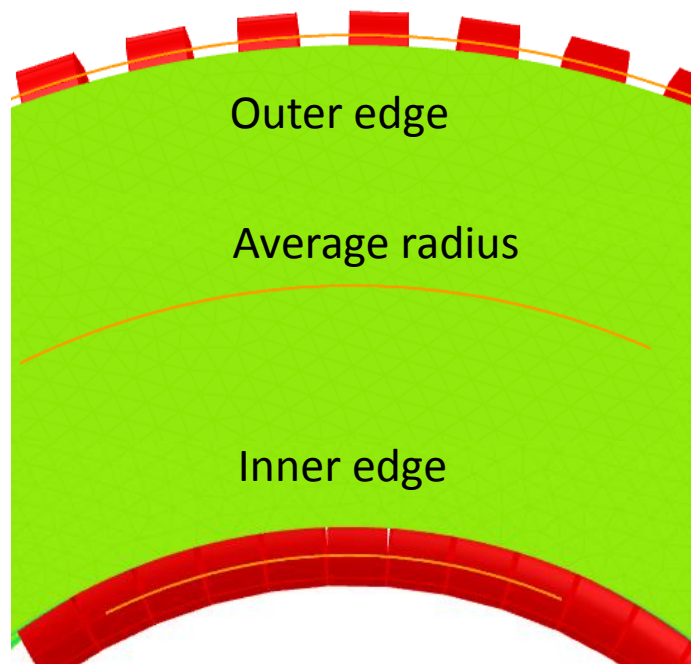
Figure 4. 5. Section through core showing detail of profile arcs and coil location
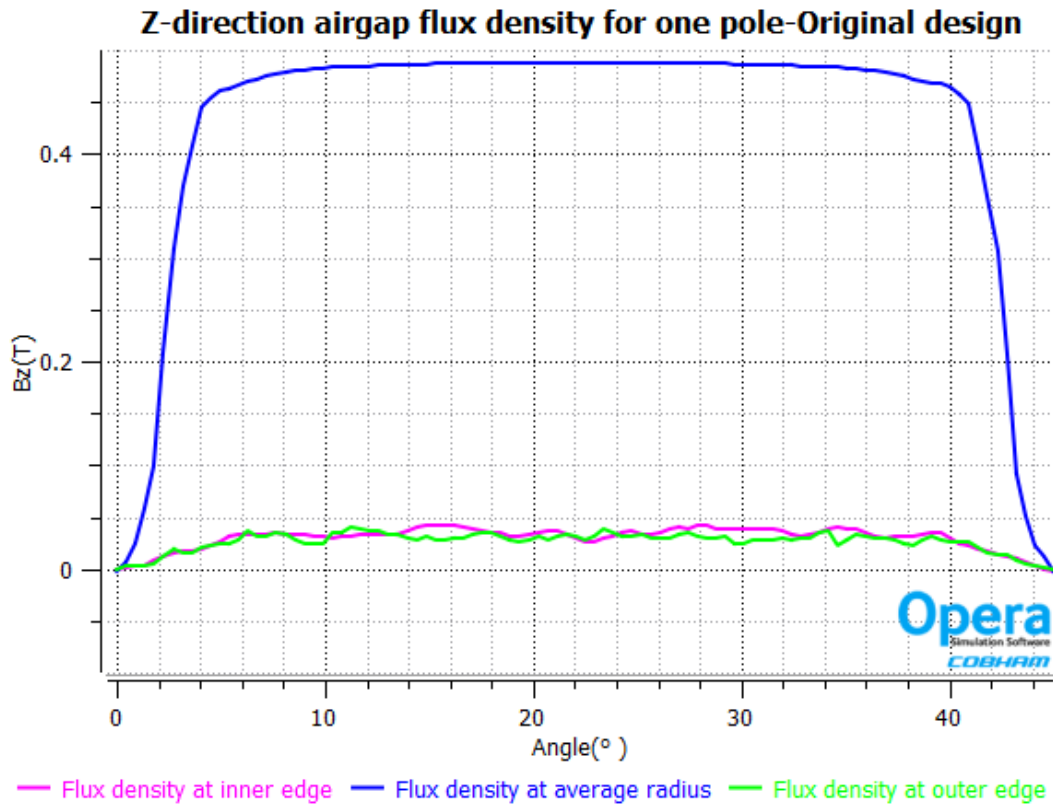
Figure 4. 6. Flux density along three arcs for the original design

In addition to producing additional flux density for the conductors which extend beyond the outer edge of the core, a degree of magnet overhang is also likely to increase the flux density over the remainder of the core, particularly near the edges in a manner which is similar to overhanging the magnets beyond the stator core in conventional radial field machines [40][41].

To establish the return in terms of increase torque from extending the rotor magnets beyond the inner and outer edge of the stator core, the original rotor design was modified as shown in the Figure 4. 7. All the remaining dimensions of the core remained fixed.

<div style="text-align:center">

Original design   Modified design

</div>
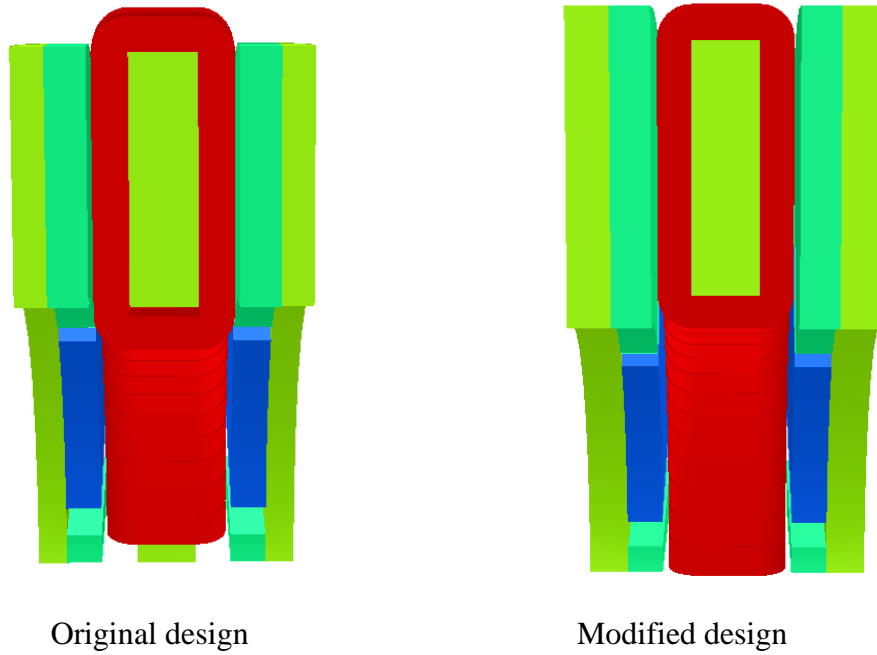
Figure 4. 7. Cross section view of the original design and the modified new design

Airgap flux density profiles along the same arcs defined in Figure 4. 5 for the new design are shown in Figure 4. 8. Following modification, the airgap flux around the inner and outer edge of the coils are improved to level comparable to the flux density at the centre of the core.
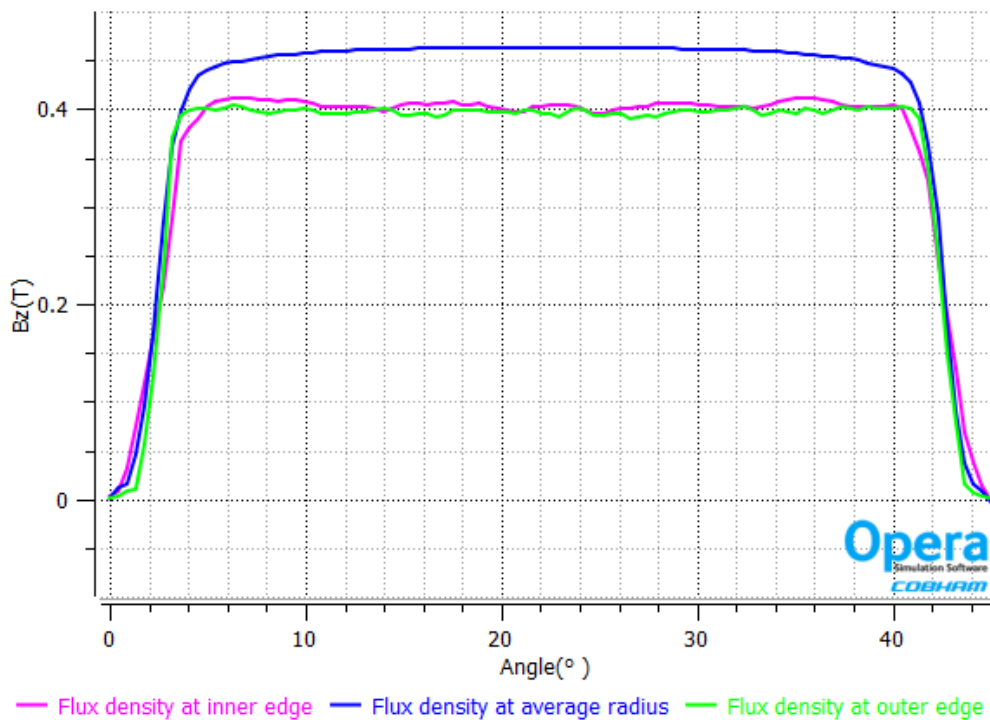
Figure 4. 8. Axial component of flux density along three arcs for the modified design with magnet over-hang

Based on these initial investigation several modified designs were proposed and assessed in terms of the torque density. The proposed design features are as follows:
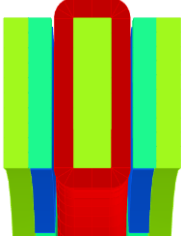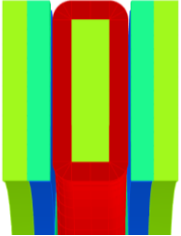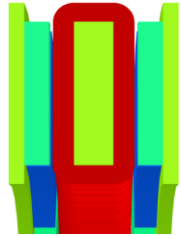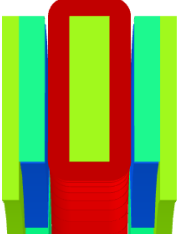
- New design1: Rotor magnet and back iron extended to the inner and outer edge of the coil.

- New design 2: The rotor back iron inner and outer radii are extended to the edge of the stator coils, while the dimensions of the magnets remain the same. The rotor back iron thickness was reduced to pro

- New design 3: The magnet sizes remain the same, the cross section area of the rotor back iron is kept the same as that used in new design 2, but the rotor back iron is extended towards the inner edge only.

- New design 4: The rotor dimensions remained the same as in new design 3, an external cylindrical rotor is added to interact with the outer edge of the coil. The radial airgap equal to the 1mm axial airgap.

- New design 5: This is a variant on new design 4 but with the back iron of the plate rotor and cylindrical rotor extended and joined together.

- New design 6: The cylindrical rotor at the outer edge in new design 4 is removed and replaced with a cylindrical rotor at the inner edge.

- New design 7: The cylindrical rotor at the outer edge in new design 5 is moved to inner edge
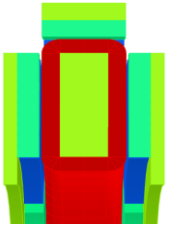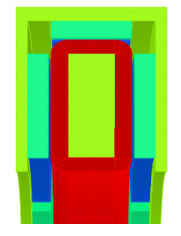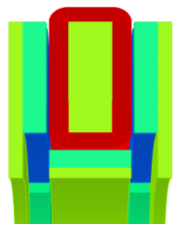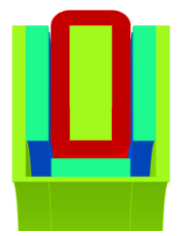
It is worth noting that new designs 4 and 5 which have additional magnet arranged around the outer edge of the core would require that the stator fixing points would need to be moved to the inner radius. These considerations also illustrate that it is not possible to fully enclose the stator with rotating magnets since there is a need to provide a means of fixing the stator core to the casing.

Cross-sections through the stator and rotor of each of the proposed designs are shown in the Table 4. 1 along with the leading dimensions and torque performance predicted by three-dimensional finite element analysis for the design current density of 30A/mm^2

rms. The rotor and stator back iron thickness for each new design was re-calculated to accommodate the flux entering the back iron.

Table 4. 1. Summary of key dimensions and performance of the rotor design variants

	Original	New design 1	New design 2	New design 3
Schematic				
Stator back iron length (mm)	9.51	12.00	9.51	9.51
Rotor back iron length (mm)	4.80	4.80	3.70	3.70
Weight (Kg)	5.19	6.40	5.20	5.12
Torque (Nm)	41.10	51.50	42.60	42.70
Torque density (Nm/Kg)	7.92	8.05	8.19	8.37

	New design 4	New design 5	New design 6	New design 7
Schematic				
Stator back iron length(mm)	13.40	13.40	11.30	11.30

Rotor back iron length(mm)	3.70	3.30	3.60	3.40
Outer (Inner) rotor back iron length	6.30	3.40	2.00	2.00
Weight (Kg)	7.25	7.40	5.69	5.85
Torque (Nm)	58.12	58.15	46.69	49.60
Torque density (Nm/Kg)	8.02	7.86	8.21	8.47

As shown by Table 4. 1, the various modifications provide varying degrees of enhancement in the torque, with several designs exceeding the 50Nm specification. It is worth noting that since the stator coil remains fixed in all these designs, they all exhibit the same copper loss at the design coil current density of 30A /mm^2. There are several interesting observations on these design variants:

- New design 2 is able to achieve a 0.5Nm increase in torque for the same mass of 5.19kg.

- New design 3 is able to achieve a further small increase in torque of 0.1Nm but in this case with a reduction in mass, giving an overall improvement in torque density from 7.92 Nm/kg to 8.34Nm/kg with little or no complication in terms of machine manufacture.

- New designs 4 and 5, in which an array of radially magnetised are arranged around the outer edge of the core, achieves the highest torque of all the design variants considered at over 58Nm. However, these increased torque ratings are achieved at the expense of a disproportionate increase in mass, resulting in a drop in torque density. Indeed, new design 5 has a lower torque density than the original plain rotor design.

- New design 6 and 7 follows the same principle as new design 4 and 5, but add the cylindrical rotor is at the inner edge. As will be apparent from Table 4. 1, there is an enhancement to the torque from using the axially oriented

conductors at the inner edge. However, as would be expected, the increases in torque are smaller than achieved with new designs 4 and 5 in which the additional tangential force is produced at a larger radius. In the case of new design 7, a torque of 49.6Nm is achieved at the highest torque density of all the variants concerned at 8.47Nm/kg. Since it offers both the highest torque density and is within touching distance of meeting the 50Nm specification, new design 7 was selected for further design optimisation.

Sensitivity study was carried out on the new design 7, where the key dimensions are adjusted for maximum torque density, and the torque produced for the new design 7 after sensitivity study is 51.4Nm which achieves 50Nm specification. It should be noted that the results shown for new design 7 in the later context refers to the results of the model after sensitivity study.

The flux density distribution on the surface of the rotor back iron for new design 7 after sensitivity study is shown in Figure 4. 9. As will be apparent and indeed expected, flux density at the centre of each magnet pole stays relatively low compared to the region under the pole transition. This is a common feature of rotor cores in permanent magnet machines and cores with uniform cross-sections are dimensioned on the basis of the flux at the pole transition region. Hence, there is some scope to reduce the rotor core mass by profiling the thickness of the rotor core.
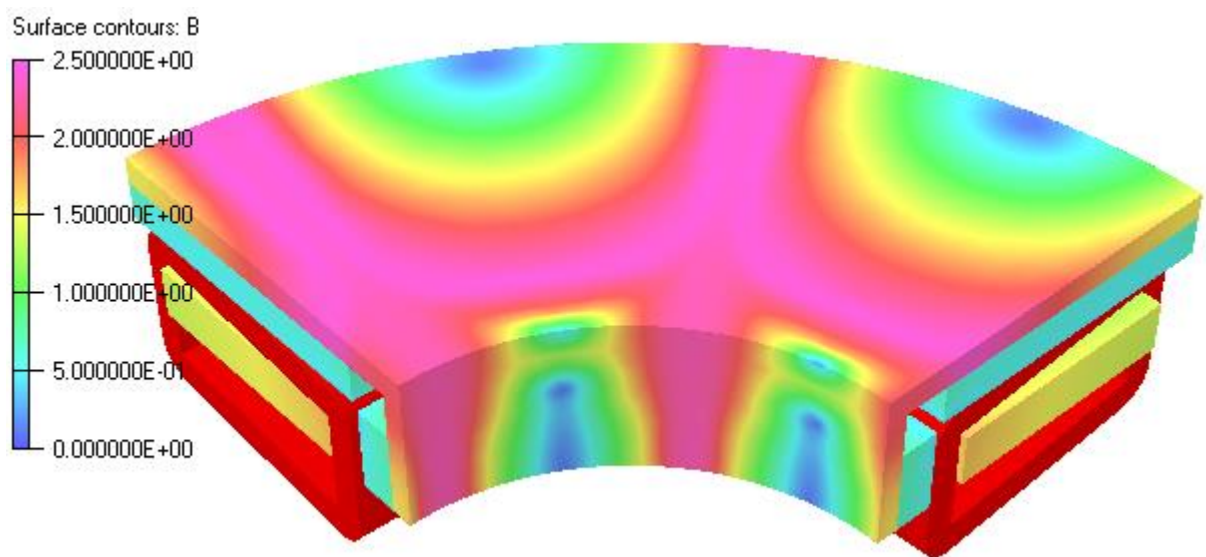
Figure 4. 9. Flux distribution for rotor back iron of the new design 7 (after sensitivity study)

99

An optimization of the rotor back iron geometry for new design 7 was established based on the predicted flux density distribution in the rotor core. The thickness of the rotor back core at the centre of the magnet pole can be reduced and gradually increased to the maximum at the edge of each magnet pole as shown in Figure 4. 10.

As indicated in the figure, the magnets are bonded on the bottom face of the rotor which remains as a flat face, while for rotor top faces profiled such that back iron thickness varies from being at its thinnest at the centre of the magnet pole and thickest at the edge of the magnet pole.

The three-dimensional predicted flux density distribution throughout the profiled rotor back iron design for optimised new design 7 is shown in Figure 4. 11. The same scaling between flux density and colour was maintained to allow a direct comparison with Figure 4. 9. For the profiled rotor back iron design, the maximum flux density on the surface of the rotor geometry is 2.48T while for the plain rotor core geometry, the maximum flux density is 2.40T. However, the key aspects of interest are any differences in the resulting torque and the extent of any mass savings.
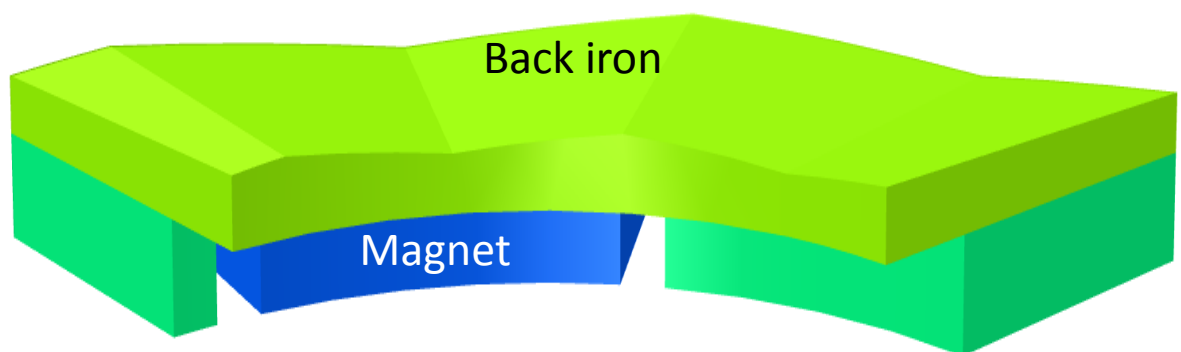
Figure 4. 10. New rotor geometry with profiled back iron thickness
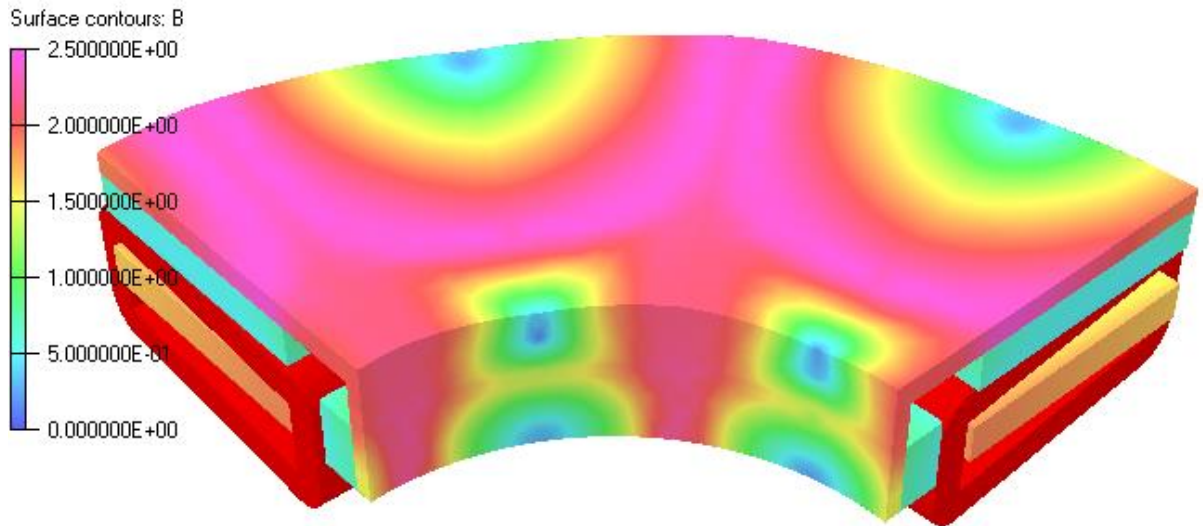
Figure 4. 11. Flux distribution for rotor back iron of the new design 7 with 1.5mm maximum depth profiling

To investigate the benefits of back iron profiling, the torque waveform of the model with and without rotor back iron geometry profiling were calculated using three-dimensional finite element analysis. In the first instance, the depth of the material removed from the middle of the magnet pole was 1.5mm. The resulting torque waveforms are shown in Figure 4. 12.

As shown, the model with the flat rotor back iron is predicted to produce a slightly higher torque, which suggests that there is a greater degree of magnetic saturation with the profiled rotor .Two further profile depths were considered, viz. 1mm and 2mm which sit either side of the first case considered. The torque density of the three profiled designs are alongside the plain rotor core are summarised in Table 4. 2.
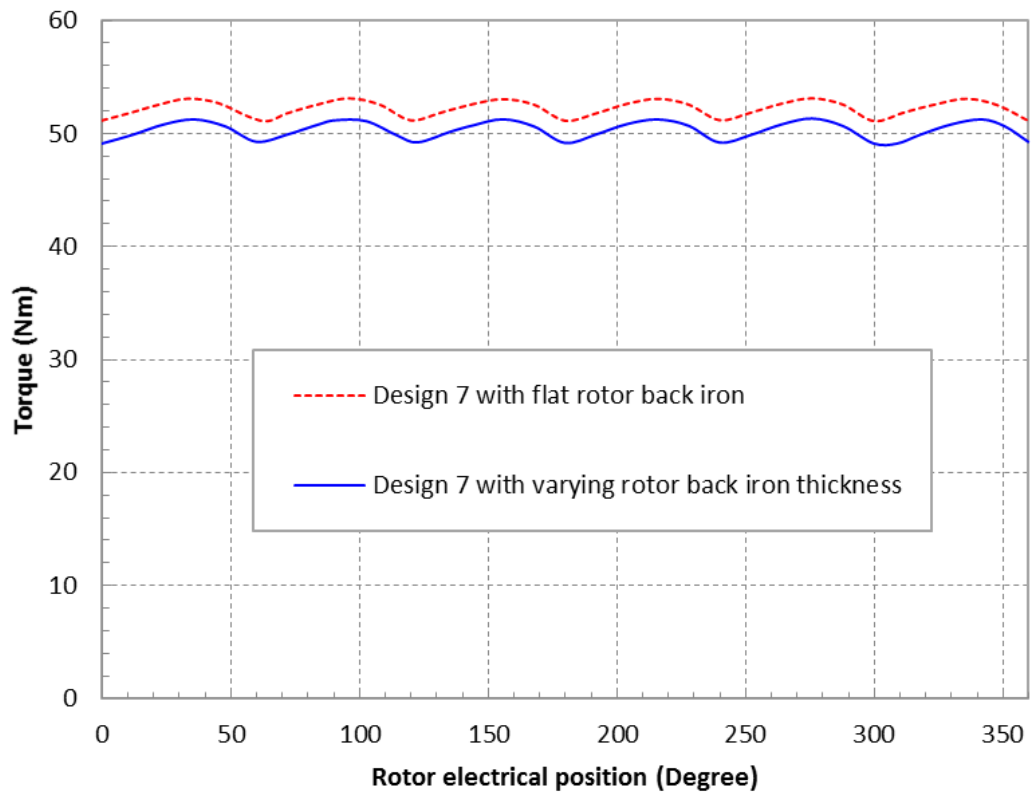
Figure 4. 12. Torque prediction produced by the new rotor design7 with flat back iron and with varying rotor back iron

Table 4. 2. Summary of key parameter of the topology with different thickness taken from the centre of pole

Design type	Maximum rotor back iron length (mm)	Maximum thickness taken from rotor (mm)	Weight (Kg)	Torque (Nm)	Torque density (Nm/Kg)
new design 7– plain rotor back iron (after sensitivity study)	4	0.0	6.04	51.37	8.50
Profiled design 1	4	1.0	5.90	50.72	8.60

Profiled design 2	4	1.5	5.83	50.31	8.63
Profiled design 3	4	2.0	5.76	49.91	8.66

It can be seen from the table that the torque produced diminishes slightly as depth of the profiling increases. However, the rate of torque reduction is less than the reduction in mass and hence the torque density improves. Although the torque density improves as more material is removed from the rotor, it is important to recognise that the mechanical integrity of the rotor needs to be considered, in particular avoiding excessive bending due to the large magnetic forces of attraction. This issue is revisited in chapter 5.

On the basis of the electromagnetic findings in Table 4.2, a profile depth of 1.5mm was selected as the preferred design for subsequent machine optimisation.

4.2.3   Stator winding layout

Having fixed on a 12 coil, airgap winding, there are relatively few design variations that can be considered. The winding layout used for the previous electromagnetic models were based on the winding being represented by a series of discrete sub-coils spread uniformly around the core as shown in Figure 4. 13 (a). In this case, each of the 12 phase coils are represented by 5 sub-coils. This winding layout is a common winding layout for this type of topology. The voids between successive coils is an inevitable feature of this type of winding because of the need to accommodate the winding within a fixed coil depth at the inner radius.

An alternative winding layout is to simply employ 12 rectangular coils as shown in Figure 4. 13 (b) with a single large triangular void between successive coils. This has the effect of concentrating the conductors at the outer edge around the centre of the coil span rather than distributing them across the full coil span. It is worth noting that this arrangement is likely to be more straightforward to manufacture point. Both winding topologies are concentrated windings and with the same number of turns of the same individual cross-section.

The phase back EMF waveforms and the line-line back EMF waveforms for both coil arrangements were predicted using three-dimensional, magneto-static finite element simulations. The resulting emf waveforms for the rectangular coil and radial coil arrangements are shown in Figure 4. 14. The accompanying Fourier transform of the back EMF waveforms are shown in Figure 4. 15 and Figure 4. 16. Compared to the original design with the more distributed radial coil arrangement, the rectangular coils tend to produce a more trapezoidal waveform. The fundamental component of the individual phase voltages with the rectangular coils is 7.4% higher, while the 3rd harmonic content of evenly distributed radial coil windings is only 6% of the 3rd harmonic content of the rectangular shaped coil winding topology. However, the line voltages of the two different winding distribution are similar, as shown in Figure 4. 14. which is to expected given that the star connection will tend to cancel the third harmonic.

(a). Radial coils   (b). Rectangular coils
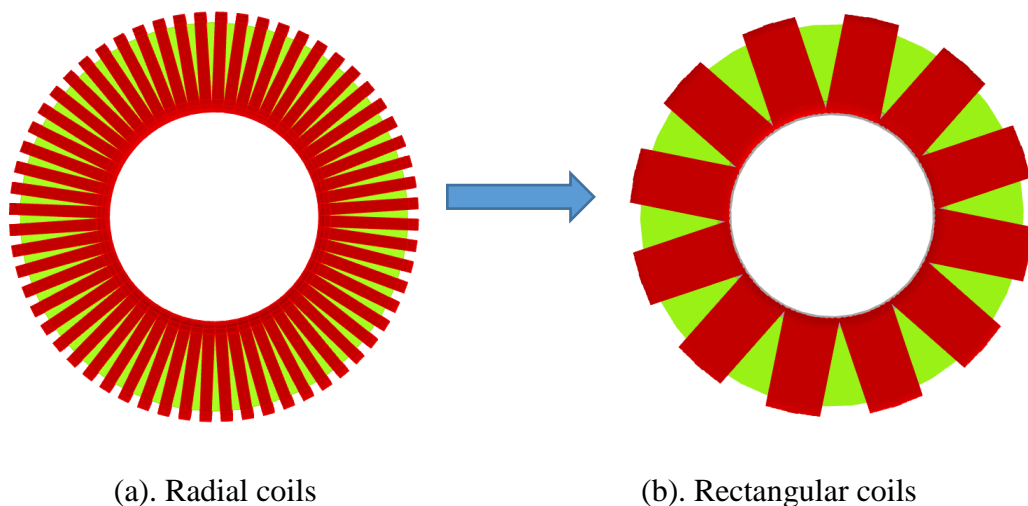
Figure 4. 13. Schematic of two different winding arrangements
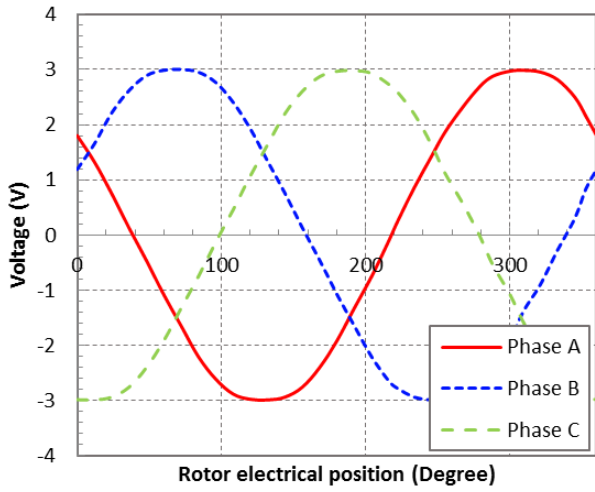
(a). Phase emf for radial coils   (b). Phase emf for rectangular coils
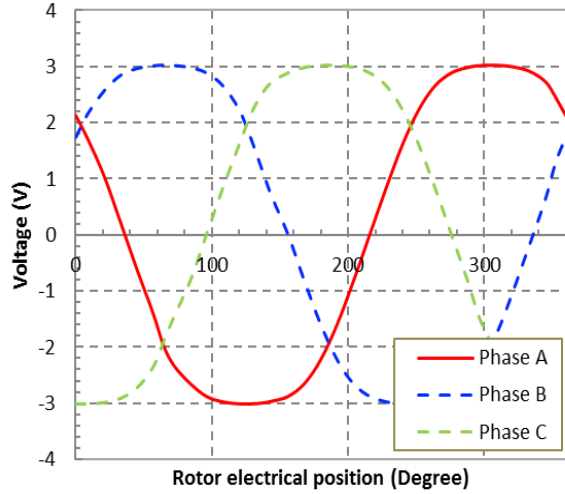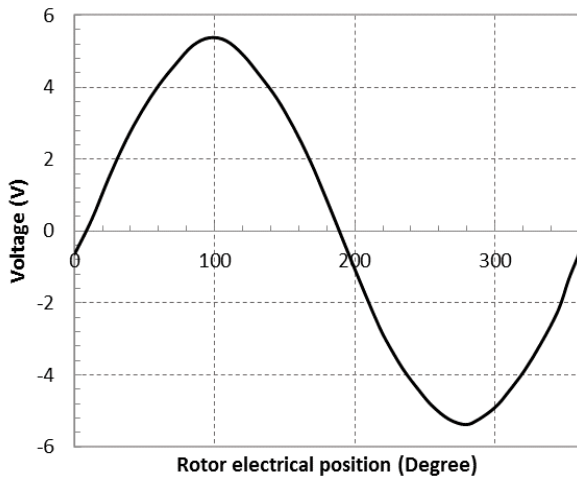
(c). Line-to-line emf for radial coils   (d). Line-to-line emf for rectangular coils
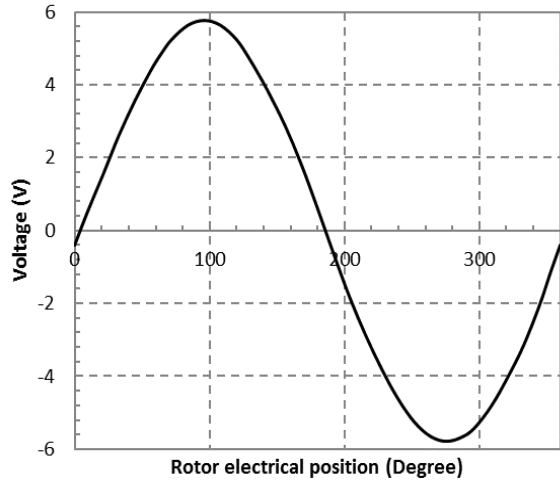
Figure 4. 14. Induced back EMF waveforms for radial and rectangular coils
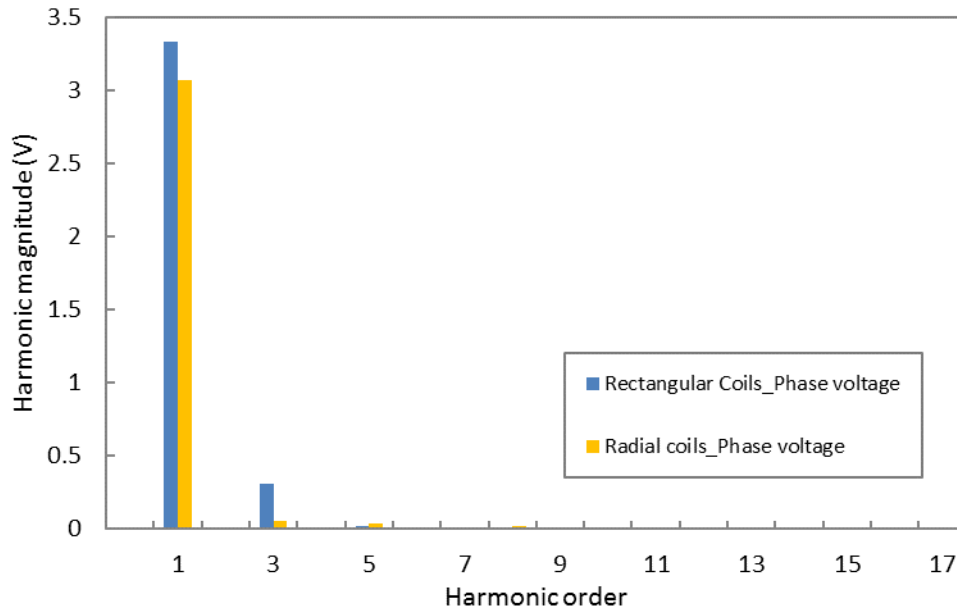
Figure 4. 15. Fourier transforms of the phase emf for both winding layouts
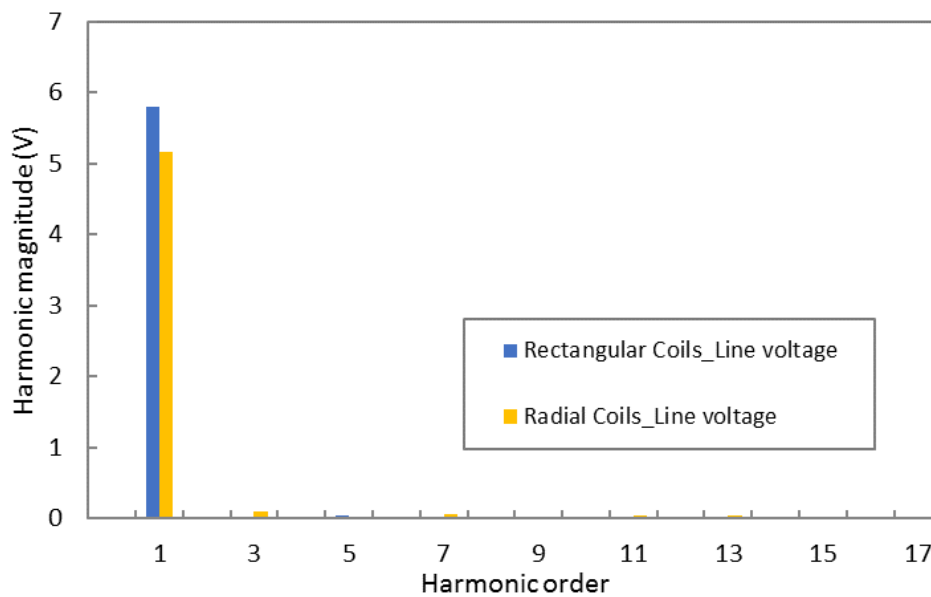
Figure 4. 16. Fourier transforms of the line-to-line emf for both winding layouts

The torque waveforms for both winding arrangements with sinusoidal phase currents at an rms current density of 30A/mm^2 were calculated using a further set of three-dimensional, magneto-static finite element analysis. The resulting torque waveforms are shown in Figure 4. 17. It can be seen from the figure that the average torque produced by the model with the rectangular coils is 7.4% higher than the model with

the radial distributed coils. This is to be expected given the FFT of the back EMF waveforms show previously. Although the third harmonic content in the rectangular coils is higher than the radial coils, with star connection, all the triplen harmonics are eliminated. On the basis of this analysis, the rectangular coils were selected.
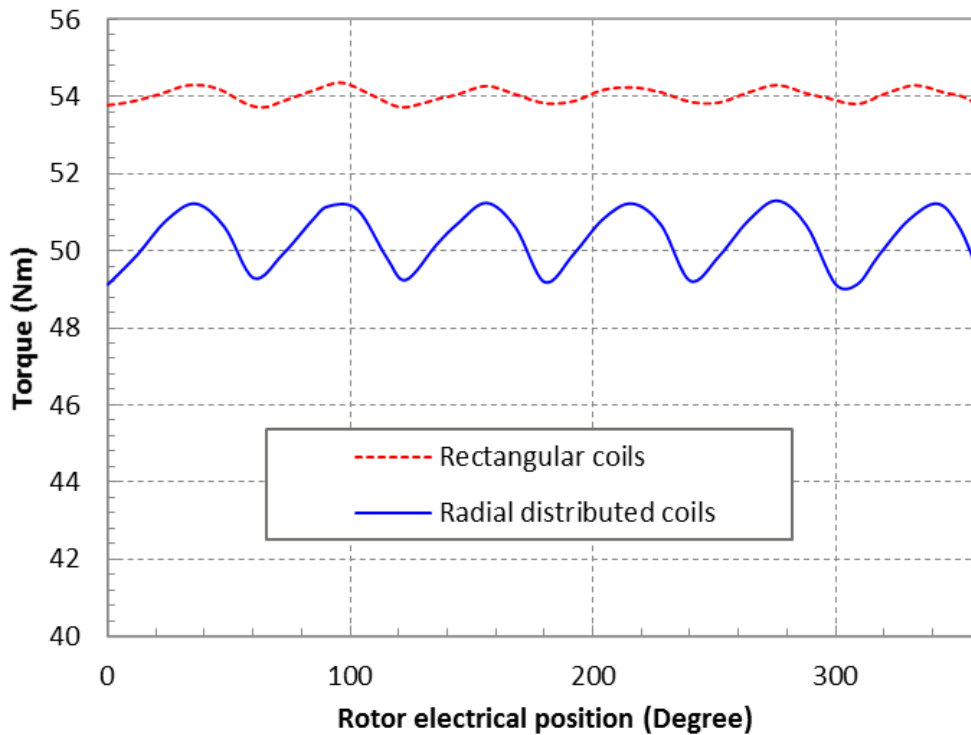
Figure 4. 17. Torque waveform for both winding arrangements (note suppressed torque axis) at an rms current density of 30A/mm².

4.2.4 Summary of electromagnetic optimisation

At the outset of this chapter, the initial machine design produced a torque of 41.1Nm at an rms current density of 30A/mm², achieving a torque density at this current density of 7.92Nm/kg. A summary of the performance enhancements achieved with the cumulative addition of various design features is summarised in Table 4. 3. As will be evident, the final design which incorporates all the optimised design features, although optimised sequentially, produces 54.02Nm at a torque density of 9.27Nm/kg which yields an improvement of 23% in torque density (taking the original design as the 100% baseline).

Table 4. 3. Summary of the impact of design feature

Design Feature	Final selection	Torque (Nm)	Mass (kg)	Torque density (Nm/Kg)
Rotor geometry	New design 7 in Figure 4. 9	51.37	6.04	8.50
Rotor profiling	1.5mm deep profile	50.31	5.83	8.63
Stator coil	Rectangular coils	54.02	5.83	9.27

4.3 Eddy current effect investigation for optimized topology

4.3.1 Eddy current effect on machine performance

As discussed in chapter 3, there are significant mechanical, manufacturing and thermal benefits of manufacturing the stator core as a single solid component from a bar of Cobalt Iron. However, the use a solid (i.e. non-laminated) stator core will present electromagnetic challenges with induced eddy currents, in terms of both eddy current screening reducing the electromagnetic torque and eddy current losses affecting efficiency and temperature rise. In Chapter 3, an investigation into the influence of eddy currents on torque and back EMF waveforms was undertaken on the original machine design using three-dimensional, transient, magneto-dynamic finite element simulations. . In this section, eddy current effects on the optimised design are considered, including the consideration of losses.

Figure 4. 18 shows the predicted normalised back EMF waveform for the optimised design at rotational speeds of 100rpm, 300rpm and 500rpm. The effect of the induced eddy current on the back EMF waveform is, unsurprisingly, very similar to the behaviour observed in Chapter 3 with the original design. The normalised maximum induced voltage reduced as the rotational speed increases due to increased eddy current screening and there is a small but increasing phase shift in the back EMF waveforms with increasing speed.
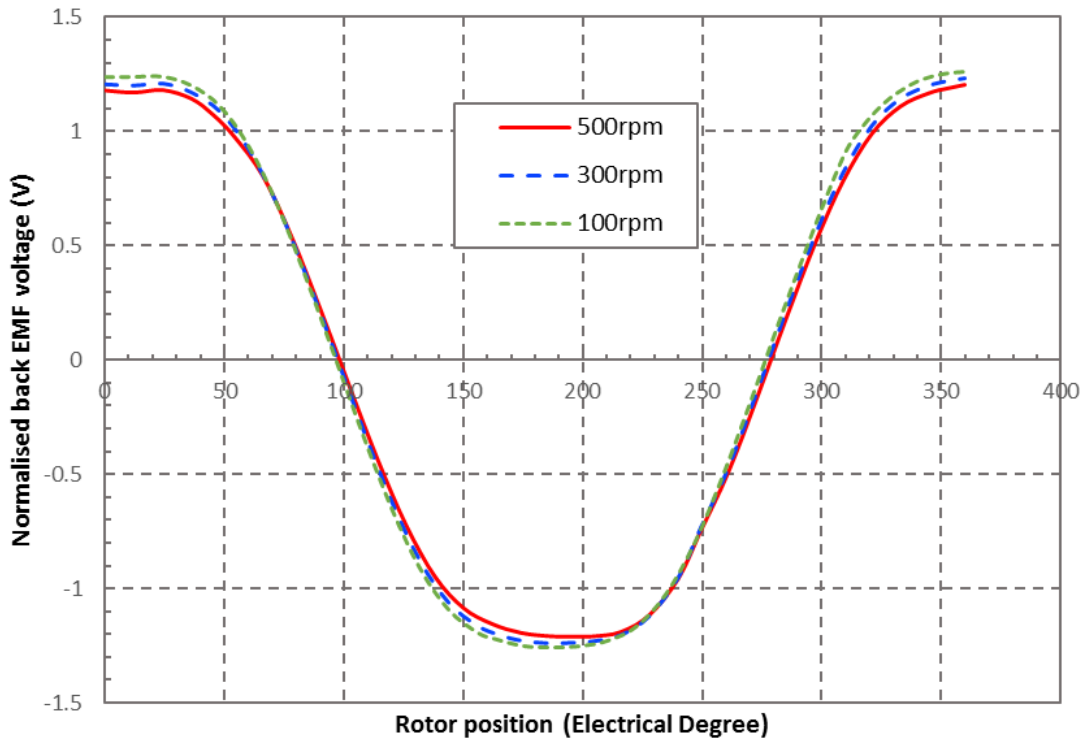
Figure 4. 18. Eddy current effect on back EMF waveform for optimised topology under different speed (all emfs normalised to unit speed)

The effect of eddy currents on torque performance of the machine was also investigated. The magneto-static predicted torque waveform for the optimised design is shown in Figure 4. 19, alongside corresponding torque waveforms predicted using three-dimensional magneto-dynamic finite element analysis at rotational speeds of 10rpm, 100rpm and 500rpm. The predicted average torque produced by the optimised topology with solid iron core reduces by 19.6% at 500rpm compared to static predictions.
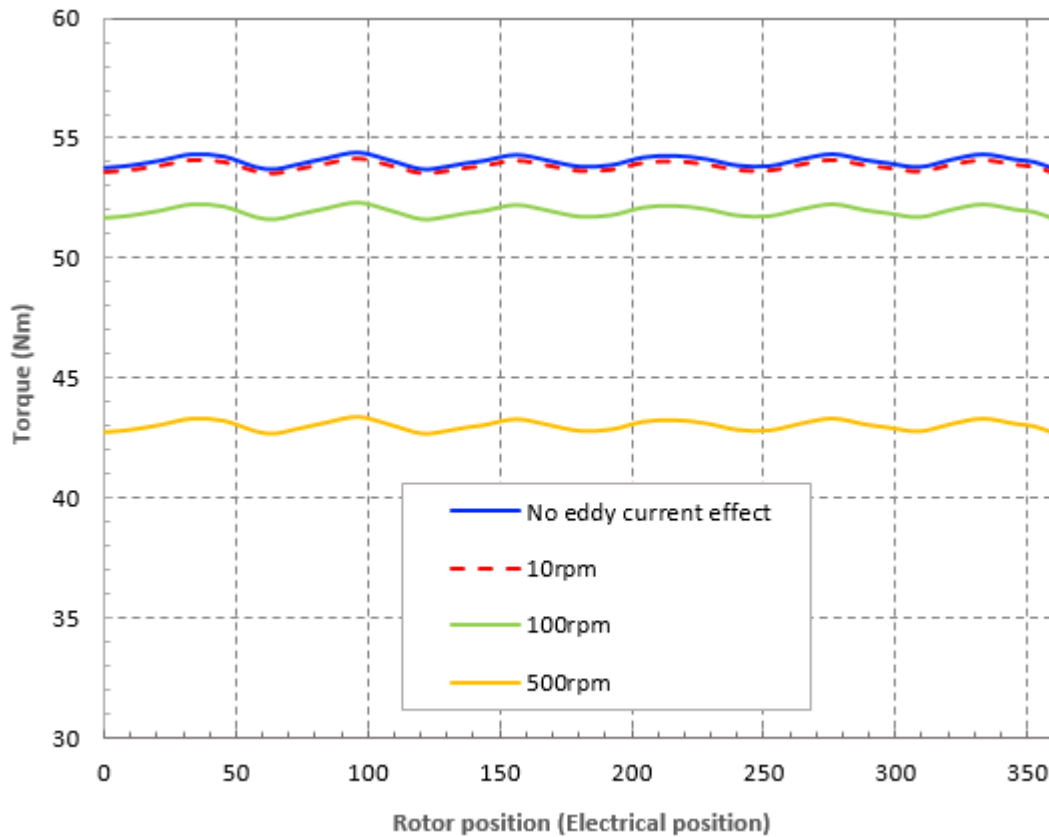
Figure 4. 19. Influence of eddy currents on torque performance for optimised topology at different rotational speeds

4.3.2   Influence of eddy currents on transient machine performance

The previous predictions of EMF and torque were obtained for constant rotational speed. While this provides a useful indication of the degree of eddy current phenomena in the solid core, the target application for this machine is a highly transient application with intervals of rapid acceleration and deceleration. Hence, the effect on the mechanical transient response of the motor of the induced eddy currents was investigated.

The feature in OPERA 3D which allows the integration of simple mechanical constraints such as inertia and friction to be added into a transient coupled electromagnetic and mechanical model was used. Since the emphasis in these simulations was on the impact of eddy currents on acceleration, the simulation was based on a current driven solution rather than a voltage drive solution. As the simulation is based on an enforced current, it is not necessary to specify a particular

number of turns per coil providing the magnitude of the current scales to give the desired current density in the coil regions of the finite element model. In this case, the number of turns per coil was set to 1 which results in a peak sinusoidal current of 289A. The start-up phase of the currents involved transient ramp up time of 75ms, during the period of 0s-75ms, the sinusoidal current is multiplied by a factor of time/0.075 to simulate the transient start up process of a current waveform. The applied three phase currents which provided input to the magneto-dynamic transient finite element model are shown in Figure 4. 20. Since this is a transient model, the frequency of the current applied varies with the machine speed, i.e. the applied current is always in phase with the induced back emf.

The transient simulation started with the rotor at standstill The equation for the motor dynamics is: [42]

$$T_e = T_l + B\frac{d\theta}{dt} + J\frac{d^2\theta}{dt^2}$$ (4. 1)

Where T_l is the load torque, B is the viscous friction coefficient and J is the moment of inertia. The input parameters required by the finite element model to simulate such dynamic environment is the inertia, load torque and the friction torque.

The moment of inertia of rotor can be estimated by a summation of the moment of inertias of a series of cylinders whose individual moments of inertia are given by [43]:

$$J = \frac{1}{2}m(r_1{}^2 + r_2{}^2)$$ (4. 2)

Where r_1 and r_2 are the inner and outer radius of the ring, and m is the cylinder mass which is assumed to be uniformly distributed. The exact moment of inertia of the load (with due allowance for the gearbox) was not specified. However, on the basis of some guidance, the total moment of inertia was set to 11 times of the rotor inertia, giving an overall moment of inertia of 0.3 kgm^2. The friction torque was set at 5% of the total torque which is 2.5Nm and the load torque at a fixed 20Nm. Although there was some uncertainties in these values, they result in mechanical dynamics with time constants comparable to the real system and with timescales that are influenced by eddy current effects.
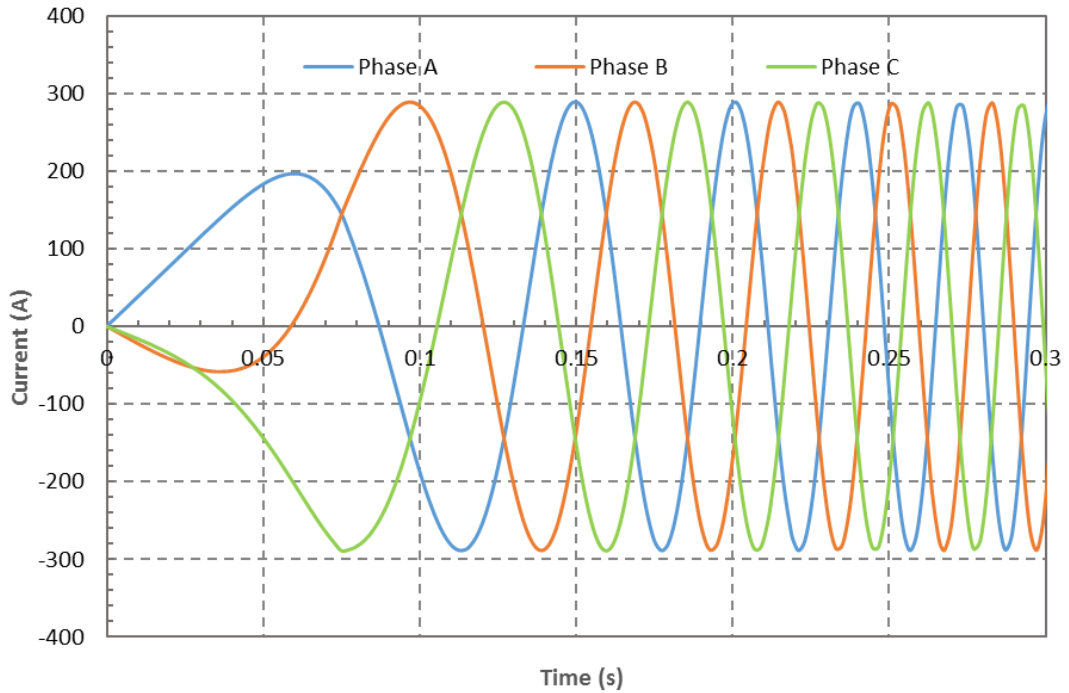
Figure 4. 20. Ramped up phase currents applied to the transient finite element model (1 turn per coil)

With all mechanical parameters set and the current in Figure 4. 20 applied to the three-dimensional transient fintie element model, the first simulation was performed with the electrical conductivity of the cores and magnets set to zero to eliminate eddy currents and hence produce magneto-static conditions. A further simulation was performed with the electrical conductivities set to the appropriate values which results in eddy currents beign induced in the magnets and cores. The resulting transient speed response profiles under loaded condition is shown in Figure 4. 21 for both magneto-static and magneto-dynamic simulations. It is worth noting that in thes two simulations, the machine was allowed to accelerate up to a speed which was far in excess of the maximum rated speed of 500rpm since non speed control was applied. The machine was simply supplied with a current waveform that under magneto-static condutions would produce a continuous torque of 50Nm.

As can be seen, there is some evidence of redcued acceleation due to the effect of eddy currents but the speed profile is not affected very significantly up to the rated speed. By way of example, iat 0.316s, the magnetostatic model reaches 500rpm while the model which accounts for eddy currents on reaches 472rpm, which corresponds to 6% drop in speed due to eddy current.

The transient torque performance of the machine under load with and without eddy current effect is shown in Figure 4. 22. The torque gradually increases as the current applied gradually increases from 0, the torque profiles with and without taking eddy current effect into consideration starts to deviate after 50ms or so. As speed increases and the current settles to its steady state value with a 298A peak, the effect of eddy currents on the torque gradually become more pronounced. At 500rpm or so, torque predicted by the model with eddy currents drops to 45.2Nm while the for the model without eddy current effects, the torque produced is 54.1Nm, i.e a reduction of ~20%. The simulations have demonstrated that even with mechanical dynamic parameters at the lower end of the dyanmic response expected in a VGV system, that a machine with a solid core is able to remain competitive in terms of acceleration and speed profile, at least when confined to operation between 0 and 500rpm. On this basis, a solid core was selected for the prototype machine.
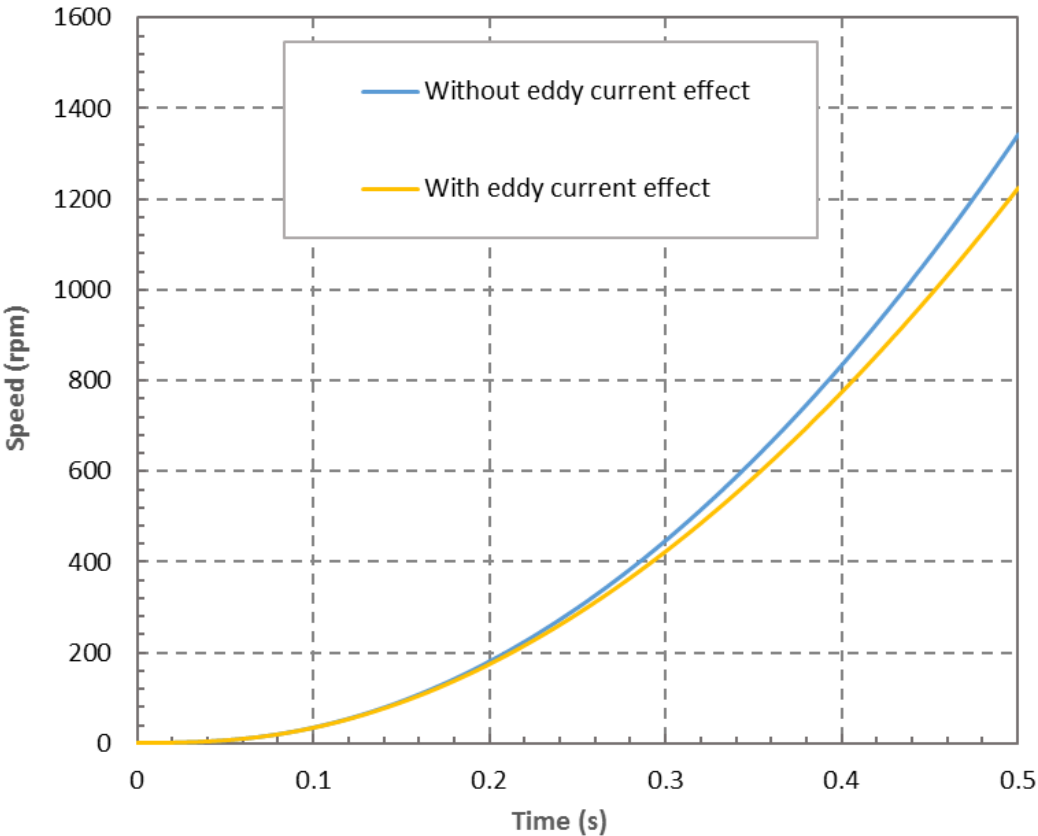
Figure 4. 21. Transient speed profile against time
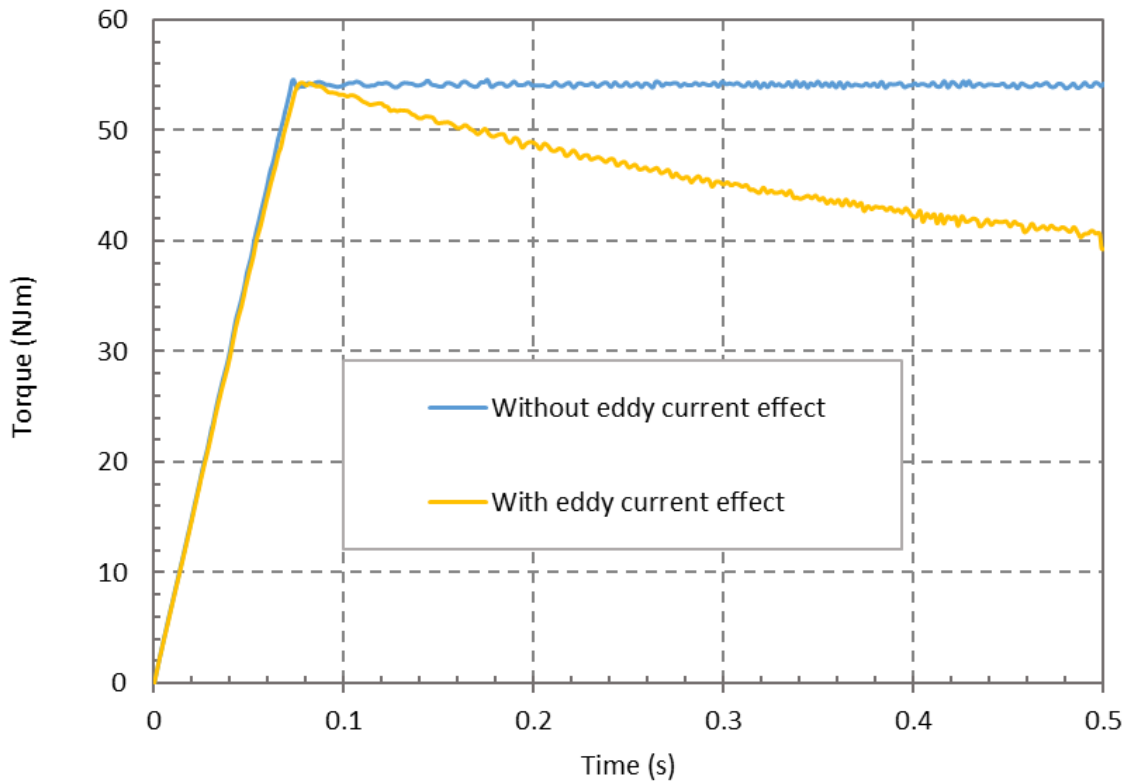
Figure 4. 22. Transient torque profile against time

4.4 Detailed calculation of electromagnetic loss

In this section, the loss generated inside the machine is evaluated. As discussed previously, the use of a solid stator core will results in a very significant increase in stator core loss. This is likely to be unsustainable on a continuous basis. This section investigates the various losses in the machine as a pre-cursor to thermal modelling.

4.4.1 Copper loss

The high current density employed in this machine will dictate that the copper loss density will be a significant factor in the thermal behaviour of the machine. The copper loss was calculated using an RMS phase current density of 30A/mm^2 at the coil packing factor k_p of 0.5. The temperature coefficient of resistance was included in the loss evaluation in terms of calculating the loss at a specified temperature:

$$R_{ph} = \frac{N_c \rho_{cu} l}{A} \qquad (4.3)$$

$$R_{ph}(T_2) = R_{ph}(T_1)[1 + \alpha_T(T_2 - T_1)] \qquad (4.4)$$

$$P_{ph} = J^2{}_{rms} A^2 k_p{}^2 R_{ph} \qquad (4.5)$$

The resulting copper loss per phase is calculated and shown in Figure 4. 23 over the temperature range 20**°**C to 200**°**C. It is interesting to put this loss into context by recognising that this loss is produced in a phase coil which has a mass of 0.28kg. This corresponds to a challenging loss density of 1.9kW/kg at 20°C and 3.4kW/kg at 200°C. Based on specific heat capacity of 385 J kg^{-1} °C^{-1}, this loss density will give rise to an adiabatic temperature rise rate of 4.9°C s^{-1} at 20°C rising to 8.9°C s^{-1} at 200°C.
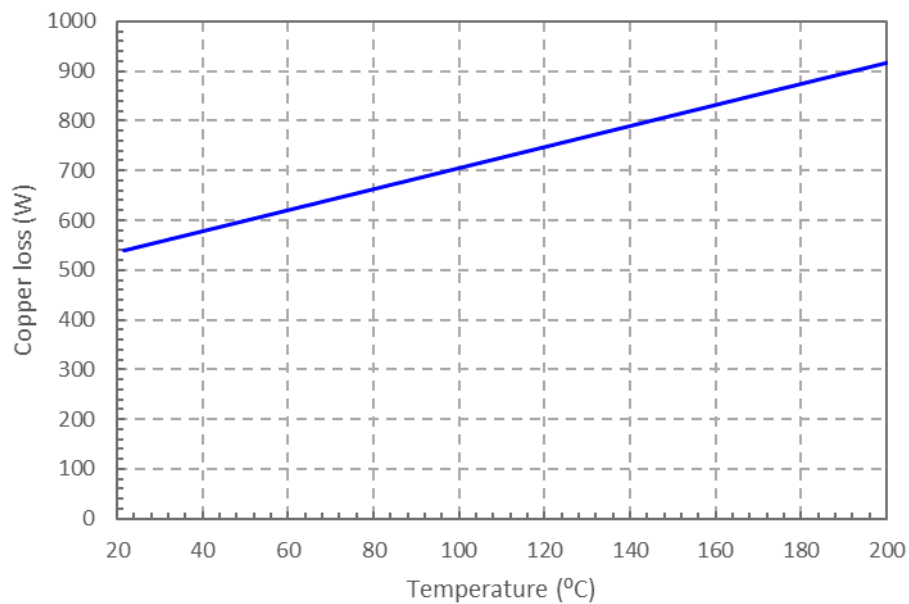
Figure 4. 23. Variation in copper loss per phase with varying coil temperature

4.4.2 Stator core loss

The solid stator core is exposed to time varying localised flux densities which vary in magnitude throughout the core. These time varying flux densities will generate core loss. The absence of slotting will tend to reduce the harmonic content of the stator flux densities but there will still be some harmonics in addition to the fundamental frequency. Despite the highly intermittent operating duty cycle and the relatively low

fundamental frequency of 33Hz (8 pole at 500rpm), the solid nature of the core material used will inevitably lead to a high iron loss especially for the eddy current loss.

The calculation of core loss in electrical machines using so-called loss separation methods is well developed with several published models. In these methods the loss is assumed to be made up from 3 components. These are hysteresis loss, classical eddy current loss and so-called excess loss. There are well established expressions for each of these losses which are often used in combination with magneto-static finite element predicted flux densities as a post processing calculation. However, published methods are formulated for laminated structures in which any induced currents are resistance-limited, i.e. the eddy current reaction field is insufficient to result in any significant field re-distribution within the core. This is a good approximation for almost all machines with laminated cores, with the possible exception of extremely high speed machines with fundamental frequencies of several kHz.

However, the use of a solid core and hence the presence off very large induced eddy currents is likely to introduce excessive errors into core loss models developed for laminated cores and hence a different approach that includes the effect of field re-distribution must be adopted. In order to calculate the core loss in the solid stator core, a three-dimensional, magneto-dynamic transient finite element simulation is used to calculate the time variation in flux density in each individual finite element with full capture of the eddy current reaction field. Having established these flux density variation, the resulting loss in each individual element with a volume V due to the three constituent components of the overall core loss are given by:

$$P_{hyst} = k_{hyst} B_{peak}{}^{B_{peak}} f V \qquad (4.6)$$

$$P_{eddy} = \frac{J_{rms}{}^2}{\sigma_{Fe} \rho_{Fe}} V \qquad (4.7)$$

$$P_{exc} = \frac{\sqrt{\sigma_{Fe}}}{\rho_{Fe}} k_{ex} \left| \frac{dB}{dt} \right|^{1.5} V \qquad (4.8)$$

It is worth noting that the hysteresis loop is calculated on the basis of the major loop. The time-averaged loss per unit volume distribution of hysteresis loss, eddy current

loss, excess loss and the total loss for each element is shown in Figure 4. 24, Figure 4. 25, Figure 4. 26 and Figure 4. 27. The loss distribution plots are all for the case of a 50Nm and 500rpm operating points. As will be apparent, the eddy current loss is the dominant component of the overall core loss, which is unsurprising given the solid iron core. The MATLAB script for processing the 3-dimensional data for evaluating the core losses is attached in appendix I
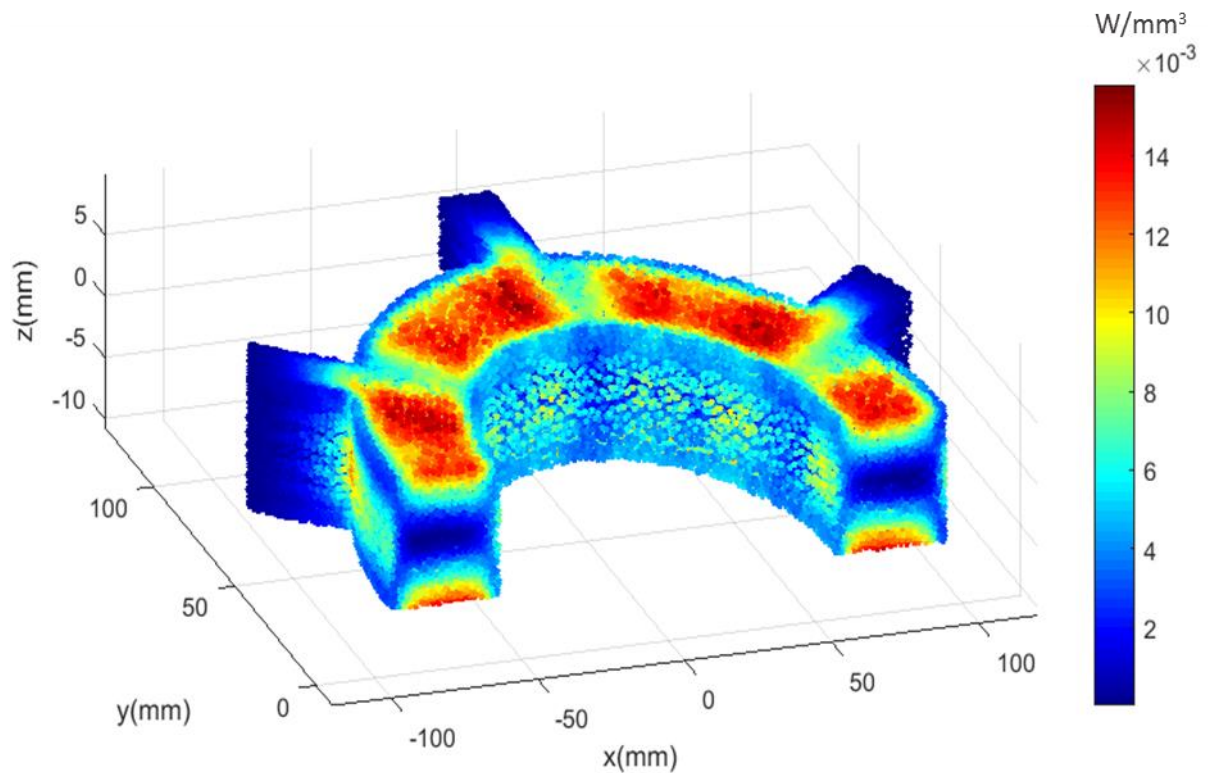
Figure 4. 24. Average eddy current loss density for each element in stator
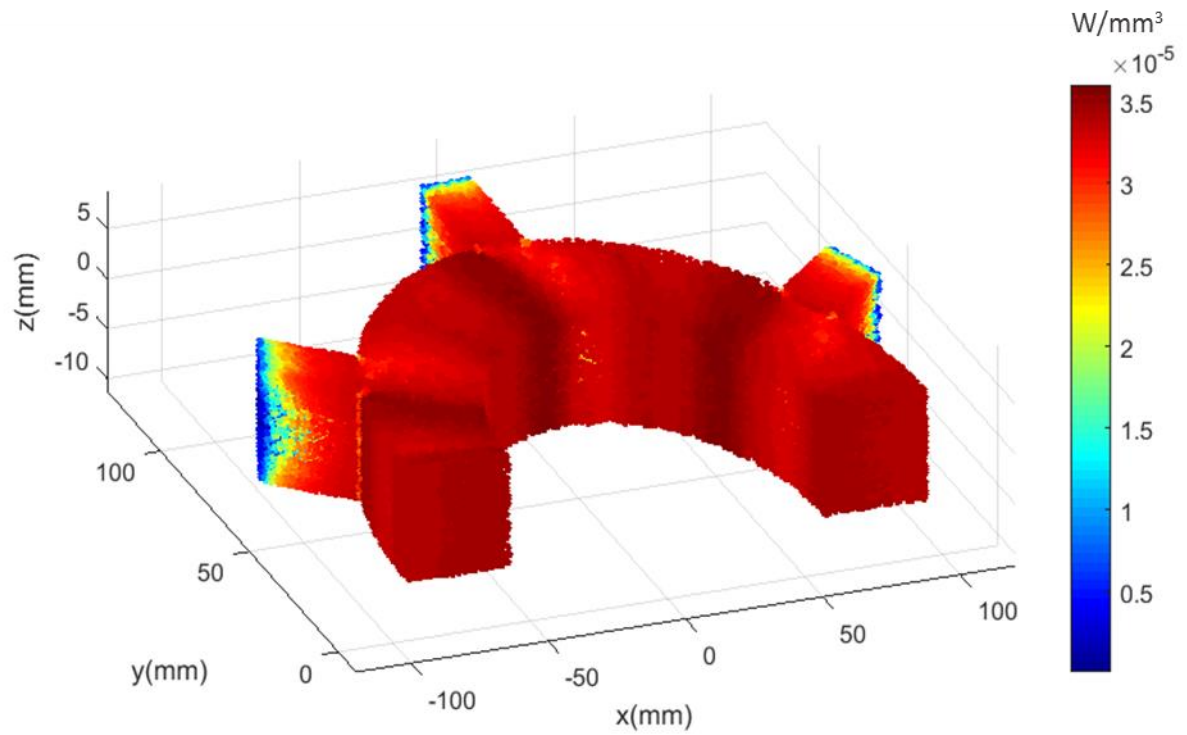
Figure 4. 25. Average hysteresis current loss density for each element in stator
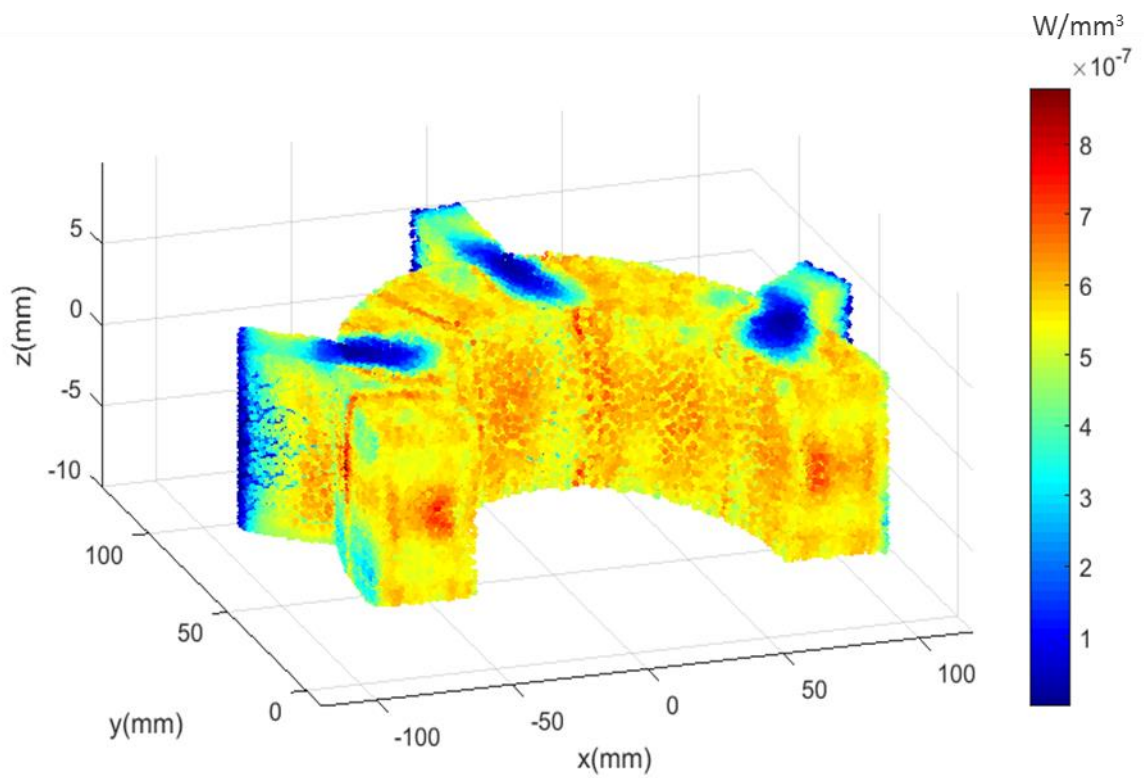
Figure 4. 26. Average excess current loss density for each element in stator
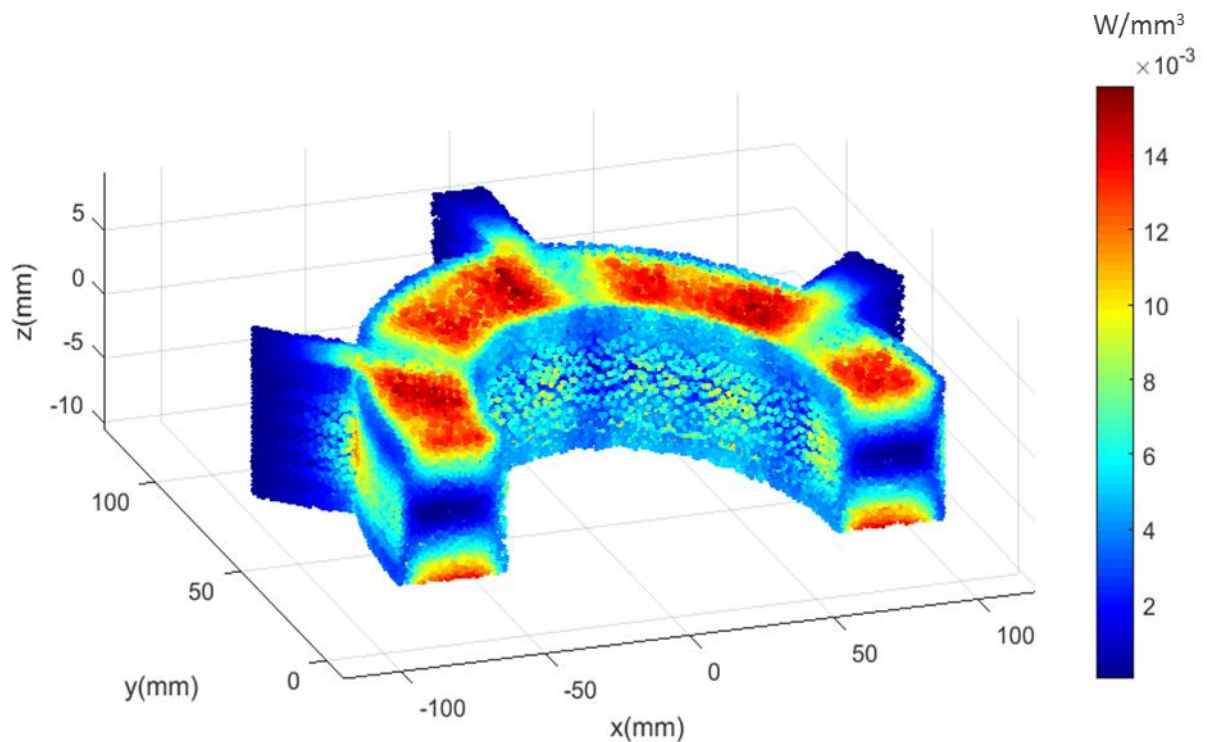
Figure 4. 27. Total iron loss density distribution in stator

The overall eddy current component of loss calculated using the MATLAB script during the simulation is shown in Figure 4. 28. The FE model is solved as a time-stepped transient model in which a speed of 500rpm is imposed at t=0. This leads to an initial transient in the calculated loss before setting to a quasi steady-state condition.

The total core loss for the stator can be obtained by a summation of average of the hysteresis loss, eddy current loss and excess loss over one complete electrical cycles. The simulation was repeated at 4 different rotational speeds (50rpm, 100rpm, 500rpm and 1000rpm). The resulting variation in the total iron loss as a function of rotational speed is shown in Figure 4. 29. As can be seed, even at a modest speed of 500rpm, the predicted core loss is equal to 20% of the output power, an inefficiency which when combined with the copper losses calculated previously, would not be acceptable for a continuously running type application.

119
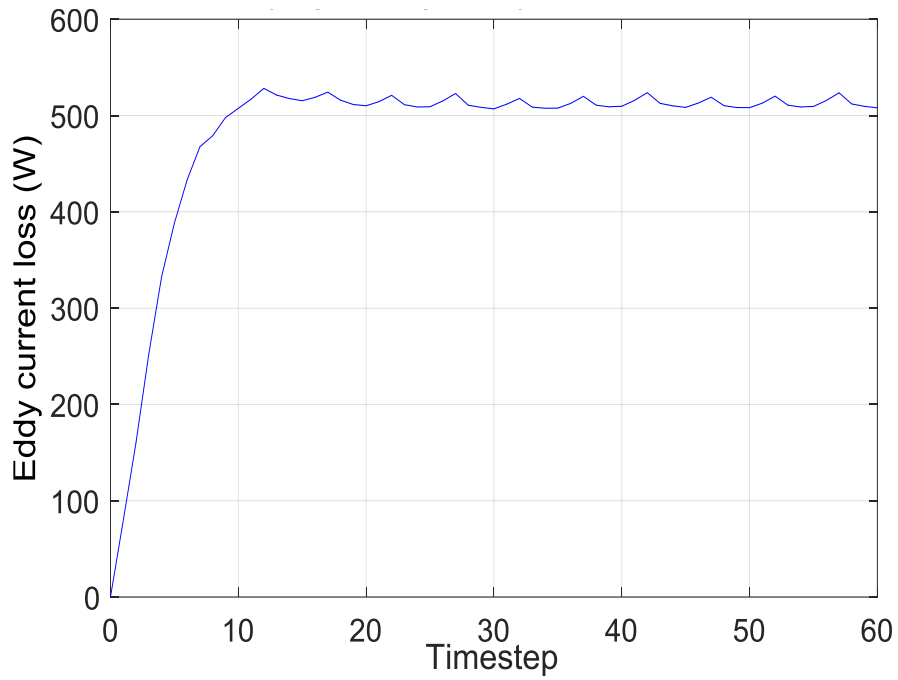
Figure 4. 28. Average stator eddy current loss over model time-step
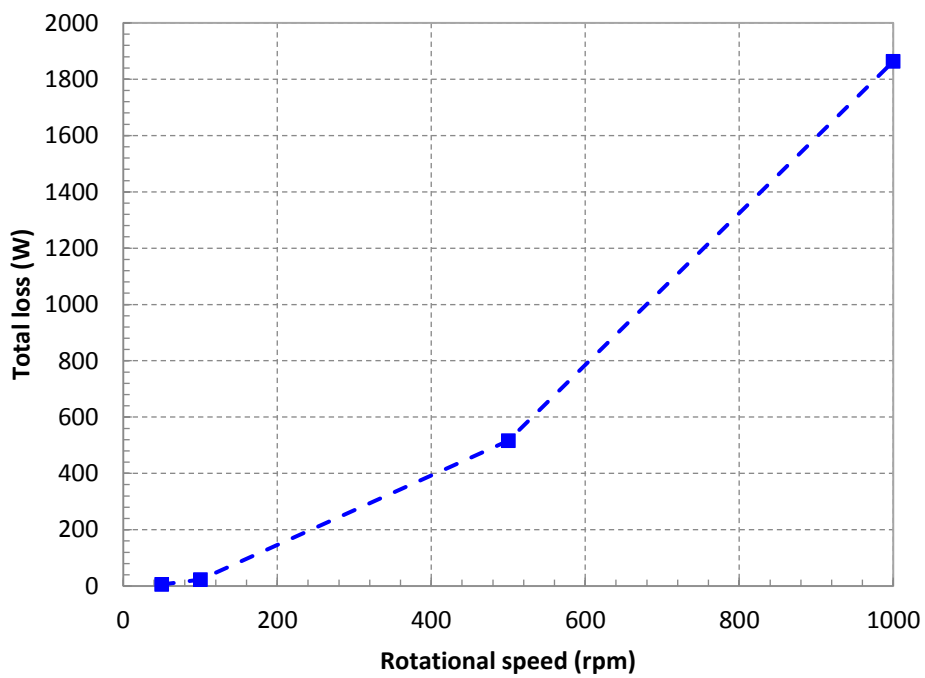
Figure 4. 29. Total stator core loss at different operating speeds

Figure 4. 30 shows snapshots of the induced current density distribution predicted by the finite element model under rotational speed for rotational speeds of 50rpm and 500rpm. It can be seen that, as would be expected, as the speed increases, the induced current density tends to crowd towards the surface of the stator core, i.e. skin effect.

A straight line is placed across the centre of the stator cross section as shown in Figure 4. 30. The variation in the magnitude of the induced eddy current density field along the profile line defined in Figure 4. 30 (a) is shown for different rotational speeds in Figure 4. 31, where each value is normalised to the surface value in each case.

(a). 50rpm   (b). 500rpm
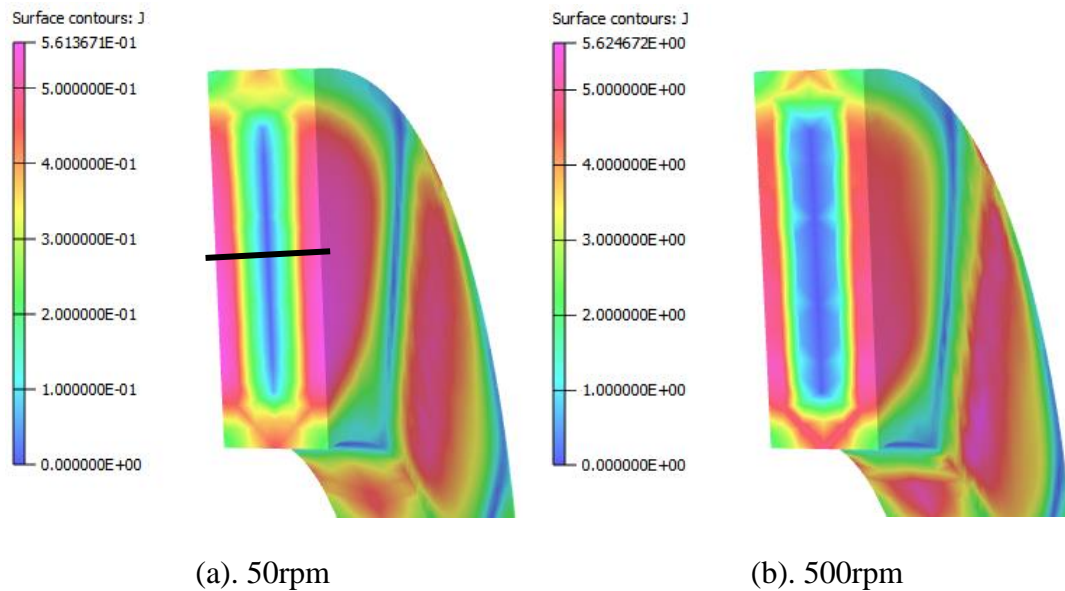
Figure 4. 30. Cross-sections through the stator core showing colour contours of induced eddy current at under different machine speeds
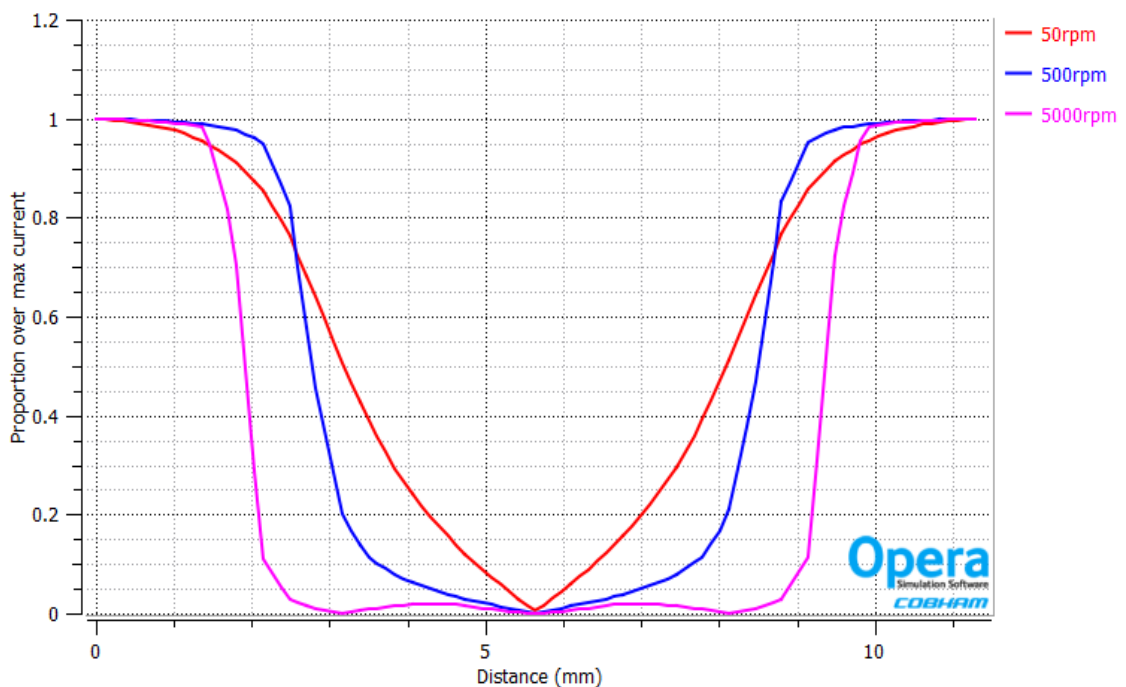
Figure 4. 31. Induced current density field along the profile line defined in

Figure 4. 30

4.4.3 Rotor loss

In comparison to the loss in stator core, the loss in rotor core and eddy currents in the rotor magnets should be small. The various components of rotor loss are evaluated in this section.

The method employed for calculating the iron loss for the rotor part uses the same finite element field predictions from the transient three-dimensional model. The hysteresis loss in the permanent magnets was not investigated in this case, as the rare-earth permanent magnet material exhibit negligible, if any, hysteresis loss [44] considering the hysteresis loop for the permanent magnet material is wide. [45].

The resultant distribution of eddy current loss in the rotor back iron and permanent magnets is shown in Figure 4. 32 for the case of a transient start-up to a steady-state speed of 500rpm. As will be apparent, the eddy current loss generated in the rotor part is much lower than in the stator. This is to be expected given that rotor is exposed to a near static field. It is also evident from Figure 4. 32 that the loss in the rotor core is approximately twice that in the rotor magnets. The average eddy current loss density distribution for the mesh element in rotor magnet and the average iron loss density for the elements in rotor back iron are shown in Figure 4. 33 and Figure 4. 34 respectively.
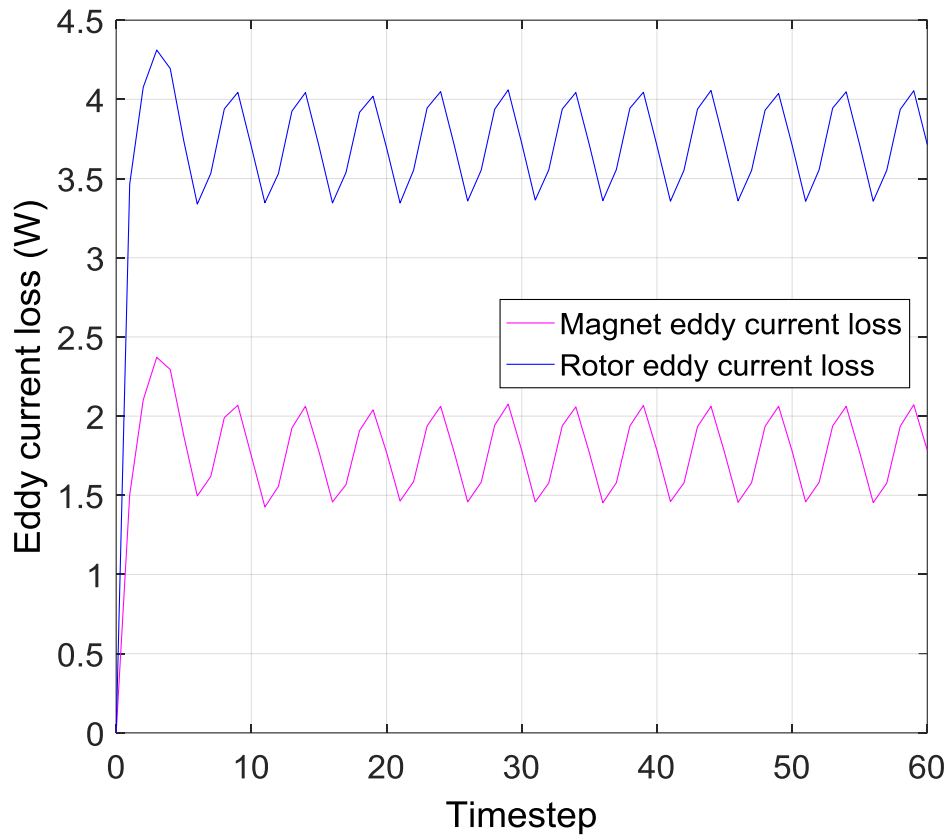
Figure 4. 32. Calculated eddy current loss for rotor back iron and rotor magnets
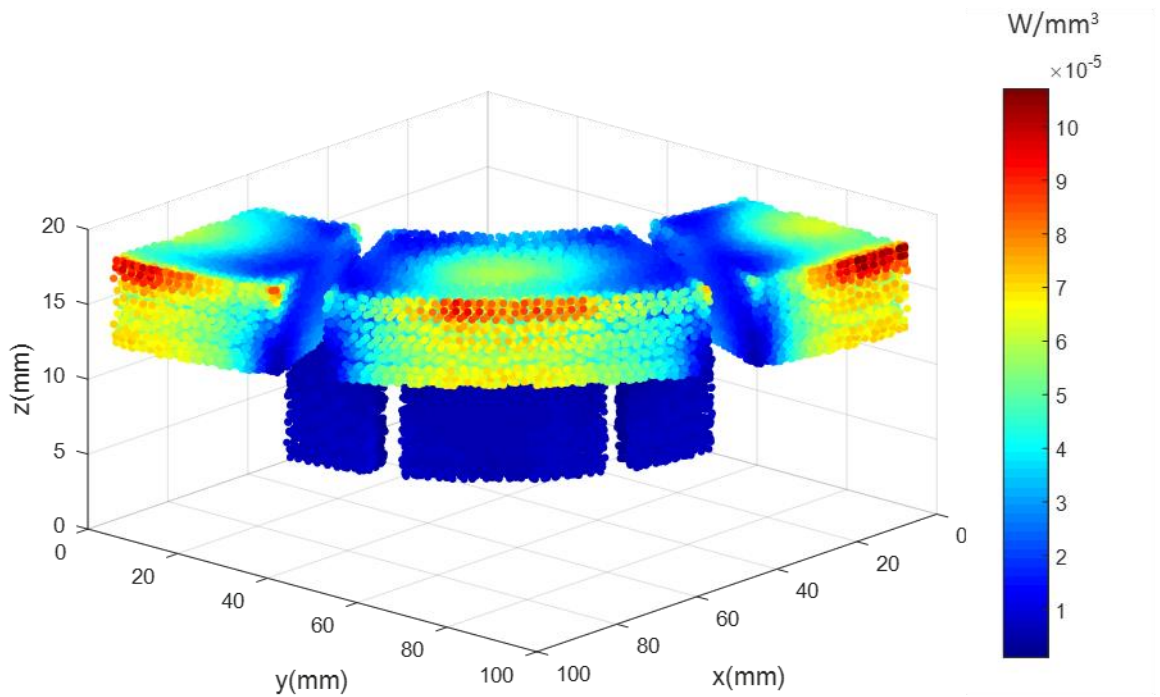
Figure 4. 33. Eddy current density distribution for each element in rotor magnet
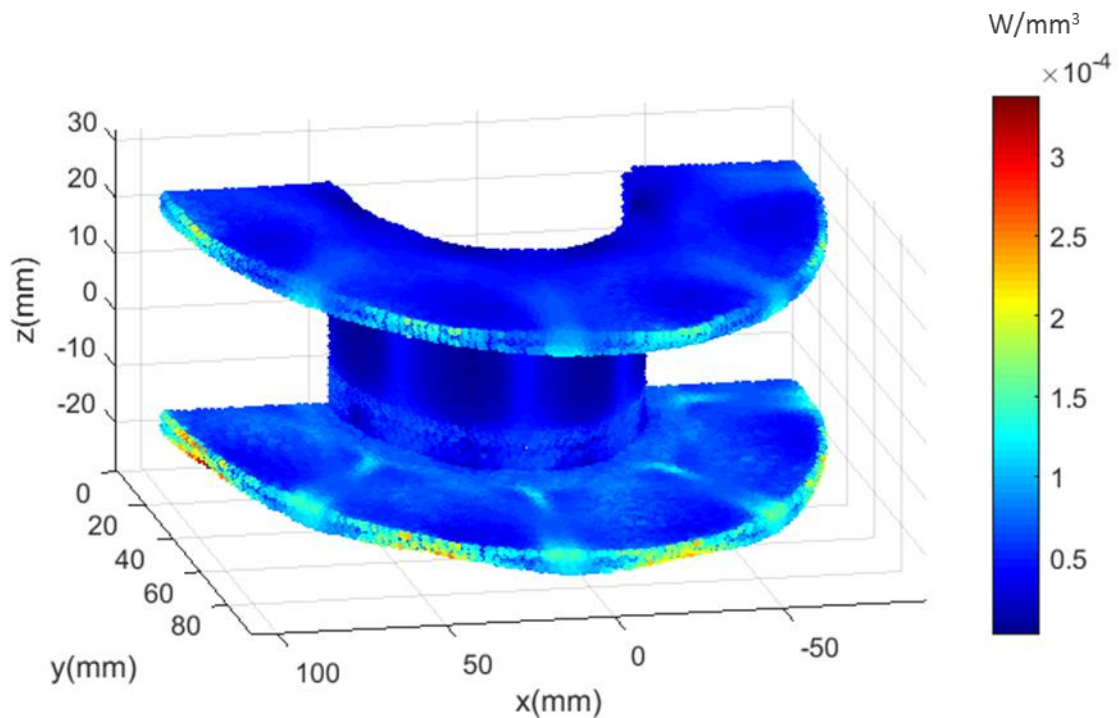
Figure 4. 34. Total loss density distribution in rotor back iron

4.5 Thermal modelling

Thermal modelling provides a basis for estimate of machine's safe operating condition and overload capability, ensuring that the materials used in the machine such as PM material, magnet bonding material and insulations remain within their specified temperature limits.

It is particularly important to evaluate the transient temperature behaviour of the preferred design for the machine in this case since it is operating at copper loss and core loss levels which are far in excess of those encountered in many electrical machines. Moreover, whereas there is a great deal of published studies on the thermal performance of conventional radial field machines and guidelines for current densities for different types of cooling, there is very little in the way of useful information on the thermal behaviour of non-slotted TORUS machines.

There are three mechanisms by which losses generated within the machine can be transferred to some external ambient, viz. convection, conduction and radiation. The heat transfer within and between solid components in the machine is predominantly

by conduction. The transfer of heat from the rotor and from the outer casing will be predominantly by convection. In this topology, the coils themselves are exposed directly to the forced air flow generated to the rotor and hence forced convection may be a more significant contributor to the removal of copper loss than is the case in conventional radial field machines. Heat transfer by radiation is normally moderate at the temperatures encountered in electrical machines.

The thermal analysis was carried out in OPERA 3D finite element thermal modelling module. Both static and transient thermal capability is provided by the software package, within which, the temperature rise, heat flux can be computed in three dimensions [27]. The cooling condition in this case is determined to be natural air convection since the heat generated would be very transiently and very locally at the coils, the forced air-cooling would help with the cooling of the coils to some extent. However, the forced air-cooled machine requires inlet and outlet, which requires slot to be cut in casing.

4.5.1 Thermal solver

Steady-state thermal solver

In the steady-state thermal solver within OPERA 3D, the following equations are used to calculate the temperature distribution throughout the machine for a given distribution of loss:

$$q_h = -k\nabla T \qquad\qquad (4.9)$$

$$\nabla \cdot q_h = Q \qquad\qquad (4.10)$$

$$\nabla \cdot k\nabla T = -Q \qquad\qquad (4.11)$$

The heat flux density q_h is given by equation (4. 9), the heat source density Q is the divergence of the heat flux density given by equation (4. 10). By combining (4. 9) and (4. 10), the temperature distribution can be calculated by equation (4. 11).

Several boundary conditions are required in the static thermal solver to describe the coupling between the solid regions of the machine in which het flows by conduction according to equation (4.14) and its immediate surroundings. A variety of boundary

conditions to replicate the effects of either a thermal insulator, a prescribed level of heat transfer, thermal contact resistance, heat transfer from a surface by conventions and/or radiation are available in static thermal solver.

In addition to a representation of the geometry of the machine (including structural elements such as the casing) the input parameters required for the model are the thermal conductivity of each region, heat transfer coefficients to represent convection from different surfaces, the thermal contact conductance between solid components and the surrounding ambient reference temperature. In addition, the localised sources of heat are required, i.e. the copper loss density and iron loss density for the stator in this case. Figure 4. 35 shows the location and type of the various boundary and interface conditions which must be defined in a thermal model of the machine.
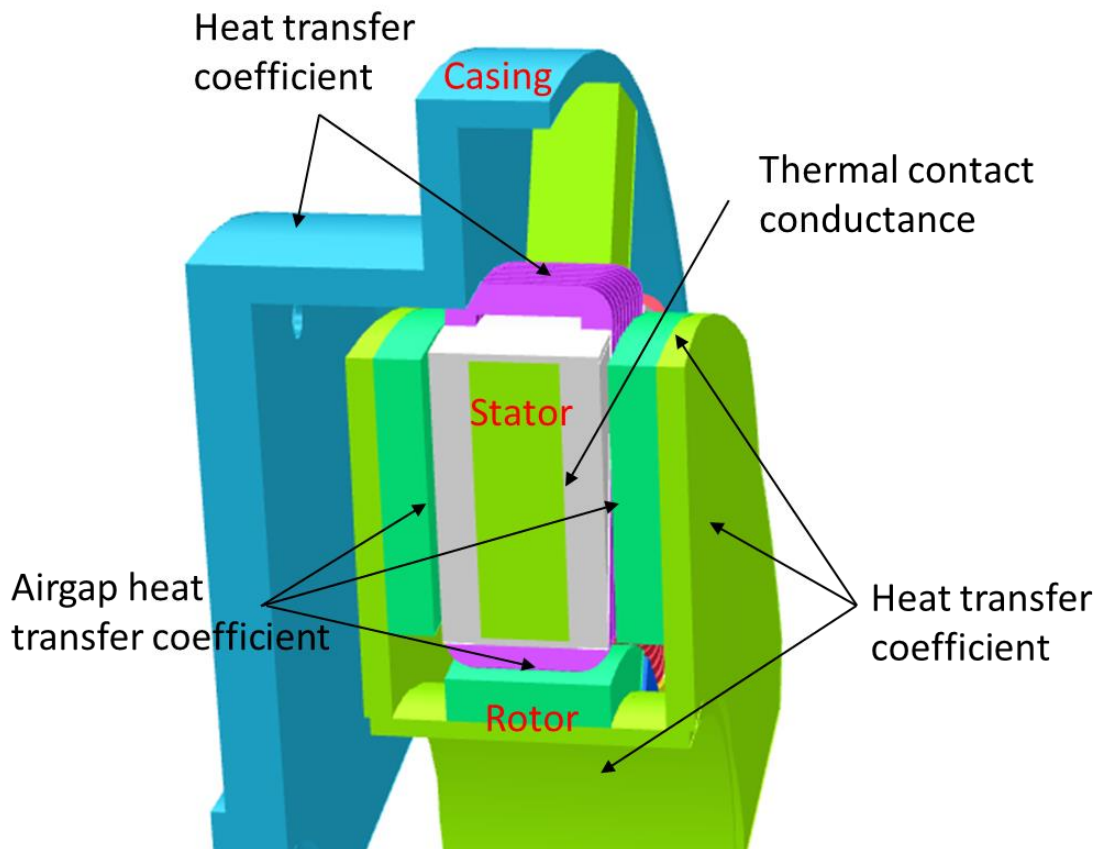
Figure 4. 35. Required input parameters for static thermal model set up

Transient thermal solver

The transient thermal response of the machine can also be modelled using a three-dimensional thermal model within the OPERA 3D environment. The equations employed are:

$$q_h = -k\nabla T \qquad\qquad\qquad (4.\,12)$$

$$Q - \rho C \frac{\partial}{\partial t} T = \nabla \cdot q_h \qquad\qquad\qquad (4.\,13)$$

The same thermal conductivities and boundary conditions used in the static solver can also be used for the transient solver. The additional information required for each region is the definition of specific heat capacity of the material C and mass density ρ.

4.5.2 Thermal model parameter definition

- **Thermal conductivities**

The thermal conductivities of the material in the various solid structures, i.e. cores, magnets, casing and hub, can be straightforwardly obtained from manufacture data and are summarised in Table 4. 4. However, the copper thermal conductivity of the coils is more complex given that it is a composite structure made up of copper, wire insulation, varnish applied during coil manufacture and potential some voids. It is usually not possible to model each individual conductor in a coil and hence, the thermal conductivity of electrical machine coils is generally specified in terms of an equivalent bulk thermal conductivity. It is also important to note that the thermal conductivity of a coils is very anisotropic, being a maximum in the direction along the copper wire and a minimum across the coil cross-section. Hence, two equivalent thermal different conductivities in orthogonal directions need to be specified for a bulk coil region.

To a reasonable approximation, the thermal conductivity along the direction of the wire is simply given by the product of the slot packing factor and the thermal conductivity of copper, since the thermal conductivity of copper is some two orders of magnitude greater than the thermal conductivity of enamel, varnish and the air voids. The thermal conductivity across the coil cross-section is more difficult to calculate, as it depends on numerous factors.

If the conductor is regularly distributed (for example, with square conductors) in the slot and the number of turns per slot is small, the thermal modelling of each individual conductor is possible. [46] It is rarely this case as round conductors are employed in most machines, and the distribution of them is generally irregular.

Normally for a slotted machine with wound-wire coils, the copper would only take up ~40- 50% of the slot, this being the so called slot packing factor or slot fill-factor. Although this is a slotless machine the same principles apply and only 50% or so of the coil cross-section will be made up of copper rather than voids and various insulation materials. A schematic cross-section through a coil in the TORUS non-slotted machine is shown in Figure 4. 36 alongside an equivalent homogeneous region with a modified thermal conductivity.

Copper   Enamel   Air and varnis

Equivalent thermal conductivity

(a). Actual slot cross-section

(b). Equivalent representation of the coil cross-section slot
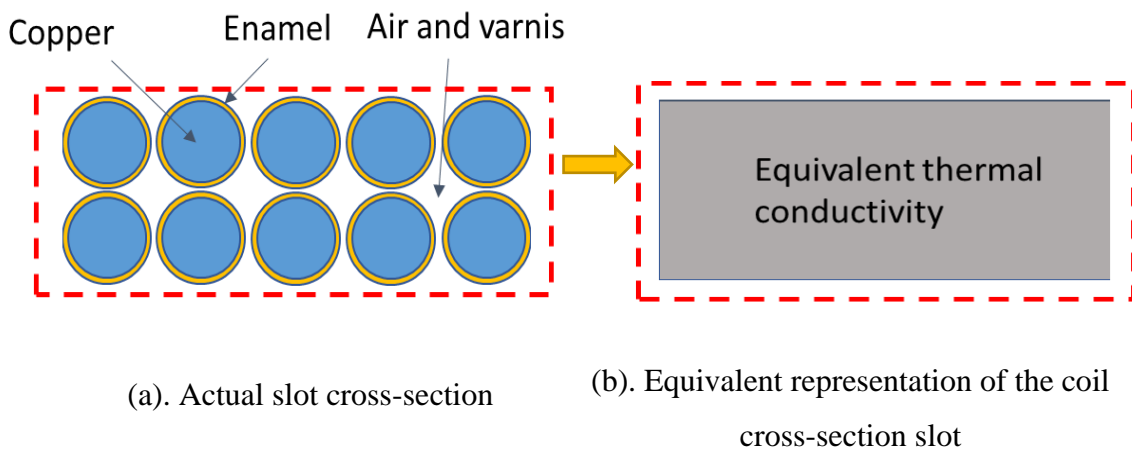
Figure 4. 36. Equivalent thermal conductivity representation for a stator coil cross-section

The evaluation of the equivalent thermal conductivity in slot is different from the equivalent conductivity along the radial direction. As shown in Figure 4. 36 (a), the equivalent thermal conductivity over the cross-section is affected by mixture of several components.

The equivalent thermal conductivity for the coil was calculated using a well established equation from [47] in which copper is designated as material 1and the insulation as material 2:

$$k_{equivalent} = k_2 \frac{(1 + k_p)k_1 + (1 - k_p)k_2}{(1 - k_p)k_1 + (1 + k_p)k_2}$$

(4. 14)

It is worth noting that equation (4.18) is based on the simplifying and reasonable assumption that the copper enamel has the same thermal conductivity as the impregnation material, i.e., the varnish applied during or after the coil is wound. In the case of the coils for the preferred machine design, an estimated thermal conductivity

of 0.63W/mK was established based on a coil packing factor of 50% and a thermal conductivities of 385W/mK and 0.2W/mK for the copper and insulation respectively.

- **Contact thermal resistance**

It is worth noting that between any two solid components there will be some additional contact thermal resistance due to imperfect surfaces. They key contact surface in this machine is the contact between the PEEK insulating cover and the core. The thermal resistance contributed at this interface could be significant. To improve thermal conduction across this interface, a thermal grease was used in the manufacture of the prototype machine as described in Chapter 6. In recognition of this, the thermal modelling employed the thermal contact conductance of the thermal grease 29kW/m^{2}K between the stator core and PEEK face.

- **Specific heat capacities**

The specific heat capacities of the solid materials were simply drawn from manufacturer data. In the case of the coil, it is important to obtain a representative value for this composite structure as the coil is a source of a significant proportion of the loss. In the finite model the coil is represented by homogeneous which is the size of the overall coil. The effective specific heat capacity of the entire coil region is given by:

$$c_{coil} = \frac{k_p \rho_{Cu} c_{Cu} + (1 - k_p)\rho_v c_v}{k_p \rho_{Cu} + (1 - k_p)\rho_v} \tag{4.15}$$

While the effective density is given by:

$$\rho_{coil} = k_p \rho_{Cu} + (1 - k_p)\rho_v \tag{4.16}$$

The worst case estimate for a 0.5 packing factor coil, it is assumed that the voids between individual conductors are filled by air for which is it reasonable in the context of the copper properties to assume that ρ_v and c_v are equal to zero. This assumption yields a specific heat capacity of 385 Jkg^{-1}K^{-1} and an effective density of 4450 kgm^{-3}.

The heat capacity of the coil will increase if the voids between conductors are filled with some form of epoxy or insulation. No specific heat capacity data is available for the Durapot 862 epoxy which was used in the prototype machine described in Chapter 6. In

the absence of a grade specific value, a typical published value of 1000 $Jkg^{-1}K^{-1}$ was used [48]. The manufacturer supplied density of Durapot 862 is 1200 kgm^{-3}.

Substituting in for the various factors in equations (**4.15** and (**4.16** with a coil packing factor of 0.5 yields an equivalent specific heat capacity for the full coil structure of 458 $Jkg^{-1}K^{-1}$ and an effective density of 5050 kgm^{-3}. The product of the specific heat capacity and the density provides a useful indicator of thermal capacity and is in effect the heat capacity per unit volume. For non-filled coil and the 100% filled coil the values are 1.71×10^6 $Jm^{-3}K^{-1}$ and 2.31×10^6 $Jm^{-3}K^{-1}$ respectively.

In practice a 100% fill factor will not be achieved and the effective density and specific heat capacity will lie in the range between the two cases shown above. In addition, it is important to recognise that the losses are generated only in the coil. Hence, the thermal mass of the copper and epoxy will play slightly different roles in limiting the rate of rise of temperature.

Table 4. 4 summarises the various thermal properties for the different materials in the model [49] in which the coil assigned best case thermal conductivities and specific heat capacities.

Table 4. 4. Parameters definition for thermal analysis

Material	Thermal conductivity (W/mK)	Specific heat capacity (J/Kg.K)	Density (Kg/m³)
Aluminium	205	900	2700
Air	0.025	1001	1.2
Cobalt iron	12	450	8120
Copper	385	385	8940
Durapot 862 epoxy	0.58	1000*	1200

Filled coil best case (0.5 packing factor and 100% epoxy fill)	192 along the wire direction 0.63 across coil cross-section	458	5050
PEEK	0.29	320	1320
Samarium cobalt	12	376	8400

- **Boundary condition heat transfer coefficients**

In order to capture the convective behaviour on the exposed surfaces of the machine, pre-specified heat transfer coefficients were used as boundary conditions rather than modelling the detailed air-flow and resulting heat transfer, an approach that would require the addition of CFD into the model.

The exposed surface can be divided into three categories:

o   Surfaces which are not rotating and remote from the airgap in which heat transfer is largely governed by natural convection such as the casing and the outer edge of the coil. These were assigned heat transfer coefficient values of $10W/m^2K$, a value which is representative of natural convection.

o   Surfaces which face onto to main working airgaps in which the rotation of the rotor will impact significantly on the heat transfer. Although there is no general expression to describe the heat transfer coefficient for salient airgap, the heat transfer coefficient for non-salient airgap (for example, the surface PM machine) can be estimated by the use of Nusselt number. [46]. For an axial field permanent magnet machine, expressions detailed in [50] provide a reasonable method for calculating heat transfer coefficient based on a combination of Reynolds number, Taylor number and Nusselt number.

$$R_{e\delta} = \frac{v l_g}{v_{air}} \tag{4.17}$$

$$T_a = R_{e\delta}{}^2 \frac{l_g}{r_o} \tag{4.18}$$

$$N_u = \begin{cases} 2, & \text{if } T_a < 1700 \\ 0.128T_a{}^{0.367}, & \text{if } 1700 < T_a < 10^4 \\ 0.409T_a{}^{0.241}, & \text{if } 10^4 < T_a < 10^7 \end{cases} \tag{4.19}$$

Having established the Nusselt number, the heat transfer coefficient for the airgap can be approximated by the following:.

$$h = \frac{N_u k_{air}}{l_g} \tag{4.20}$$

o Surfaces which are rotating but do not face the airgap, e.g. back of the rotor cores. A similar approach ca be adopted to the airgap, although the spinning surface is now in an open environment which requires some modification of the equations. However, the heat generated in the rotor is not significant and will not be the hottest region of the machine, same heat transfer coefficient as in airgap is adopted for the rotating surface of rotor.

The resulting heat transfer coefficients for each region are shown in Figure 4. 37 for the particular case of a rotor speed of 500rpm.
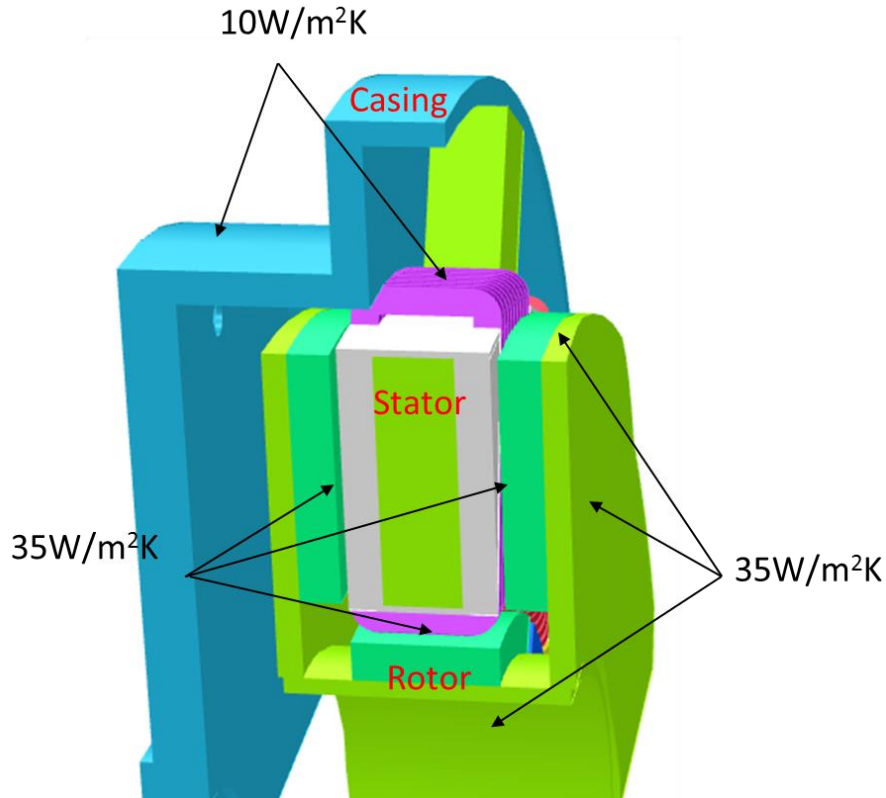
Figure 4. 37. Heat transfer coefficients for a rotational speed of 500rpm

4.5.3   Steady-state thermal modelling results

Steady-state thermal analysis was carried out using the model with the input parameters detailed in the previous section. Figure 4. 38 shows resultant steady-state temperature through the machine using a colour map contour with the direction of the heat flow indicated by arrows. The heat source in this model is the copper loss together with the stator and rotor iron loss and magnet eddy current loss at 500rpm rotational speed and 50Nm operating point.

As will be apparent, the stator is by far the hottest region, and usually for an electrical machine, the core is hotter than the coil even though the coil is operating at a high current density. This is a result of the very high eddy current loss in the core at 500rpm (~516W). The main heat path for the stator iron loss to ambient is via the contact surface between the stator and the casing which is a rather limited area. There are two principal heat paths for the copper loss generated in the coil, through the airgap convection and through conduction to the PEEK insulation.

133

It is clear, and not unexpected, that the losses generated at 500rpm are unsustainable in steady-state, which predicted localised temperatures of 2260°C.
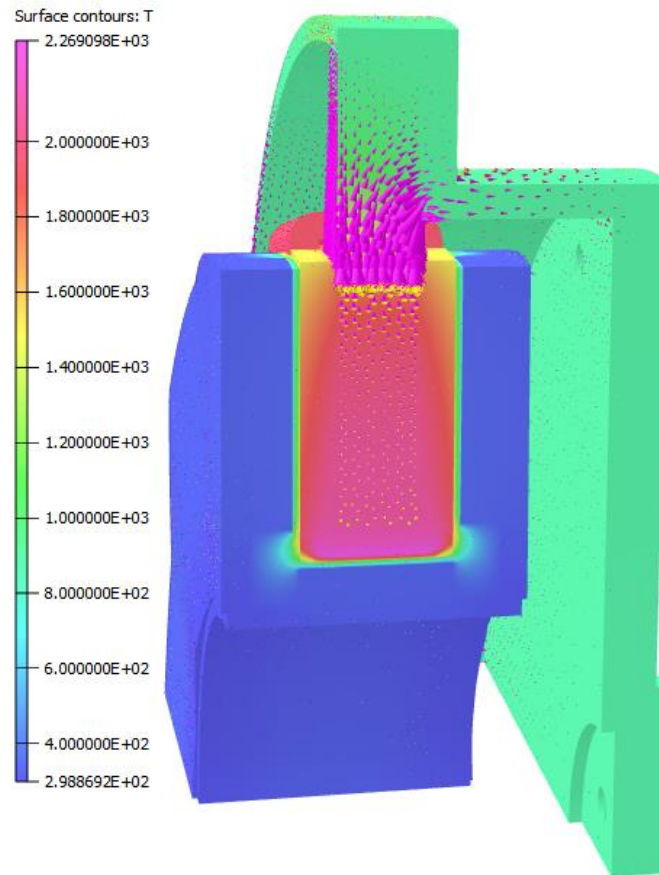
Figure 4. 38. Coloured contour of the temperature distribution with static thermal solver

The maximum steady-state temperature for each component as a function of coil current density was obtained by repeated runs of the steady-state thermal solver, in all cases with a core loss at 500rpm. It is worth mentioning that due to the presence of a 1mm thick PEEK insulation sleeve (discussed in greater detail in chapter 6) which was not taken into consideration in the electromagnetic design, the space available for coil is reduced compared to that assumed in the electromagnetic design. To maintain the same level of ampere-turns which leads to same level of torque, the actual current density employed was increased from the 30A/mm^2 specified in Chapter 2 to 36A/mm^2. The current density value shown in this plot is the actual current density with the reduced coil volume. This series of steady-state thermal simulation provides an estimation of the steady-state temperatures reached in different regions of the machine when applying a certain level of current density.

The maximum temperature against the current density with the packing factor of 0.52 (the value achieved in the prototype section in chapter 6) is plotted in Figure 4. 39. As will be apparent, beyond current densities of ~10A/mm^2(for which the maximum temperature is 181°C) these conditions cannot be sustained. However, as noted previously, this application only requires intermittent operation.
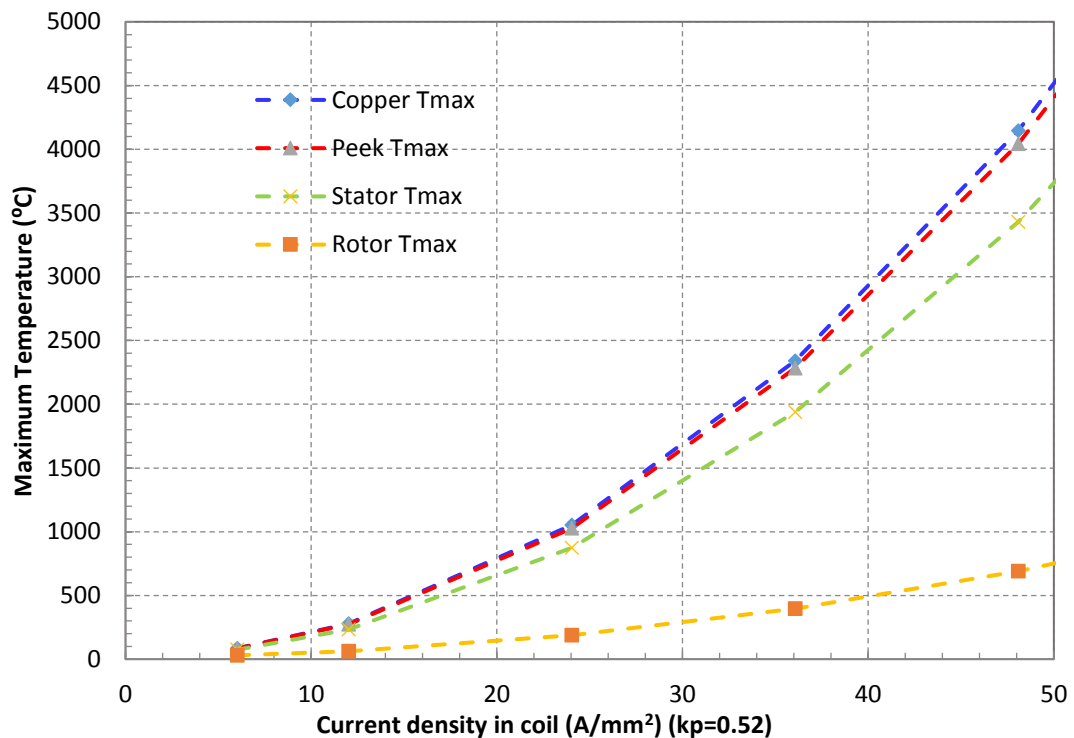
Figure 4. 39. Maximum temperature obtained from static thermal solver over varying current density

4.5.4 Transient thermal modelling results

Three-dimensional transient thermal analysis was performed over an interval of 30 seconds in all cases using the same thermal model parameters as used in the steady-state analysis, including rated core loss which corresponds to a torque of 50Nm at 500rpm . The simulation was performed for the rated operating condition of an rms current density of 36A/mm^2 in the coil (recalling that this was increased from the nominal 30A/mm^2 to account for the loss of slot area to accommodate the PEEK cover).

The nature of the simulation capability of OPERA 3D does not allow the loss to be changed at each time step in response to the calculated temperature. It is possible to provide a time varying loss as a look-up table in OPERA 3D but this is a-priori

determined variation. In order to cater for the change in coil resistance within the simulation the following procedure was adopted to cater for the limitation in OPERA 3D:

1. A full simulation was performed with a fixed copper resistance based on the room temperature of 20°C. This simulation will lead to an over optimistic outcome compared to a model that increases the copper loss at each time step to account for the change in wire resistivity. However, the resulting coil temperature rise can be converted into a time varying resistance and hence loss look-up table.

2. The loss look-up table calculated in step 1 can then be used as input to a further transient simulation which in turn generates a transient coil temperature response which can be again converted to a time varying resistance and hence loss look-up table.

3. Step 2 can be repeated until a prescribed level of convergence is achieved between successive simulations.

Using this procedure, the rate of rise temperature rise predicted in the stator, rotor, stator coil, PEEK and casing at each time step during the first pass of the model (with a fixed loss look-up table) is shown in Figure 4. 40. The initial rate of rise of temperature is 4.6°C/s which starts to increase as the amount of heat to be spread into the remainder of the structure and to be transferred from the exposed surfaces is not as smaller than the heat generated. The resulting temperature rise predicted by this first pass model was converted into a corresponding copper loss variation and fed into a second pass simulation. The temperature rises predicted with this second pass are shown in in Figure 4. 41. The coil temperature rise from this second pass of the simulation was converted into a corresponding time variation resistance. A comparison of the two time varying resistances calculated by the two passes of the simulation are shown in Figure 4. 42. Although further iterations would yield further convergence, even after two passes, the resistance converges reasonably even after only two iterations.
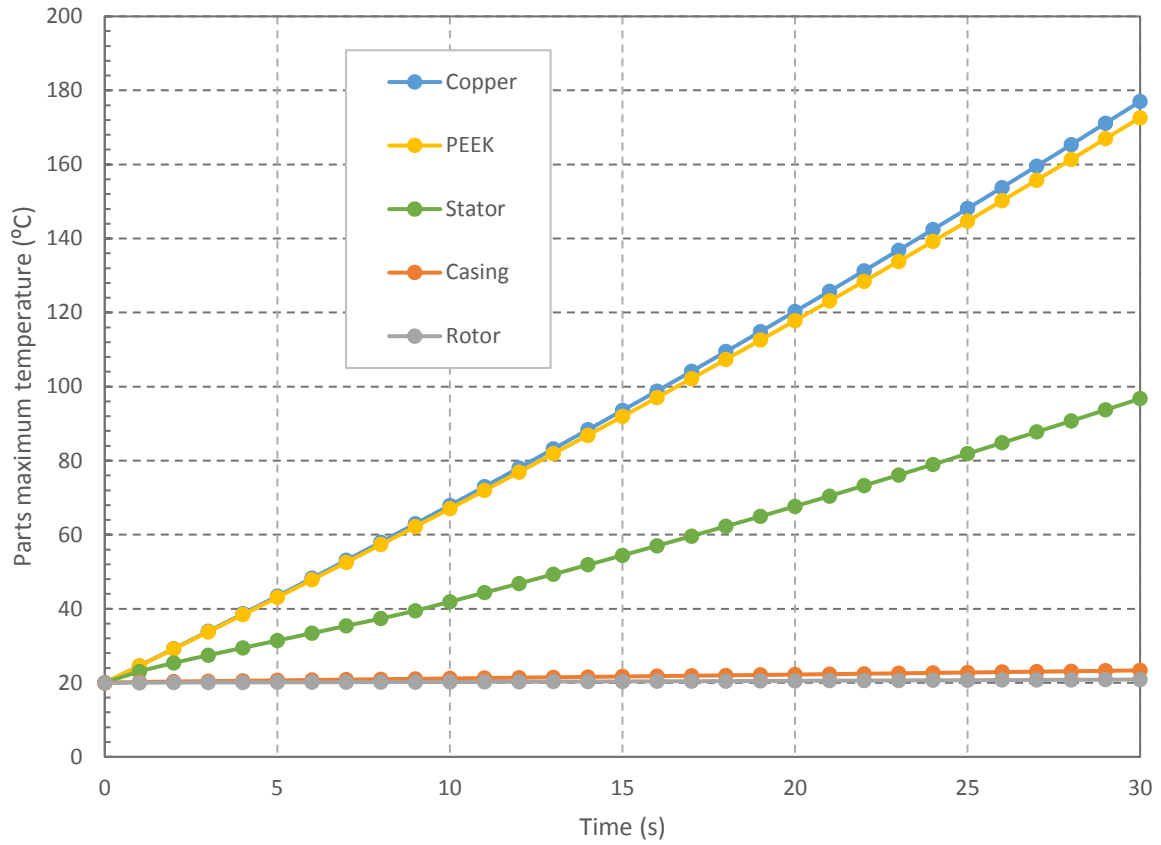
Figure 4. 40. Temperature rise in machine components with a fixed copper loss with current density of 36A/mm^2 (based on coil resistance at 20°C)
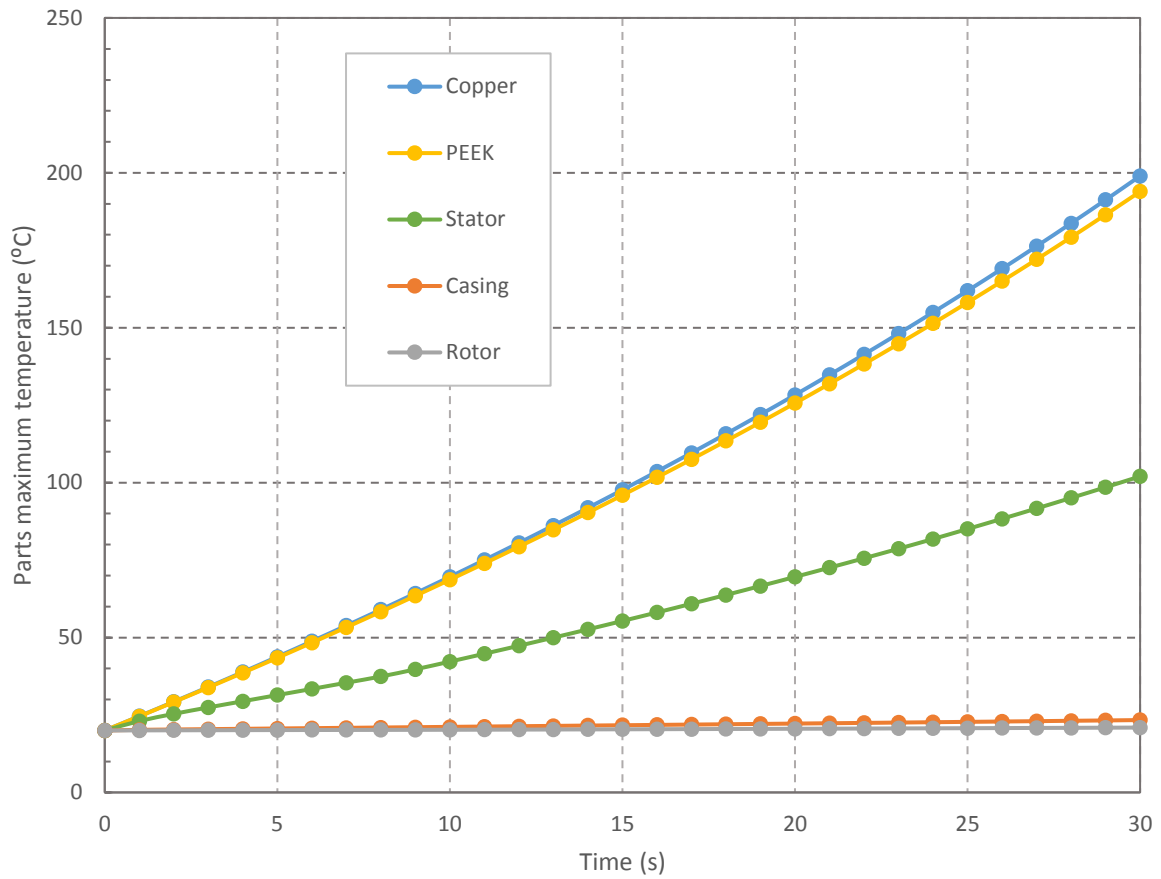
Figure 4. 41. Temperature rise in machine components with coil resistance variation calculated from the temperature from the fixed copper resistance model
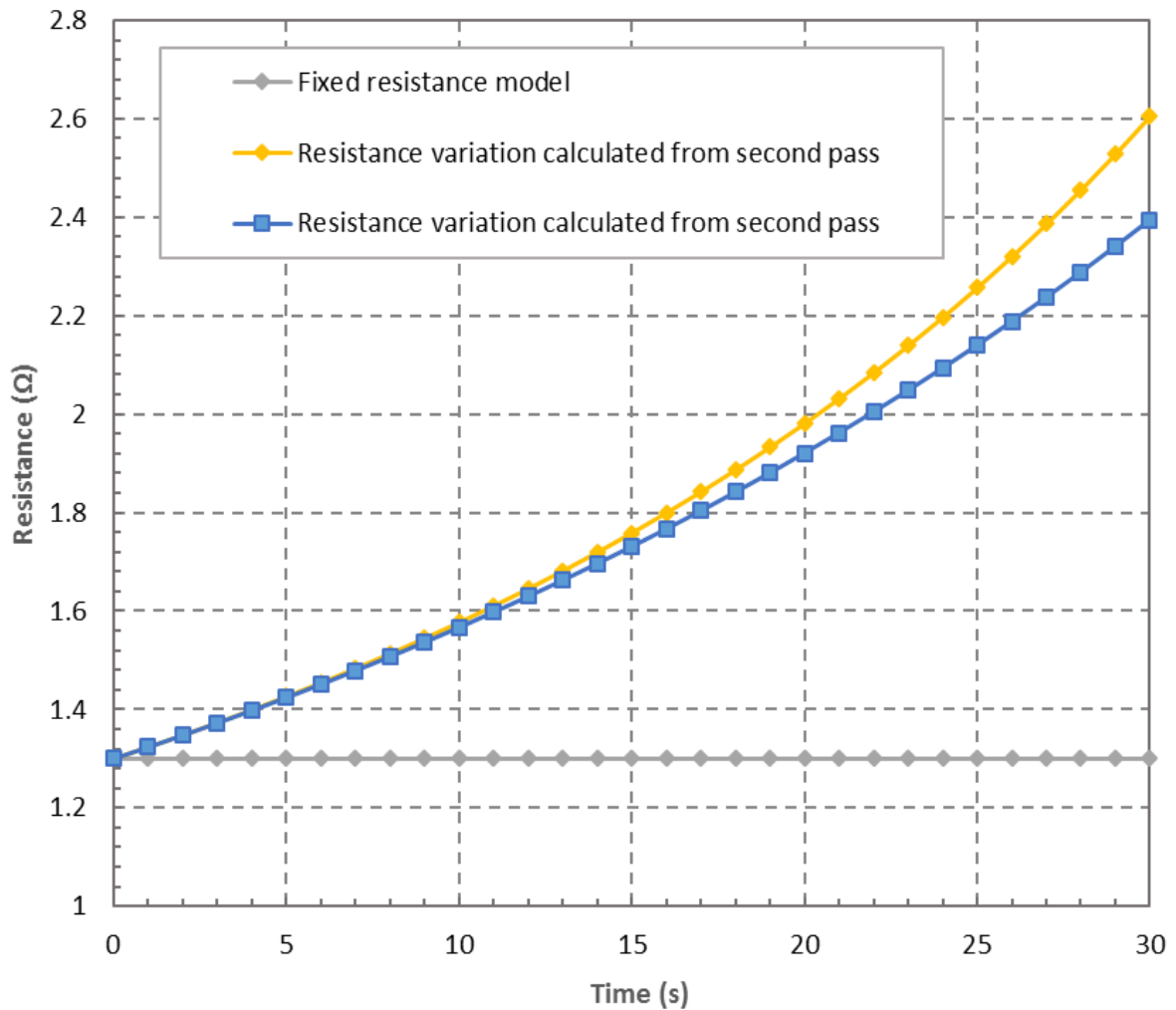
Figure 4. 42. Updated copper resistance variations

As will be apparent from Figure 4. 41, this level of combined loss can be sustained for ~30s before the temperature reaches 200°C. In service, the exact duration for which 50Nm could be sustained will depend on the interval before the next operation, and in particular whether this is sufficiently long for the starting temperature to return to 20°C. The thermal model, although based on several simplifying assumptions nevertheless illustrates that the preferred design can sustain rated performance for ~30s, which is likely to be adequate for the target application.

CHAPTER 5.   MECHANICAL ANALYSIS AND MANUFACTURING DESIGN OF PROTOTYPE MACHINE

5.1 Introduction

With the detailed electromagnetic analysis and thermal analysis of the TORUS non-slotted machine established from the previous chapters, the mechanical related issues are addressed in this chapter. The main mechanical challenges associated with this topology of machine is discussed and analysed in order to establish a practical mechanical structure of for prototype machine.

There are several potential mechanical challenges faced in designing and constructing a prototype. In addition to the usual considerations of rotor magnet containment and sizing of the shaft which are common in all rotating machines, there are specific mechanical issues relate to a double-sided axial field machine that need to be addressed. These include the large axial net force on the machine structure if the axial spacing of the two rotors are not perfectly matched and the deflection of the rotor core, and to a lesser extent the stator core, caused by the large forces of attraction between the stator core and rotor magnets.

For the purposes of mechanical design and analysis, the various electromagnetic forces were calculated using the static electromagnetic solver in OPERA 3D, while the resulting mechanical deflections and stresses were calculated in the mechanical solver which is also available in OPERA 3D.

Having established suitable dimensions and configurations for the various components. Engineering drawing of the stator, rotor, and the casing were produced in SOLIDWORKS, The detailed engineering drawings for the stator, rotor and its mechanical support structure are contained in Appendix II.

5.2 Stator position displacement tolerance evaluation

In a double-sided axial field topology, the stator and rotor are separated by axial mechanical clearances. These clearances are controlled by the fixing points for the stator core on the casing, the positioning of the shaft and bearing within the stator case and the stack-up of the rotor elements on the shaft. Although each set of rotor magnets generates a significant attractive force on the stator, the forces produced by each of the two rotor sections are in opposite directions and hence nominally balance each other in terms of the net force on the rotor structure and stator structure. This is in one of the major advantages of a double-sided configuration over a single-sided machine.

With identical mechanical clearance between both rotor sections, the forces should balance completely. However, in practice, due to manufacture tolerances and variations in assembly, exactly identical mechanical clearances are difficult to achieve. Hence, some level of deviation of the stator position from the true machine centre line in inevitable, resulting in an unbalanced axial force.

The axial attractive force between the stator and each rotor was is established for the double-sided axial field machine topology using a series of three-dimensional finite element calculations with varying levels of mechanical offset of the stator relative to the two rotors. Figure 5. 1 shows the magnitude of the axial force acting on both rotors with the stator progressively being displaced from the central position towards one of the rotors. The force shown is for the case of rated $30A/mm^2$ current density applied to stator winding. The influence of the armature field is likely to result in the magnitude of the unbalanced force being higher than the corresponding force under open circuit condition.

The force is shown up to the maximum an offset of 0.9mm, which is the limit imposed for increments of 0.1mm by the starting mechanical clearance of 1.0mm. It is important to recognise however, that the effective magnetic airgap in this machines is 6mm and hence the offset only corresponds to ~15% of the magnetic airgap.

It is interesting to note that even at 1mm, the net force on the stator (~430N) is still small in comparison to the forces on the individual rotors in the ideal balanced case, which are ~1200N.
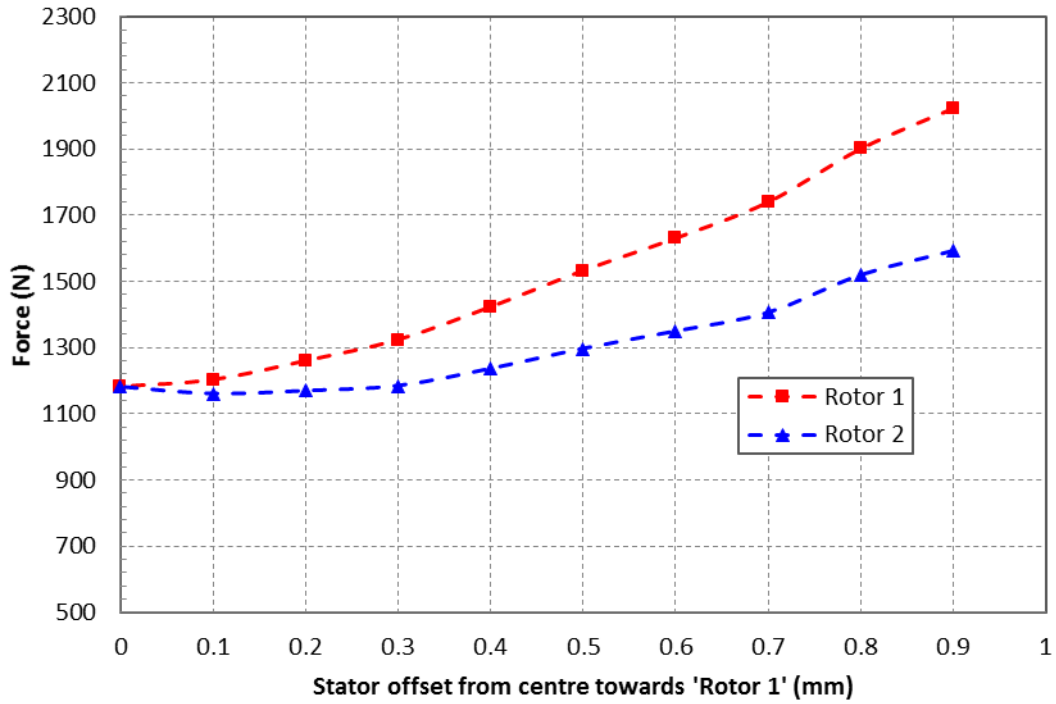
Figure 5. 1. Magnitude of the axial force on two rotors as stator gradually deviate from centre

The corresponding net force experienced by the stator due to any unbalanced mechanical clearance is shown in Figure 5. 2. This is also equal and opposite to the net force on the entire rotor assembly. The variation in force is near linear with stator axial offset and corresponds to a negative-stiffness of ~ 475N/mm.
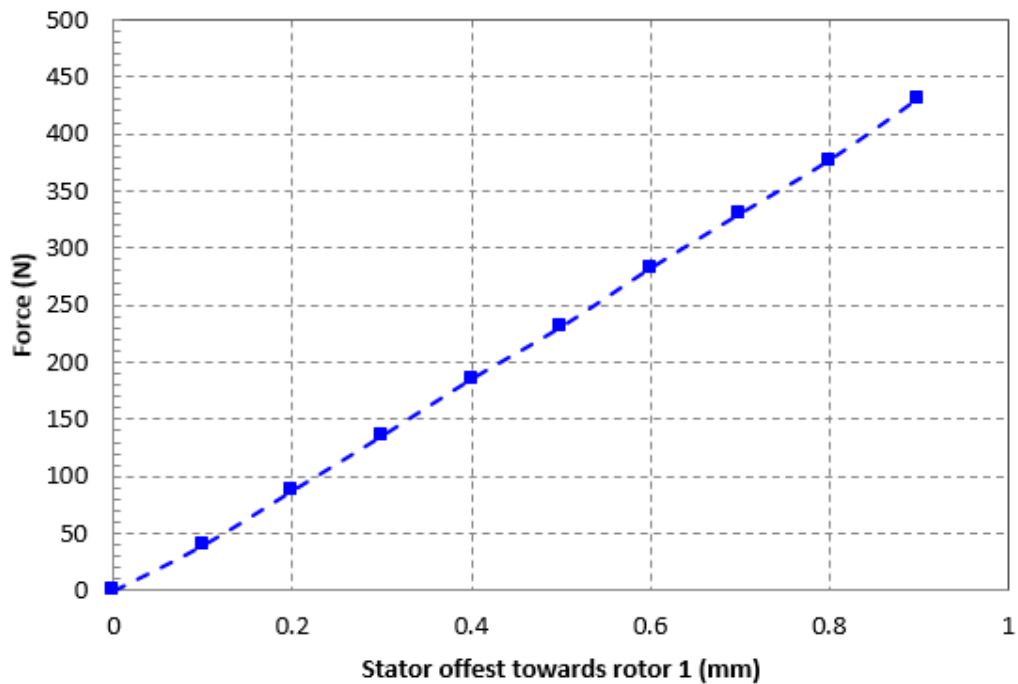
Figure 5. 2. Variation in axial force on the stator with offset towards rotor section 1

The calculated un-stiffness of ~475N/mm demonstrates the care that needs to be taken in terms of ensuring precise location and avoiding any axial 'play' in the final assembly.

5.3 Calculation of centrifugal loading on magnets

For surface mounted permanent magnet machines, especially for high-speed radial field PM machine, a high strength containment sleeve is often used to counteract the large centrifugal force on the permanent magnets. For an axial field machine, this is also potentially a concern since the outer radius of the magnets in an axial field machine are usually similar with the stator outer radius. In addition in an axial field machine the magnets are present at the very outer diameter of the machine, whereas in a conventional internal rotor radial-field machine the rotor magnets are located at ~60% of the rotor diameter depending on the exact split ration adopted.

The machine topology proposed combines both radially magnetised magnets adjacent the inner stator bore and axially magnetised magnets on the main rotor pole faces. In order to ensure that the final design has adequate mechanical integrity it is necessary to calculate the centrifugal stress and hence establish any need for containment for both types of magnets.

5.3.1   Axially magnetised rotor magnets

The centrifugal force due to the rotor rotation acting on a magnet piece with a mass, m, at average radius r_{ave} is given by:

$$F_{cen} = m\omega^2 r_{ave} \qquad (5.1)$$

The centrifugal loading applied on these magnets is predominantly shear stress. The shear stress can be calculated using:

$$\tau = \frac{F_{cen}}{A} \qquad (5.2)$$

In this case, the area A in (5.2) is the contact area between the magnet face and the rotor core. At the maximum rotational speed of 500rpm, the shear stress applied on a permanent magnet for the prototype machine dimensions is 170kPa.This shear stress would be largely borne by the adhesive bond between the magnets and the rotor core. There would also be a contribution from the axial force attraction force in combination of with the coefficient of friction to yield a tangential force. The shear strength of the bonding adhesive used to bond the rotor and the magnets is therefore a key factor. The relationship between the shear modulus and the tensile modulus is given by:

$$G = \frac{E}{2(1 + v)}$$
(5.3)

The Poisson's ratio of adhesive is typically in the range of 0.3 to 0.5. [51] Therefore, the shear modulus provided by the magnet-bonding adhesive is 33% to 38% of its tensile modulus.

Due to a relatively low operating speed, a high temperature magnet-bonding adhesive is likely to be sufficient to withstand the centrifugal force acting on the magnet. The adhesive selected for use in the prototype is Duracol NM25 which is a high temperature magnet-bonding adhesive. This has a manufacturer's quoted tensile strength of 68MPa which corresponds to a shear strength of 25MPa. Although the actual tensile strength provided by the glue is inevitably dependent on factors such as contact surface roughness, vibrations and surrounding temperature, the shear strength provided by a magnet-bonding adhesive is much higher than the 170kPa centrifugal loading. Hence in this case, additional support such as fibre glass banding at the outer radius is not required.

In addition the centrifugal loading, the other force acting on these magnets is an axially oriented attractive force. Three-dimensional electromagnetic finite element analysis was carried out in order to evaluate the magnitude and direction of the force experienced by the magnets in axial direction. Net axial direction force variation is established for one of the magnets with the magnets gradually moved away from the rotor back iron as shown in Figure 5. 3.
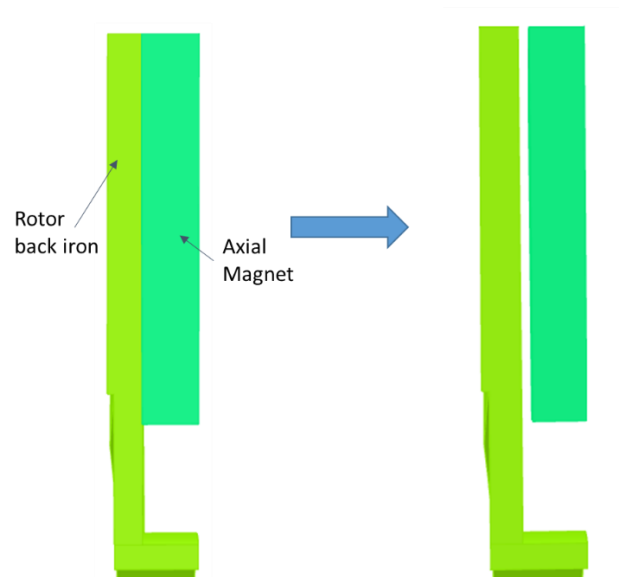
Figure 5. 3. Magnet gradually moved away from the rotor back iron

During the calculation of the forces, the correct armature current distribution was applied to the stator winding so that the influence of the armature field is taken into consideration. The variation in the magnitude and direction of the net axial force on one magnet piece as a function of the distance between the contact face of the rotor back iron and the magnet is shown in Figure 5. 4. It can be seen that as expected, when the distance between the rotor back iron and the magnets increases, the net axial direction force decreases. Over the range of separations considered, the direction of the force remains unchanged and towards the rotor core, which is a consequence of the fact that the distance from the magnet to stator is still much greater than the distance between the rotor and the magnet. Hence, the axial force applied to the magnets will act to as to retain the magnet keep pressing the magnet towards on the rotor core and fix it in place. Even when there is a finite gap due to the thickness of the adhesive layer, the direction of force is still towards the rotor core which will assist with retaining the magnet in position against the effect of the centrifugal loading.
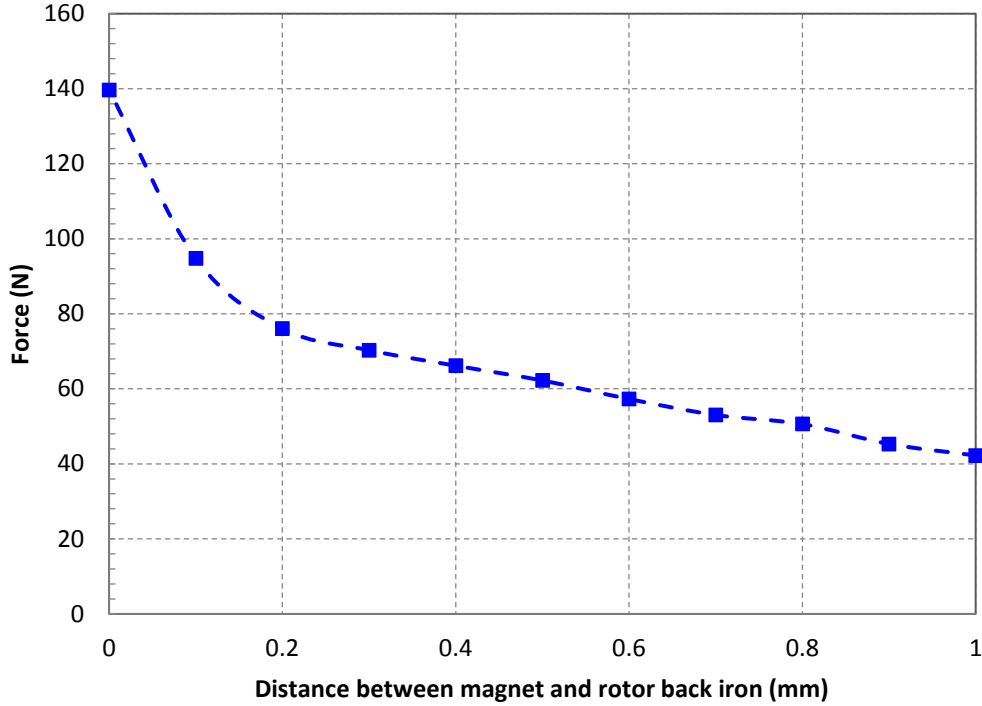
Figure 5. 4. Finite element predicted variation in the magnitude of the net axial force on magnet

5.3.2 Radially magnetised rotor magnets

For the ring of radially magnetised magnets that are located within the bore of the stator, the dominant force acting on the magnets is a centrifugal force. In many respects, the mechanical considerations for these magnets are similar to those in conventional radial-field permanent magnet machines. In many such machines, some form of sleeve is used to retain the magnets. The thickness of containment sleeve of given material properties can be calculated via the expressions for stress in equation(5.4): [52]

$$
\begin{aligned}
\sigma_{max} = \frac{\rho_{ct}\omega^2}{8} & \left[(3 + v_c)\left(\frac{d_{co}^2}{2} + \frac{d_{ci}^2}{4}\right) - (1 + 3v_c)\frac{d_{ci}^2}{4} \right] \\
& + \left(\frac{d_{ci}^2 + d_{co}^2}{d_{co}^2 - d_{ci}^2}\right)\left(\frac{m_{eq}r_{meq}\omega^2}{\pi d_{co}}\right)
\end{aligned}
\tag{5.4}
$$

Where, m_{eq}, the equivalent mass of the magnet and r_{meq}, radius of gyration is given by:

$$m_{eq} = \frac{\pi}{4}\left(d_{mo}{}^2 - d_{mi}{}^2\right)\left(\frac{\alpha \rho_m}{180} + \left(1 - \frac{\alpha}{180}\right)\rho_{ip}\right) \qquad (5.5)$$

$$r_{meq} = \frac{\sqrt{2}}{2}\sqrt{\frac{\left(d_{mo}{}^4 - d_{mi}{}^4\right)}{4\left(d_{mo}{}^2 - d_{mi}{}^2\right)}} \qquad (5.6)$$

Figure 5. 5 defines the various diameters used in the calculation.

σ_{max} is the maximum hoop stress on the inner bore of the containment, and is ultimately limited by the tensile strength provided by the manufacturer of the containment sleeve material. The containment material considered in this study is carbon composite C427277.
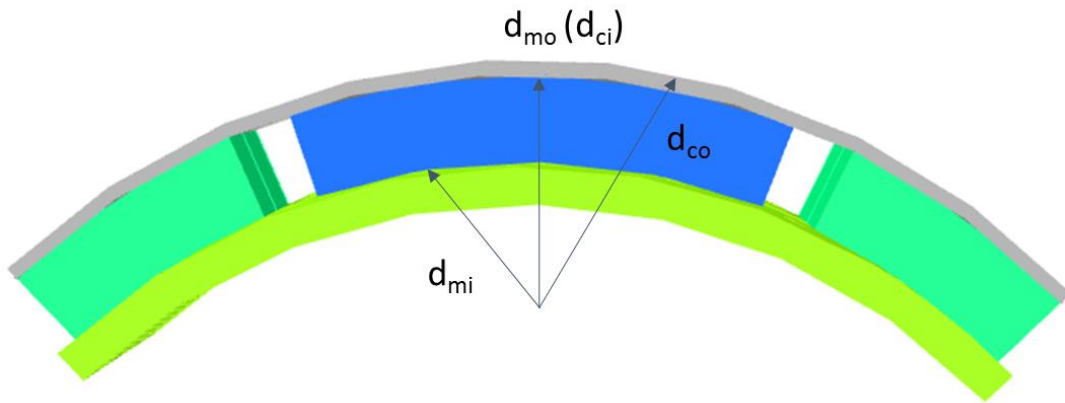
Figure 5. 5. Dimensions used for calculation of containment level stress

Using on the series equations above before, the minimum containment thickness required to maintain the maximum stress within a pre-defined maximum operating stress can be calculated. To ensure that cyclical and thermal loading can be reliably accommodated by the containment, the maximum design stress was set to be approximately half of the ultimate tensile strength (UTS) of the carbon composite.

With the maximum stress criteria of the material being 1GPa, the minimum thickness required for the containment is 0.0015mm for a magnet outer diameter of 101.52mm at 500rpm. Given that this analysis is based on the magnet acting as a dead-weight on the composite sleeve, i.e. the adhesive bond is not accounted for, this analysis

demonstrates that the inclusion of some adhesive forces and reluctance forces will ensure that at this modest speed, no specific containment is required.

Overall, these calculations have demonstrated that although the rotor magnets are subjected to centrifugal loading, the magnitude of the forces at the modest speed of 500rpm are so low that no specific provision beyond adhesive bonding of the magnets to the rotor core is required.

5.4 Detailed deflection calculation

When compared with the more common radial field machine, the main mechanical challenge faced by axial field machines is managing the axial attractive force between the rotor elements and the stator. Although the magnitude of this force under different circumstances has been discussed in the previous sections, the resulting stress and deflection of the structure requires further analysis and investigation.

In axial field machines, the geometry of the rotor and stator core can be regarded as thin plates, a geometry that it prone to deflection. From previous studies, it is shown that for an axial flux permanent magnet machine, the active mass which include the mass of the iron, the copper in the stator winding and the weight for permanent magnet on the rotors, accounts for only 1/3 of the total mass. [53] The remaining mass, is mostly structural support to maintain the airgaps. In this section, the degree of deflection of the rotor and stator cores due to attractive magnetic forces are investigated.

5.4.1   Calculation of stator deflection

For a double-rotor, single-stator axial field permanent magnet topology, the stator will only experience a small net force if it is located midway between the rotors (in a perfectly symmetrical position, the net force will be nominally zero). While some minor deflection of the stator is still likely to happen, the maximum force acting on the stator is during the assembly process [7]. The assembly of the machine involves stacking up the various stator and rotor parts one on another starting with one of the rotor elements. When only one rotor and one stator is in place in the casing, the machine is effectively a single sided axial flux machine with large attractive force applied on both stator and the rotor.

The stress applied to the stator due to the axial direction attractive force from the rotor can be estimated using:

$$q = \frac{B_g{}^2}{2\mu_o} \qquad (5.7)$$

A schematic of a stator with an outer radius face fixed and an inner radius which free is shown in Figure 5. 6. The stress q due to the axial attractive force from the rotor during assembly is applied uniformly on the stator core between the outer radius r_{out} and inner radius of the rotor magnet r_{in}. In practice, the stress is only applied to the area covered by the magnets. To simplify the analysis, the stress q is assumed to act on the entire surface between r_{in} and r_{out}, i.e. spread across the pole pitch. Hence, the Maxwell stress is taken an equivalent by multiplying the width/pitch ratio of the magnet.
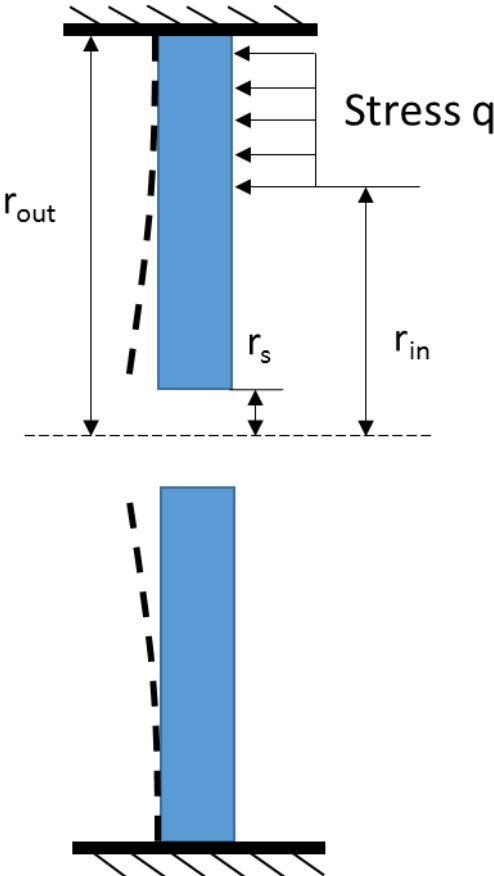
Figure 5. 6. Stator with outer radius fixed, inner radius free

The possible deflection of the stator during assembly is calculated through analytical approach, circular plate theory is employed in the calculation. A flat circular plate with

149

its outer diameter fixed and inner diameter free is modelled. The maximum axial deflection of the stator plate under stress q with the outer circular face at radius r_{out} fixed is given by [54]

$$y_s = \frac{-q r_{out}^4}{D} \left(\frac{C_1 L_{14}}{C_4} - L_{11} \right)$$

(5.8)

Where, the plate constant D can be described by Young's modulus E, Poison's ratio v and the thickness of the stator core in equation (5.9)

$$D = \frac{E t^3}{12(1 - v^2)}$$

(5.9)

The expression for constant C_1, C_4, L_{14} and L_{11} can be found in the following equations:

$$C_1 = \frac{1 + v}{2} \left(\frac{r_s}{r_{out}} \right) \ln \left(\frac{r_{out}}{r_s} \right) + \frac{1 - v}{4} \left(\frac{r_{out}}{r_s} - \frac{r_s}{r_{out}} \right)$$

(5.10)

$$C_4 = \frac{1}{2} \left[(1 + v) \frac{r_s}{r_{out}} + (1 - v) \frac{r_{out}}{r_s} \right]$$

(5.11)

$$C_7 = \frac{1}{2} (1 + v^2) \left(\frac{r_{out}}{r_s} - \frac{r_s}{r_{out}} \right)$$

(5.12)

$$L_{11} = \frac{1}{64} \left\{ 1 + 4 \left(\frac{r_{in}}{r_{out}} \right)^2 - 5 \left(\frac{r_{in}}{r_{out}} \right)^4 \right.$$
$$\left. - 4 \left(\frac{r_{in}}{r_{out}} \right)^2 \left[2 + \left(\frac{r_{in}}{r_{out}} \right)^2 \right] \ln \left(\frac{r_{out}}{r_{in}} \right) \right.$$

(5.13)

$$L_{14} = \frac{1}{16} \left\{ 1 - \left(\frac{r_{in}}{r_{out}} \right)^4 - 4 \left(\frac{r_{in}}{r_{out}} \right)^2 \ln \left(\frac{r_{out}}{r_{in}} \right) \right.$$

(5.14)

A maximum resultant deflection of the stator back iron of 0.388µm is obtained through the application of the above equations to a circular plate with thickness of 11.3mm and an elastic modulus of 210GPa and a Poisson's ratio of 0.3.

The finite element stress module in OPERA 3D was employed to verify the displacement obtained via the analytical expressions. The force of 1100N on the stator was predicted using three-dimensional electromagnetic finite element analysis. In the mechanical modelling, the stator was modelled as a circular plate with its outer radial face fixed as the support face, ring shaped face facing the airgap between radius r_{in} and r_{out} as the force load face. The deformed stator under load is shown in the Figure 5. 7, the displacement in axial direction is represented by the surface colour contour. As if often the case in mechanical deflection finite element analysis, the visual deflection shown is greatly exaggerated. The maximum deflection calculated by the finite element model is 0.423µm, which is in reasonable agreement with the corresponding deflection obtained via analytical method.
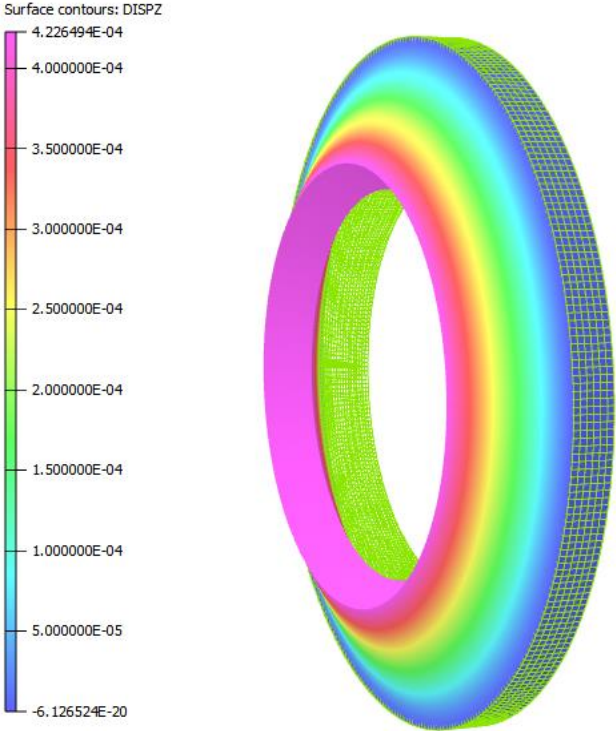
Figure 5. 7. FE predicted stator ring deflection (colour scale in mm)

In practice, for axial field machine, the stator core is usually not a plain circular plate as it requires some means to attach it to the casing. The actual proposed stator geometry is shown in Figure 5. 8. In this proposed stator geometry, the outer diameter of the

stator is extended by adding some rectangular shaped projections with curved outer shape onto the original circular ring. By adding these projections, the stator can be firmly attached inside the casing as shown in Figure 5. 9.
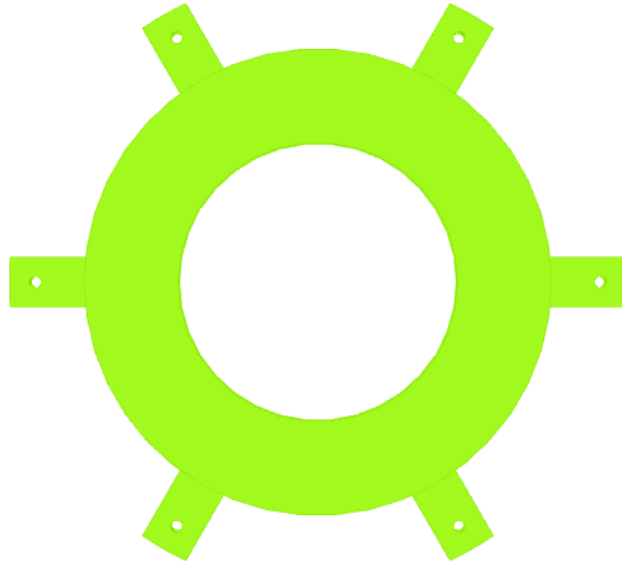
Figure 5. 8. Stator core design including attachment features
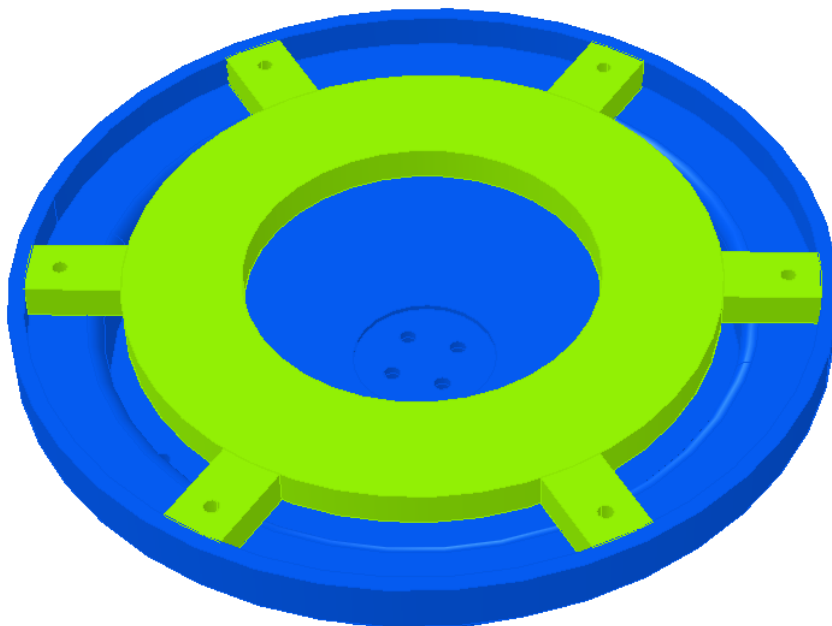
Figure 5. 9. Stator in casing

The deflection of this fully featured geometry was predicted using three-dimensional finite element structural analysis, again with the calculated total force applied uniformly distributed over the main section of the core. Figure 5. 10 shows the

predicted deflection of the ring. Rather than fixing the outer radius face, the contact face between the stator and casing, i.e. the face of the rectangular piece which is in contact with the casing, was set to be mechanically fixed within the finite element model. The maximum deflection under this arrangement is increased to 1.939µm. Overall, the mechanical arrangement of the stator result in deflections that are not significant in the context of the various working airgaps in the machine, even during assembly. However, the forces mean that care must be taken when assembling the machine. Once the machine is assembled and the axial stack-up adjusted to produce balanced airgaps the force acting on the stator will be reduced to a low level (10s of Newtons with little discernible deflection of the stator).
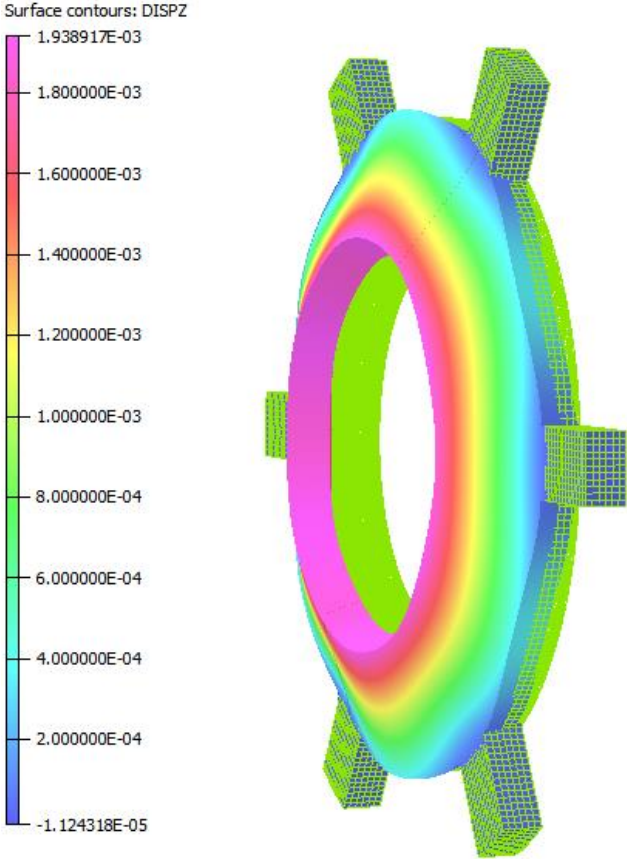
Figure 5. 10. Finite element predicted deflection of the stator core (scale shown is in mm)

5.4.2 Rotor deflection

Unlike the stator, where the net axial direction force is largely balanced by the presence of a pair of rotors producing nominally equal and opposite forces, the individual rotor sections experience a large and continuous attractive force even in the fully assembled machine. To compound the problems of rotor deflection, the rotor core is much thinner than the stator core, often by factor of at least two since it only carries the flux associated with one set of magnet poles. Furthermore, the rotor cores are fixed at their inner edge (where the interface with the shaft) unlike the stator core which is fixed at its outer edge. This is also likely to results in much larger deflections.

Circular plate theory can also be applied to calculate rotor core deflection. For the rotor core, the stress, q is again assumed to be acting on the entire magnet pitch. The inner radius of the rotor r_r is supported by rotor shaft, and in this case the maximum deflection occurs at the outer radius of the rotor. Figure 5. 11 shows a schematic of rotor core deflection under stress q, and two different possible support arrangements for the rotor.

The stiff rotor support, which is equivalent to a fixed cylindrical bore at inner radius interfacing with a circular shaft, provides the best case support for minimising rotor deflection. In contrast, a point rotor support represents the worst case for the rotor deflection with only one edge at the rotor inner radius being fixed with the other edge free to move. In the case of the prototype machine designed in this thesis, the actual core and shaft arrangement is more likely to be representative a stiff shaft support. However, additional calculations of deflection using a point support model provides a pessimistic upper bound on the deflection.

(a). Stiff support   (b). Point support
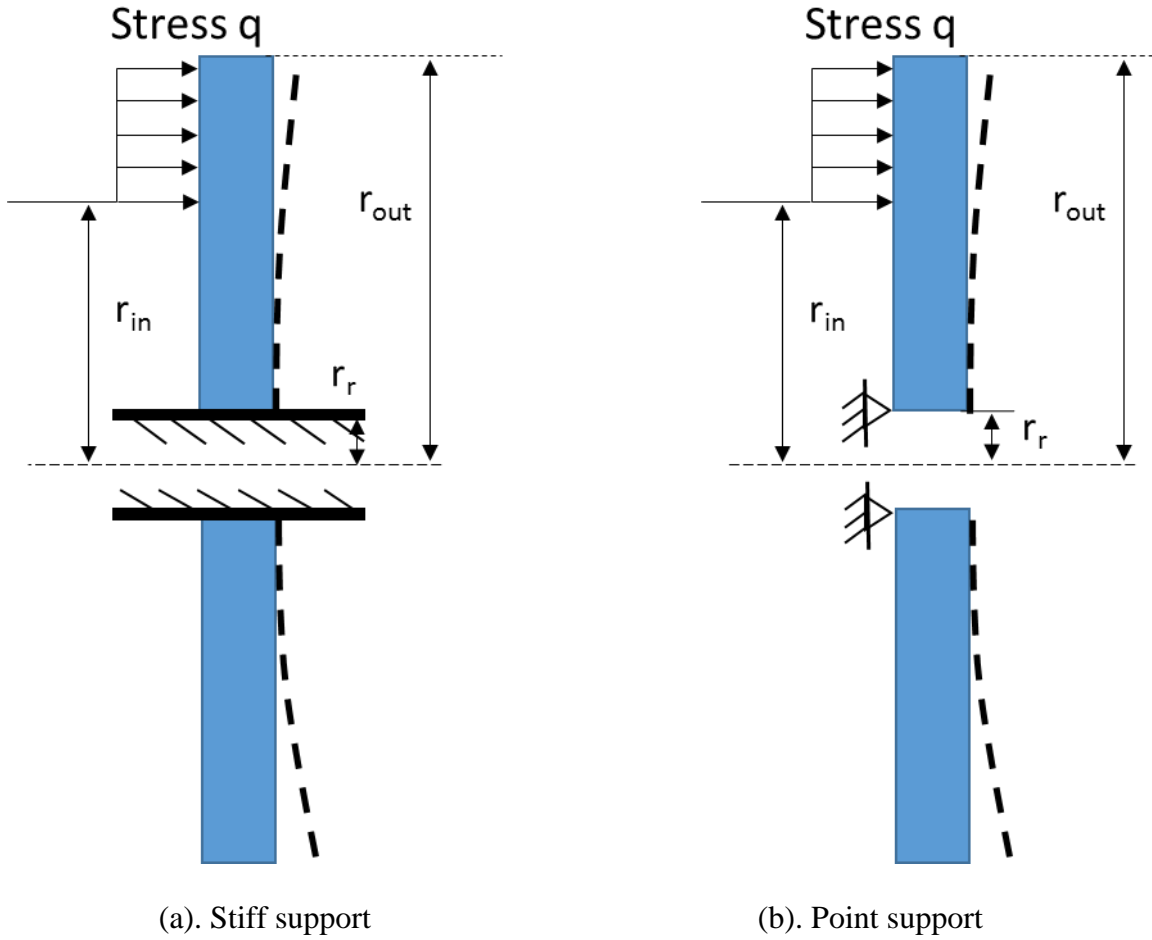
Figure 5. 11. Two possible rotor core support models

The maximum rotor deflection for a stiff support is given by:

$$y_r = M_r \frac{r_{out}^2}{D} C_2 + Q \frac{r_{out}^3}{D} C_3 - q \frac{r_{out}^4}{D} L_{11} \tag{5.15}$$

Where Mr is the unit radial bending moment of the shaft and is described by

$$M_r = \frac{-q r_{out}^2}{C_8} \left[\frac{C_9}{2 r_{out} r_r} (r_{out}^2 - r_{in}^2) - L_{17} \right] \tag{5.16}$$

And the unit shear force Q_f is

$$Q_f = \frac{q}{2 r_r} (r_{out}^2 - r_{in}^2) \tag{5.17}$$

The constants C₂, C₃, C₈, C₉, L₁₁ and L₁₇ are given by

$$C_2 = \frac{1}{4}\left[1 - \left(\frac{r_s}{r_{out}}\right)^2\left(1 + 2\ln\left(\frac{r_{out}}{r_s}\right)\right)\right] \tag{5.18}$$

$$C_3 = \frac{r_s}{4r_{out}}\left\{\left[\left(\frac{r_s}{r_{out}}\right)^2 + 1\right]\ln\left(\frac{r_{out}}{r_s}\right) + \left(\frac{r_s}{r_{out}}\right)^2 - 1\right\} \tag{5.19}$$

$$C_8 = \frac{1}{2}\left[1 + v + (1-v)\left(\frac{r_s}{r_{out}}\right)\right] \tag{5.20}$$

$$C_9 = \left(\frac{r_s}{r_{out}}\right)\left\{\frac{1+v}{2}\ln\left(\frac{r_{out}}{r_s}\right) + \frac{1-v}{4}\left[1 - \left(\frac{r_s}{r_{out}}\right)^2\right]\right\} \tag{5.21}$$

$$L_{11} = \frac{1}{64}\left\{1 + 4\left(\frac{r_{in}}{r_{out}}\right)^2 - 5\left(\frac{r_{in}}{r_{out}}\right)^4\right.$$
$$\left. - 4\left(\frac{r_{in}}{r_{out}}\right)^2\left[2 + \left(\frac{r_{in}}{r_{out}}\right)^2\right]\ln\left(\frac{r_{out}}{r_{in}}\right)\right\} \tag{5.22}$$

$$L_{17} = \frac{1}{4}\left\{1 - \frac{1-v}{4}\left[1 - \left(\frac{r_{in}}{r_{out}}\right)^4\right] - \left(\frac{r_{in}}{r_{out}}\right)^2\left[1 + (1+v)\ln\left(\frac{r_{out}}{r_{in}}\right)\right]\right\} \tag{5.23}$$

The resultant deflections for the two different shaft supports were calculated using the analytical equations. In each case, the variation in deflection across the rotor core was calculated. As the thickness of the rotor core increases, the difference in calculated deflection between the two support methods decreases. It can be seen from Figure 5. 12 that the maximum deflection with the point support model for a rotor back iron thickness of 2mm is calculated to be 0.9mm which would take up the full mechanical clearance. While the actual shaft support would be much firmer than the point support, so the maximum deflection should be closer to the value predicted by the stiff support for this 2mm thick rotor core, i.e. 0.356mm.
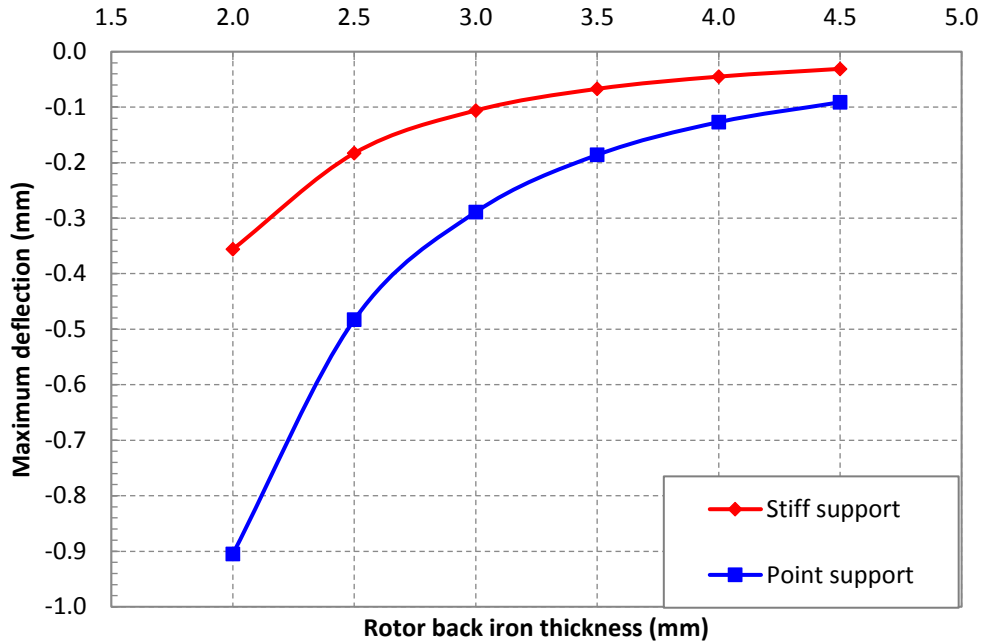
Figure 5. 12. Deflection calculated via an analytical method for two different support condition for varying rotor back iron length

The OPERA 3D finite element stress solver was used to predict the deflection for the rotor elements for both a fixed inner face and for a fixed edge, these two constraints in effect replicating the stiff and point supports used in the analytical model. The resulting rotor maximum deflections calculated for a series of rotor core thicknesses for the fixed face shaft interface model are shown in Figure 5. 13 along with the corresponding values calculated analytically. The deflections predicted with analytical equations shows good agreement with the corresponding finite element predicted values, with improved agreement as the rotor back iron thickness increases. The finite element model was also used to predict rotor deflection with the point support, despite the fact that this will be an overly pessimistic assumption for the prototype machine. The resulting deflections are shown in Figure 5. 14 which also exhibit good agreement between the finite element and analytical approaches.

As will be apparent from Figure 5. 13 even with the best case model for the constraint on displacement at the interface with the shaft, the deflections of the rotor cores are significant in relation to the mechanical clearance. This may result in the thickness of the rotor core being sized on the basis of mechanical rather than

electromagnetic considerations. On the basis of the deflections predicted, a rotor back iron thickness of 4mm or so, which would result in a deflection of ~0.05mm would seem like a reasonable trade-off between deflection for a 1mm mechanical clearance and rotor mass.
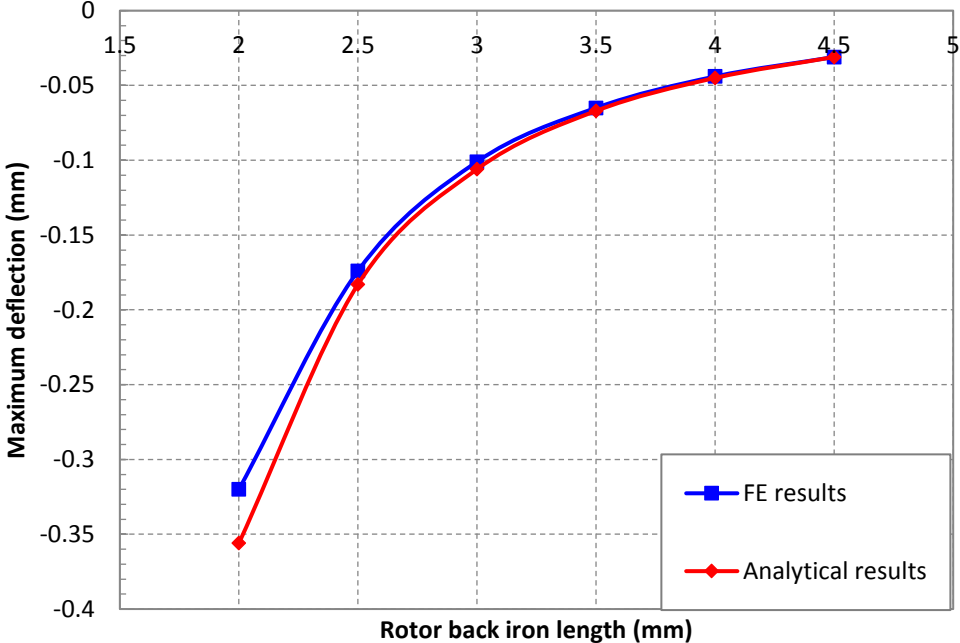
Figure 5. 13. Comparison of finite element predicted and analytically calculated maximum rotor deflection with fixed inner face
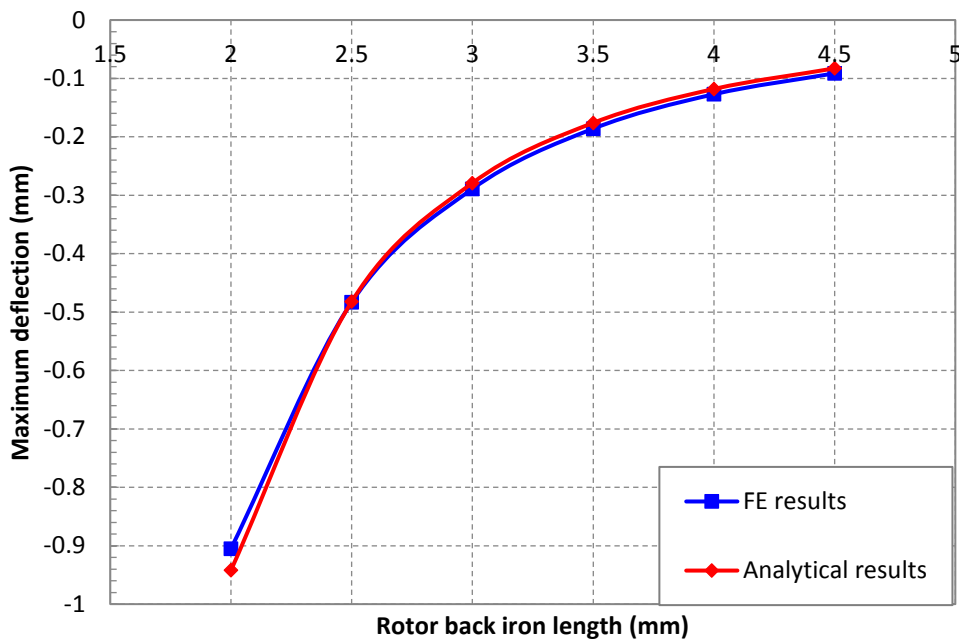
Figure 5. 14. Comparison of finite element predicted and analytically calculated maximum rotor deflection with fixed inner edge

5.4.3   Deflection for various rotor back iron geometries

The previous modelling of rotor deflection was based on the assumption of the rotor back iron being a plain circular ring. However, as discussed in chapter 4 the preferred rotor design following optimisation is not a plain ring. As shown previously in section 4.2.2, rotor back iron, which was shown previously in Figure 4. 10, has a varying thickness in order to reduce mass. In the absence of analytical equations for this specific rotor geometry, finite element stress analysis of the preferred rotor was performed.

Alongside the rotor back iron geometry of Figure 4. 10, several alternative back iron geometries which attempt to achieve the same purpose, i.e. to reduce the rotor back iron thickness at the centre of the pole, were analysed in terms of their deflections. A series of Finite element stress calculation were performed on all of the proposed geometries to identify the optimum rotor geometry from both mechanical point of view and electromagnetic point of view.

Schematics of the various rotor geometries considered are shown in Figure 5. 15. These show the rear face of the rotor core (i.e. not the face onto which the magnets are attached) with the details of the feature highlighted. The various features of the rotor designs are as follows:

- **Rotor geometry 1**: This is the optimized design 7 rotor geometry for the weight reduction established in section 4.2.2. For practical considerations, the section close to the inner radius is flat in order to allow clamping the rotor into position.

- **Rotor geometry 2**: This is based on rotor geometry 1, but with extra circular ribs at the mean radius and at the outer radius to provide extra mechanical stiffness for the rotor core. However, these ribs will inevitably introduce additional mass.

- **Rotor geometry 3**: This rotor design takes a different approach to reducing mass by taking our a series or rectangular 'pockets' which in effect leaves a series of full thickness ribs between adjacent rectangular pockets to increase the overall mechanical stiffness of the rotor core. These rectangular pockets are not uniform in depth. At the centre of the magnet pole, the pockets are 2.5mm deep while at the edge of the magnet pole, the corresponding rotor back iron is cut away with relatively shallow rectangular pockets which are only 0.5mm deep.

- **Rotor geometry 4**: This rotor design is based on rotor geometry 3 but with the addition of eight equispaced ribs along radial direction. These are located under the edges of each magnet pole and taper down in height from 6mm at the shaft to 0.1mm at the outer edge
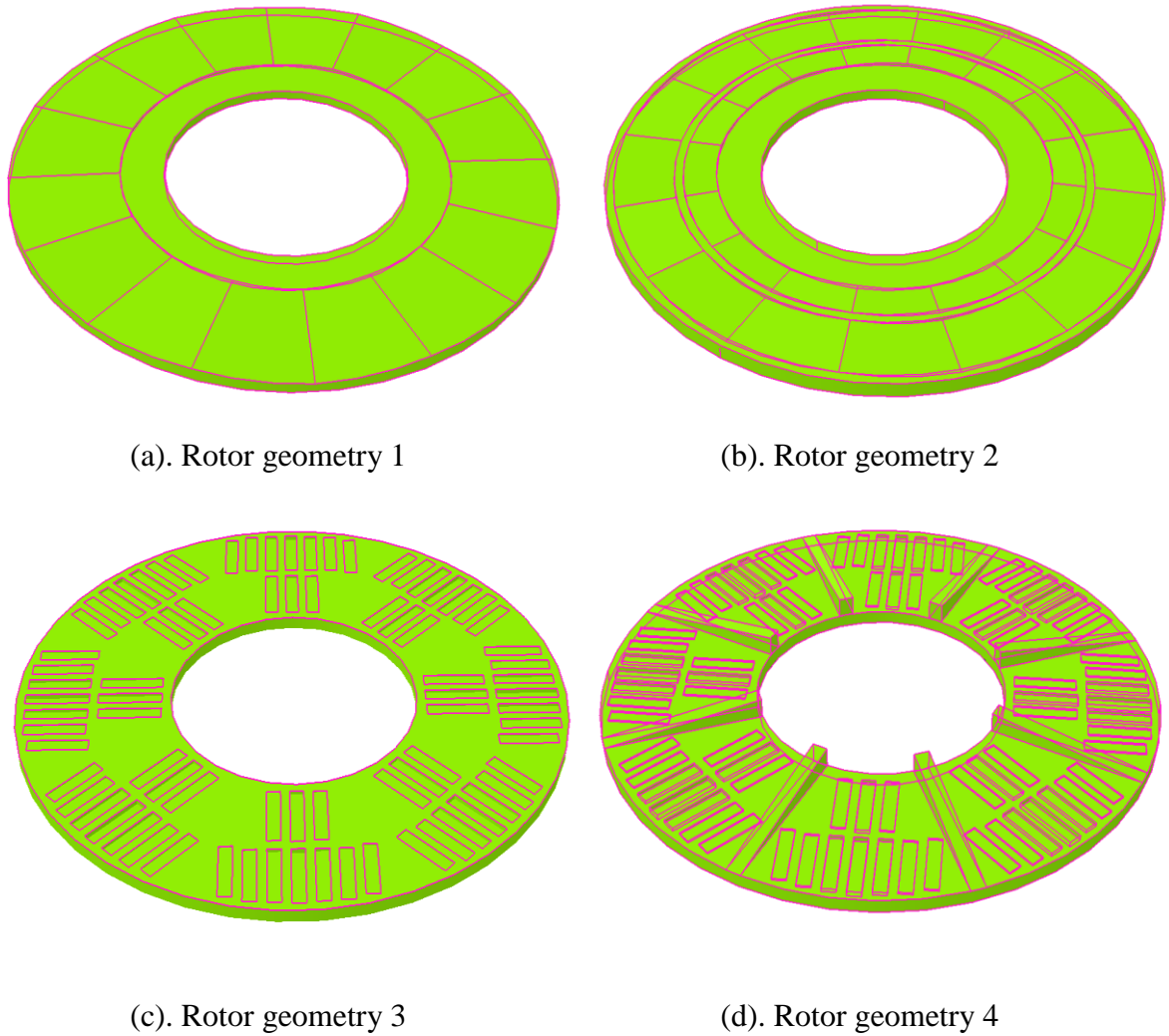
(a). Rotor geometry 1   (b). Rotor geometry 2

(c). Rotor geometry 3   (d). Rotor geometry 4

Figure 5. 15. Proposed rotor back iron geometry for deflection analysis

The resultant deflection for each rotor geometry was calculated using the OPERA 3D stress solver. The axial load applied to the rotor was 1180N (corresponds to a uniform stress of 0.06MPa), this being the finite element calculated axial force on each rotor core under rated electromagnetic conditions. Both stiff and point supports defined in section 5.4.2 were considered. A close up of predicted deflection for rotor geometry 1 near the rotor inner radius with both shaft supports (shaft not shown in the model) are shown in Figure 5. 16. At the inner edge of the rotor at the interface with the shaft, the stiff support shows that the inner bore remains firmly in contact with the shaft with virtually zero deflection at the inner radius. In the case of the point support, since only the inner edge is fixed, the other edge is free to move, hence the deflection exits even at the inner radius of the rotor plate. It is apparent that from the rotor deflection shape shown in Figure 5. 16 (b), the point support is undesirable for the prototype machine.
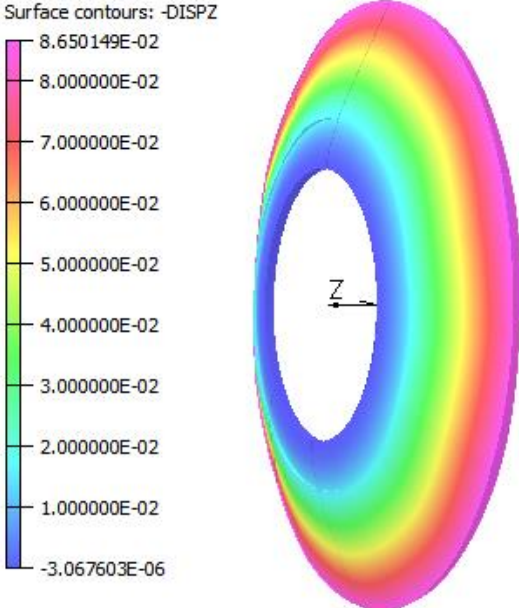
The coloured contour maps of rotor maximum deflection for each rotor geometry with a stiff support at the shaft interface are shown in Table 5. 1. The maximum deflection under both types of support and the mass of the rotor for each rotor geometry are also listed in Table 5. 1. The deflection of rotor geometry 1 is the highest, while rotor geometry 4 shows the lowest rotor deflection. However, this 5% decrease in deflection is achieved at the expense of a 14% increase in mass.

(a). Stiff support   (b). Point support
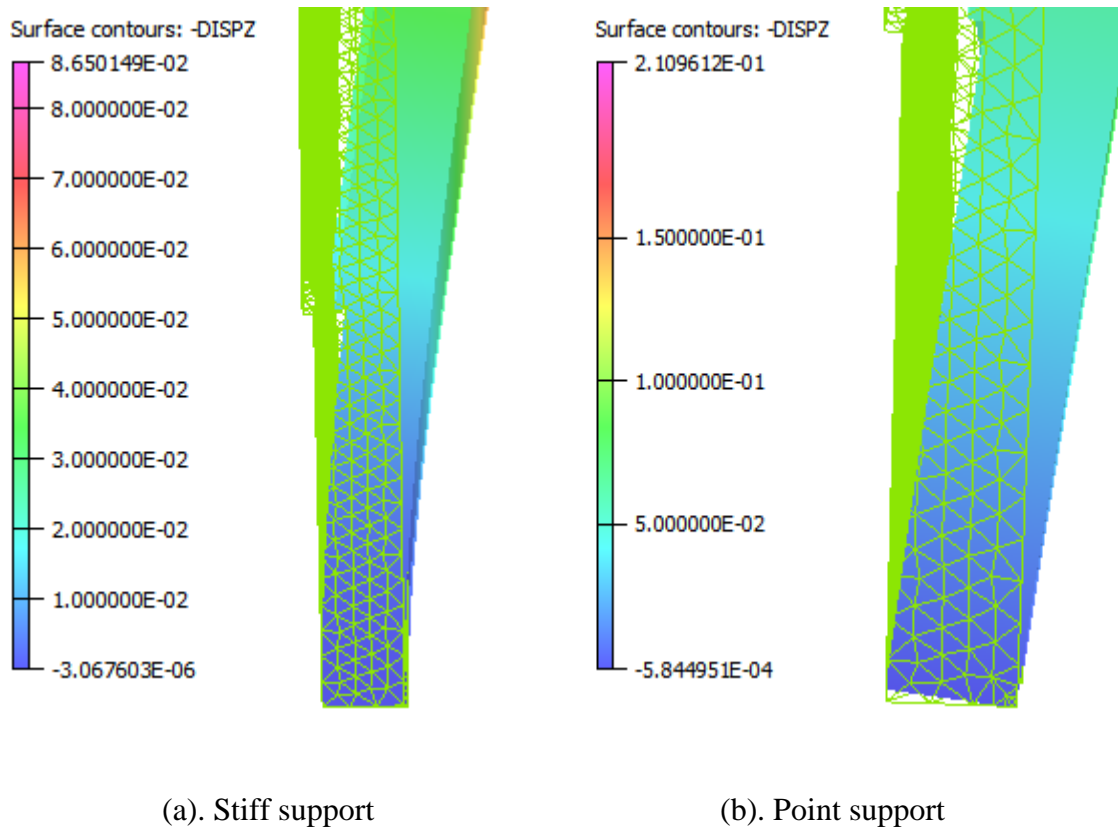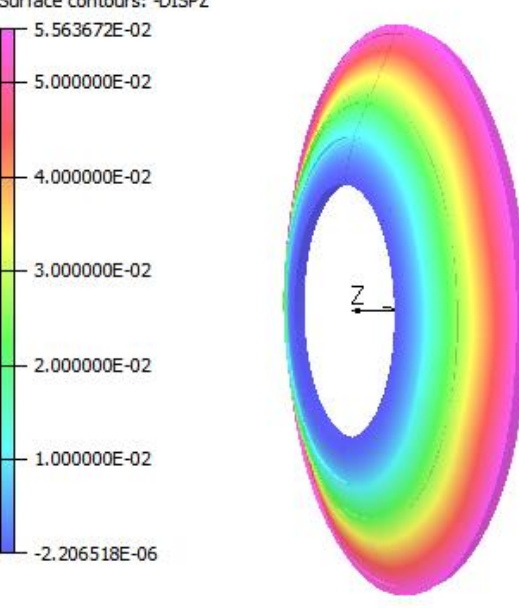
Figure 5. 16. Rotor deflection with two different support method for rotor geometry 1

Table 5. 1. Summary of the rotor deflection analysis for different rotor geometries

Rotor geometry 1
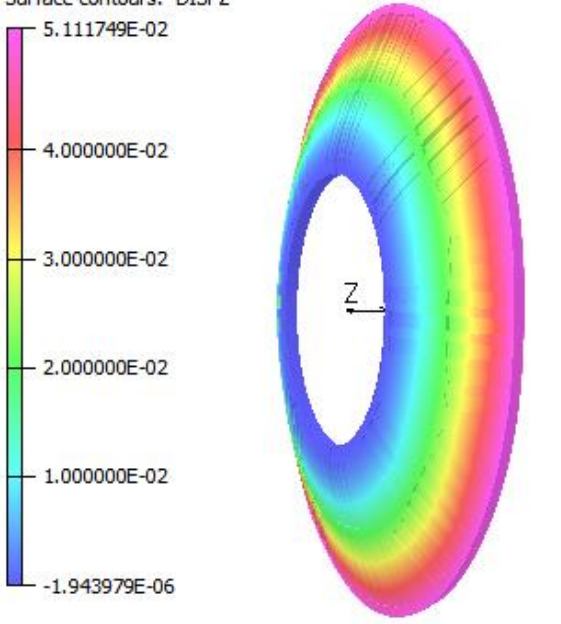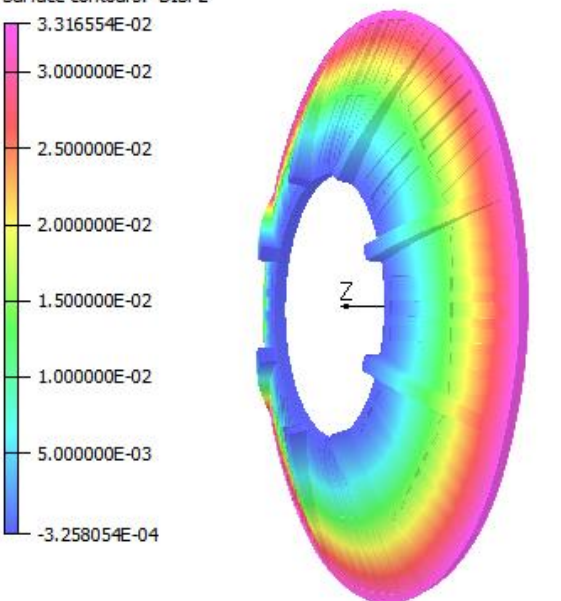
Surface contours: -DISPZ	Maximum deflection with stiff support (mm)	0.086
	Maximum deflection with point support (mm)	0.21
	Weight (Kg)	1.27
Rotor geometry 2		
Surface contours: -DISPZ	Maximum deflection with stiff support (mm)	0.056
	Maximum deflection with point support (mm)	0.16
	Weight (Kg)	1.47
Rotor geometry 3		
	Maximum deflection with stiff support (mm)	0.051

	Maximum deflection with point support (mm)	0.17
	Weight (Kg)	1.37
Rotor geometry 4		
	Maximum deflection with stiff support (mm)	0.033
	Maximum deflection with point support (mm)	0.16
	Weight (Kg)	1.47

As would be expected, the colour contours show that the deflection increases with increasing distance from the shaft. The deflections shown in Table 5. 1 are for the case of a single rotor core only subjected to the pre-calculated electromagnetic force. In practice, the magnets attached to each core and these will impact to some degree of the overall deflection, although being separate pieces which are attached with adhesive, their influence is far from straightforward.

The four rotor geometries are modelled together the magnet pieces, Figure 5. 17 shows the maximum deflection of the back iron of rotor geometry 1 with stiff shaft support under axial rated direction attractive stress. It can be seen that with permanent magnets mounted on the rotor core, the maximum deflection of the rotor plate is reduced by 49% under same load force. Although this calculation involves some simplifications, viz. the stress applied to the rotor core is a uniform equivalent stress while the actual shaft support may not be as stiff in practice as that modelled. This model, nevertheless, provides a good representation of the deflection that will be achieved in practice. In this case, the 0.042mm maximum deflection of the rotor core with rotor geometry 1 is less than 5% of the overall airgap.
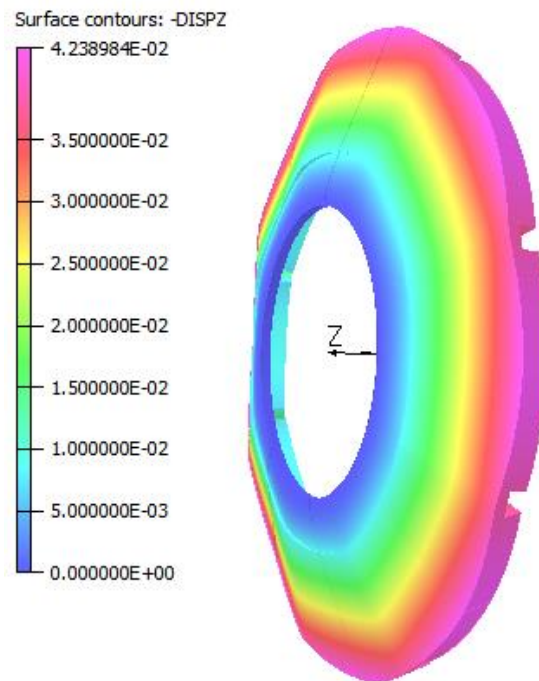
Figure 5. 17. FE predicted deflection for rotor geometry 1 with magnet

The finite element predicted deflections with different support condition for all four rotor geometries proposed are summarised in Table 5. 2 along with their corresponding mass. The deflections predicted on the assumption of the stiff support are likely to provide the more realistic prediction of the deflection. In all the cases considered, the inclusion of the permanent magnet mounted on the rotor into the models reduce the deflection compared to the models of the core alone.

As will be apparent, when the effect of the rotor magnets are included, rotor geometry 4 exhibits the smallest deflection, but this is only marginally better than a plain ring

(which is slightly lighter). All the predicted deflection values with an assumed stiff support are below 0.05mm, i.e. below 5% of the mechanical clearance. Even with the very pessimistic assumption of a point support, where is largest deflection is only 0.106mm which is ~10% of the mechanical clearance. It is worth noting that although the performance in terms of rotor core deflection can be improved significantly with the various design features, e.g. rotor geometry 4 has almost half the deflection of rotor geometry 1, this is achieved at the expense of additional mass. Given that rotor geometry 1 has a deflection which is well within the limits that can be managed in practice with a 1mm mechanical clearance, this was kept as the preferred design because of its lower mass.

Table 5. 2. Summary of finite element predicted rotor core deflections at rated stator current

Rotor plate geometry	Maximum deflection (rotor core only) (mm)		Maximum deflection (rotor core with magnet) (mm)		Rotor core mass (Kg)
	Point support	Stiff support	Point support	Stiff support	
Plain ring	0.127	0.045	0.068	0.025	1.46
Rotor geometry 1	0.211	0.087	0.106	0.042	1.27
Rotor geometry 2	0.159	0.056	0.105	0.034	1.47
Rotor geometry 3	0.165	0.051	0.099	0.031	1.37
Rotor geometry 4	0.161	0.033	0.077	0.023	1.47

5.5 **Finalised demonstrator manufacturing design**

Having analysed various aspects of mechanical performance using finite element analysis, the layout of the prototype machine and the dimensions of the mechanical support structure for the stator and rotor elements, e.g. rotor hub, casing, shaft and were designed in SOLIDWORKS for construction of the prototype. The mechanical design of the machine components and the assembly is described in this section.

5.5.1 Stator

The stator core, as mentioned previously, was assumed to be a plain ring shaped iron core for electromagnetic analysis. For the prototype, rectangular projections were added to the outer edge of the stator core to securely locate it in the casing. In order to locate the 12 coils, a total of 12 projections were added, but only 6 of these are used to attach the core to the casing, the remaining 6 being shortened to reduce the mass of the core. The final design of the stator core is shown in Figure 5. 18.
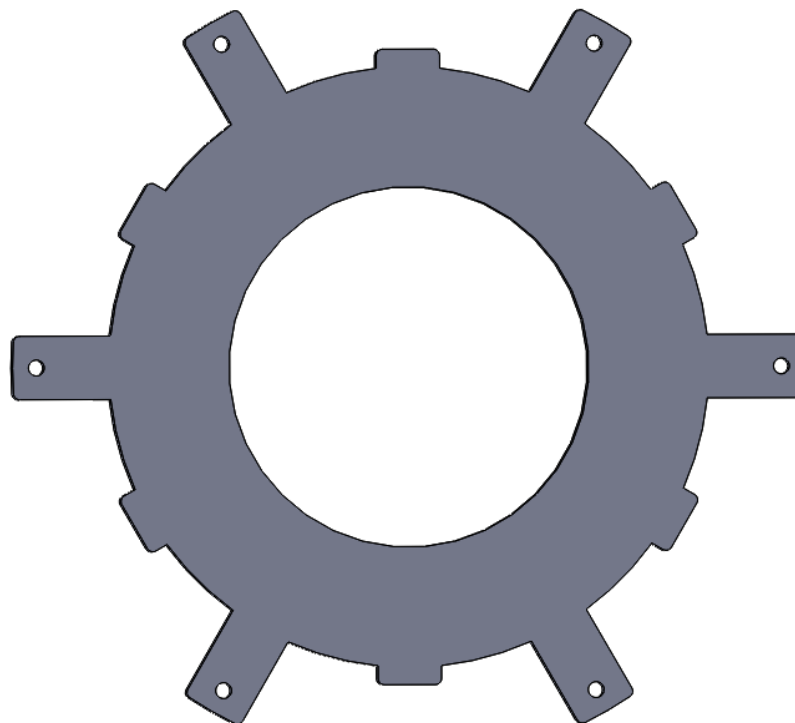
Figure 5. 18. Stator core

To precisely and securely fit the coils to the stator core, a machined insulation cover was designed. This provides an additional layer of protection, provides precise slots to locate the individual coils and assists in transmitting the torque from the coils. Figure 5. 19(a) shows the stator core together with the insulation layer. The projections on the core fit locate the insulating cover as shown. The insulation cover is shaped to provide rectangular slots for the coils. The insulation thickness between the bottom of the coil slot and the core was set to 1mm. Figure 5. 19**Error! Reference source not found.**(b) shows the schematic of the stator with insulation and the coils. This insulation cover

will be machined from a solid block for the demonstrator, but could be produced by additive manufacturing or injection moulding in production.
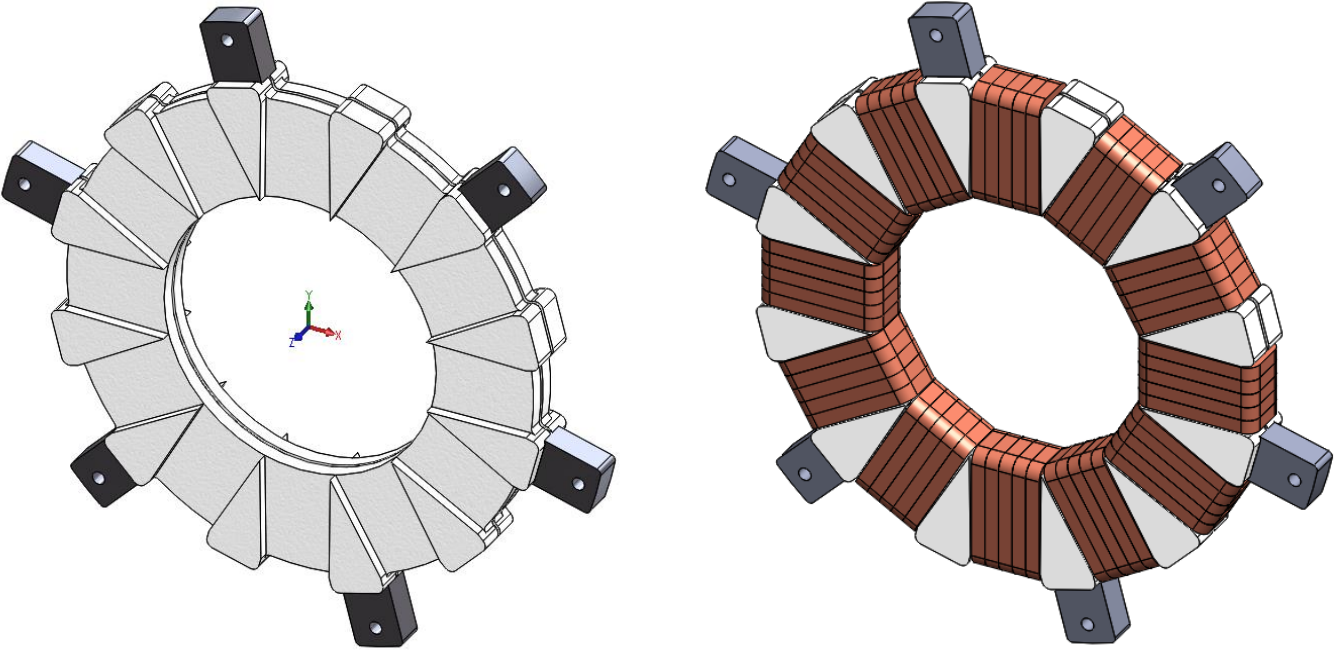
(a). Stator with insulation layer   (b). Stator with insulation cover and the coils

Figure 5. 19. Stator design (a). with insulation cover (b). with insulation cover and stator coil

5.5.2   Rotor

The rotor geometry is formed by two ring shaped cores and one interconnecting cylindrical rotor core. For the ease of manufacture, the rotor was divided into an 'L-shaped' rotor where one rotor core is manufactured as a single part with the cylindrical rotor core. The other rotor element is simply formed by the other rotor core. Flanges at the rotor inner radius are used to locate and fix of the rotor core to the L-shaped sections. The two rotors sections are clamped together by two endplates.

A front view of the front of the "L shaped" rotor together with magnets is shown in Figure 5. 20(a). A back view of the other rotor section is shown in Figure 5. 20(b) in which the wavy pattern back iron can is evident.

168
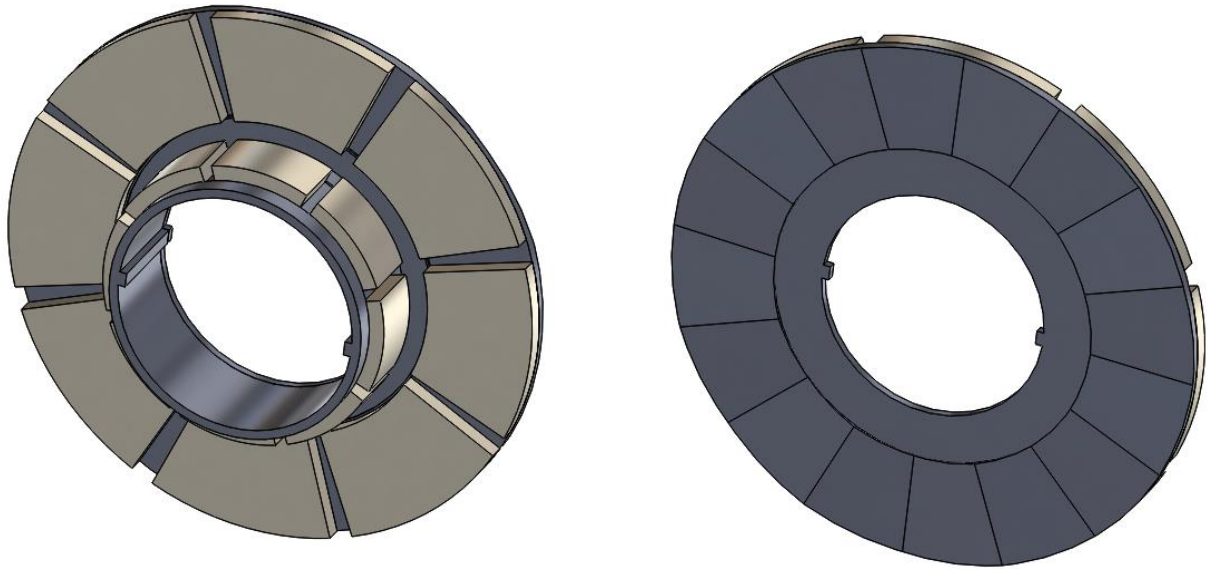
(a). 'L-shape' rotor with magnets attached   (b). Rotor back iron detail

Figure 5. 20. Rotor design (a). 'L-shape' rotor element (b). Other rotor core element

5.5.3   Structural support

A cut away view of the design for the structural support used for the demonstrator machine is shown in Figure 5. 21. The main structural support for the stator is the thin-Aluminium walled casing. A non-structural front face cover was incorporated, although this provides no mechanical function. For the prototype machine, this was manufactured from transparent polycarbonate. For a machine that operates in a harsher temperature environment, this could be replaced with a thin Aluminium sheet. The main structural support for the rotor is the rotor hub, end plate and bearings. The rotor hub is used to fill in the space between the main output shaft and the rotor inner radius and provide a means of connecting the rotor to the shaft. Angular contact bearings were selected for the prototype as the bearing needs to accommodate potential axial direction force due to any imbalanced forces on the rotor. A key feature of the angular contact bearing is an ability to deal with an axial force. Angular contact bearings are usually used in pairs as a single angular contact bearing can only accommodate axial force in one direction. In this machine, two angular bearings are arranged in a back-to-back arrangement to accommodate axial force in both directions. A pre-load is required to ensure the balls in the bearing is in good contact with the bearing race. An aluminium nut was designed to sit at the end of the stationary shaft to provide the required pre-load for the bearings.

169
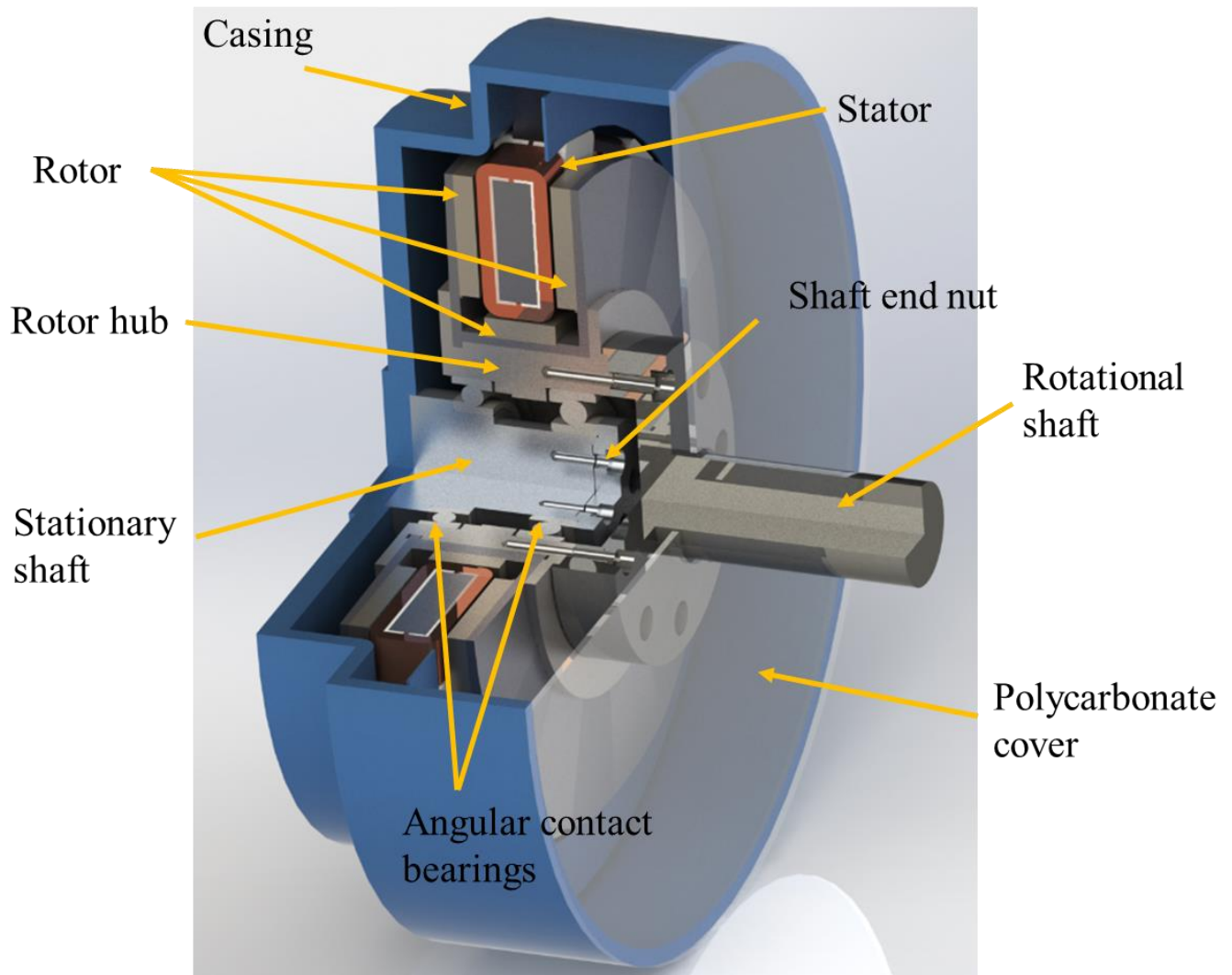
Figure 5. 21. Cut-away view of the prototype machine assembly

Rather than having one shaft that runs through the entire machine, two separate shafts were employed for different purposes. The shorter shaft on the left hand side of Figure 5. 21 is stationary and is equipped with two bearings. The longer rotating shaft on the right hand side of Figure 5. 21 is attached to the rotor cores via the rotor hub. The rotors is connect to the rotor hub with a keyway, while two endplates are bolted on the rotor hub to clamp the two rotor elements into place.

The stator is held inside the casing with a series of bolts on the back of the casing. An exploded view of the machine components is shown in Figure 5. 22. The main elements in the machine are numbered, which cross-reference to the part number and

its material or model number listed in Table 5. 3. Assembly is achieved by successively stacking the components starting with the attachment of the stationary shaft to the machine casing. The assembly detail will be further explained in chapter 6 which deals with the construction of the demonstrator machine.
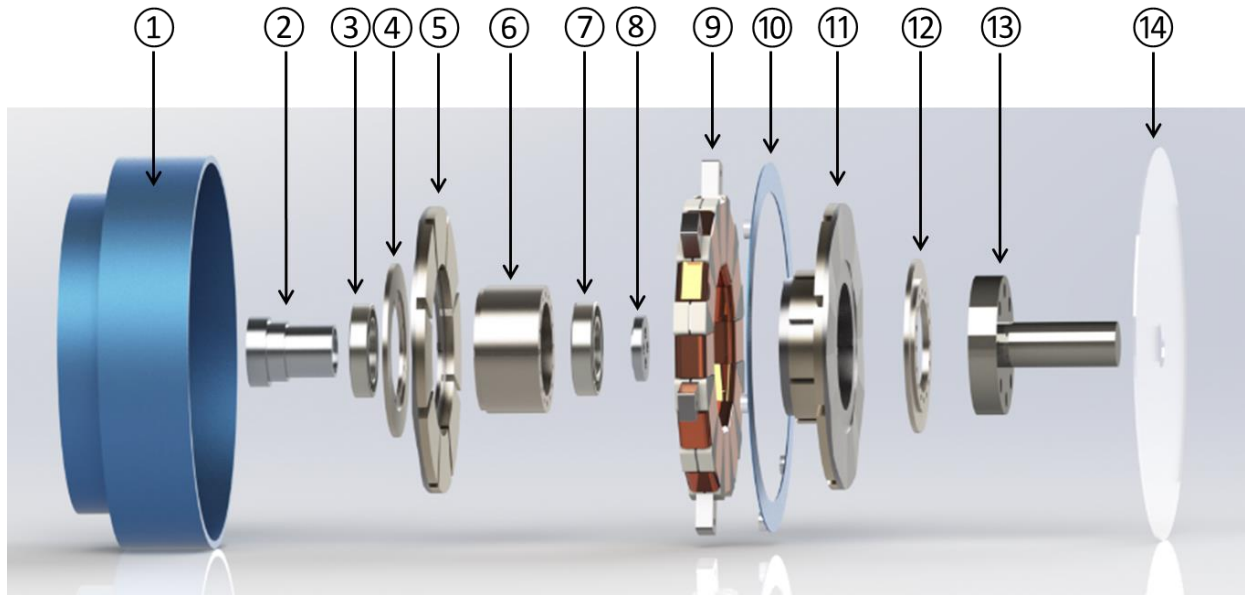
Figure 5. 22. Exploded view of designed prototype machine components

Table 5. 3. Summary of machine components

Part Number	Part	Material
①	Outer casing	Anodised aluminium
②	Stationary shaft	Aluminium
③	Angular contact bearing 1	71908 series with 40 bore, 62 OD &12mm thick
④	Hub endplate-non drive end	Titanium
⑤	Rotor endplate	Cobalt iron

⑥	Rotor hub	Titanium
⑦	Angular contact bearing 2	7007 series with 35 bore, 62 OD &14mm thick
⑧	Shaft end nut	Aluminium
⑨	Stator core and coil	Cobalt iron & copper & PEEK insulation
⑩	Cover for inter-connection wires	Anodised aluminium
⑪	Rotor-L shaped	Cobalt iron & samarium cobalt
⑫	Hub endplate-drive end	Titanium
⑬	Shaft	Aluminium
⑭	Top cover of the machine	Polycarbonate

CHAPTER 6.   CONSTRUCTION OF DEMONSTRATOR MACHINE

6.1 Introduction

The construction process of the demonstrator machine is detailed in this chapter. The demonstrator machine was manufactured in accordance with the electromagnetic optimisation of Chapter 4 and the mechanical design of Chapter 5. A full set of engineering drawings is contained in Appendix II.

The construction of the stator core, stator winding, rotor core, and rotor magnet bonding process is described in this chapter along with the assembly process for this unusual topology.

6.2 Stator and rotor core construction

The stator and rotor core were manufactured from a solid cobalt iron billet provided by Vacuumschmelze. The as-supplied of non heat-treated VACOFLUX 50, which the dimension of 50mm×260mm×530mm, is shown in Figure 6. 1. The cobalt iron was supplied without prior heat-treatment as this makes the alloy brittle and difficult to machine by any mechanical process. Having machine the components, these were returned to Vacuumschmelze for final heat treatment to realise the full magnetic properties.

The cobalt iron block was firstly split into three blocks (shown in Figure 6. 2) followed by surface grinding. The billet was split from the centre. One of the resulting blocks was used for the L-shaped rotor section, while the other resulting blocks was further split into two blocks to manufacture of the stator and the flat rotor core.
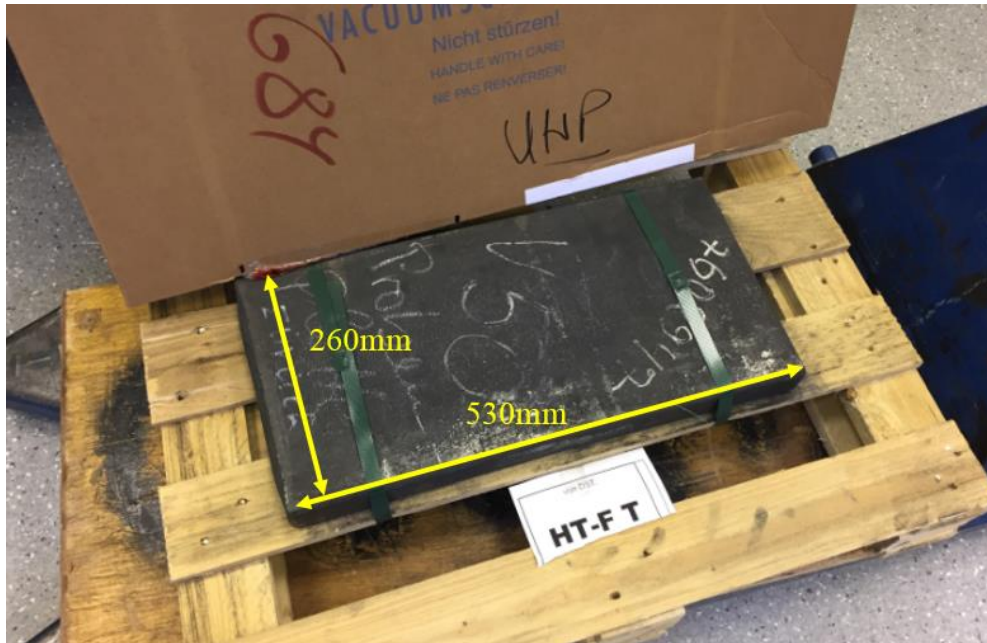
Figure 6. 1. As-supplied solid cobalt iron material billet
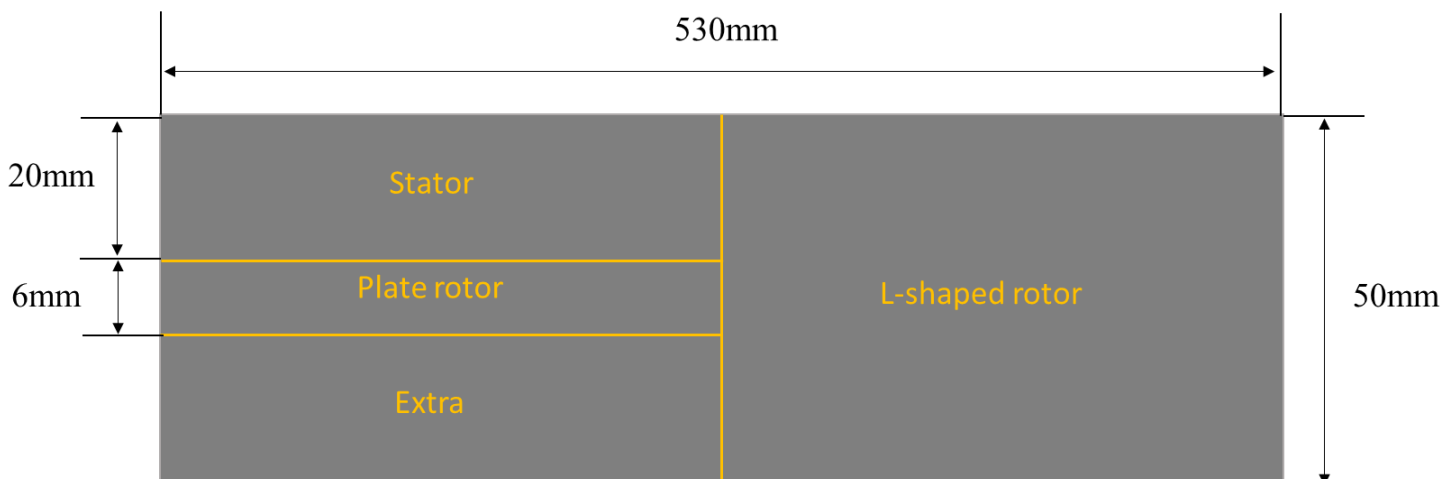
Figure 6. 2. Cobalt iron split into three blocks for the stator and rotor core manufacture

The stator profile was manufactured by a wire electric-discharge machining (wire-cut EDM machine) and then returned to Vacuumschmelze for heat treatment. The stator core following heat-treatment anneal is shown in **Error! Reference source not found.**.
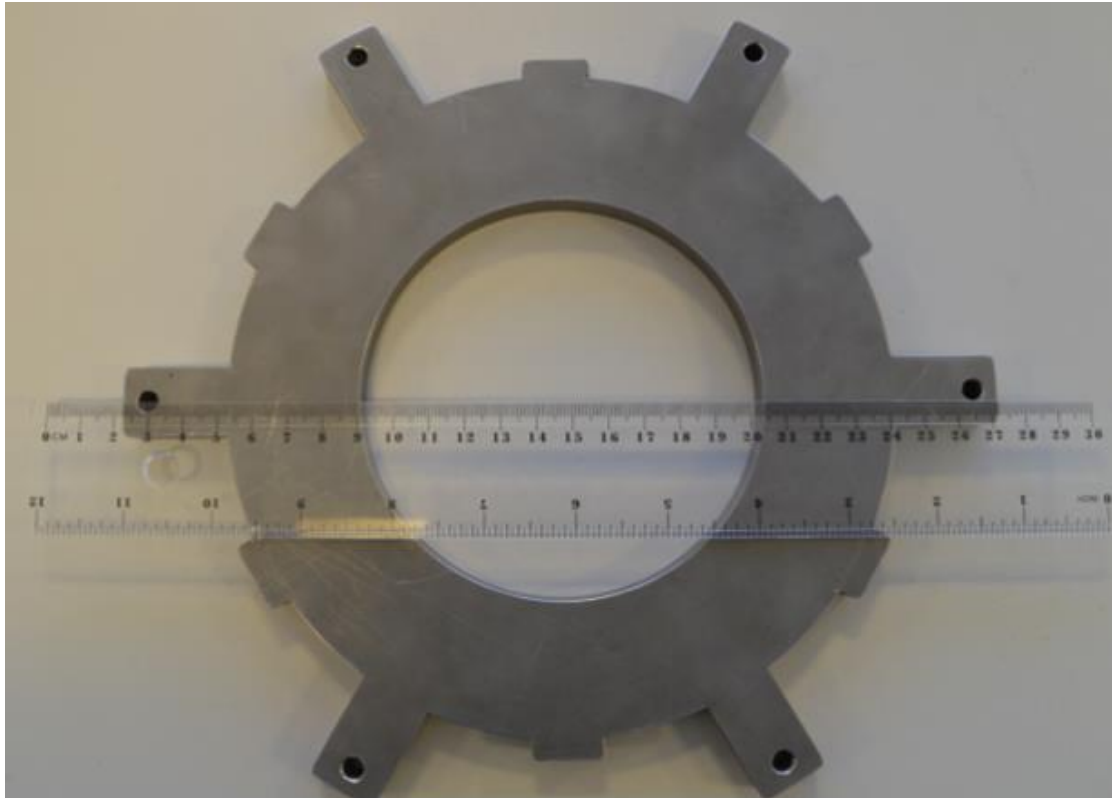
Figure 6. 3. Manufactured stator core after anneal

Compared to the manufacture of the stator core, the rotor core has a much more demanding, in particular the waved pattern on the rotor core back. The back surface of each rotor core required 3D profile milling and hence for the manufacture of the rotor, a combination of wire EDM and CNC profile milling was used. The wire-cut EDM was used for machining the outer and inner edge of the rotor (including keyways), and 3D profile milling was used to machine the waved pattern on the rotor back iron. The L-shaped rotors and flat plate rotor following wire EDM machining is shown in Figure 6. 4, while Figure 6. 5 shows one rotor back face after CNC milling. In order to connect the rotor with the rotor hub, two flanges at the inner edge were added using turning which also used to incorporate a step on the rotor face to aid the positioning of the permanent magnets. Following all the machining stages, the rotor components were returned to Vacuumschmelze for final heat-treatment.

(a). L-shape rotor after wire EDM
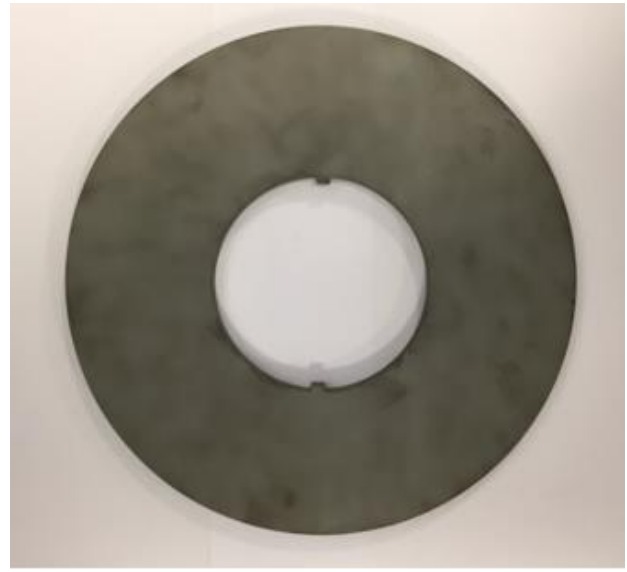
(b). Plate rotor after wire EDM

Figure 6. 4. Rotor core after wire EDM and before 3D milling
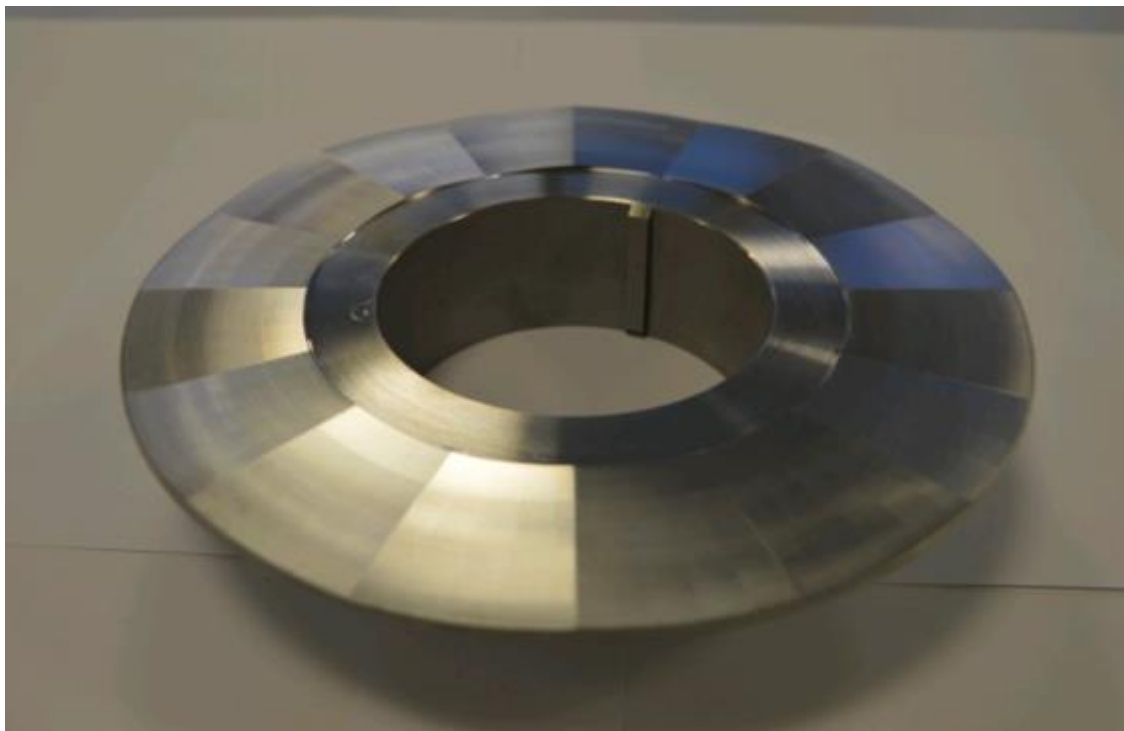
(a). 'L-shape' rotor – back view

Allow the positioning of the permanent magnet
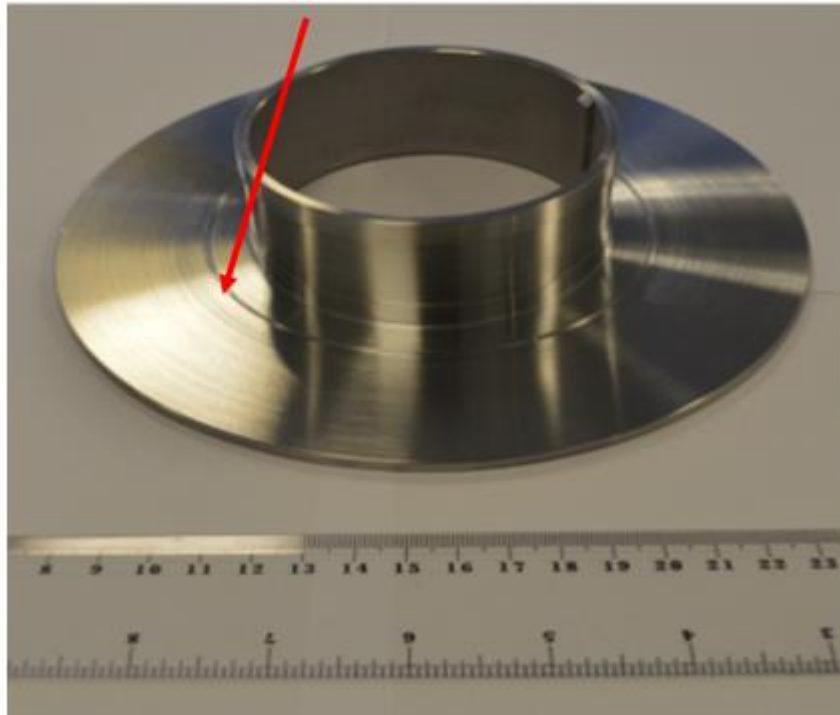
(b). 'L-shape' rotor – front view
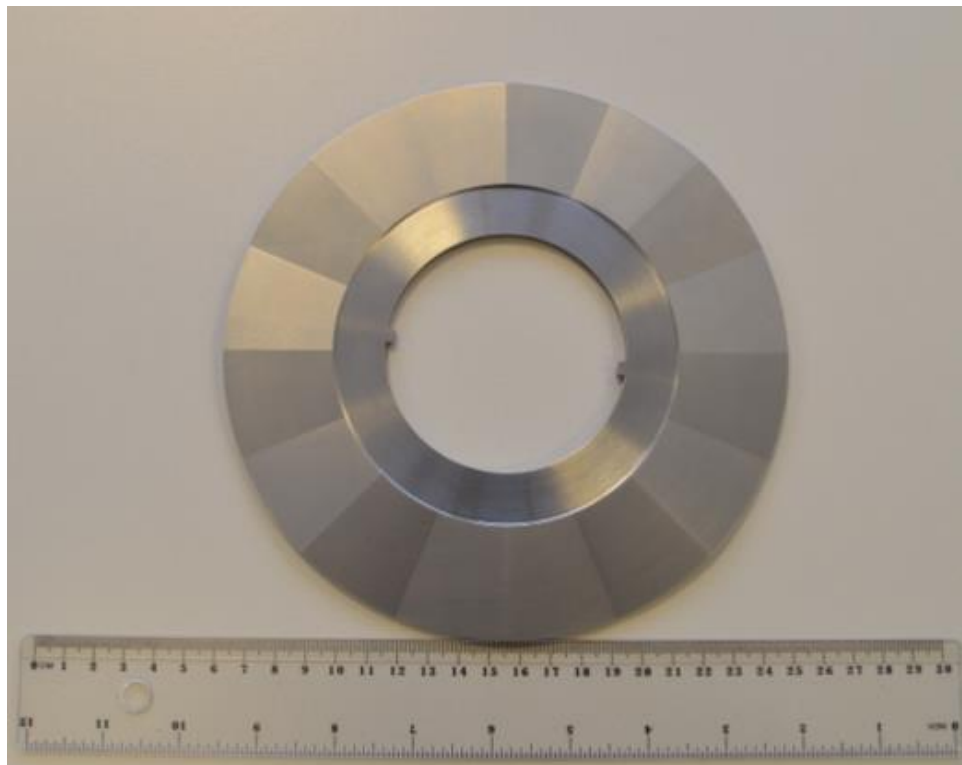
(c). Plate rotor – back view

Figure 6. 5. 'L-shape' rotor and plate rotor cores after 3D milling

6.3 Stator construction

6.3.1 Stator insulation

The winding employed in the demonstrator machine is an airgap winding, with copper wire being toroidally wound in-situ onto the stator core. To avoid the edges of the core damaging the enamel of the copper, it is usual in all types of machine to include some secondary insulation between the stator core and the coils. This is often simply a so-called slot liner in conventional radial field machines. The use of a simple slot-liner is not so straightforward in this type of machine, and given that the tension required on to coil to retain a well-define coil thickness will directly force the winding into the edges of the core, a more substantial and robust secondary insulating cover was deemed necessary. Moreover, since this is an airgap winding, this structure is required to transmit the torque produced on the coils to the stator casing. An engineering drawing of the insulating cover design, which includes features to aid location on the core, is shown in Appendix II.

The selection of a material for the insulating layer was influenced by the fact that the temperature of the coil could potentially reach up to 200°C. Due to the direct contact between the insulation layer and the copper coil, the insulation layer in the demonstrator machine must be capable of withstanding this temperature. It would also be useful if the material exhibited reasonable thermal conductivity.

Additive layer manufacturing (ALM) was initially considered for the construction of a shaped insulating cover, the properties of several electrical insulators are listed in Table 6. 1. [55][56][57][58] For additive manufacturing, nylon is most commonly used material used. However, the maximum operating temperature of nylon is insufficient for this application. A more suitable insulating material with high temperature capability (high within the context of insulating thermoplastics) is PEEK (Polyether ether ketone). PEEK material was chosen in preference to PTFE due to its higher thermal conductivity and lower coefficient of thermal expansion. Although PBI and PAI materials seems to provide the necessary maximum service temperature and superior thermal conductivity, the price of these materials is much higher(about 10 times in £/mm^3) for the same dimension compared to PEEK material. Hence, PEEK

was selected as the preferred material, even though it is itself a relatively expensive material.

Some variants of PEEK can be used in additive manufacturing. However, there are several difficulties with additive manufacturing in this application:

- The overall size of the insulation layer exceeds the part-size of most of the ALM machines, which would necessitate that the insulation part has to be made up from several individual parts.

- As the insulation layer is fitted between the stator iron and the coil and takes up space that would otherwise be occupied by the coil, there is strong drive to make the wall thickness very thin. However, for the structure to be sufficiently stiff to resist warping during the additive manufacturing, manufacturers recommended a minimum wall thickness of 1.5mm. This would severely compromise the machine performance as it would reduce the cross-section of coil significantly

- Although there are grades of PEEK like material which can be used for additive manufacturing, it is not a widely used material and the cost of producing an insulating cover (even with a 1.5mm wall thickness was very high).

Some trials were undertaken using Polylactic Acid (PLA) which is a common material used for 3D printing. Figure 6. 6 shows the attempt for additive manufacturing a quarter of the insulation part with 0.5mm wall thickness using PLA.. As apparent, even with nylon material, additive manufacturing the insulation part with a thin wall thickness is not possible, the finished part is not able to mechanically support itself.

Table 6. 1. Summary of insulating thermoplastic properties

Insulating material	Electrical insulator	Service temperature (^{0}C)	Thermal conductivity (W/mK)	Coefficient of thermal expansion (μm/m.K)	ALM
Nylon (6 or 12)	✓	80-160	0.24-0.28	80	✓

PEEK 450G	✓	250	0.32	45	✓
PTFE	✓	190-250	0.25	100	?
PAI (Torlon) grade 4301	✓	250	0.53	31	✓
PPS (Rylon) GF 40	✓	200-260	0.25	51	?
PBI (Celazole)	✓	260–400	0.41	25	?

Figure 6. 6. Additive manufactured quarter of insulation component with 0.5mm wall thickness (shown with construction scaffolding in place)

Due to the many limitations of ALM for the proposed part, the components for the demonstrator machine were produced by CNC milling from a rectangular block PEEK material. The insulation part after machining is shown in Figure 6. 7. The insulation part is designed to form a rectangular channel into which the coils are wound to

enhance the mechanical support for coils. Following some machining trials, the wall thickness of the insulation part ended up at 1mm. Although this compromises the coil thickness, it is still thinner than could be achieved with additive manufacturing. Two identical PEEK insulation cover will be assembled on top of two stator faces leaving and the coils are wound directly on the PEEK insulation faces. Prior to fitting the PEEK insulation covers onto the stator core, a layer of thermal grease was pasted on top of the stator core to increase the thermal conductivity at the interface between the core and the cover.
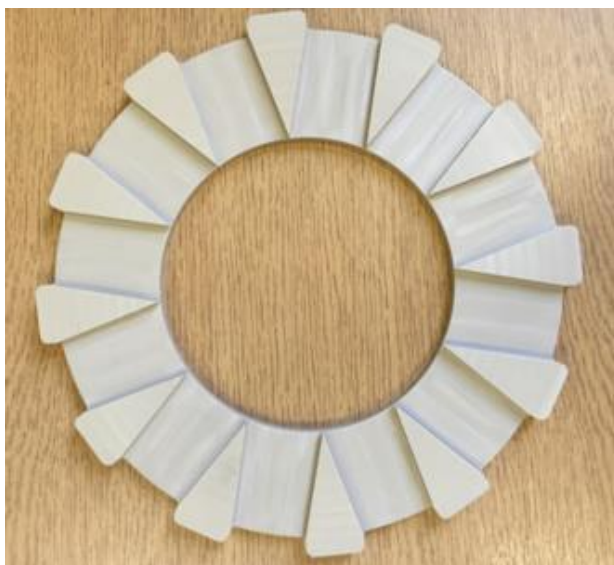
(a). PEEK insulation – Front view   (b). PEEK insulation – Back view
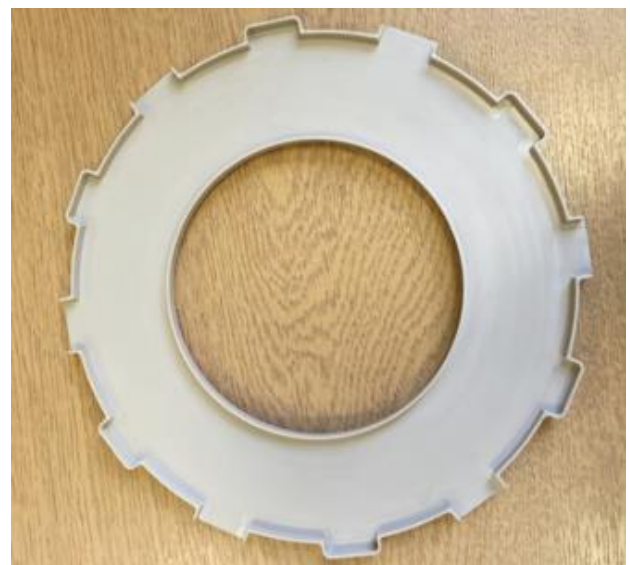
Figure 6. 7. Manufactured PEEK insulation cover (one produced for each side of the stator core)

6.3.2   Stator winding

The stator coils are wound in-situ directly on top of the PEEK insulation. The stator prior winding is shown in Figure 6. 8.

The Number of turns for each coil is determined predominantly from the need to match the voltage of the converter. More specifically, the rated voltage provided by the drive should be higher than the induced back EMF to ensure the machine is capable of operating in motoring mode at the highest maximum speed, with sufficient overhead

to accommodate the coil impedance at rated current. The rated current available from the drive is another limiting factor where the machine current should not exceed the machine rated current. Based on these design principle, individual coils of 200 turns were selected, which resulted in the use of wire with a diameter of 0.6mm. This nominally results in a 5 layer winding with 40 turns in each layer.
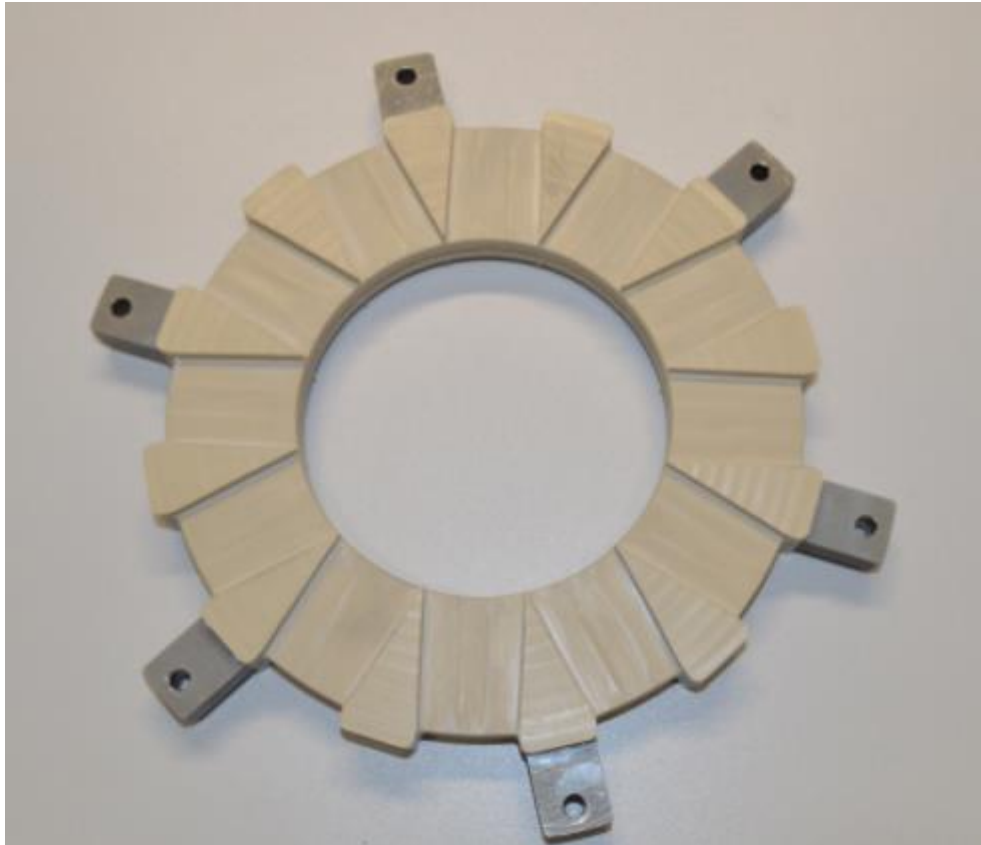
Figure 6. 8. Stator with PEEK insulation

Four thermocouples were embedded at various coil layers and in different phases inn the machine to provide an indication of coil temperature. More specifically, one thermocouple was located in both phase A and phase C, with two located in phase B. Two thermocouples were placed on the bottom layer of coil close to the PEEK insulating cover, and two thermocouples were placed in the centre of the coil between the 2nd and 3rd layers. The exact position of the thermocouples are described in Chapter 7. This arrangement of thermocouples in the coil ensures the coil temperature at different layer is monitored and by having thermocouples at same position in different phase, the temperature measured by the thermocouples has its own reference by comparing with the other phase. Due to the relatively low thermal conductivity of the insulating cover and across the coil cross-section, the copper loss generated in the coils

was anticipated to produce large temperature gradients within the coil region, with the temperature at the bottom layer close to the PEEK insulation likely to be the hottest point in the coil. The temperature measuring bead of the thermocouple was covered by a PTFE sleeve before being embedded in the coils to provide some electrical insulation and prevent damage to the wire insulation layer during the winding process. No adhesive was used to fix the thermocouple, in the expectation that it would be secured by the winding itself. Figure 6. 9 shows the position of one of the thermocouple in the mid-layer of the coil and the manner in which it is fixed in place by the coil itself.

Figure 6. 9. Thermocouple embedded in the coil mid-layer

The stator following completion of the winding is shown in Figure 6. 10 (a). The isolation from each phase to the stator core was tested with by means of a 'Megger test' at a voltage up to 1000V. The resistance of each individual coil were measured by Cropico DO5000 microhmmeter and compared with the estimated values. The calculated phase resistance was 5.18Ω, while the measured resistance for phase A, B

and C was 5.70Ω. The discrepancy between the measured and calculated results may result from:

- The connection wire connecting the coils in each phase of the demonstrator machine is not accounted for in the resistance calculation

- During the resistance calculation, average length of the coil in the mid-layer is used to represent the length/turn for the actual coil, with thermocouple embedded, longer wire length may be used for each turn

Once the insulation and balance of the three phase coils was checked, the coils were varnished with high temperature low viscosity epoxy (Durapot 862). The varnish of the coils serves two purpose in this case.

- Provide additional mechanical support for the winding.

- Improve thermal conductivity within the coil

As shown in Figure 6. 10 (b), the coil tends to bulge above the surface of the PEEK after 5 layers of winding, which impinges on the airgap and could potentially result in contact with the rotor magnets. By varnishing the coil, and clamping the coil during curing the bulging coil can be squeezed down to remain within the slot provided by the PEEK insulation cover. With this particular low viscosity epoxy, the voids between turns can be readily filled with the epoxy, which provides good rigidity and could protect the coil enamel from abrasion due to vibration.

The service temperature of the Duropot 862 is 315°C, which is well above the designed operating temperature of the coil. With its low viscosity, it is able to fill the small voids between the turns, which improves the equivalent thermal conductivity of the coil. As shown in Table 6. 2, the thermal conductivity of the Durapot 862, although modest in comparison to metals, is vastly superior to the thermal conductivity of air.
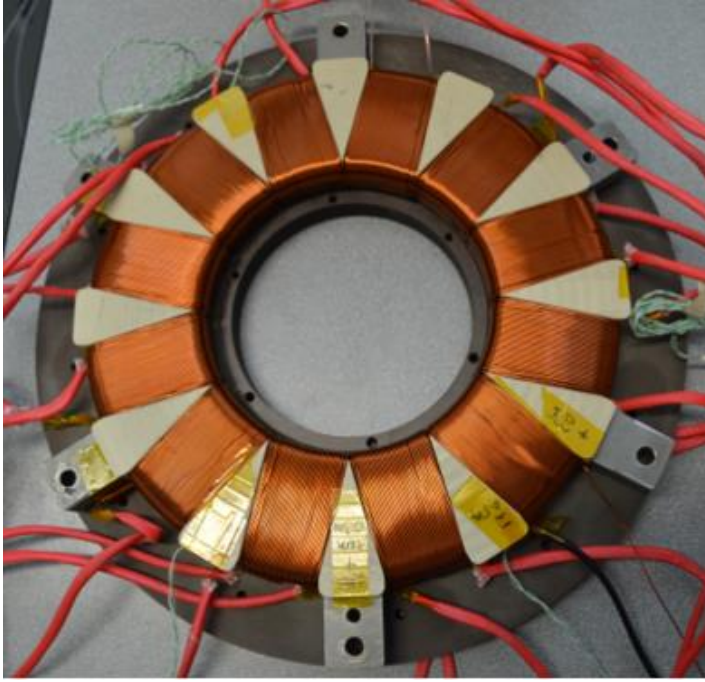
| (a). Stator with coils | (b). Coils bulging above the PEEK surface prior to potting |

Figure 6. 10. Stator after winding

Table 6. 2. Thermal conductivity comparison between Durapot 862 and air

Material	Thermal conductivity (W/mK)
Air	0.025
Durapot 862	0.57

To successfully varnish the coil and restrain the coil within the insulation slot during the curing process, a bespoke stator clamp was manufactured from Tufnol sheet. Tufnol was chosen as it does not stick to Duropot 862 once the varnish is cured. In addition, it could withstand the oven curing temperature of 120°C. The stator coils are pressed to stay within the permitted area during the curing of the varnish, and once the varnish is set, the coils are held firmly by Duropot 862. The varnish process of the coils follows the following steps:

185

1. Place the stator on the tufnol clamp

2. Brush the epoxy on the coil, wait for it to sink into the coil and brush on another layer

3. Place the other side of the tufnol piece on top of the stator and tighten the screws to ensure the clamp to press the coils

4. Place the clamped stator in the oven to cure the varnish

The process is repeated several times until the copper wire on the top layer is rigidly held by the varnish. Figure 6. 11 shows step 2 and 3 during the varnish process, and Figure 6. 12 shows the stator coil after varnish and connection wires are tidied up.
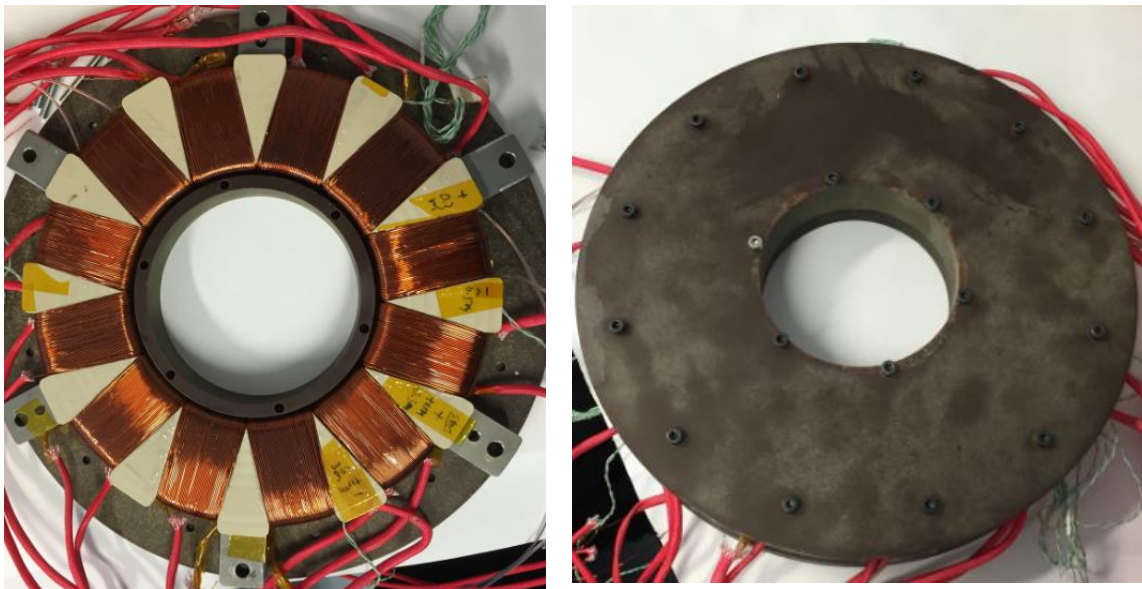
(a). Epoxy is brushed onto the winding   (b). Stator clamped by Tufnol clamp

Figure 6. 11. Coil varnish process
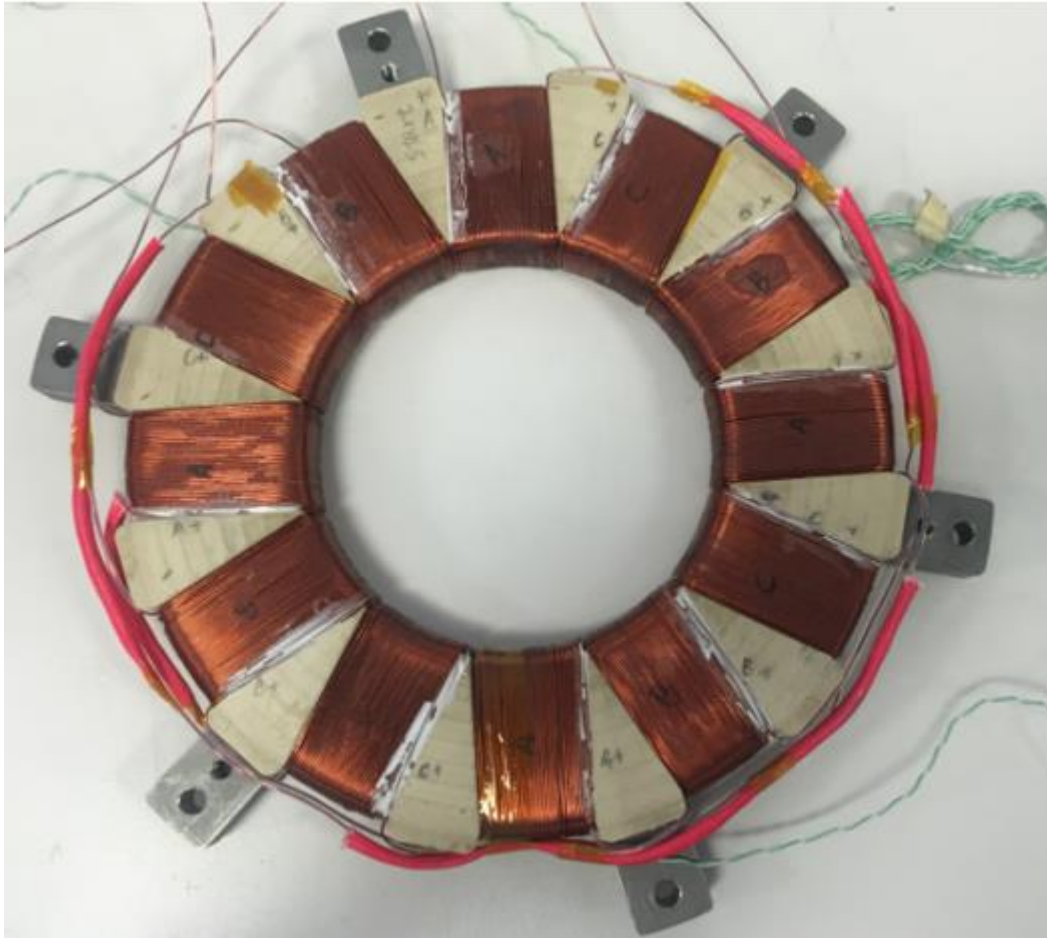
Figure 6. 12. Stator coil after varnishing with Durapot 862

In addition to the 4 thermocouples embedded in the coils, 2 extra thermocouples were added to monitor the temperature of the PEEK and the edge of the stator iron. The exact positions are detailed in Chapter 7.

6.4   **Rotor magnet bonding**

A bespoke magnet jig was made to assist the rotor permanent magnet bonding process. The material used for jig is aluminium to avoid any magnetic engagement with the permanent magnets. Figure 6. 13 shows the separate magnet jigs used for the axial field magnets bonding and radial field magnets bonding. The magnets are held firmly by the bolts pressing on the brass strip, once the magnets are in position, the bolts are released to free the jig.

(a). Radial field magnet jig   (b). Axial field magnet jig

Figure 6. 13. Magnet jigs for holding the permanent magnets during bonding process

The entire bonding process was carried out on a milling machine (which was used solely as a means of controlling the movement of the jig). The bonding process was achieved via the following steps:

1. Hold the rotor and magnet jig in place on the milling machine and thoroughly clean the surface of the magnet and rotor face

2. Brush on a thin layer of magnet bonding adhesive, in this case, Duralco NM25, onto the magnet. This is high temperature adhesive which is routinely used for magnet bonding.

3. Push the magnet jig down on the rotor face until any surplus magnet glue is squeezed out

4. Use a cotton bud to wipe away any excess extra magnet adhesive

5. Release the screws on the magnet jig and remove the jig

6. Use a clamp to clamp the magnet in place to allow the magnet adhesive to cure

The key steps during magnet bonding is shown in Figure 6. 14.

(a). Magnet glue brushed on the rotor
for the axial direction magnet

(b). Axial direction magnet is placed on
rotor

(c). Magnet glue brushed on the rotor
for the radial direction magnet

(b). Radial direction magnet is placed on
rotor

Figure 6. 14. Key steps in magnet bonding

High temperature adhesive Duralco Nm25 was selected as the magnet glue for the permanent magnet bonding, the adhesive is free of magnetic particles or conductive fillers that could potentially interfere with the magnetic field, hence makes it ideal material for bonding the permanent magnet. Its rated service temperature is 260^0C, which makes it suitable for high temperature application. [59] The bonding process is similar for both the axial direction magnet and radial direction magnet, while for the 'L-shaped' rotor it is slightly more complicated. For the 'L-shaped' rotor, the radial direction magnets were bonded on the rotor face first, followed by the axial field magnets. Since the radial and axial field magnet at a given point around the periphery have the same polarity, the axial magnets are repelled by the radial magnets ed. Hence, minor modification to the magnet jig were made and the magnets were clamped before the magnet jig was removed. A small slot was introduced into the magnet jig to allow the clamp to clamp on the magnet face before is the jig was removed as shown in Figure 6. 15. The rotor after permanent magnet bonding is shown in Figure 6. 16.

Figure 6. 15. Slot to accommodate the clamp before the magnet jig is removed

<div align="center">
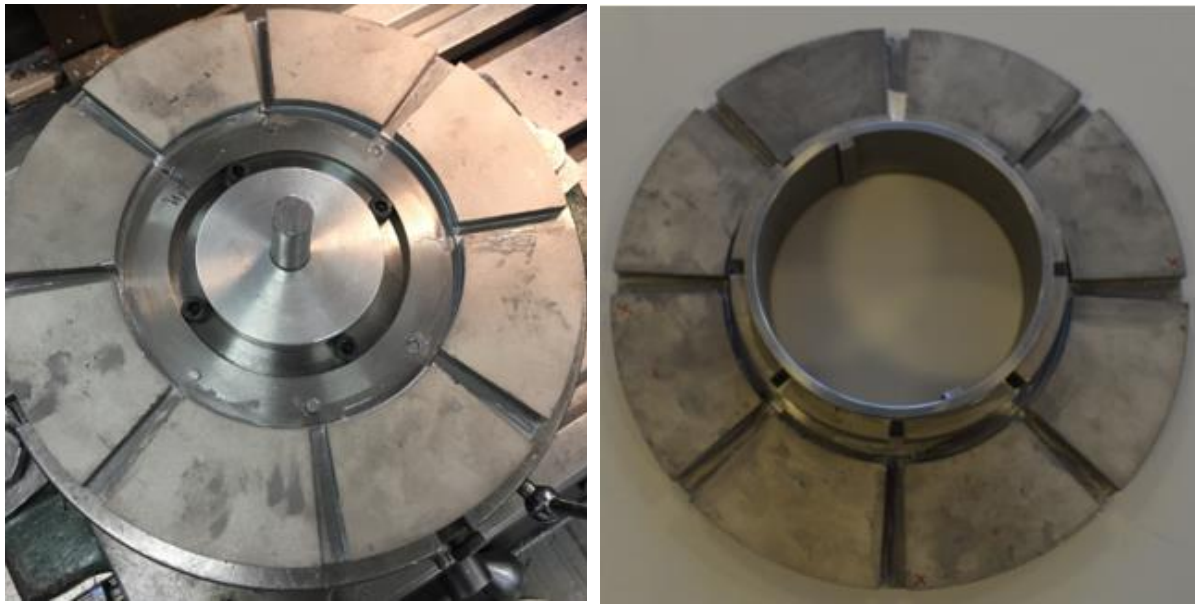
(a). Plate rotor   (b). 'L-shaped' rotor

Figure 6. 16. Rotors with permanent magnet

</div>

6.5 Other rotor components

The construction of the remaining elements of the rotor are described in this section. A non-magnetic rotor hub is used to connect the rotor to the stationary shaft via two angular contact bearings. Two slots were cut out to locate the flanges on the rotor geometry and two endplates were fitted on both ends of the rotor hub to clamp the two rotors sections together with through bolts.

The rotor hub and accompanying endplates were manufactured from Grade 5 Titanium alloy Ti 6Al-4V. This material is well suited to the manufacture of the hub due to its low density, high strength and, in particular, a similar thermal expansion coefficient to cobalt iron. Figure 6. 17 shows the rotor hub and its endplates from different views. The rotor hub incorporates two keyways along the axial direction and one step around the circumferential face of the rotor hub. The two keyways locate the rotor position and ensures the rotors to rotate together with the rotor hub, the step in circumferential face is to prevent the plate rotor core (from moving axially due to the axial direction attractive force during the assembly. Axial direction movement of the plate rotor is limited by the step in the rotor hub and the hub endplate. Figure 6. 18 shows the assembled rotor hub, hub endplates, angular contact bearings on the stationary shaft,

although in this case, the hub endplate, the stationary shaft and one of the angular contact bearing is not visible. The stationary shaft end nut provides the essential pre-load to the back-to-back arrangement of angular contact bearings. The bearings sits inside the rotor hub connecting the stationary shaft and the rotating rotor hub.
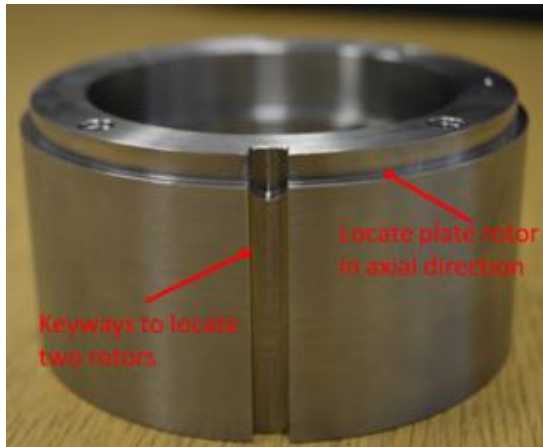
(a). Rotor hub – side view
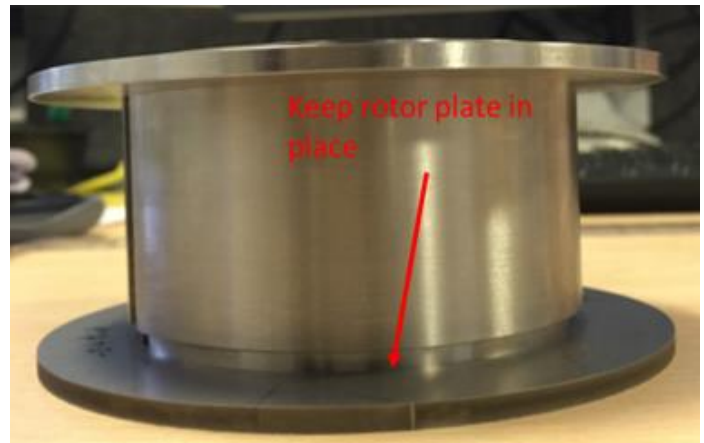
(b). Rotor hub with its enplates

(c). Rotor hub – top view

(d). Rotor hub endplates

Figure 6. 17. Manufactured rotor hub and end-plates
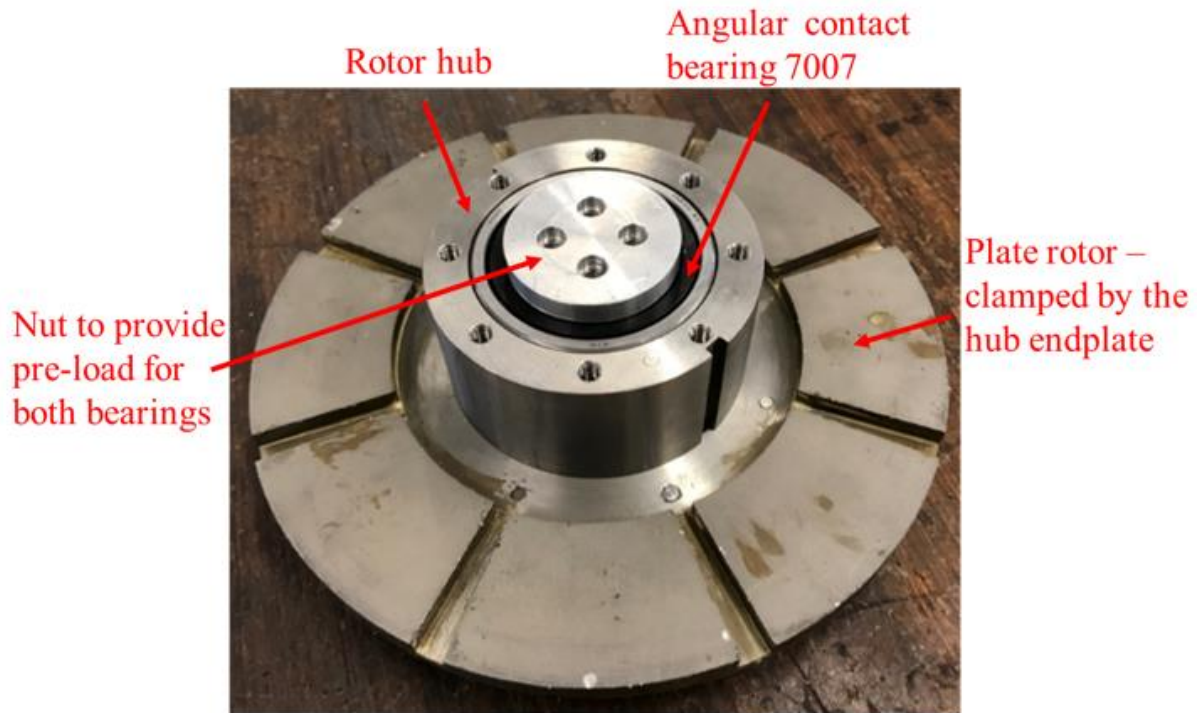
Figure 6. 18. Assembly of the rotor hub, plate rotor, bearing and the stationary shaft

The other rotating element is the rotating shaft, which is shown in Figure 6. 19. This rotating shaft is made from EN8 steel and is mounted on top of the hub endplate. .

Figure 6. 19. Manufactured shaft

6.6 Machine casing

The machine is enclosed by an aluminium housing and a polycarbonate front cover. The aluminium casing provides the main structural support for the stator and allows it to be mounted onto a test-rig. The polycarbonate cover does not provide any mechanical function to the machine other than sealing the font face to avoid the ingress of debris. The aluminium casing was anodised to improve its appearance. On top of the machine casing, a connection box allows the incorporation of 6 k-type thermocouple connectors and one MIL spec power connector. The connection box was also manufactured from aluminium and anodised. The front and back of the machine casing is shown in Figure 6. 20, the connection box is shown in Figure 6. 21.
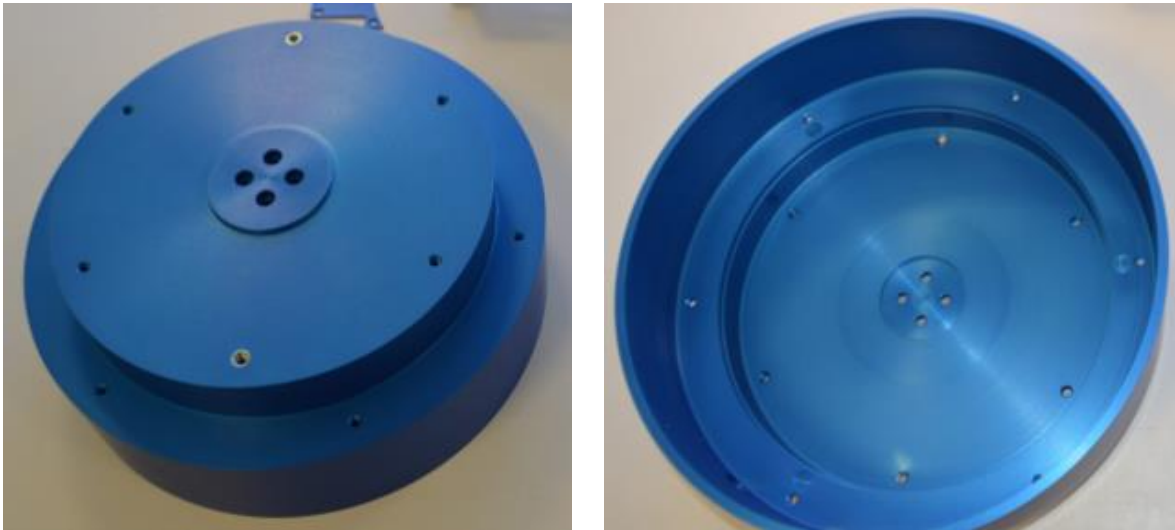
| (a). Back of the casing | (b). Front of the casing |

Figure 6. 20. Casing after anodising

Figure 6. 21. Connection box after anodising

6.7 Machine assembly

The assembly of permanent magnet machines is always challenging because of the large forces of attraction and repulsion that are present. This is especially the case for this prototype machine where there are both the axial radial oriented permanent magnets. The overall process of the machine assembly was carried out as follows:

1. Fit angular contact bearing 71908 on the stationary shaft, and bearing 7007 inside the rotor hub.

2. Mount the plate rotor on the rotor hub, clamped by the hub endplate.

3. Slide the rotor hub on to the stationary shaft along with the bearing and rotor.

4. Secure the aluminium stationary end nut to provide necessary pre-load to the bearing and prevent any axial movement of the plate rotor.

5. Bolt the stationary shaft onto the casing

6. Locate and fix the stator in casing by bolting down on the casing back, make connections for the wire and thermocouples within the connection box.

7. Use bespoke tooling to gently push down the 'L-shape' rotor along the keyway on to the rotor hub.

8. Place the other hub endplate on top of the 'L-shape' rotor and secure the screws.

9. Fit the connection box onto machine casing

10. Place the rotating shaft on top of the hub endplate, bolt the shaft down on the hub.

11. Mount on the top polycarbonate cover, close the machine.

Some key steps during the assembly is shown in Figure 6. 22. In Figure 6. 22, (a) and (b) shows the machine assembly at step 4 and 5, where the plate rotor is already fitted on the rotor hub and then fixed inside the machine casing. (c) and (d) shows the assembly process of the machine stator into casing, while (d) and (f) shows the assembly process for the 'L-shaped' rotor with the bespoke manufactured tool. This bespoketool can be used to push the rotor down or lift it up, by rotating the screw at the centre which presses onto the cylinder, the rotor is easily pushed down or lifted up. Once the rotor is in place, the hub endplate can be fixed on top of the rotor to clamp

both rotors together. (g) and (h) shows last few steps of the machine assembly, where the connection box is fitted on the casing, the rotational shaft is assembled and the polycarbonate cover is placed on top to the machine casing to close-off the machine.

(a). Assembled rotor hub on the stationary shaft

(b). Stationary shaft and plate rotor in casing

(c). Stator assemble process

(d). Stator in casing
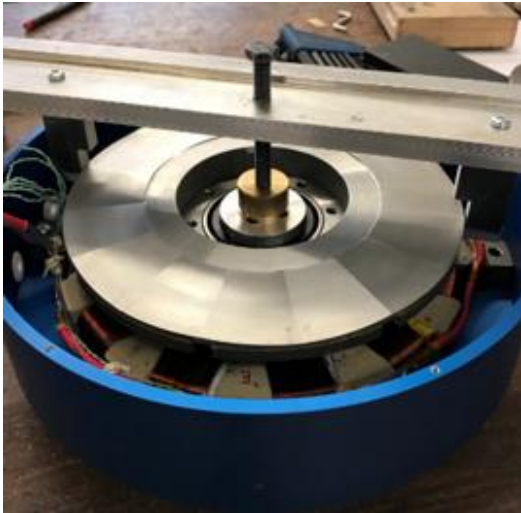
(e). 'L-shape' rotor assemble process using special tool

(f). Rotor held by hub endplate
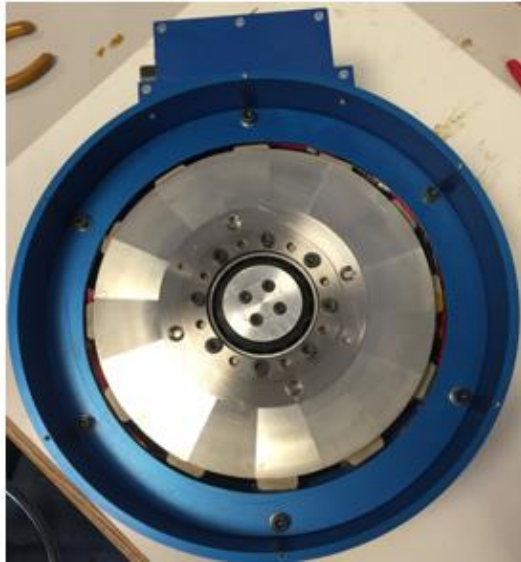
(g). Connection box fitted on casing
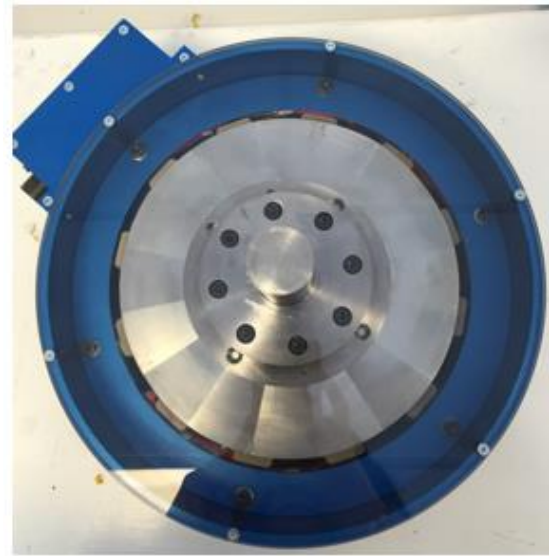
(h). Shaft and top cover assembled

Figure 6. 22. Key steps of machine assemble process

CHAPTER 7.   EXPERIMENTAL VALIDATION OF THE DEMONSTRATOR MACHINE

7.1 Introduction

This chapter describes the experimental testing of the prototype machine manufactured in chapter 6. The testing includes both no-load and on-load testing, including short-term testing at overload conditions. The measurements performed include open-circuit back EMF, full torque versus current characteristic at a range of speeds, transient start-up to a range of final speeds and transient thermal performance.

7.2 General arrangement of the test-rig

A block diagram of the test-rig established to undertake the testing is shown in Figure 7. 1. The overall test-rig is controlled by a dSPACE control system. The TORUS axial field machine coupled to a dynamometer via an in-line torque transducer. The TORUS machine is driven from a three-phase Control Techniques sp2403 power converter. A rotary encoder is fitted on the machine shaft to provide position signals to both the dSPACE and the Control power electronic converter via a Motrona GV210 encoder splitter.

Localised temperatures at a series of locations within the machine are measured using thermocouples which are signal conditioned and then logged by the dSPACE. These temperatures are monitored by dSPACE which can disable the converter via a relay. Once any of the measured temperatures in the machine or the average current exceeds a pre-set threshold, the dSPACE sends a signal immediately to the relay to put the drive into an inhibit state. This provides near instantaneous and reliable protection for the machine during extreme situations such as converter faults or overcurrent. This additional protection was introduced following an earlier converter malfunction which led to the temperature of one phase increasing to 450℃ within a few seconds causing damage to the coil.

The measured torque signal from the torque transducer, the measured machine currents, and the speed feedback from the drive is fed into a 12-bit digital storage oscilloscope (Yokogawa DL850) for data acquisition.
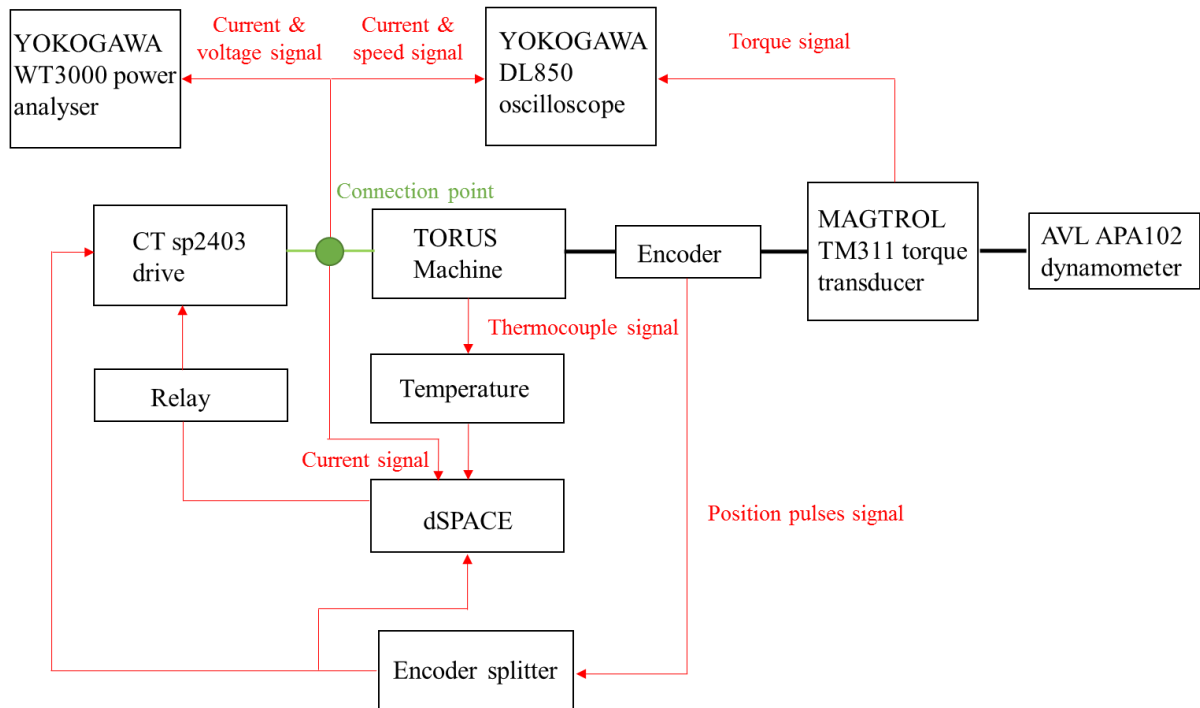
Figure 7. 1. Block diagram of the test rig

7.3 Test-rig components

The major items of equipment in the testing such as the drive inverter and dynamometer machine in the test rig proposed in the section 7.2 is separately introduced in detail in this section.

7.3.1 Control Techniques sp2403 drive

Control Techniques sp2403 is a commercially produced three-phase power converter which is used to provide power to the machine. It has a rated voltage of 400V, a maximum continuous output current of 29A and a nominal power at 400V of 15kW. Each of these specifications exceed the specification of the TORUS tested machine.

There are several control modes available in the converter [60].

- Open loop mode

- RFC mode – induction motor

- Closed loop vector mode – induction motor with speed feedback

- Servo mode – permanent magnet brushless motor with speed feedback

- Regen mode

Open loop or RFC control mode provides less control over the machine as the current generated by the drive is not accurately controlled due to the absence of feedback loop. For planned test rig proposed in previous section, close loop control mode should be considered to control motor performance. To achieve that, current generated by the drive need to be control with respect to the machine feedback. For the prototype machine, since it is a permanent magnet machine, the servo mode should be used to drive the machine. Rotary encoder is used for the speed signal required for the feedback loop.

The parameter setting of the drive can be either through the front panel of the drive unit which is fitted inside the drive cabinet, or through CTSoft, which is a computer based software. The parameters setting is available in standard list format or live block diagrams through the software, monitoring is also available for the software.

7.3.2   Rotary position encoder

An incremental rotary encoder was used for measuring rotor position and rotational speed of the machine. It provides 1024 pulses per revolution and configured with ABZ signal output channels, with channel A and channel B providing quadrature pulse trains and Z is the index channel which provides one pulse per revolution [61]. The two quadrate channels, A and B, allow the direction of rotation to be determined. The so-called hollow-shaft encoder used for the prototype machine (LIKA C81) is shown in Figure 7. 2. [62]. The specifications of the encoder are listed in Table 7. 1. Specification of the rotary encoder

Figure 7. 2. Hollow-shaft encoder

Table 7. 1. Specification of the rotary encoder

Parameter	Description
Encoder type	Quadrature incremental encoder
Resolution	1024 pulse per resolution
Output signals	ABZ
Supply voltage	5V-30V

7.3.3 Dynamometer

The TORUS demonstrator machine was tested by coupling it to an AVL APA 102 dynamometer which provides full four-quadrant torque-speed capability. This dynamometer can operate in either speed or torque control modes. For the prototype machine testing, the AVL was operated in both modes for different tests.

For open circuit testing on no load, the AVL was operated in closed-loop speed control mode to ensure the TORUS test machine rotates at constant speed to obtain an induced

EMF waveform. For on-load testing, the AVL is operated in torque mode to apply a given load torque. The maximum rated speed is ±18,000rpm and the rated torque is ±120Nm. [63] which is more than adequate for the testing. Although the AVL has its own in-built torque transducer, this was not used for the measurement of torque due to offset problems.

7.3.4   MAGTROL torque transducer

The torque produced by the TORUS machine was measured by a MAGTROLTMHS 312 in-line torque transducer shown in Figure 7. 3. The specification of this particular model is listed in Table 7. 1. [64]. The transducer also provides an additional speed measurement. The transducer consists of a hardened stainless steel shaft along with guide bearing and an integral electronic measurement conditioning units contained in the aluminium casing. An external power supply and display unit is used to power the torque transducer and display the torque, speed and power.

Figure 7. 3. MAGTROL TMHS 312 torque transducer

Table 7. 2. Specification of the torque transducer

Parameter	Value

Rated torque	200Nm
Sensitivity	25mV/Nm
Maximum speed	24000min-1
Pulse wheel	60 pulses/Rev

7.3.5 dSPACE

dSPACE is a commercial platform for real time control, which can be programmed using automatic code generation tools from a Mathworks Simulink model. It can be used in conjunction with ControlDesk software, which enables real-time measurements and monitoring. A range of expansion cards to provide specific functionality can be added to the base dSPACE system. In the experimental setup used in the machine testing described in section 7.2, the dSPACE system used contains a DS1005 PPC board as the main processor, the DS2002 A/D board, DS 2101 D/A board, DS3001incremental encoder interface board and DS 4001 timing and digital I/O board.

The dSPACE system is responsible for setting the speed reference for the power converter, measuring and logging machine temperatures and providing over-temperature and over-current protection. Real-time information from the test equipment is displayed to the user via a control desk interface running on the host laptop. The block diagram in Figure 7. 1 shows the interconnection and functionality of each expansion cards.

- DS2002 provides 9 A/D channels for the machine temperature measurements, average phase current measurements and torque measurement input.

- DS4001 enables the digital signal output from dSPACE to control the status of the relay which is wired into the power converter.

- DS3001 provides the ability of the encoder signal processing to obtain the speed and position of the machine during rotation.

- DS2101 provides 2 D/A output channels, one to set the speed reference and the other to output to oscilloscope to provide an analogue representation of the machine speed.
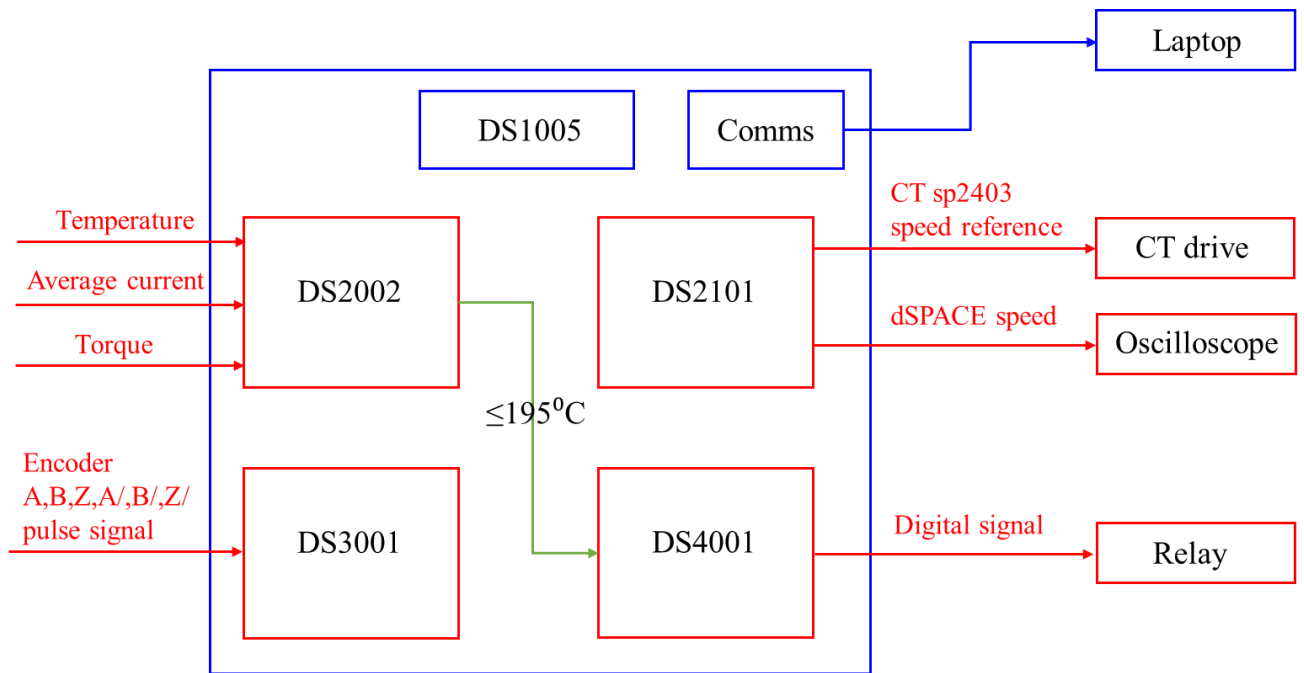
Figure 7. 4. Block diagram of dSPACE system

7.4 Drive train configuration

Figure 7. 5 shows the mechanical arrangement of the TORUS machine, the AVL dynamometer, the MAGTROL TM311 in-line torque transducer and the couplings that connect these three main elements of the drive-train.
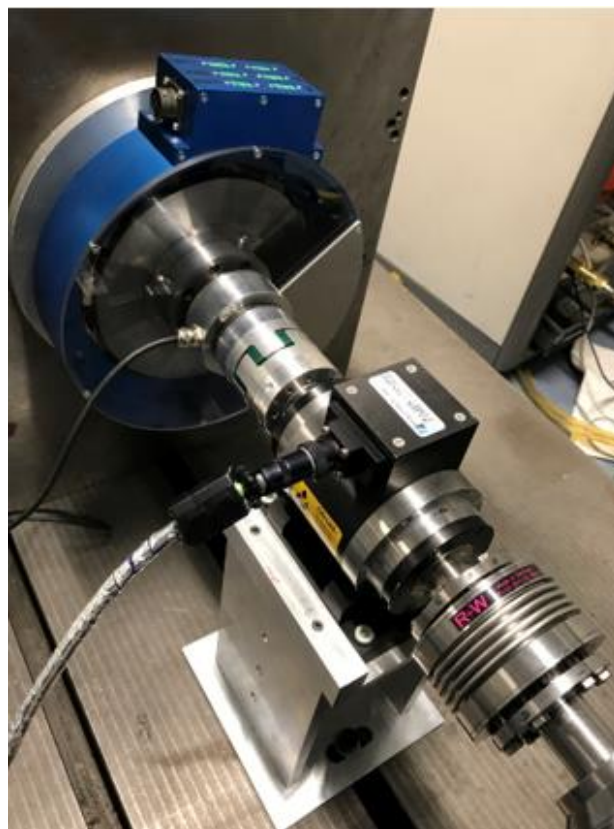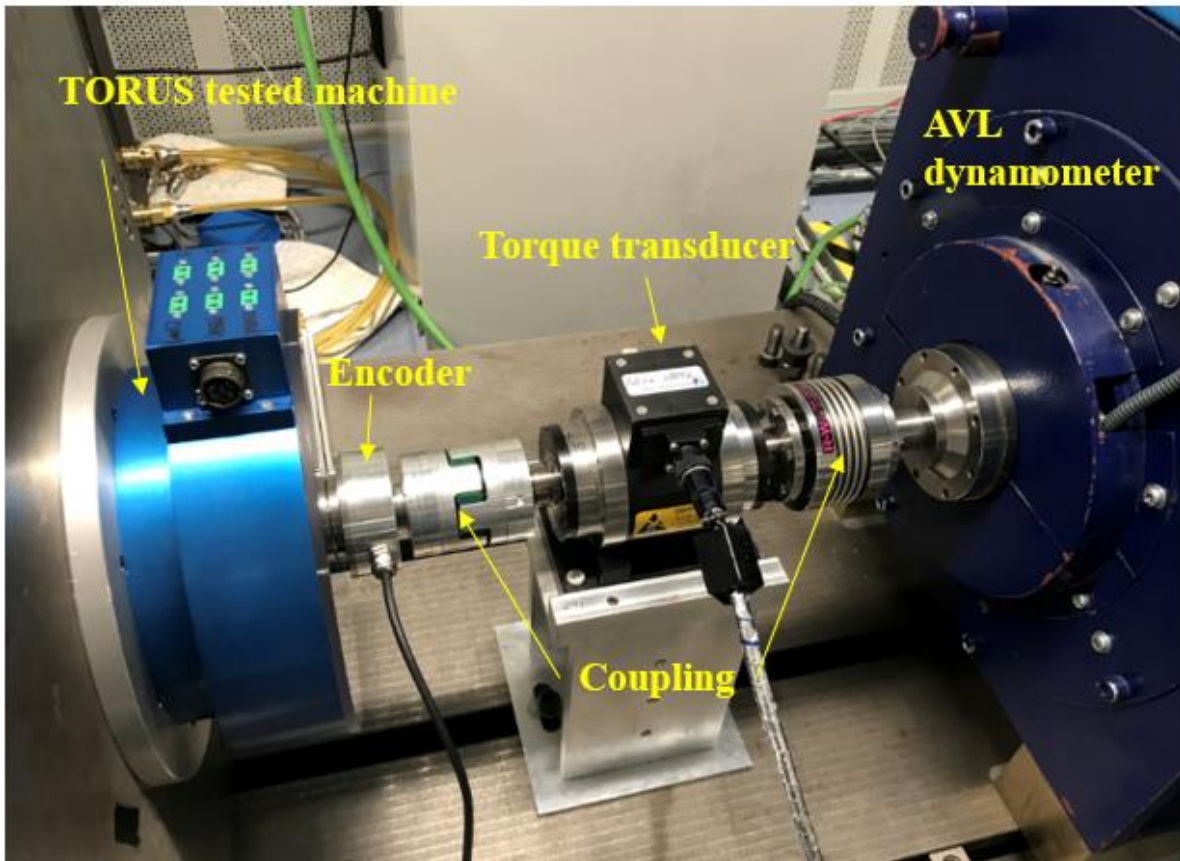
Figure 7. 5. Machine coupled to the AVL dynamometer

Figure 7. 6 shows the test cell with the various items of test equipment in place. The encoder splitter is fitted inside the drive cabinet. Figure 7. 7, shows the various control and monitoring systems which are located outside the test-cell.

The Control Techniques converter and dSPACE is controlled via separate laptops outside the test cell. Parameters such as reference speed and current limit for the Control Techniques converter are set and monitored from the parameter setting and monitor panel on the drive control laptop via CTsoft software. The dSPACE system, which is located within the test-cell, is controlled by the right hand side laptop using automated generated code from a SIMULINK model. The temperatures of the prototype machine, machine current and machine speed are monitored and displayed on the laptop screen via ControlDesk software. The laptop screens of Figure 7. 7 show the monitor panel of the CTsoft for the converter control laptop and the interface of the ContrlDesk for the dSPACE control laptop.

The Yokogawa DL850 oscilloscope, which is remote controlled from the PC, captures 12-bit representations waveforms of torque and speed from torque transducer, current from the converter. Signals representing the machine current and converter output voltage are fed into a Yokogawa WT3000 power analyser outside the test cell along with the speed and torque output from the torque transducer.
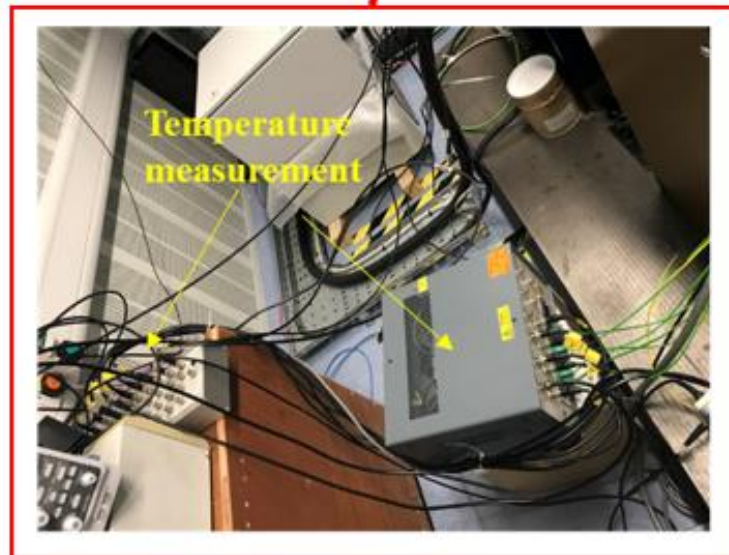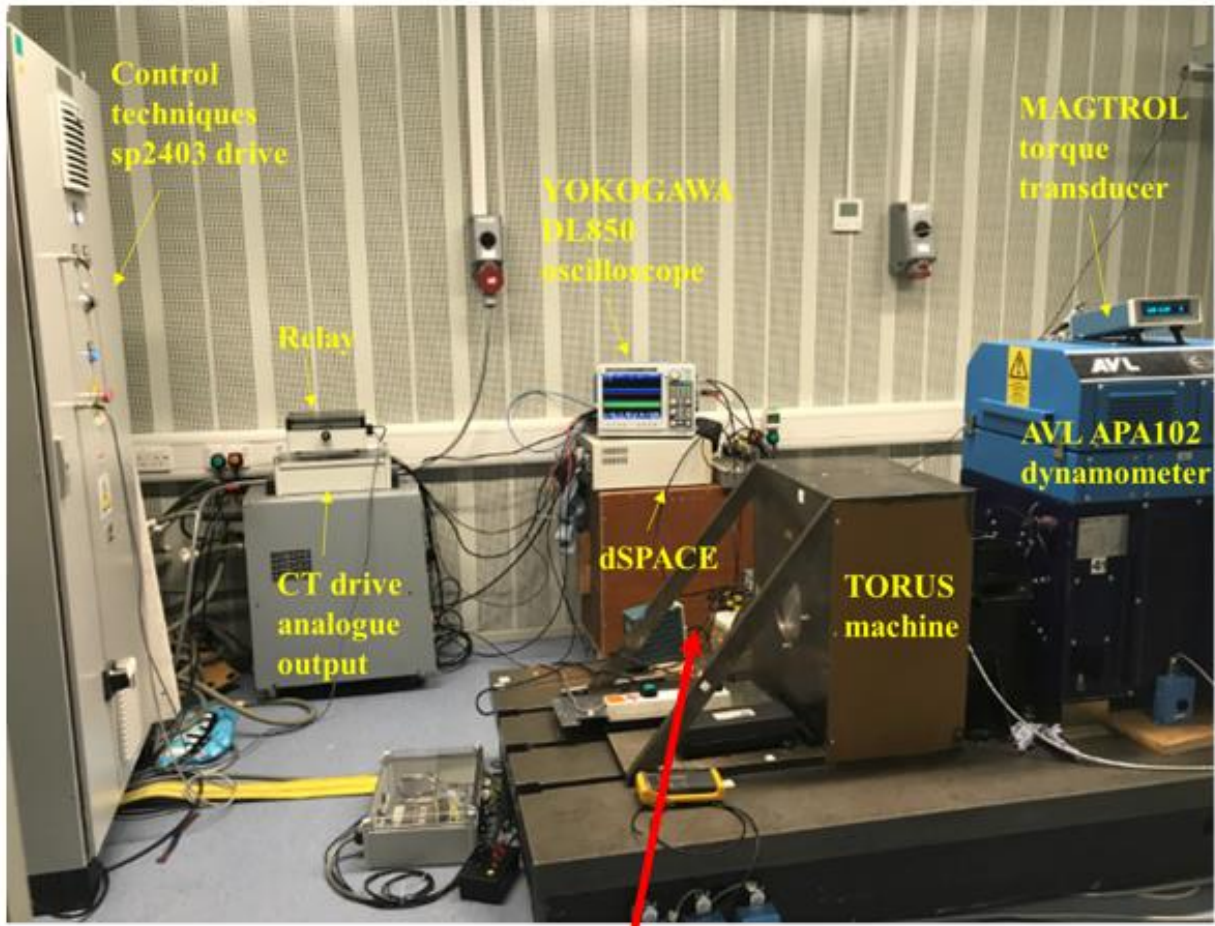
Figure 7. 6. Test bench set up in test cell
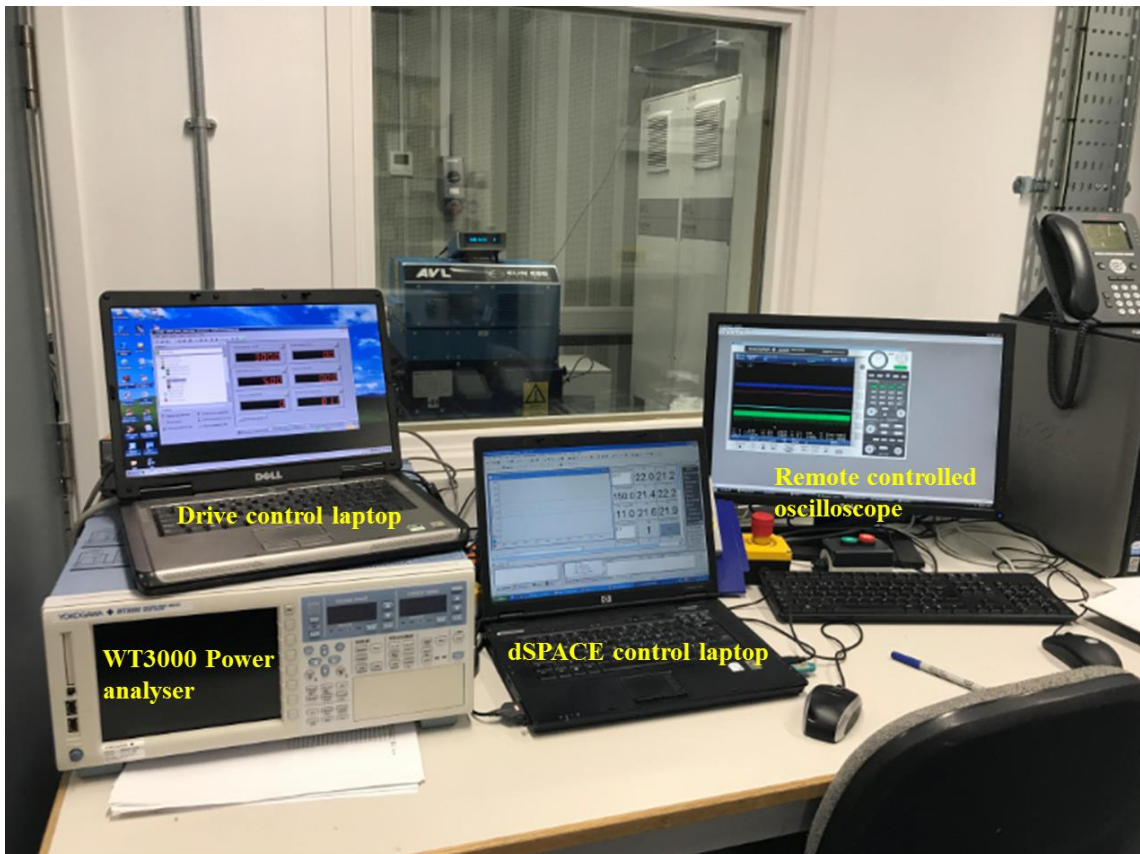
Figure 7. 7. Experimental set up for parameter setting and monitoring, control and display

7.5 Experimental no load measurements

The first tests undertaken were a series open circuit measurements of the induced back emf of the machine. These tests provide an initial validation for the prototype machine in terms of its performance. For these tests, the Control Techniques converter was disconnected from the TORUS prototype machine. The TORUS machine was driven at a series of constant speeds by the AVL dynamometer operating in closed-loop speed control mode. The phase to neutral back EMF waveforms of the machine at 100rpm, 300rpm and 500rpm were captured and are shown in Figure 7. 8. It can be seen from the figure that the three back EMF waveforms are well balanced.

The measured back EMF waveforms at these three speed set-points, normalised with respect to rotational speed, are shown in Figure 7. 9. As will be seen, there is a small progressive reduction in magnitude and an increase in phase shift with rotational speed,

behaviour which is indicative of the presence of increasing eddy current screening in the stator core.
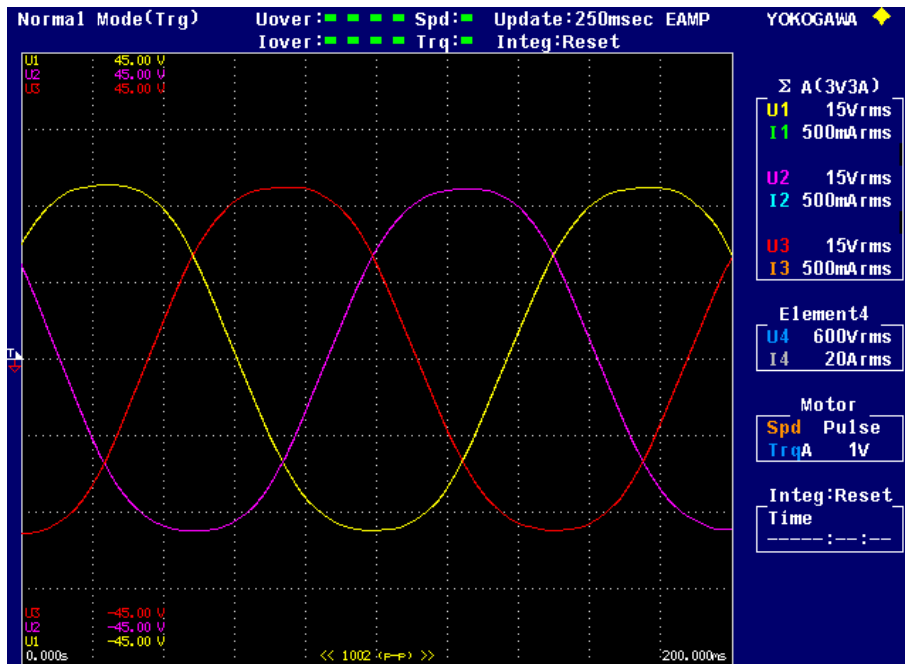
(a). 100rpm
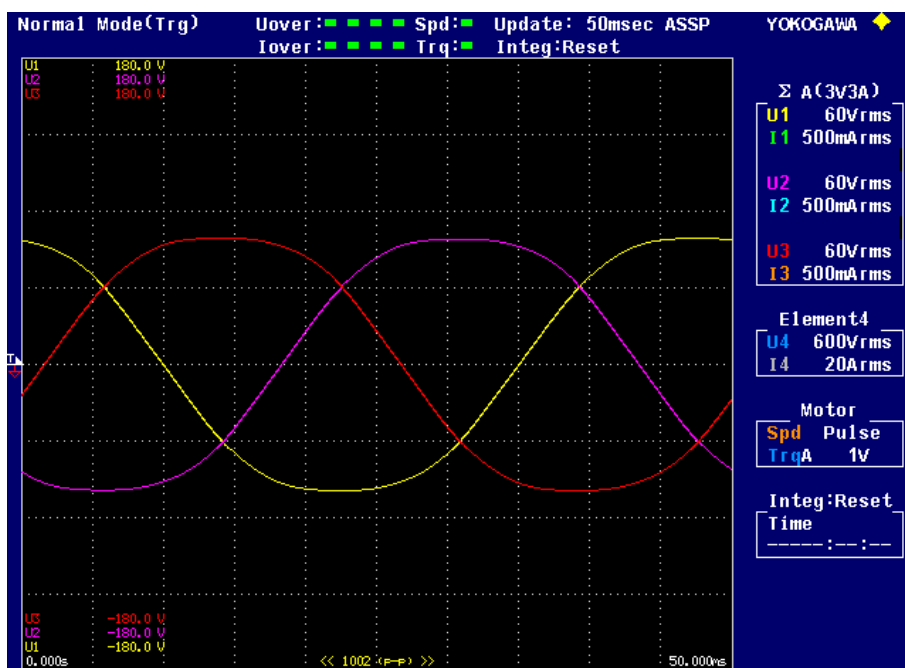
(b). 300rpm
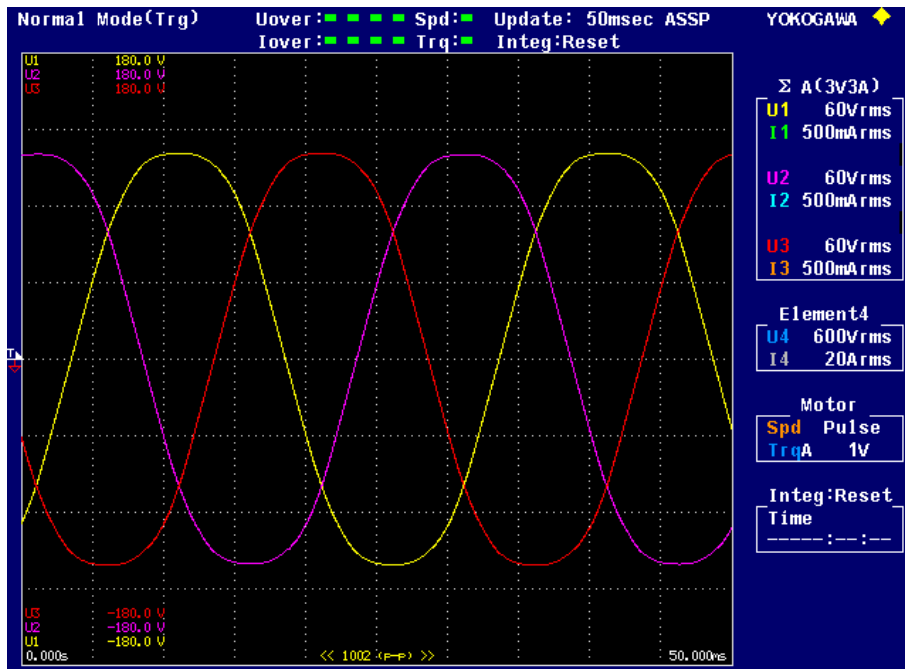
(c). 500rpm

Figure 7. 8. Open-circuit induced 3 phase back EMF at a series of speeds (Note different voltage scales on plots)
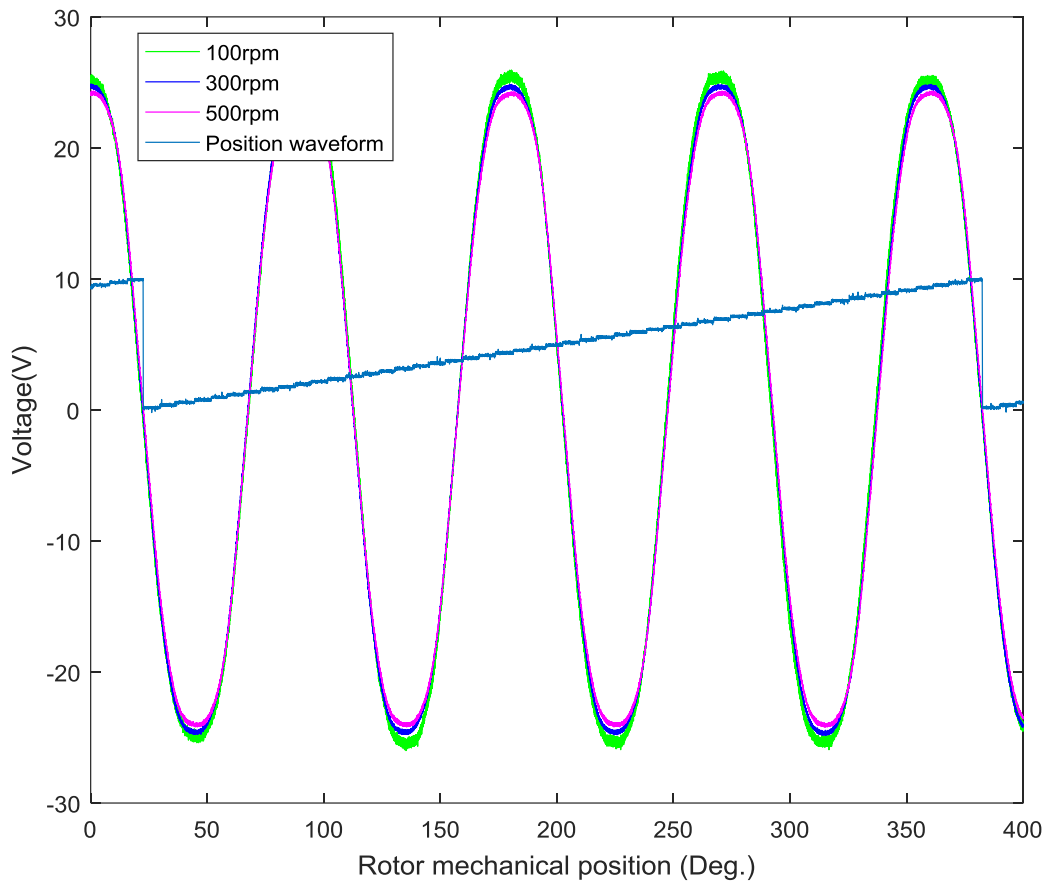
Figure 7. 9. Normalised back EMF with reference rotor position waveform

Figure 7. 10 shows the torque measured (shown in blue trace) during open circuit test at 500rpm rotational along with the phase emf for phase A (shown in yellow trace). This 10.3Nm torque produced by the dynamometer (measured by the in-line transducer) is the torque required to rotate the TORUS machine at 500rpm and hence overcome losses in the TORUS machine. In this case, the presence of significant core loss in the solid core (which is dominated by eddy currents) requires an input power of 540W for rotation on no-load at 500rpm. The finite element predicted core loss of the prototype machine under open circuit condition is 430W. Recognising that the measured torque includes friction and aerodynamic losses in the TORUS machine, there is a reasonable correlation between the measured input power and the predicted core loss at 500rpm.
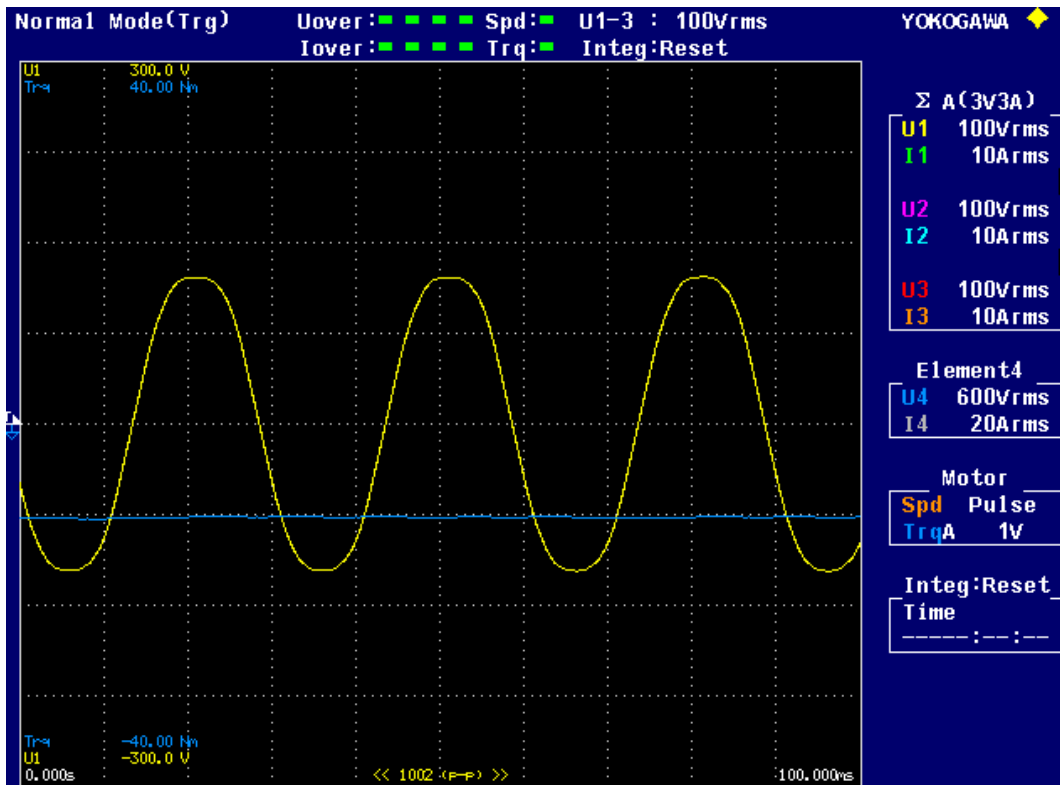
Figure 7. 10. Torque measurement from the torque transducer under open circuit condition with rotational speed of 500rpm along with phase A EMF

A comparison between the measured and predicted EMF at 500rpm is shown in Figure 7. 11. In this case, the predicted EMF was derived from a magneto-dynamic finite element that included the effects of eddy currents. As will apparent from, the measured and predicted EMF waveform are in excellent agreement in terms of both in magnitude and waveform shape.
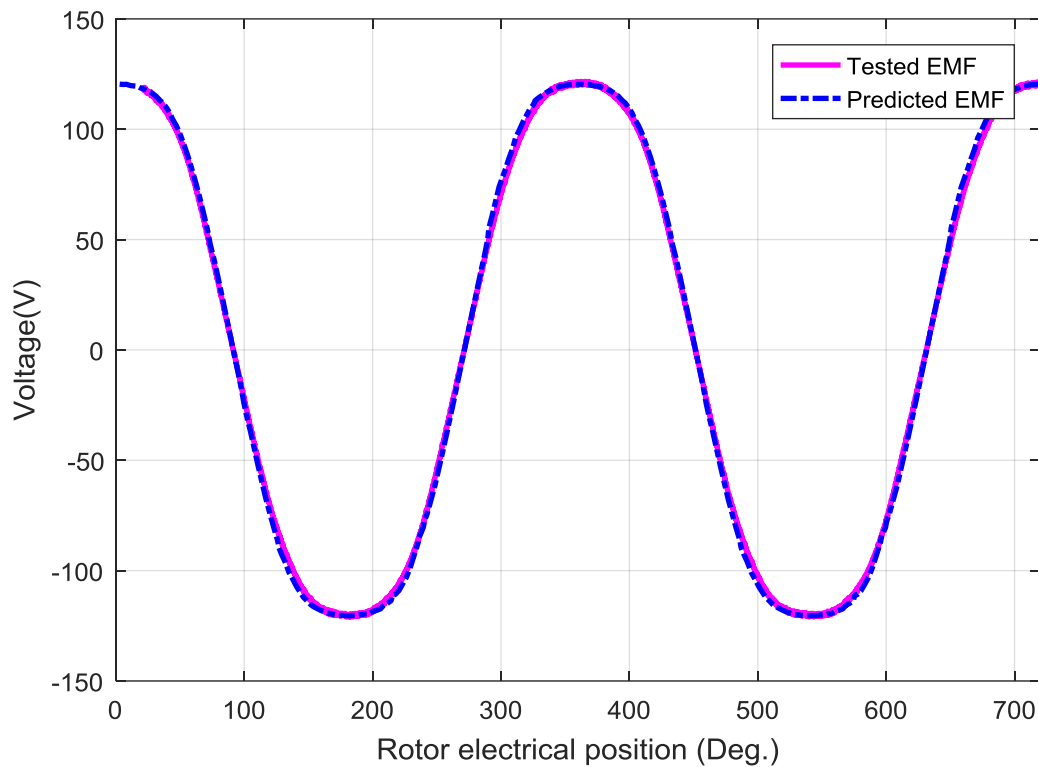
Figure 7. 11. Comparison of FE predicted and measured induced back EMF at 500rpm

7.6 On-load testing

For the on load testing, the Control Techniques drive was re-connected with TORUS machine and set-up in close loop servo mode to provide precise speed control of the TORUS machine. The AVL dynamometer was configured to operate in torque control mode so that it can provide a precise and controllable torque load on the TORUS machine. In order to undertake on-load testing the following procedure was adopted:

1. The speed demand was set for the Control Techniques Converter and the TORUS machine accelerated up to the speed set-point.

2. A torque demand was entered into the AVL dynamometer and this load torque was applied to the TORUS machine

3. After allowing a very short interval for the measurements to settle, torque and current measurements were recorded. These measurements were taken without allowing the machine to reach steady-state thermal conditions.

4. The next load torque point was set and step 2 and 3 repeated to cover a prescribed load set points.

5. A new speed demand was set and steps 2-4 repeated.

During testing, a maximum temperature of ~190°C was set as a threshold and if this was exceeded a particular test was terminated. Since these were manual tests in which the current was applied on a semi-continuous basis, only modest current densities up to ~17A/mm^2 rms were used. Shorter-term tests with higher currents are described later in section 7.7.

Measured current waveforms for a 15Nm load torque operating point at 100rpm and 300rpm are shown in Figure 7. 12. The current was measured using a Tektronix TCPA300 current probe and recorded on a YOKOGAWA DL850 digital oscilloscope.
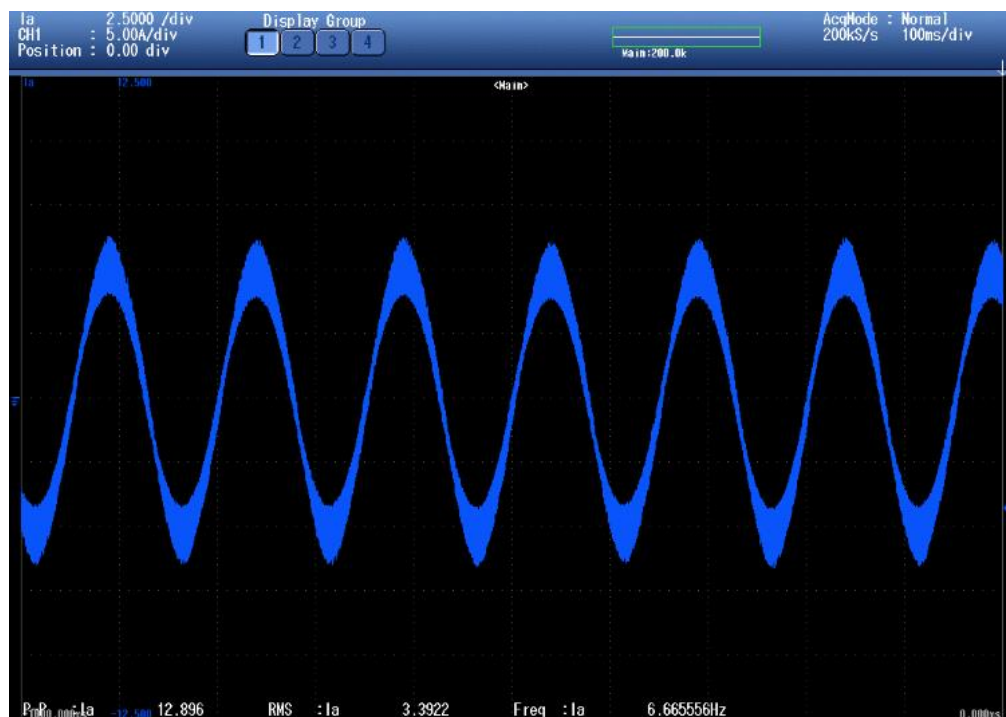
(a). 100rpm
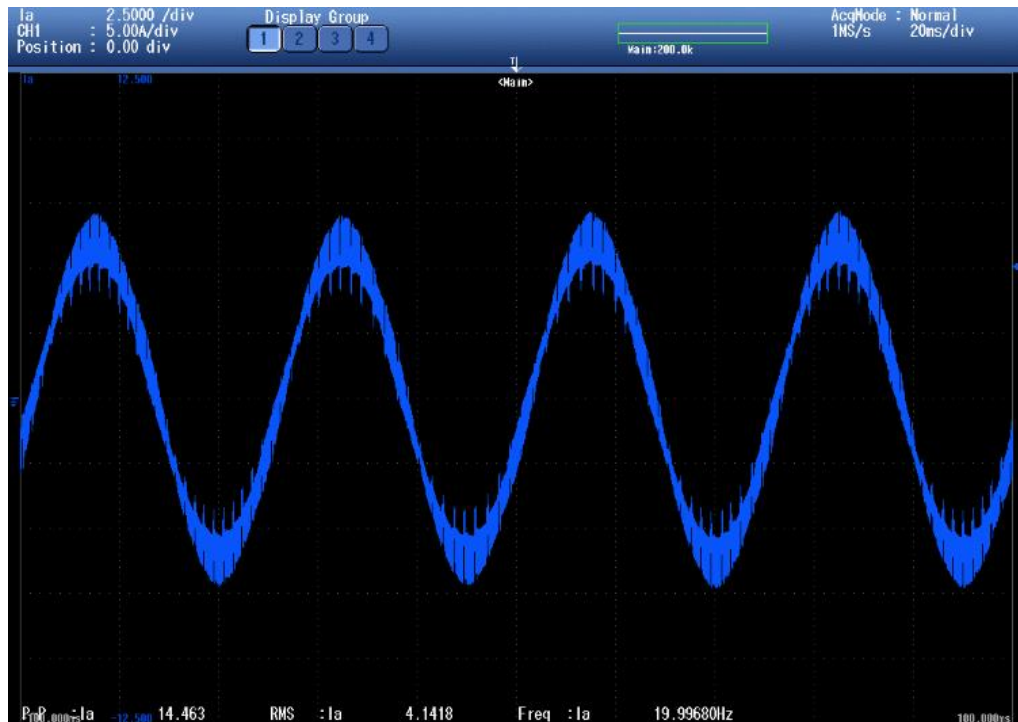
(b). 300rpm

Figure 7. 12. Measured phase A current waveform at 15Nm load torque

The performance of the TORUS was measured at numerous combinations of rotational speed and load torque. **Error! Reference source not found.** shows the average measured torque as a function of the measured rms current density at 10rpm, 50rpm, 100rpm, 300rpm and 500rpm. As shown, finite element predictions were performed using magneto-static analysis and using magneto-dynamic analysis with eddy currents included at the maximum speed of 500rpm.
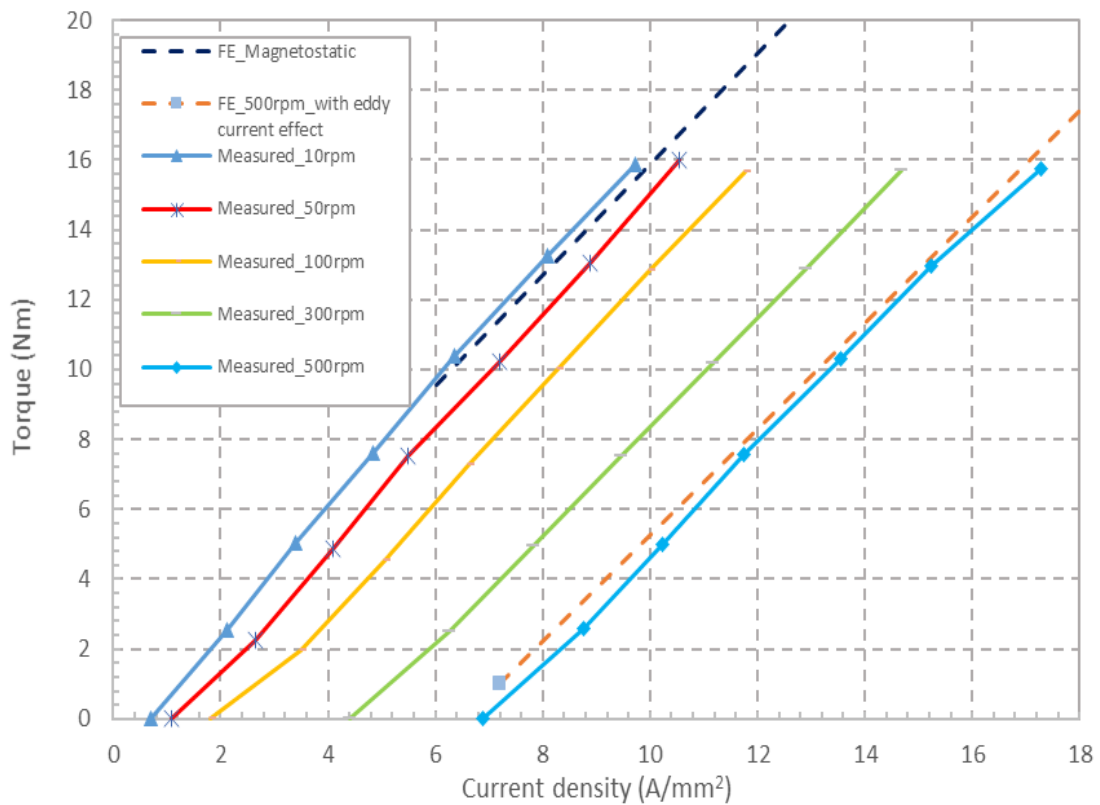
Figure 7. 13. Comparison of finite element predicted and measured torque as a function of rms current density

As will be apparent the measured torque performance of the prototype machine is in good agreement with finite element predictions at the appropriate speed. The measured torque increase with current over this limited range shows good linearity. It is also evident that eddy currents in the solid stator core play a large part since the torque versus current relationship is strongly influenced by the rotational speed.

It is interesting to note that even at 0Nm of torque demand on the AVL dyno torque demand, the measured current density required in the TORUS machine to maintain the machine rotational speed increases. At 500rpm, a current density of 6.8A/mm² is required to simply rotate the TORUS machine on no-load. This input power is predominantly required to overcome the TORUS machine core losses, although some minor contributions from various friction and aerodynamic drag will also be present. This is consistent with the torque predicted by extrapolating back the torque at 500rpm finite element model that includes eddy currents to zero net torque. Although the finite element model does not include the full representation of core loss, it does include the eddy current contribution, which is by far the dominant contributor in this solid core.

A comparison between the two set of finite element predictions, with and without eddy currents, show the significant contribution element predictions he model excluding the eddy current effect.

7.7 Transient response and short-term torque testing

The on-load measurements in section 7.6 are for essentially continuous conditions. However, this testing was limited to current densities up to ~17 A/mm^2 or so due to temperature rise limitation. In order to extend the current density range beyond 20A/mm^2 it was necessary to establish a more controlled approach to limiting the duration of the period in which currents flow in the TORUS machine.

In the approach adopted, the TORUS machine was still operated in speed mode with the AVL dynamometer in torque control model. However, rather than provide a set point torque demand for the AVL dynamometer, a controlled torque profile was used, using the so-called 'recall mode' capability of the AVL dynamometer. More specifically, a trapezoidal load torque demand was applied to the AVL dynamometer, with quasi steady-state measurements being taken during the flat-top of the trapezoidal load torque profile. A typical torque profile involved for lower end of torque demand is formed by a 4s long linear ramp from zero to rated torque, a 12s interval of constant torque demand followed by a 4s linear ramp back down to zero torque. While for the high load torque of 80Nm, the ramp time is reduced to 3.5s, and duration for constant torque demand is decreased to 5s. The duration of linear ramp torque region and the constant torque region of the trapezoidal profile was adjusted and summarised in Table 7. 3 to accommodate the increased losses incurred at higher torque rating. In this way, high levels of current density and torque can be reliably tested without overheating the machine.

Table 7. 3. Time duration for trapezoidal torque demand profile under different load torque

Torque set-point (Nm)	Duration of linear ramp torque region (s)	Duration of constant torque region of trapezoidal profile (s)
5	4	12
15	4	12
30	4	12
50	4	12
80	3.5	5

The detailed testing procedure is as follows:

1. Rotate the TORUS machine at a low rotational speed of 10rpm on no-load.

2. Apply a 1Nm load with the AVL dynamometer.

3. Reduce the speed demand to back to 0rpm.

4. Apply torque profile in recall mode.

5. Increase the speed demand to 10rpm or 500rpm when the load torque applied is at the set-point (flat-top region of trapezoidal profile).

6. Speed, torque and current response is recorded.

7. If temperature gets too high during the test, the torque and speed demand will be manually dropped, test is stopped.

Steps 1-3 were required to stabilise the zero speed starting speed as the controller experienced difficulties with a zero speed demand with zero load torque applied. Speed, torque and current were measured and captured by YOKOGAWA DL850 12-bit oscilloscope. The oscilloscope is set to trigger at the level change of the speed demand, i.e., as the speed demand changes over the set level, the oscilloscope is triggered to capture an 2s long interval of data. The load torque applied to the TORUS machine by the AVL dynamometer was 5Nm in the first set of tests, for speed increases from 0rpm

to 50rpm, 0-100rpm, 0-300rpm and -0-500rpm. In all cases, the acceleration rate was set to 2000rpm per second.

The resulting measured results are shown in Figure 7. 14, Figure 7. 15 and Figure 7. 16. The red signal in the figures represent speed demand, which is a step change from stand still to the target speed (although the Control Techniques converter had an imposed maximum acceleration rate). The orange signal indicates the actual speed response of the machine, the signal was taken from the speed feedback of the Control Techniques drive. The blue signal represents the corresponding phase current output from the drive. The cyan signal shows the torque response during the speed change.
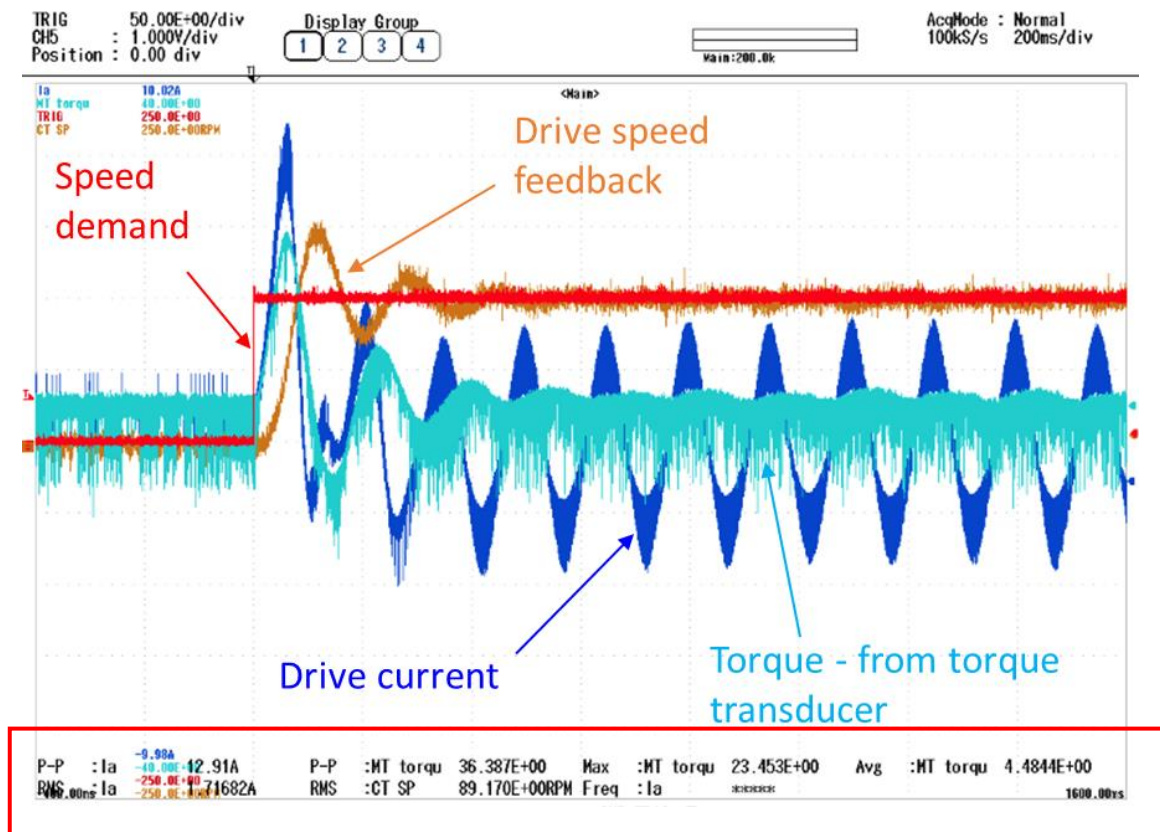
Figure 7. 14. Machine torque and speed response over a transient speed demand change to 100rpm with 5Nm load torque

Figure 7.14 shows the torque, speed and drive current transient response for the machine at 5Nm load torque and 100rpm speed demand. As shown in the bottom of the figure, the rms phase current to drive the machine is 1.7A, and average torque of 4.48Nm is achieved. The transient period for the machine to achieve demand torque and speed level is about 0.42s.

219

Figure 7.15 and Figure 7.16 shows torque, speed and drive current transient response for the machine at the same load torque, but at 300rpm and 500rpm speed demand. The phase rms current to achieve 300rpm speed demand is 2.43A and the average torque once the torque is stabilised achieved is 5.6Nm. The transient period for 300rpm speed demand is 0.5s. As for 500rpm speed demand, the transient period is even longer, and the oscillation in torque, current and speed is larger. As speed goes up, the eddy current loss is more severe, the required rms phase current to drive the machine is 3.18A which is higher, the average torque is 6.4Nm. The difference between the load torque would be the drag torque caused by eddy current.
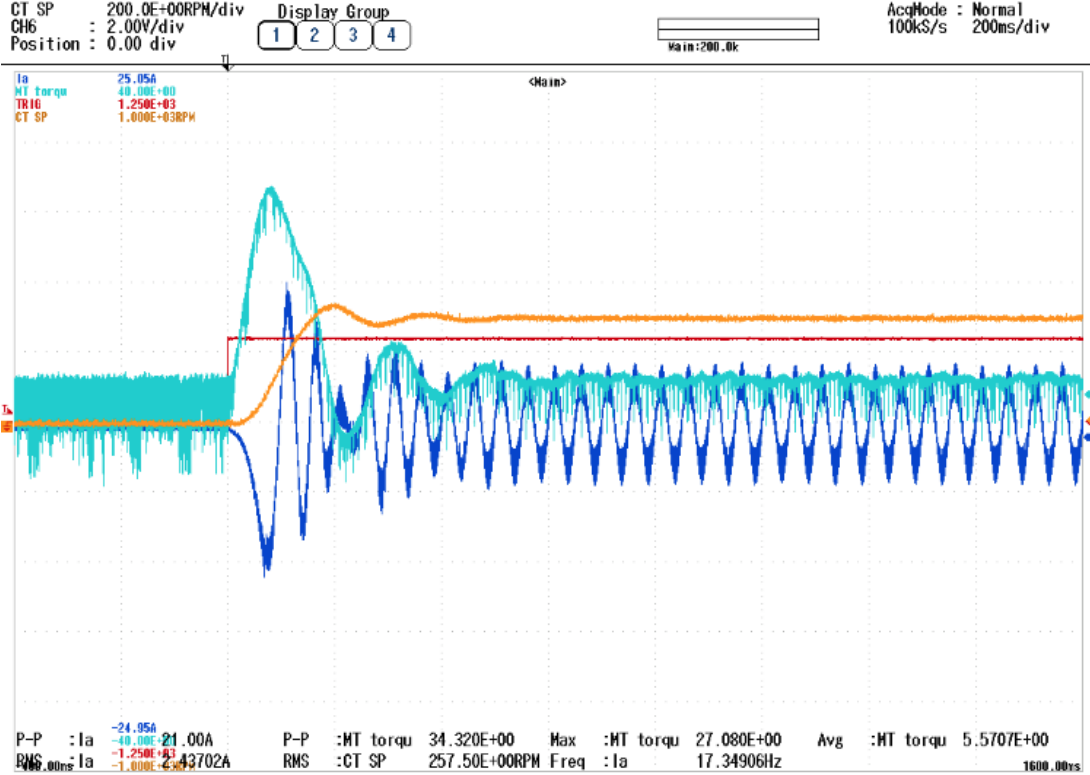
Figure 7. 15. Machine torque and speed response over a transient speed demand change to 300rpm with 5Nm load torque
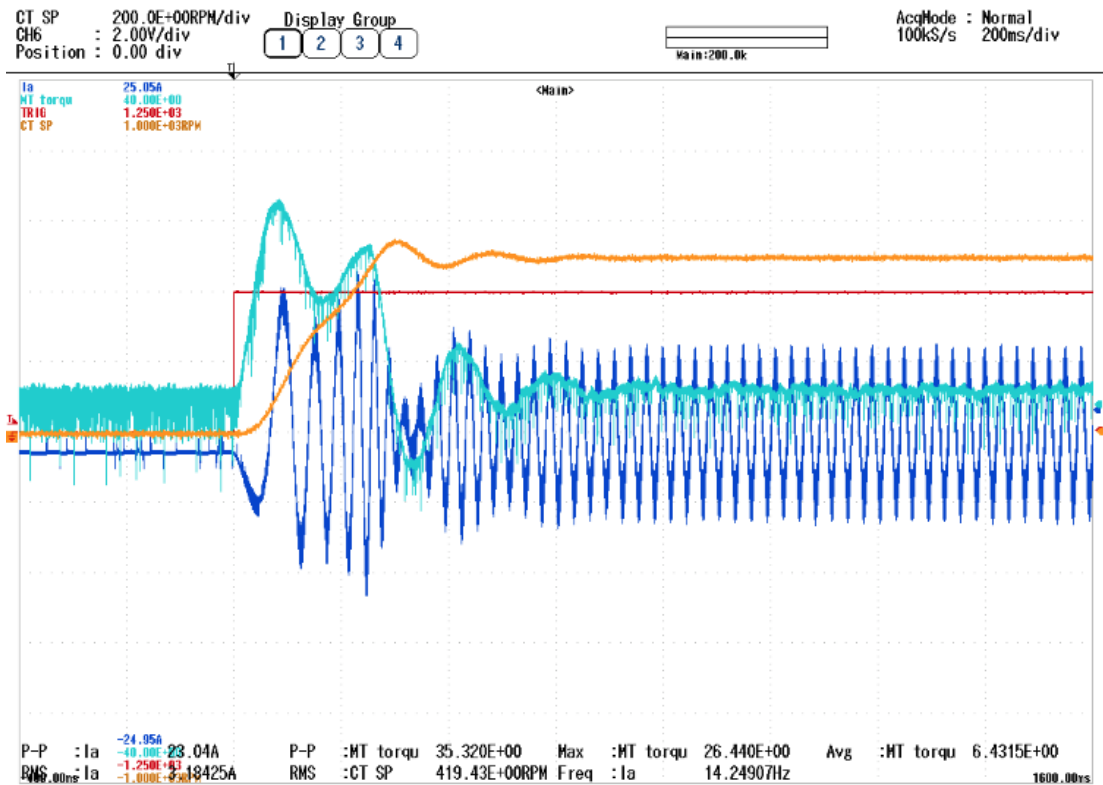
Figure 7. 16. Machine torque and speed response over a transient speed demand change to 500rpm with 5Nm load torque

The transient speed response with different speed demand levels are superimposed on each other in Figure 7. 17. As would be expected, increasing the speed demand results in an increase in the time taken for the machine to reach steady state. At 500rpm speed demand, 500rpm is reached in 0.23s, but it takes a further 0.05s for the overshoot and subsequent oscillations introduced by the Control Techniques drive speed controller to settle.
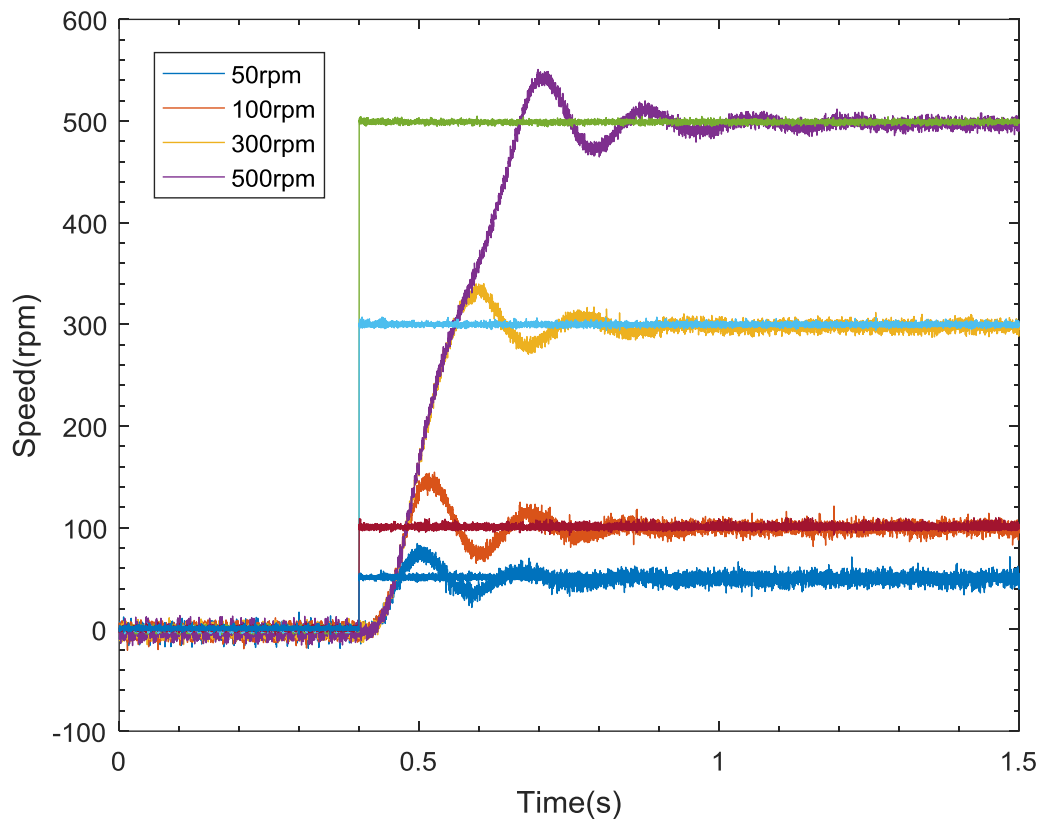
Figure 7. 17. Superimposed measured transient speed response with a fixed 5Nm load torque applied by the AVL dynamometer at a series of step changes in speed demand

Having obtained the transient response at a relatively low load torque of 5Nm, a series of higher load torques were applied by the AVL dynamometer the TORUS prototype machine to test its overload capability. All three phase currents were recorded using a set of three LEM LA125-P current transducers (rated current 141Arms) since only one Tektronix TCPA300 current probe was available. The measured current from the current probe and the current transducer is in good agreement as shown in Figure 7. 18 for the particular case of a 15Nm load torque with speed demand change from standstill to 10rpm. It can be seen that the phase A current obtained from two different measurement are in good agreement.
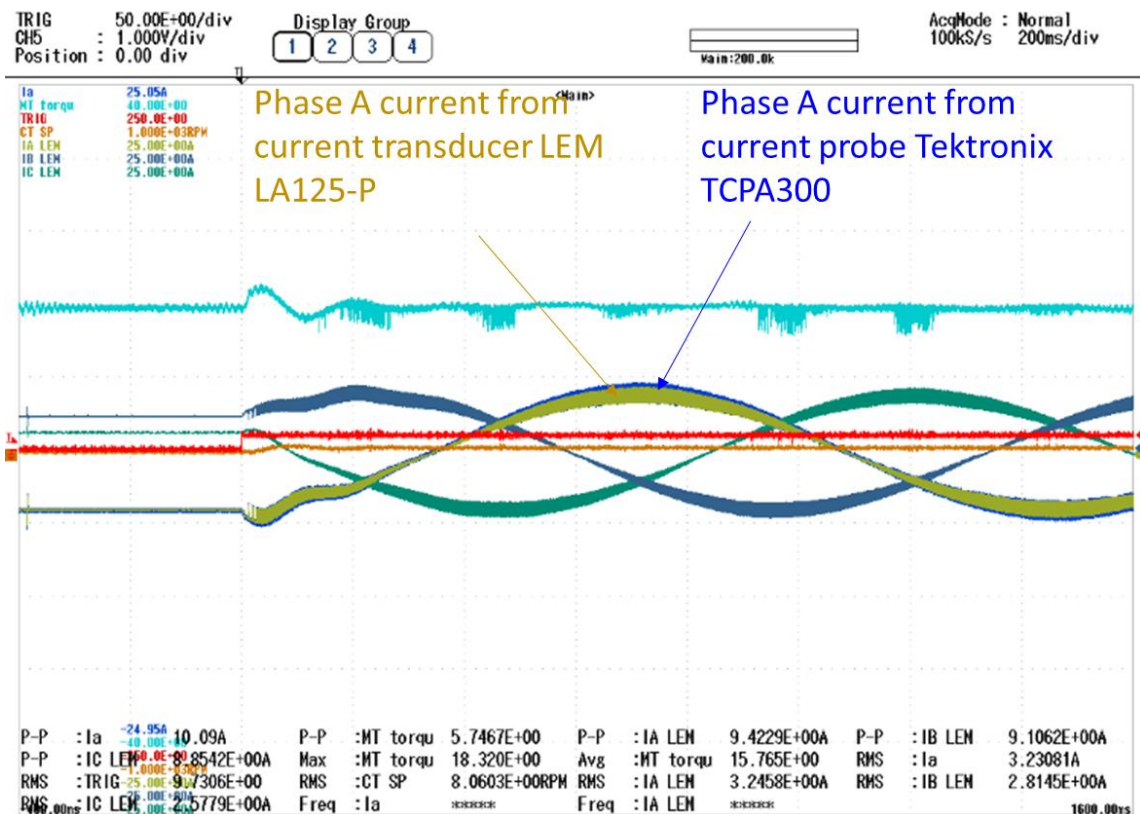
Figure 7. 18. Phase A current measured via two different methods with 15Nm load torque and zero to 10rpm speed demand change

Further tests were undertaken for 30Nm, 50Nm and 80Nm load torque set points. In each case, two speed changes were used, viz. zero to 10rpm (which gives a reasonable approximation to magneto-static conditions in steady state) and zero to 500rpm. It should be noted that although the load torque test point was set to 80Nm for final series of tests, controller and calibration difficulties with the AVL dynamometer limited the actual applied torque (as measured by the Magtrol in-line torque transducer) to ~75Nm. These difficulties also prevented higher torques from being applied with the profiled torque feature.

Most of the transient response of the torque, current and speed of the machine for selected combinations of load torque and speed demand are shown in Appendix III, machine with load torque of 75Nm which is the most extreme case is shown in Figure 7.19 and Figure 7.20 for speed demand of 10rpm and 500rpm. The same colour representation for the various traces were adopted except that the current output from the drive is now shown as a yellow signal on the screen, which is derived from the current transducer measurement. The transient period for 500rpm speed demand is 0.56s which is much longer compare to the 10rpm speed demand. It can be seen that under 500rpm and 75Nm

223

load torque operating point, the phase rms current is 15.5A which leads to a current density of 48.5A/mm^2.

As will be apparent, the prototype TORUS machine managed to operate successfully under transient conditions up to 75Nm at 500rpm.
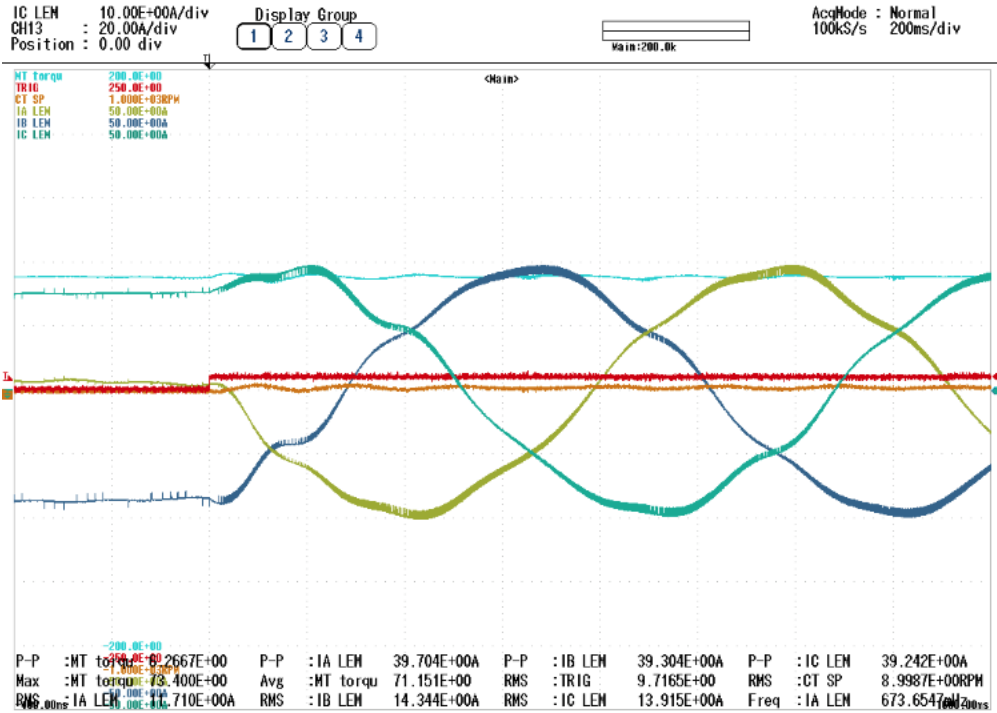
Figure 7. 19. Transient response under 75Nm load torque with speed demand change to 10rpm
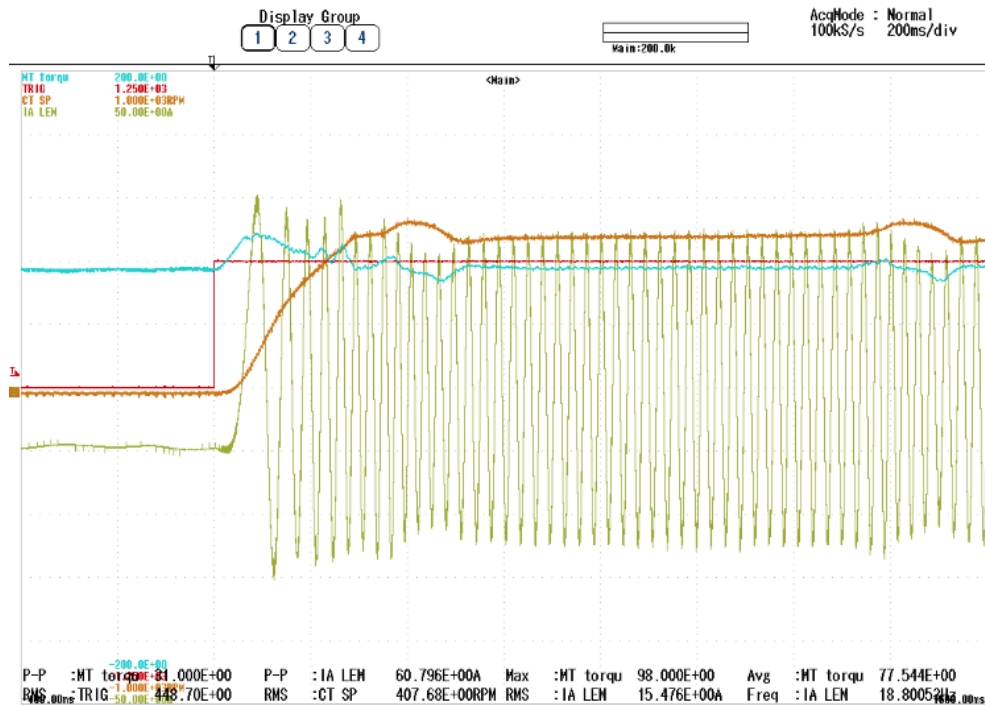
Figure 7. 20. Transient response under 75Nm load torque with speed demand change to 500rpm

The average torque and rms drive current can be extracted from the transient measurement. This allows the torque versus current density characteristics to be significantly extended in terms of current density. Figure 7. 21. shows the torque characteristics which demonstrate that the relationship between torque and current (strictly current density) remains essentially even up to an rms current density of 60A/mm^2. As will be apparent, the measured torque shows excellent agreement with the three-dimensional finite element predictions, including the effect of eddy currents which cause a significant reduction in torque for a given current density with rotational speed of 500rpm.
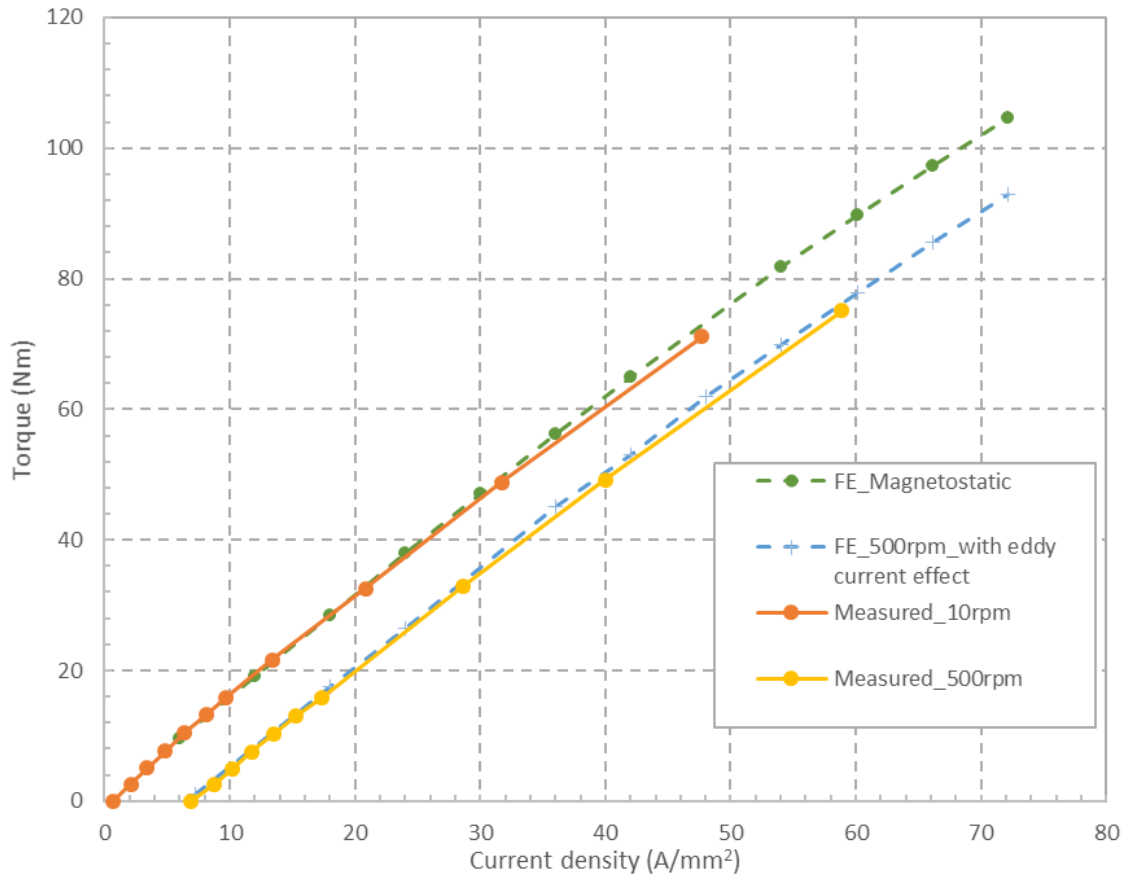
Figure 7. 21. Finite element predicted and measured torque versus current density characteristics at 10rpm and 500rpm

7.8 Thermal performance at high load torques

The torque performance of the machine under high current density overload conditions was experimentally validated in previous sections. In this section, the transient thermal behaviour of the machine under high current density is addressed.

The temperature rise within different regions of machine over for the high load torque test (50Nm, 75Nm) was measured experimentally using an array of 7 thermocouples distributed around the machine as described in Table 7. 4 and shown in Figure 7. 22.

Table 7. 4. Location of the distributed thermocouples

Thermocouple number	Location
1	In the bottom layer of a coil from phase A – between the stator core and coil
2	In the bottom layer of a coil from phase B – between the stator core and coil
3	Between the 2nd and 3rd layer of a phase B coil
4	Between the 2nd and 3rd layer of a phase C coil
5	On the surface of the PEEK insulation
6	On the surface of the stator core – on the rectangular projection near the interface between the casing and the stator core
7	Outside the stator casing to measure ambient

The thermocouples in the coil were embedded during the winding process and are held in position by the coil conductors and/or the varnish applied during coil manufacture. The thermocouples on the surface of the PEEK and the stator core, were bonded onto the surface using a heat resistant epoxy adhesive Araldite 2014-1[65]. The ambient temperature measuring thermocouple is fixed near the surface of the polycarbonate cover as shown in Figure 7. 23.
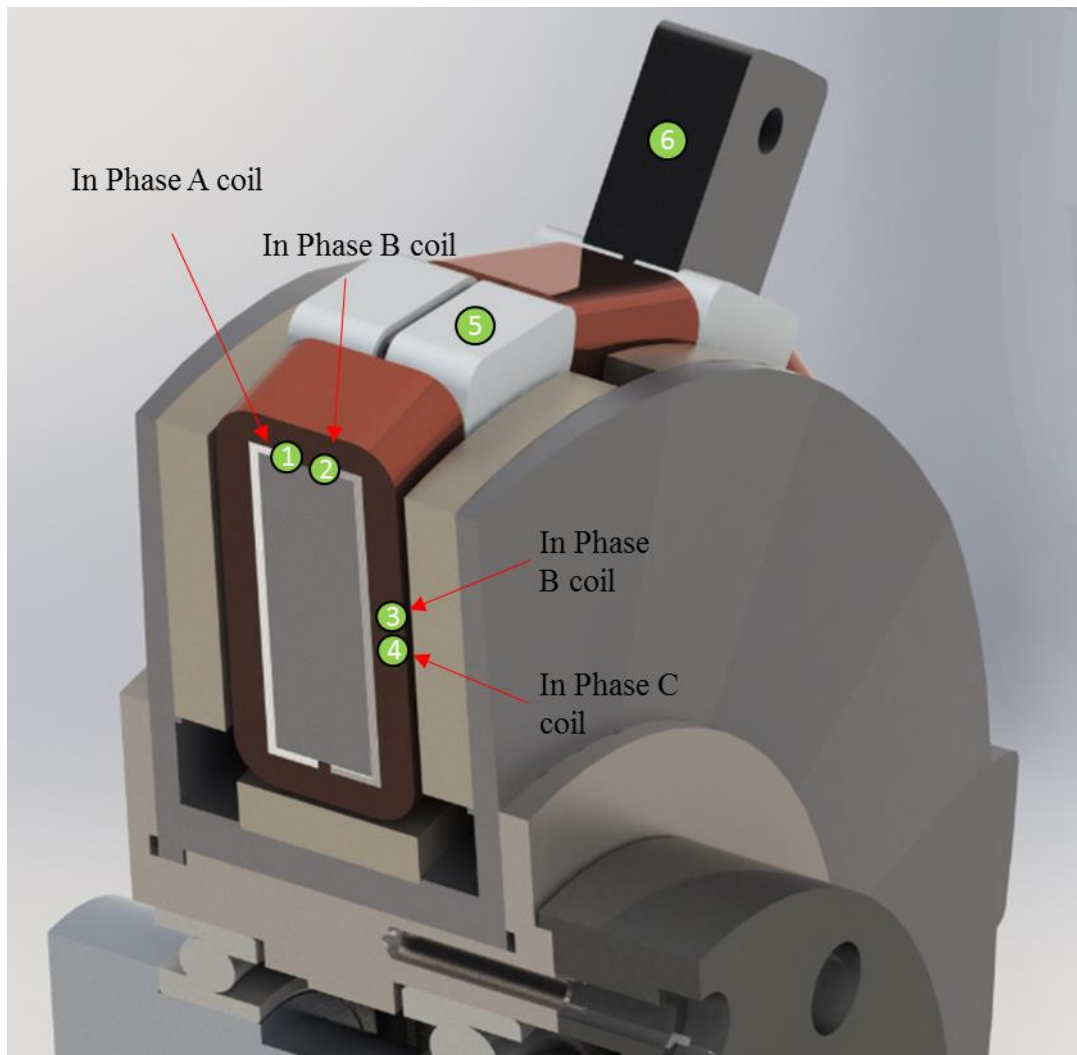
Figure 7. 22. Locations of the thermocouples indicated on the section view of the prototype machine
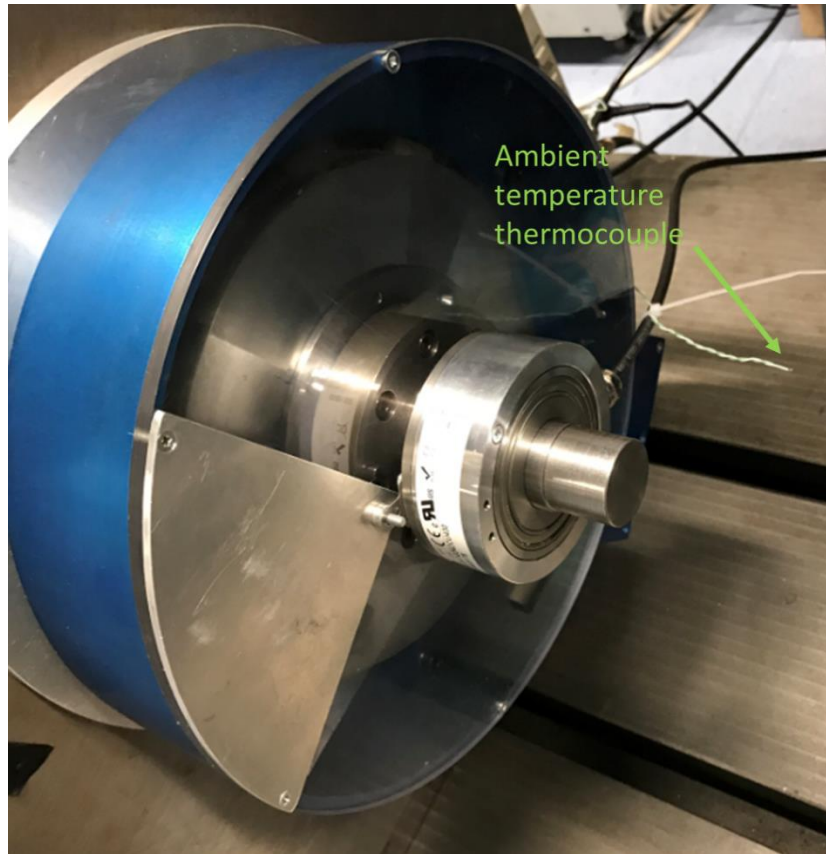
Figure 7. 23. Ambient temperature thermocouple position (attached to encoder cable)

The temperature rise for the thermocouples with 50Nm load torque with the speed demand changes from 0rpm to 500rpm are shown in the Figure 7. 24. Between 0 and 1 second, the torque is increasing which corresponds to the interval in which the AVL dynamometer ramps up the load torque. At 1 second, the targeted 50Nm is reached and the load torque is kept constant for the set time. It should be noted that during this period, although the load torque from AVL dynamometer is increasing, the machine is maintained standstill due to the speed control from the Control Techniques Drive. In order to maintain the rotor at standstill against the action of the 50Nm load applied by the AVL dyno, the TORUS machine must produce a matching 50Nm which results in the rapid increase in the temperature. After 2 seconds, there is a dramatic increase in the measured torque, with the instantons torque increasing up to ~70Nm. This additional torque is required to accelerate the machines from 0rpm to 500rpm and its magnitude is determined by the speed control loop in the Control Techniques converter. Once the torque is stabilised at 2.5s, the machine is operating at a fixed 50Nm, 500rpm operating point from 2.5s to 17s.

The highest temperature is measured is in the coils, with some spread between the different coil thermocouples. In general, the thermocouples located in the bottom layer of the coil measure the higher temperatures. The highest temperature rise in the coil during 14.5 seconds is 116.7°C from 44.6°C to 161.3°C. As for the PEEK insulation, its temperature during a transient period does not change significantly, the temperature only increases about 2°C. Since it is a plastic material, the thermal conductivity is far less than a metal, which makes it a good thermal insulation. The iron loss generated in the stator core still could find its own path out through the aluminium casing, while the copper loss generated in the coil is much localised as the only contact surface is the PEEK insulation. After 17s, the load torque profile starts to drop, the temperature of the coil keeps rising.
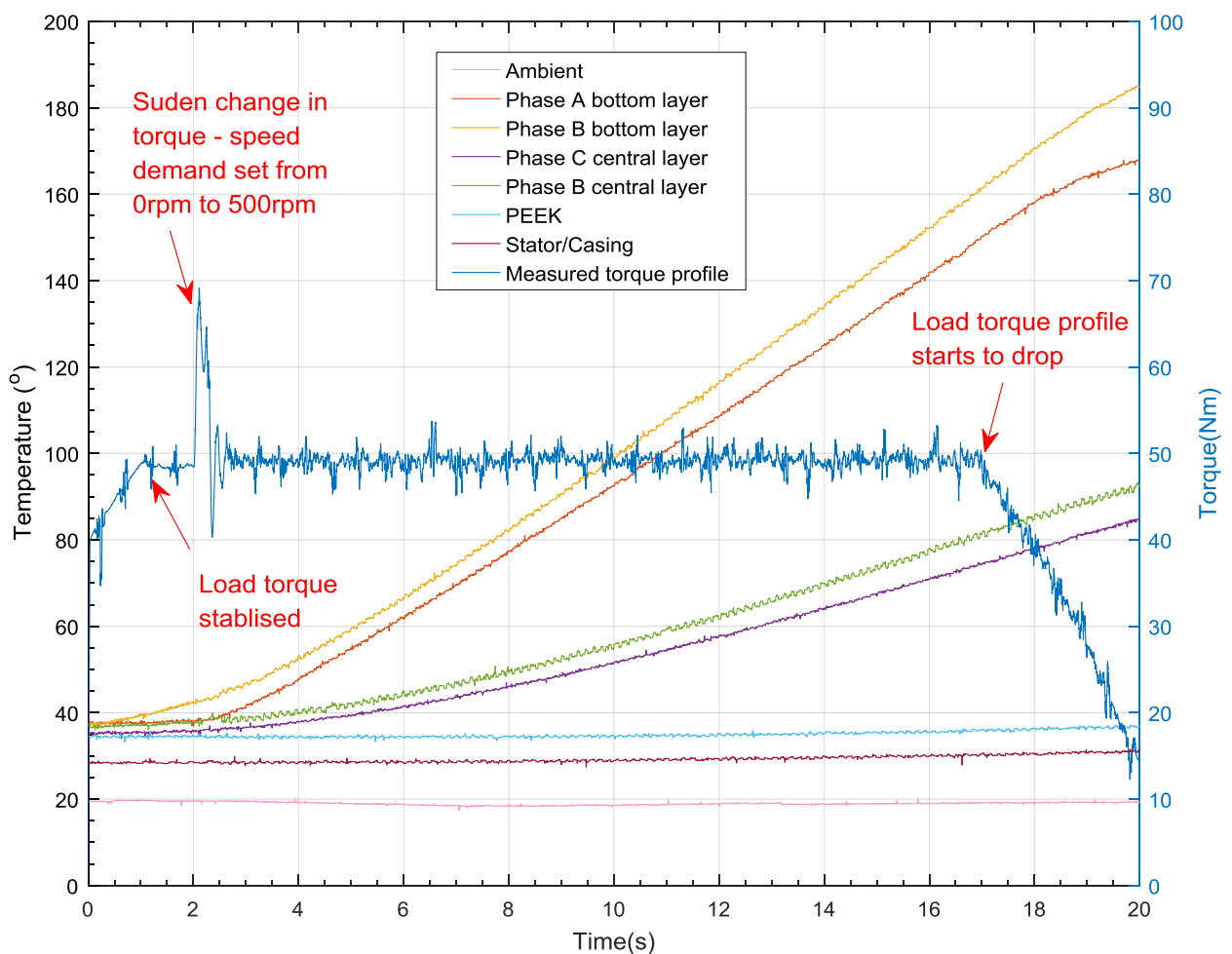
Figure 7. 24. Temperature rise within machine under 50Nm load torque profile within 20 seconds

The corresponding temperature data for the 75Nm load torque test is recorded and shown in Figure 7. 25. Since the load torque is increased, the duration over which 75Nm was applied was reduced to 5s. As will be apparent, the compared to the 50Nm load torque test, the temperature rises much more rapidly in this 75Nm case. Once the speed demand is raised to 500rpm, the transient torque which includes the accelerating torque demanded by the converter speed loop increases to 92.8Nm. The rate of temperature rise is steeper after the torque has settled with the machine operating at a near steady-stator of 75Nm at 500rpm. The coil temperature rises from 47.1°C to 116.2°C within 4.5 seconds. Rather than simply let the load torque ramp down to zero, several measures were taken during the ramp down time of the load torque to avoid excessive temperature rise. The speed demand was also reduced to 10rpm, with the resulting torque demand from the speed loop causing the torque to oscillate for a while. To further reduce the temperature rise rate, the AVL load torque demand was dropped to zero from 75Nm to more abruptly remover the principal sources of loss.
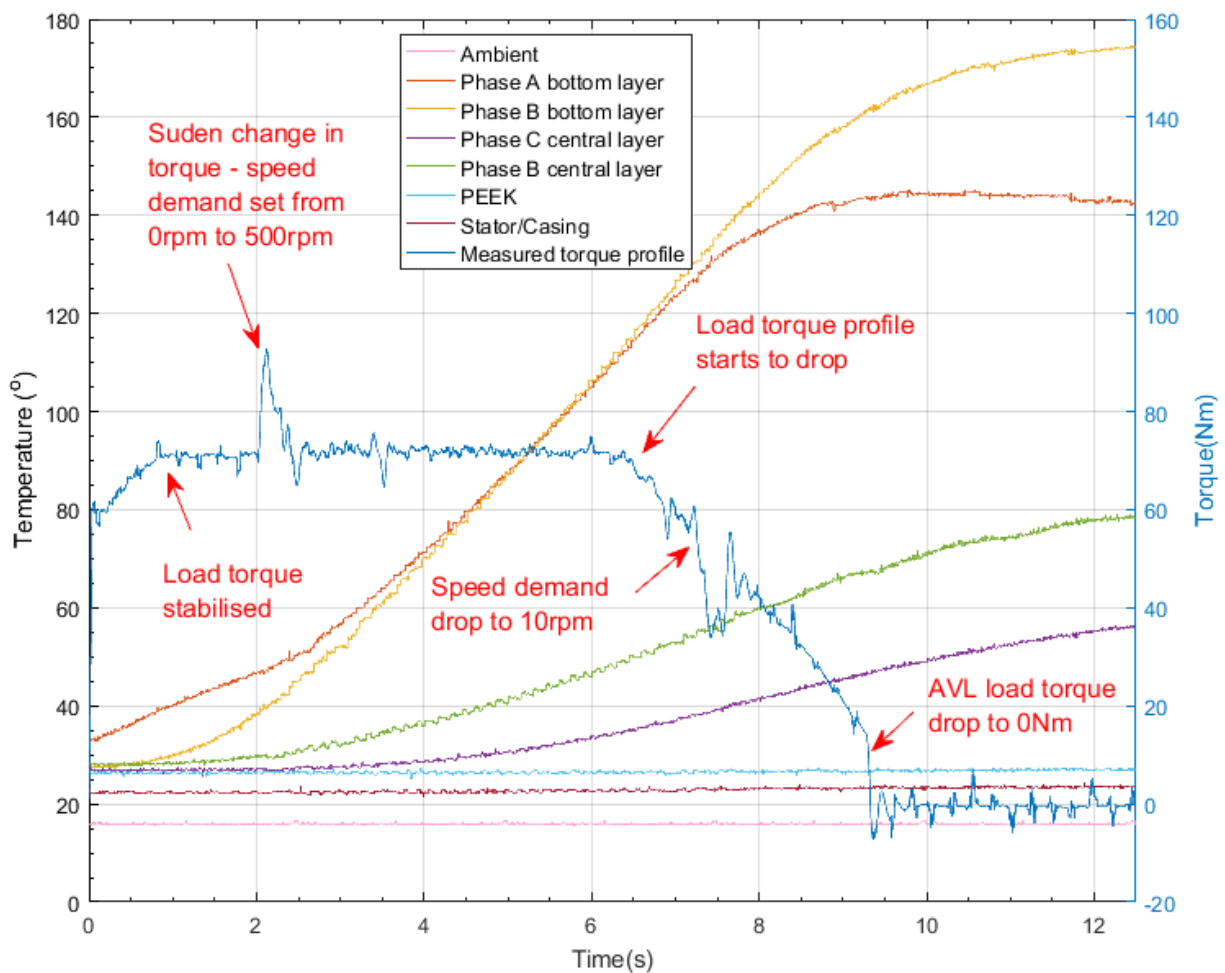
Figure 7. 25. Temperature rise within machine with 75Nm load torque profile

231

An estimate of slope of the temperature rise under continuous 50Nm, and 75Nm load torques can be obtained thee measure temperature data. From Figure 7. 24, the temperature rise in interval 6s to 8s is 15.2^0C , giving a temperature rate of rise of 7.6^0C/s. In the case of a load torque of 75Nm, the rate of rise is 18^0C/s. These rates can be used to provide an indication of the duration for which these torques could be sustained for a coil temperature rise from 20^0C to 200^0C. For a constant load torque of 50Nm, the coil temperature is estimated to rise up to 200^0C within 23.7 seconds while for a constant load of 75Nm, the coil temperature will reach to its limit within 10 seconds. Although this estimation does not account for the variation in copper resistance due temperature, it nevertheless provides a reasonable estimate of transient thermal behaviour. It also provides some experimental reassurance that the prototype TORUS machine can produce 50Nm for a duration of 20-30s as set out in the original performance specification.

On the other hand, the measured results also provides experimental validation with the FE predicted temperature rise in machine from Chapter 4. The 3D thermal modelling predicted time for the machine winding to rise up to 200^0C is within 30 seconds at ambient temperature of 20^0C, which is within a reasonable margin with 23.7 second obtained from testing results. The temperature rise rate in the interval of 6s to 8s predicted by FE is 5.1^0C/s and it is lower than the measured 7.6^0C. One of the reason for the differences between the FE predicted results and testing results comes from a higher copper starting temperature. During the thermal test, the copper is not completely cooled down to ambient temperature, the initial temperature of the winding starts at around 35^0C while in FE, the initial temperature of all parts are assumed to be ambient temperature of 20^0C.

CHAPTER 8.   CONCLUSION

This thesis has described an in-depth investigates into several aspects of the performance of permanent magnet axial field machines. The programme of research was undertaken within the context of a specification for a VGV e-actuation system aero engine. This specification is characterised by an intermittent duty and low speed operation and these features have inevitably resulted in studies into several issues for which there is limited published information, in particular very-short term operation at extremely high current densities and the use of a solid rotor core and the eddy current issues that arise.

The design studies of chapters 2 and 3 demonstrated that, as expected, slotted axial field machines (both TORUS and YASA variants) can achieve higher torque densities than an equivalent slotless axial field machines. However, the differences narrow and then cross-over as the machines are pushed to very high levels of current density. The ability of slotless machines to maintain a near linear relationship between torque and current up to extreme levels of current density makes them well-suited to intermittent actuation type applications.

The design studies undertaken demonstrated that the nature of the magnetic field distributions and coil locations in slotted TORUS machines required a re-appraisal of the conventional approaches to the selection of slot/pole combinations. The most significant finding was that a 12slot-8pole combination, which is very common in radial field machines, turns out not to be suitable for a slotted axial field machine.

A series of alternative variants of a double-sided slotless axial field machines were investigated using three-dimensional finite element analysis to optimise the geometry. This optimisation considered the use of radially magnetised on either the inner bore of the core or around the edge to generate torque from the axially oriented conductors of the toroidal winding. It was demonstrated that the highest torque density (though not necessarily the highest overall torque) was achieved by incorporating an array of magnets on the inner bore. Following optimisation, a torque density of 9.27Nm/kg was predicted for the short-term design rms current density of 30A/mm^2.

Chapters 3 and 4 explored the influence of eddy currents in a solid Cobalt-Iron core. There is very little quantitative information in literature on the performance of

electrical machines with solid cores. Extensive transient, three-dimensional analysis was used to demonstrate that although there is some reduction in the torque produced at 500rpm due to eddy current screening, a design based on a solid core was still a viable proposition electromagnetically with other mechanical, manufacturing and thermal benefits. Although the eddy current screening proved not to be excessive, it was shown that core losses in the machine, which were dominated by eddy currents, would be unsustainable for continuous operation. In practice, a laminated core may have been preferred if a particular product was being developed, but a solid core was selected for the prototype in order to validate these novel findings and explore the influence of significant core eddy current loss experimentally.

A transient finite element thermal model was developed in chapter 4 with thermal capacity of the machine being a key factor because of the transient nature of the operation. This thermal model demonstrated that at a 50Nm and 500rpm operating point, the coil temperature increased at an average rate of ~6.2°C/s which would result in an interval of ~29s for the peak coil temperature to rise to 200°C.

It is well recognised that axial field machines pose many mechanical challenges. The analysis presented in Chapter 5 demonstrated that advanced three-dimensional analysis is useful in terms of ensuring that the magnetic components are themselves sufficiently stiff to avoid excessive deflection. The analysis demonstrated that the large effective magnetic airgap of a slotless topology is helpful in terms of the reducing the axial force on the rotor core. The profiling of the rotor core thickness introduced in chapter 4 could still be implemented without excessive bending or the need for additional structural support.

The manufacture of the prototype machine in chapter 6 discussed several interesting features, including the use of a PEEK insulating cover to provide robust secondary insulation, the design of bearing system to accommodate the axial loads on individual rotor elements and a means of assembling the entire machine.

Chapter 7 described the design and set-up of a comprehensive experimental test-rig for measuring the performance of the prototype machine. Excellent agreement was obtained between predicted and measured open-circuit and on-load electromagnetic performance, including at speeds of 500rpm where eddy current effects are significant. Of particular note was the ability to predict the current density required to produce net torque at different speeds (i.e. the current density offsets at zero output torque in Figure

7.25). This demonstrated the value of full transient three-dimensional electromagnetic finite element modelling. The prototype machine demonstrated linearity of torque with current and mechanical integrity (in particular an ability to transmit high torques from an airgap winding) up to the limit of the test equipment available. The measured rate of rise of temperature in the coil at a 50Nm, 500rpm operating point was 7.6°C/s which is in reasonable agreement with the value predicted by thermal modelling in chapter 4. Overall, this programme of research has advanced the understanding of the performance of axial field machines and demonstrated the value of three-dimensional finite element modelling for the most challenging electromagnetic conditions such as the influence of eddy current screening in a solid core on torque production.

On the basis of research undertaken, there are several aspects that would merit future investigations:

- Methods for effectively laminating a stator core which provide sufficient mechanical stiffness to deal with the axial forces calculated in chapter 5.

- The integration of a series of fine slits into the stator core to break up eddy current paths while also maintaining sufficient mechanical stiffness.

- The use of winding thermal capacity as a design objective for optimisation. The focus in the design reported in chapters 3 and 4 were on torque density. For transient thermal performance, it may be helpful to consider an increased thermal mass as a design objective.

- Although the machine thermal behaviour is dominated by the thermal capacity, there would be benefits in increasing the cooling in terms of the repetition rate of the duty cycle even if this has limited effect on the transient behaviour. A more comprehensive thermal model with greater focus on surface heat transfer coefficients would be an interesting and challenging piece of research and essential for detailed optimisation of the cooling system.

- Ultimately, achieving much higher torque densities will require conductor insulation that can withstand much higher temperatures. A detailed assessment of the performance that could be obtained with high temperature (400°C) insulted wire would make a useful contribution. In this regard it is worth noting that the very simple coil geometry might well be a good fit to high temperature wire, which tends to more prone to damage during winding and coil insertion.

REFERENCE

[1] "HPC Variable Stator Vane Operation." [Online]. Available: https://vimeo.com/96325701.

[2] R. Newman, "The More Electric Engine Concept," *SAE Tech. Pap.*, no. 724, 2004.

[3] Z. Nasiri-Gheidari and H. Lesani, "A Survey on Axial Flux Induction Motors," *Prz. Elektrotechniczny (Review Electr. Eng.*, vol. 88, no. 2, pp. 300–305, 2012.

[4] T. Lambert, M. Biglarbegian, and S. Mahmud, "A Novel Approach to the Design of Axial-Flux Switched-Reluctance Motors," *Machines*, vol. 3, no. 1, pp. 27–54, 2015.

[5] F. Profumo, Z. Zhang, and A. Tenconi, "Axial-flux Machines Drives: A New Viable Solution for Electric Cars," *IEEE Trans. Ind. Electron.*, no. Vol. 44, No. 1, pp. 39–45, 1997.

[6] H. Hakala, "Integration of Motor and Hoisting Machine Changes the Elevator Business," in *Proceedings of International Conference on Electrical Machines*, p. Vol. 3, pp. 1242–1245.

[7] B. J. Chalmers, W. Wu, and E. Spooner, "An axial-flux permanent-magnet generator for a gearless wind energy system," *IEEE Trans. Energy Convers.*, vol. 14, no. 2, pp. 251–256, 1999.

[8] M. Aydin, S. Huang, and T. a Lipo, "Axial flux permanent magnet disc machines: a review," *Res. Rep.*, pp. 61–71, 2004.

[9] V. B. Honsinger, "Performance of polyphase permanent magnet machines," *IEEE Trans. Power Appar. Syst.*, vol. PAS-99, no. 4, pp. 1510–1518, 1980.

[10] S. Huang, J. Luo, F. Leonardi, and L. T.A, "A general approach to sizing and power density equations for comparison of electrical machines," *IEEE Trans. IA-34*, vol. No.1, pp. 92–97, 1998.

[11] S. Huang, J. Luo, F. Leonardi, and T. A. Lipo, "A comparison of power density for axial flux machines based on general purpose sizing equations," *IEEE Trans. Energy Convers.*, vol. 14, no. 2, pp. 185–192, 1999.

[12] J. F. Gieras, R.-J. Wang, and M. J. Kamper, *Axial Flux Permanent Brushless Machine*. Kluwer Academic, 2004.

[13] E. E. Group, "DESIGN OF ELECTRIC MACHINES : Axial Flux Machines Contents Electric Energy Group in FIGURES," pp. 0–22.

[14] A. S. Holmes, G. Hong, and K. R. Pullen, "Axial-flux permanent magnet machines for

micropower generation," *J. Microelectromechanical Syst.*, vol. 14, no. 1, pp. 54–62, 2005.

[15] a. Mahmoudi, N. a. Rahim, and W. P. Hew, *Axial-flux permanent-magnet machine modeling, design, simulation and analysis*, vol. 6, no. 12. 2011.

[16] T. J. Woolmer and M. D. McCulloch, "Analysis of the yokeless and segmented armature machine," *Proc. IEEE Int. Electr. Mach. Drives Conf. IEMDC 2007*, vol. 1, pp. 704–708, 2007.

[17] T. A. C. Maia *et al.*, "Electromechanical design for an optimized axial flux permanent magnet torus machine for 10kW wind turbine," *2011 Int. Conf. Electr. Mach. Syst. ICEMS 2011*, 2011.

[18] A. Mahmoudi, H. W. Ping, and N. A. Rahim, "A comparison between the TORUS and AFIR axial-flux permanent-magnet machine using finite element analysis," *2011 IEEE Int. Electr. Mach. Drives Conf. IEMDC 2011*, pp. 242–247, 2011.

[19] S. H. S. Huang, M. Aydin, and T. A. Lipo, "TORUS Concept Machines: Pre-Prototyping Design Assessment for Two Major Topologies," *Conf. Rec. 2001 IEEE Ind. Appl. Conf. 36th IAS Annu. Meet. (Cat. No.01CH37248)*, vol. 3, no. 59877014, pp. 1619–1625, 2001.

[20] J. Zhao, B. Li, and Z. Gu, "Research on an axial flux PMSM with radially sliding permanent magnets," *Energies*, vol. 8, no. 3, pp. 1663–1684, 2015.

[21] A. G. Jack, B. C. Mecrow, and C. P. Maddison, "Combined radial and axial permanent magnet motors using soft magnetic composites," *"Electrical Mach. Drives, 1999. Ninth Int. Conf. (Conf. Publ. No. 468),"* no. 468, p. 25, 1999.

[22] L. Ferraris, E. Pošković, and F. Franchini, "New Soft Magnetic Composites for electromagnetic applications with improved mechanical properties," *AIP Adv.*, vol. 6, no. 5, 2016.

[23] "The YASA Product Range." [Online]. Available: http://www.yasamotors.com.

[24] J. A. Tapia, M. Aydin, S. Huang, and T. A. Lipo, "Sizing equation analysis for field controlled PM machines: A unified approach," *IEMDC 2003 - IEEE Int. Electr. Mach. Drives Conf.*, vol. 2, pp. 1111–1116, 2003.

[25] S. Huang, J. Luo, F. Leonardi, and T. A. Lipo, "A general approach to sizing and power density equations for comparison of electrical machines," *IEEE Trans. Ind. Appl.*, vol. 34, no. 1, pp. 92–97, 1998.

[26] A. Mahmoudi, S. Kahourzade, N. A. Rahim, W. P. Hew, and N. F. Ershad, "Slot-less torus solid-rotor-ringed line-start axial-flux permanent-magnet motor," *Prog. Electromagn. Res.*, vol. 131, no. August, pp. 331–355, 2012.

[27] Cobham Technical Service, "Opera-3d Reference," no. May. 2016.

[28] Cobham Technical Service, "Opera-3d User Guide," no. May. 2016.

[29] Magnetic Materials Producers Association, "Standard Specifications for Permanent Magnet Materials," *Alnico Magnets*, no. 100, p. 7, 2000.

[30] K. J. Strnat, "Modem Permanent Magnets for Applications in Electro-Technology," *Proc. IEEE*, vol. 78, no. 6, pp. 923–946, 1990.

[31] G. J. Li, "Electrical Machine Design Lecture Notes." University of Sheffield, 2014.

[32] Vacuumschmelze GmbH & Co., "Rare-Earth Permanent Magnets," vol. 3, no. 1, 2010.

[33] N. Volbers and J. Gerster, "High Saturation , High Strength Iron-Cobalt Alloy for Electrical Machines," *Proc. INDUCTICA, CWIEME*, pp. 1–4, 2012.

[34] M. Persson and P. Jansson, "Soft magnetic composite materials - use for electrical machines," *Proc. 7th Int. Conf. Electr. Mach. Drives*, vol. 1995, no. 412, pp. 242–246, 1995.

[35] G. Cvetkovski and L. Petkovska, "Performance improvement of PM synchronous motor by using soft magnetic composite material," *IEEE Trans. Magn.*, vol. 44, no. 11 PART 2, pp. 3812–3815, 2008.

[36] V. Iancu, T. Canta, D. C. Popa, and L. Szabó, "Soft Magnetic Composites Used for the Iron Core of the Electrical Machines," pp. 3–6.

[37] R. Kobler, D. Andessner, J. Passenbrunner, and W. Amrhein, "Modeling, simulation and design of an axial flux machine using soft magnetic composite," *2011 IEEE Veh. Power Propuls. Conf.*, pp. 1–6, 2011.

[38] A. G. Jack *et al.*, "Permanent-magnet machines with powdered iron cores and prepressed windings," *IEEE Trans. Ind. Appl.*, vol. 36, no. 4, pp. 1077–1084, 2000.

[39] T. A. Lipo, *Introduction to AC Machine*. John Wiley & Sons, 2017.

[40] J. M. Seo, I. S. Jung, H. K. Jung, and J. S. Ro, "Analysis of Overhang Effect for a Surface-Mounted Permanent Magnet Machine Using a Lumped Magnetic Circuit Model," *IEEE Trans. Magn.*, vol. 50, no. 5, 2014.

[41] J. P. Wang, D. K. Lieu, W. L. Lorimer, and A. Hartman, "Influence of the permanent magnet overhang on the performance of the brushless dc motor," *J. Appl. Phys.*, vol. 83, no. 11, pp. 6362–6364, 1998.

[42] P. Pillay and R. Krishnan, "Modeling, simulation, and analysis of permanent-magnet motor drives. I. The permanent-magnet synchronous motor drive," *Ind. Appl. IEEE Trans.*, vol. 25, no. 2, pp. 265–273, 1989.

[43] H. Semat and R. Katz, *Physics , Chapter 11 : Rotational Motion (The Dynamics of a*

Rigid Body). Robert Katz Publications, 1958.

[44]   I. Petrov, D. Egorov, J. Link, R. Stern, S. Ruoho, and J. Pyrhonen, "Hysteresis Losses in Different Types of Permanent Magnets Used in PMSMs," *IEEE Trans. Ind. Electron.*, vol. 64, no. 3, pp. 2502–2510, 2017.

[45]   J. Pyrhonen *et al.*, "Hysteresis losses in sintered NdFeB permanent magnets in rotating electrical machines," *IEEE Trans. Ind. Electron.*, vol. 62, no. 2, pp. 857–865, 2015.

[46]   G.-J. Li, *Electrical Machine Design*. University of Sheffield, 2014.

[47]   M. Popescu, D. G. Dorrell, L. Alberti, N. Bianchi, D. A. Staton, and D. Hawkins, "Thermal analysis of duplex three-phase induction motor under fault operating conditions," *IEEE Trans. Ind. Appl.*, vol. 49, no. 4, pp. 1523–1530, 2013.

[48]   "Specific Heat of common Substances." [Online]. Available: https://www.engineeringtoolbox.com/specific-heat-capacity-d_391.html.

[49]   H. Search, C. Journals, A. Contact, M. Iopscience, T. Table, and I. P. Address, "The specific heat capacity of GE varnish (200-400K) The specific heat capacity of GE varnish," *Physics (College. Park. Md).*, vol. 885, pp. 9–11, 1982.

[50]   N. Rostami, M. R. Feyzi, J. Pyrhonen, A. Parviainen, and M. Niemela, "Lumped-parameter thermal model for axial flux permanent magnet machines," *IEEE Trans. Magn.*, vol. 49, no. 3, pp. 1178–1184, 2013.

[51]   L. F. M. da Silva and R. D. Adams, "Measurement of the mechanical properties of structural adhesives in tension and shear over a wide range of temperatures," *J. Adhes. Sci. Technol.*, vol. 19, no. 2, pp. 109–141, 2005.

[52]   J. Paulides, "permanent magnet generator with uncontrolled rectifier for ' more-electric ' ship applications," The University of Sheffield, 2005.

[53]   H. Keppola, R. Perälä, L. Söderlund, and H. Vihriälä, "Preliminary test results of an axial flux toroidal stator wind power generator," 2014.

[54]   M. A. Mueller, A. S. McDonald, and D. E. Macpherson, "Structural analysis of low-speed axial-flux permanent-magnet machines," *IEE Proceedings-Electric Power Appl.*, vol. 152, no. 6, pp. 139–145, 2005.

[55]   Victrex, "Materials Properties Guide," 2017.

[56]   WS hamshiper Inc., "TYPICAL PROPERTIES of TORLON ® PAI."

[57]   Quadrant engineering plastic products, "PBI Celazole."

[58]   Plastics International, "Tecatron ® PPS (Polyphenylene Sulfide)."

[59]   Cotronics corp., "SPECIALTY HIGH TEMP. AHESIVES DATASHEET."

[60]   Emerson, "User guide: Unidrive SP Model sizes 0 to 6," vol. 14, 2013.

[61] "Quadrature   Encoder   Overview."   [Online].   Available: http://www.dynapar.com/Technology/Encoder_Basics/Quadrature_Encoder/.

[62] ROTAPULS, "Incremental encoder Series C81."

[63] AVL, "DYNOEXACT APA PRODUCT DESCRIPTION," 2009.

[64] MAGTROL, "TM 309 – TM 313 In-Line Torque Transducers."

[65] HUNTSMAN, "Araldite ® 2014 a/b," 2014.

APPDIX I: MATLAB SCRIPT FOR CALCULATING IRON LOSS CALCULATION

```matlab
clear;
elems_amount=25440;
timestep=30;
symmetry=8;
f=100/3;          %Frequency
speed=500;
tstart=1;   %nth timestep, the start timestep for calculating average loss


%==============Define material conductivity==================

Rho=0.42*10^-3;                %Electrical resistivity of cobalt iron, unit
ohm.mm



%=============LOAD ALL TABLES======================
Total=[];
h=waitbar(0,'Step 1 Forming table');
for i=1:timestep

    table=fopen(sprintf('time%d.table.',i),'r');
    fgets(table);% Skip unused strings
    fgets(table);% Skip unused strings
    fgets(table);% Skip unused strings
    fgets(table);% Skip unused strings
    fgets(table);% Skip unused strings
    fgets(table);% Skip unused strings
    fgets(table);% Skip unused strings
    fgets(table);% Skip unused strings
    fgets(table);% Skip unused strings
    fgets(table);% Skip unused strings
    fgets(table);% Skip unused strings
    fgets(table);% Skip unused strings
    fgets(table);% Skip unused strings
    fgets(table);% Skip unused strings
    buffer=(fscanf(table,'%f %f %f %f %f %f %f %f %f %f %f %f',[12, inf]))';
    %number of %f means number of column
    Total=vertcat(Total,buffer); % Stack tables into one table
    fclose(table);

waitbar(i/timestep,h);


end
close(h);


%==============DEFINE TABLE VARIABLES=============
elems_num=Total(:,1);                      % Element number in opera
elems_vol=Total(1:elems_amount,2);    % Element volume in opera
Bmod=Total(:,3);                           % Flux density modulus
Jmod=Total(:,4);                           % Current density modulus
x=Total(1:elems_amount,5);
y=Total(1:elems_amount,6);
z=Total(1:elems_amount,7);
Bxtot=Total(:,8);
Bytot=Total(:,9);
Bztot=Total(:,10);
```

```matlab
LossOperaAll=Total (:,12);

%===============DEFINE CONSTANTS===========

Kh = 0.016;      % Hysteresis loss coefficient
Kex = 3.7e-5;    % Excess loss coefficient
a = 1.405;
b = 0.075;



%===============HYSTERESIS LOSS CALCULATION==================

Density=8120;    %CoFe density in Kg/m^3

h=waitbar(0,'Step 2 Forming hysteresis B table');
for j=1:elems_amount
    for i=1:timestep
        elems_Bmod(i,j)=Bmod(elems_amount*(i-1)+j);  %Forming  flux  density
table
    end

waitbar(j/elems_amount,h);


end
 close(h);

Bpeak=(max(elems_Bmod))';
c=a+b*(Bpeak);

Ph=Kh*power(Bpeak,c)*f;                        % Hysteresis loss in W/Kg

h=waitbar(0,'Step 3 Calculating hysteresis loss');
for j=1:elems_amount

    PhAve(j,1)=Ph(j,1)*elems_vol(j,1)*10^-9*Density*symmetry;    %   Total
hysteresis loss in W

waitbar(j/elems_amount,h);

end
close(h);
PhSum=sum(PhAve);



%================= EDDY CURRENT LOSS =======================



h=waitbar(0,'Step 4 Forming current density table');

for j=1:elems_amount
    for i=1:timestep
        elems_Jmod(j,i)=Jmod(elems_amount*(i-1)+j);        %Forming  current
density table
    end

 waitbar(j/elems_amount,h);
```

242

```matlab
    end
close(h);


Ped_per_volume=power(elems_Jmod,2)*Rho;                 %J^2*Pho

h=waitbar(0,'Step 5 Calculating eddy current loss');
for j=1:elems_amount
    for i=1:timestep

Ped(j,i)=Ped_per_volume(j,i)*elems_vol(j,1)*symmetry;    %calculating  eddy
current loss, Ped per volume*volume
    end

waitbar(j/elems_amount,h);

end
close(h);

PedSum=sum(Ped);                              % Sum of all elements eddy current
loss

PedTot=mean(PedSum);
PedBuf=Ped(:,tstart:timestep);
PedAve=mean(PedBuf,2);                        % Average eddy current loss for
each element
plot(0:timestep-1,PedSum(1,:),'b');
xlabel('Timestep','fontsize',12);
ylabel('Power loss (W))','fontsize',12);
hold on;
%plot(1:timestep,Ped(1:500,:));               % Plot eddy current loss for
100 elements


A=[x y z Ped(1:elems_amount,2)];             % Element centroid coordinate
and loss in one table

%==================== EXCESS LOSS ============================

omega = (speed/60)*360;             % Speed of machine in degrees mechanical
per second
delta_t_mech = 1/omega;             % delta_t for one mechanical degree
theta_d = 3;                        % angle between successive data points
delta_t = theta_d*delta_t_mech;     % time between successive data points
t = delta_t*(1:timestep);
sigma=2.38*10^6;

%==================Bmod caculation=========================

 elems_Bmodex=(elems_Bmod)';

h=waitbar(0,'Step 6 Flux density table for excess loss');
for i=1:elems_amount

    Bdot(i,:) = gradient(elems_Bmodex(i,:))./gradient(t);       %dB/dt

waitbar(i/elems_amount,h);
```

```
end
close(h);

Pexc_per_volume =sqrt(sigma)*Kex.*abs(Bdot).^(3/2);          %Power loss
in W/m3

h=waitbar(0,'Step 7 Excess loss calculation');
for j=1:elems_amount
    for i=1:timestep
        Pexc(j,i)=Pexc_per_volume(j,i)*elems_vol(j,1)*10^(-
9)*symmetry;   %calculating excess current loss
    end

waitbar(j/elems_amount,h);

end
close(h);


PexcSum=sum(Pexc);
PexcTot=mean(PexcSum);
PexcAve=mean(Pexc(:,tstart:timestep),2);



%=====================TOTAL LOSS=========================

PlossSum=PedSum+PexcSum;          % Total loss at each time step
PlossTot=PedTot+PexcTot+PhSum;
Ploss=PedAve+PhAve+PexcAve;                % Average loss for each element

h=waitbar(0,'Step 8 Calculation loss density for each element');
for j=1:elems_amount

    Ploss_density(j,1)=Ploss(j,1)/elems_vol(j,1);     %calculating   excess
current loss

waitbar(j/elems_amount,h);

end
close(h);

%Ploss_density=Ploss/sum(elems_vol);        % Loss  density(Loss/whole  part
volume) in W/mm3 which is going to be used in opera



%======================Export loss data==================
Loss=[x y z Ploss_density];                    % Total loss table to be
imported in opera

save('Loss.txt','Loss','-ascii','-append');        %  Save   the   loss   to
external .txt file

% plot(1:timestep,PlossSum(1,:),'r');
% hold on;

%===================OPERA LOSS=========================
```

```matlab
h=waitbar(0,'Step 9 Calculation opera loss');
for j=1:elems_amount
    for i=1:timestep
        LossOpera(j,i)=LossOperaAll(elems_amount*(i-
1)+j)*elems_vol(j,1)*symmetry; %Forming loss from opera table
    end

waitbar(j/elems_amount,h);

end
LossOperaSum=sum(LossOpera);

plot(0:timestep-1,LossOperaSum(1,:),'m');

legend('Matlab predicted eddy current loss','Opera predicted loss');

%=======EXCESS LOSS-MORE DETAILED WAY==========


%=======x direction excess loss========
% for j=1:elems_amount
%     for i=1:timestep
%         Bx(j,i)=Bxtot(elems_amount*(i-1)+j);    %Forming Bx for elements
%     end
% end
%
% for i=1:elems_amount
%
%     Bxdot(i,:) = gradient(Bx(i,:))./gradient(t); %dB/dt
% end
%
% Pexcx_per_volume =sqrt(sigma)*Kex.*abs(Bxdot).^(3/2);          %Power
loss in W/m3
%
% for j=1:elems_amount
%     for i=1:timestep
%                 Pexcx(j,i)=Pexc_per_volume(j,i)*elems_vol(j,1)*10^(-
9);   %calculating excess current loss
%     end
% end
%
% PexcxSum=sum(Pexcx);
%
%
% %=========y direction excess loss==========
% for j=1:elems_amount
%     for i=1:timestep
%         By(j,i)=Bytot(elems_amount*(i-1)+j);    %Forming Bx for elements
%     end
% end
%
% for i=1:elems_amount
%
%     Bydot(i,:) = gradient(By(i,:))./gradient(t); %dB/dt
% end
%
% Pexcy_per_volume =sqrt(sigma)*Kex.*abs(Bxdot).^(3/2);          %Power
loss in W/m3
%
```

```
% for j=1:elems_amount
%      for i=1:timestep
%                      Pexcy(j,i)=Pexc_per_volume(j,i)*elems_vol(j,1)*10^(-
9);  %calculating excess current loss
%      end
% end
%
% PexcySum=sum(Pexcy);
%
% % %=========z direction excess loss==========
% for j=1:elems_amount
%      for i=1:timestep
%          Bz(j,i)=Bztot(elems_amount*(i-1)+j);    %Forming Bx for elements
%      end
% end
%
% for i=1:elems_amount
%
%      Bzdot(i,:) = gradient(Bz(i,:))./gradient(t); %dB/dt
% end
%
% Pexcz_per_volume =sqrt(sigma)*Kex.*abs(Bxdot).^(3/2);              %Power
loss in W/m3
%
% for j=1:elems_amount
%      for i=1:timestep
%                      Pexcz(j,i)=Pexc_per_volume(j,i)*elems_vol(j,1)*10^(-
9);  %calculating excess current loss
%      end
% end
%
% PexczSum=sum(Pexcz);
%
%
% for i=1:timestep;
%      Pexc1(1,i)=sqrt(PexczSum(1,i)^2+PexczSum(1,i)^2+PexczSum(1,i)^2);
% end
%
% Pexc1Ave=mean(Pexc1)*symmetry;
% PlossTot1=PedTot+Pexc1Ave+PhSum;
```

APPENDIX II: ENGINEERING DRAWING FOR PROTOTYPE MACHINE

SECTION AL-AL
SCALE 1 : 1

SOLIDWORKS Educational Edition.
For Instructional Use Only.

TORUS design2

Sheet 1 (Hub)

M4 tapped hole

8 of M4*10 tapped hole

8 of M5*15 tapped hole

Ø72

Ø72

80.52

Ø42

Ø55.40

Ø53.50

Ø62

84.52

13

15

5

10.30

5

5

5

5

SECTION D-D
SCALE 1 : 1

2.50

2

4.30

4

M5*15 tapped hole

2.50

SECTION B-B
SCALE 1 : 1

Ø0.85

DETAIL AK
SCALE 5 : 1

39.30

4

Ø80.52

4.30

Ø84.52

SOLIDWORKS Educational Edition.
For Instructional Use Only.

	NAME	SIGNATURE	DATE
DRAWN			
CHK'D			
APPV'D			
MFG			
Q.A			

TITLE:

Hub

MATERIAL: Titanium

DWG NO. TORUS design2   A3

WEIGHT: SCALE:1:5   SHEET 5 OF 15

Sheet 2

6 of M5 counterbore holes to suit M5 capheads @ 72 PCD

Ø8 *8 holes

Ø8

Ø20

Ø72

4 of M4 counterbore holes to suit M4 capheads @20 PCD

1.50

Ø92

Ø88

Ø62

5

7.50

1.50

4 of M4 tapped holes @20 PCD

75

19

SECTION E-E
SCALE 1 : 1

SOLIDWORKS Educational Edition.
For Instructional Use Only.

	NAME	SIGNATURE	DATE
DRAWN			
CHK'D			
APPV'D			
MFG			
Q.A			

TITLE:

MATERIAL: Aluminium

DWG NO. TORUS design2   A3

WEIGHT: SCALE:1:5   SHEET 6 OF 15

2.50

5

DETAIL I
SCALE 1 : 1

Ø91.02

Ø113.52

Ø189.20

P

F

F

DETAIL P
SCALE 2 : 1

0.75

37.84

H

3.25

2.50

0.75

0.75

0.75

DETAIL H
SCALE 2 : 1

35.30

21.45

6.925   6.925

SECTION F-F
SCALE 1 : 2

M   N

M   N

R57.50

R42.26

2.50

3.09

3

SECTION M-M
SCALE 1 : 2

15.24

3

SECTION N-N
SCALE 1 : 2

SOLIDWORKS Educational Edition.
For Instructional Use Only.

6 of M5 through all
tapped hole @235
PCD

11.30

Ø250

Ø235

Ø189.20

Ø113.52

30.40°

60°

AJ

AI

R2

DETAIL AJ
SCALE 1 : 1

R2

10.00

0.02

Ø4

DETAIL AI
SCALE 1 : 1

SOLIDWORKS Educational Edition.
For Instructional Use Only.

SECTION Q-Q
SCALE 1 : 1

2.50

3.09

3

17.24

R57.50

R40.26

Q

R

C

DETAIL U
SCALE 1 : 1

2.50

5

DETAIL T
SCALE 2 : 1

0.75

S

S

T

U

Ø113.52

Ø189.20

0.75

SECTION S-S
SCALE 5 : 1

SECTION R-R
SCALE 1 : 1

4

37.84

17.24

3

	NAME	SIGNATURE	DATE		TITLE:	
DRAWN						
CHK'D						
APPV'D						
MFG						
Q.A						

UNLESS OTHERWISE SPECIFIED:
DIMENSIONS ARE IN MILLIMETERS
SURFACE FINISH:
TOLERANCES:
   LINEAR:
   ANGULAR:

FINISH:

DEBURR AND
BREAK SHARP
EDGES

DO NOT SCALE DRAWING

REVISION

MATERIAL:
Cobalt iron

DWG NO.
TORUS design2

A3

WEIGHT:

SCALE:1:5

SHEET 9 OF 15

AC

8 of 4.3mm
diameter holes to
suit M4 holes

Ø 4.30

Ø 72

AC

3.50

2.50

1

SECTION AC-AC
SCALE 1.5 : 1

Ø 115

Ø 80.52

Ø 62

17.24

UNLESS OTHERWISE SPECIFIED:
DIMENSIONS ARE IN MILLIMETERS
SURFACE FINISH:
TOLERANCES:
   LINEAR:
   ANGULAR:

FINISH:

DEBURR AND
BREAK SHARP
EDGES

DO NOT SCALE DRAWING

REVISION

	NAME	SIGNATURE	DATE		TITLE:	
DRAWN						
CHK'D						
APPV'D						
MFG						
Q.A						

MATERIAL:
Titanium

DWG NO.
TORUS design2

A3

WEIGHT:

SCALE:1:5

SHEET 10 OF 15

Drawing 1 (Sheet 11 of 15)

AF

8 of 4.3mm
diameter holes
to suit M4

M5 tapped hole

R36

Ø4.30

AF

3.50
2
4.50
1

Ø88

Ø84.52

4.50

Ø115
Ø88
Ø62

SECTION AF-AF
SCALE 1.5 : 1

SOLIDWORKS Educational Edition.
For Instructional Use Only.

	NAME	SIGNATURE	DATE		TITLE:	
DRAWN						
CHK'D						
APPV'D						
MFG						
Q.A				MATERIAL: Titanium	DWG NO. TORUS design2	A3

UNLESS OTHERWISE SPECIFIED:
DIMENSIONS ARE IN MILLIMETERS
SURFACE FINISH:
TOLERANCES:
LINEAR:
ANGULAR:

FINISH:

DEBURR AND BREAK SHARP EDGES

DO NOT SCALE DRAWING

REVISION

WEIGHT:

SCALE:1:5

SHEET 11 OF 15

Drawing 2 (Sheet 12 of 15)

X

1.70   6

4

Ø30

Ø43.50

X

R10

4 of M4
counterbore holes
to suite M4
capheads @20 PCD

SECTION X-X
SCALE 2 : 1

SOLIDWORKS Educational Edition.
For Instructional Use Only.

	NAME	SIGNATURE	DATE		TITLE:	
DRAWN						
CHK'D						
APPV'D						
MFG						
Q.A				MATERIAL: Aluminium	DWG NO. TORUS design2	A3

UNLESS OTHERWISE SPECIFIED:
DIMENSIONS ARE IN MILLIMETERS
SURFACE FINISH:
TOLERANCES:
LINEAR:
ANGULAR:

FINISH:

DEBURR AND BREAK SHARP EDGES

DO NOT SCALE DRAWING

REVISION

WEIGHT:

SCALE:1:5

SHEET 12 OF 15

251

SECTION Y-Y
SCALE 1 : 1.5

6 of M6 through
all tapped holes
@186 PCD

4 of M5 counterbore
holes to suit M5
capheads @24 PCD

6 of M5 through
all tapped holes
for shoulder bolt
@235 PCD

R117.50

R93

Ø60
Ø46.60
Ø203
Ø250
Ø257

16.30
3.50
8
10
8
30

UNLESS OTHERWISE SPECIFIED:
DIMENSIONS ARE IN MILLIMETERS
SURFACE FINISH:
TOLERANCES:
 LINEAR:
 ANGULAR:
FINISH:
DEBURR AND BREAK SHARP EDGES
DO NOT SCALE DRAWING
REVISION

NAME | SIGNATURE | DATE
DRAWN
CHK'D
APPV'D
MFG
Q.A

MATERIAL: Aluminium

TITLE:

DWG NO. TORUS design2 A3
SCALE:1:5   SHEET 13 OF 15

SECTION AH-AH
SCALE 2 : 1

4 of M4*12 tapped hole @20 PCD

4 of M5*15 tapped holes @24 PCD

Ø35
Ø30
10
2
31.30
12
13
12
Ø40
Ø46.60
2.50
3.30

UNLESS OTHERWISE SPECIFIED:
DIMENSIONS ARE IN MILLIMETERS
SURFACE FINISH:
TOLERANCES:
 LINEAR:
 ANGULAR:
FINISH:
DEBURR AND BREAK SHARP EDGES
DO NOT SCALE DRAWING
REVISION

NAME | SIGNATURE | DATE
DRAWN
CHK'D
APPV'D
MFG
Q.A

MATERIAL: Aluminium

TITLE:

DWG NO. TORUS design2 A3
SCALE:1:5   SHEET 14 OF 15

252

SECTION AQ-AQ
SCALE 2 : 1

Ø55.40
Ø53.50
Ø62
Ø55.40
Ø46.60
Ø40
Ø30
Ø35
Ø43.50
Ø62
80.52
84.52

AQ
AQ

UNLESS OTHERWISE SPECIFIED:
DIMENSIONS ARE IN MILLIMETERS
SURFACE FINISH:
TOLERANCES:
   LINEAR:
   ANGULAR:

FINISH:

DEBURR AND
BREAK SHARP
EDGES

DO NOT SCALE DRAWING

REVISION

	NAME	SIGNATURE	DATE		TITLE:
DRAWN					
CHK'D					
APPV'D					
MFG					
Q.A			MATERIAL:		DWG NO.

TORUS machine

A3

WEIGHT:

SCALE:1:5

SHEET 15 OF 15

253

APPENDIX III: TRANSIENT RESPONSE OF THE TORQUE, CURRENT AND SPEED OF THE MACHINE
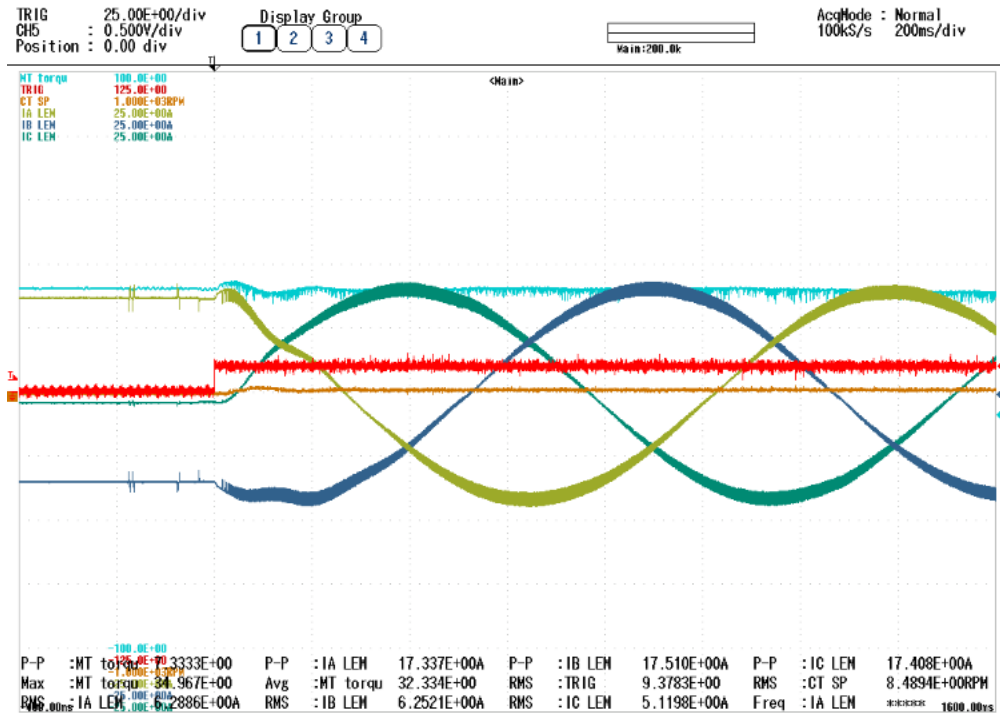
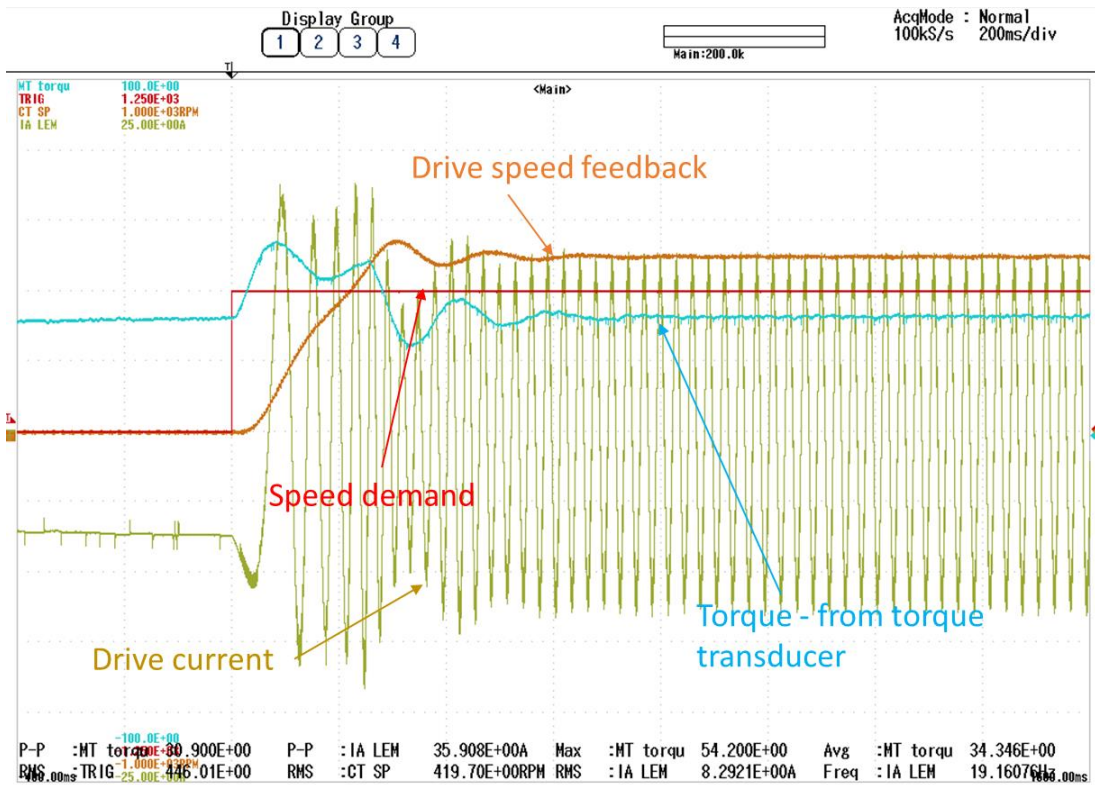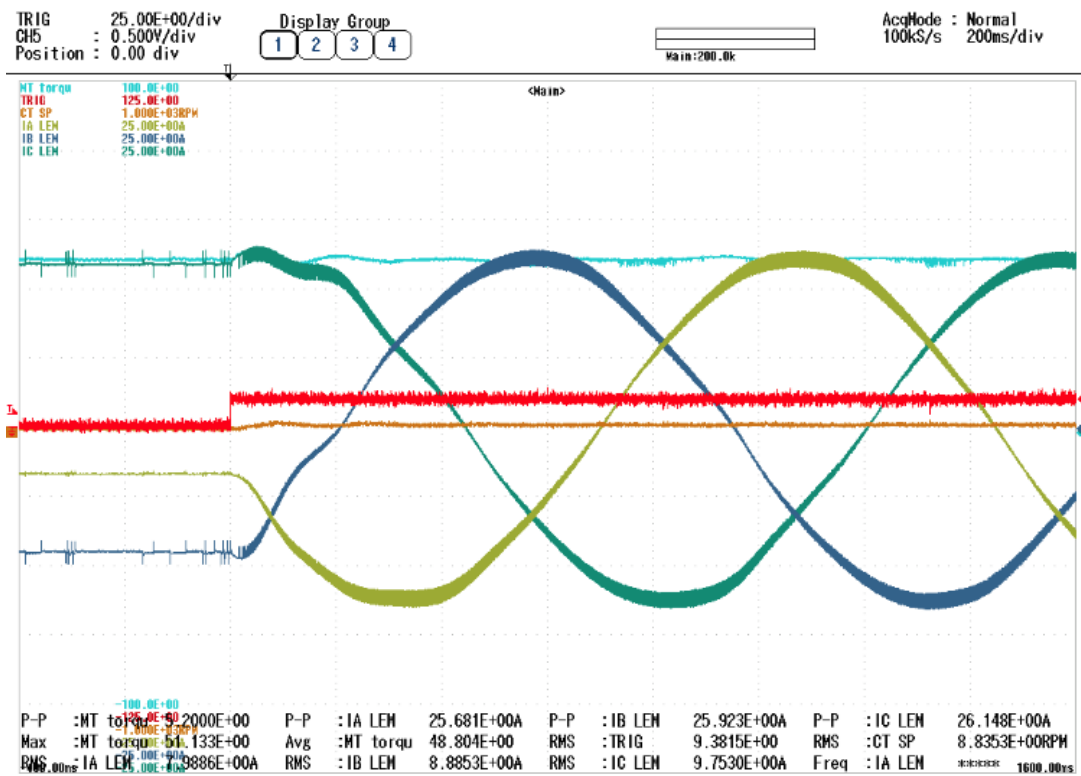**Figure 1. Transient response under 30Nm load torque with speed demand change to 10rpm**
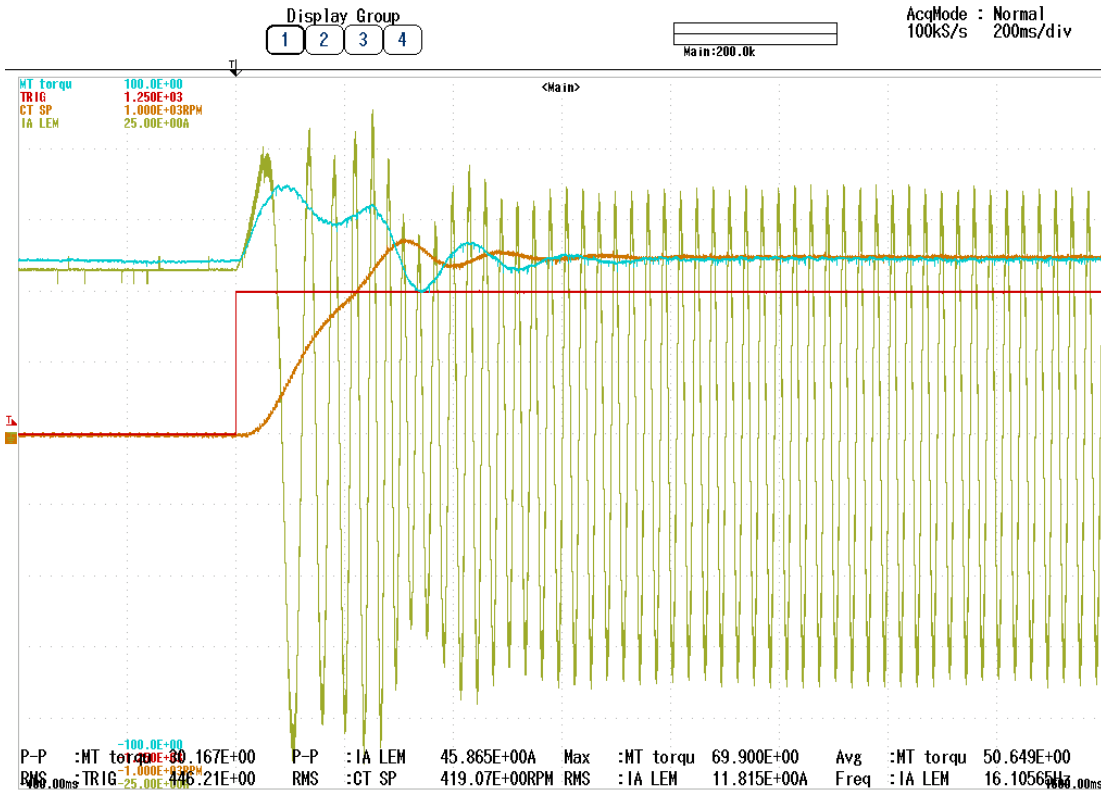
Figure 2. Transient response with 30Nm load torque and speed demand change to 500rpm

Figure 3. Transient response under 50Nm load torque with speed demand change to 10rpm

Figure 4. Transient response under 50Nm load torque with speed demand change to 500rpm